LOW MOMENTUM TRANSFER PROTON-PROTON ELASTIC SCATTERING UP TO 400 GeV

by

Dan A. Gross

Submitted in Partial Fulfillment

of the

Requirements for the Degree

DOCTOR OF PHILOSOPHY

Supervised by Professor A. C. Melissinos

Department of Physics and Astronomy

The University of Rochester

Rochester, New York

1974

FERMILAB
LIBRARY

VITAE

The author was born on December 2, 1946 in Bucharest, Romania. He attended the City College of New York from September 1964 to June 1968. He received a B.S. degree in physics in June 1968. In September of 1968, he began graduate studies in the Department of Physics and Astronomy of the University of Rochester. He has been a Guest Junior Research Associate at Brookhaven National Laboratory and at the National Accelerator Laboratory. During his graduate career the author held two teaching assistantships and four research assistantships. His thesis advisor is Professor Adrian C. Melissinos.

ACKNOWLEDGMENTS

The author wishes to express his gratitude to his thesis advisor, Professor Adrian C. Melissinos for his patience, encouragement and guidance. The advice of and close cooperation with Prof. Melissinos and Prof. Stephen L. Olsen, whose inspired work made this experiment a success, are gratefully recognized and appreciated.

The experiment described in this thesis is a result of the intense planning and execution efforts of many individuals from various institutions: V. Bartenev, A. Kuznetsov, B. Morozov, V. Nikitin, Y. Pilipenko, V. Popov, L. Zolin, The State Committee for Utilization of Atomic Energy of the U.S.S.R.; R. A. Carrigan, Jr., E. Malamud, R. Yamada, The National Accelerator Laboratory; R. L. Cool, K. Goulianos, Rockefeller University; I-H. Chiang, A. C. Melissinos, S. L. Olsen, The University of Rochester.

The author is indebted to Dr. I-H. Chiang and to Professor K. Goulianos for their friendship, and for their advice during some of the stages of data analysis. Mr. D. Nitz also helped in the late stages of the experiment.

Special thanks are due for the engineering work of Mr. T. Haelen. Thanks are also due to Mr. J. Clark for the electronics shop work.

The cooperation of the operating staff of the National Accelerator Laboratory and the Internal Target Section is acknowledged.

The analysis was made possible through the computer facilities of the National Accelerator Laboratory and The University of Rochester

Computer Center.

The author thanks Mrs. Edna Hughes for her skill and patience in the typing of the manuscript.

This work has been supported by the U. S. Atomic Energy Commission.

Finally, I wish to thank my parents and my wife for their constant understanding and love.

ABSTRACT

A hydrogen jet target was used to study pp scattering. The target was installed in the internal beam of the N.A.L. Accelerator. Solid state detectors were used to detect the low energy recoils, close to 90° from the forward direction.

A total of about 14×10^6 elastic events, equally divided between the two phases of the experiment, were obtained in the study of the low momentum transfer scattering. The forward diffraction peak (in the range $.004 < -t < .2$ $(\mathrm{GeV/c})^2$) and the real-to-imaginary ratio (in the range $.001 < -t < .04$ $(\mathrm{GeV/c})^2$) of the nuclear scattering amplitude energy dependence were derived in the range 40 to 400 GeV/c, laboratory momentum.

The results indicate a continuing shrinkage of the forward peak, even if at a reduced rate from Serpukhov energies. The zero-crossing of the real-to-imaginary ratio at about 300 GeV is strong evidence for the rise in the total cross section in the N.A.L.-I.S.R. energy region.

TABLE OF CONTENTS

		Page
VITAE		ii
ACKNOWLEDGMENTS		iii
ABSTRACT		v
LIST OF TABLES		ix
LIST OF FIGURES		x
CHAPTER		
I	INTRODUCTION	1
	1.1 Background	1
	1.2 Theoretical Concepts	2
	1.3 Experimental Confirmations	15
	References	18
II	EXPERIMENTAL TECHNIQUE	20
	2.1 Overview	20
	2.2 Experimental Technique	24
	a. Target	27
	b. Beam	36
	c. Detectors	37
	d. Detector Calibration	42
	e. Energy Degraders	46
	f. Electronics and On-line Operation	48
	2.3 Background and Its Sources	53
	2.4 Data Analysis Problems	55
	References	60

CHAPTER		Page
III	ANALYSIS OF DIFFRACTION PEAK DATA	61
	3.1 Data Management	63
	3.2 Background Subtraction	68
	3.3 Fitting the Slope and t Cuts	71
	3.4 Nuclear and Inelastic Corrections	76
	3.5 Coulomb Correction	82
	3.6 "3σ" Cuts	83
	3.7 Fits to Single Regge Pole, with No Cuts	88
	References	100
IV	ANALYSIS OF REAL PART DATA	102
	4.1 Data Management	103
	4.2 Background Subtraction	107
	4.3 Fits of Differential Cross Section	128
	4.4 Results and t Cuts	137
	4.5 A Dispersion Relation Calculation	144
	References	149
V	CONCLUSIONS	151
	5.1 Spin Effects in Proton-Proton Forward Elastic Scattering	151
	5.2 Various Models for the Slope Parameter b	155
	5.3 Chou-Wu-Yang Hypotheses	160
	5.4 Elastic Scattering and σ_T Models	166
	5.5 Shadow Scattering Approach	169
	5.6 Regge Models	176

CHAPTER		Page
5.7	Bounds from Quantum Field Theory	184
	a. Forward Scattering Theorems	185
	b. Diffraction Peak Bounds	186
	c. Fixed t Bounds	188
	d. Lower Bound Theorems	189
5.8	Asymptotic Behavior in Some Models	190
5.9	Summary	192
	References	194
APPENDIX A		199

LIST OF TABLES

Table		Page
3.1	Percentage contribution of the (Coulomb amplitude)^2 to the differential cross section; various t values and incident energies.	86
3.2	Final data on the slope parameter and the dependence on the values assumed for ρ, σ_T and θ.	87
4.1	Data on dissociated protons. Taken from ref. 4.	115
4.2	Contributions due to inelastics, background and the term $(p-p_c)^2W$, along with χ^2/(degree of freedom) for each detector (50 and 350 GeV).	125
4.3	Parametrizations used for b, σ and ρ.	127
4.4	Final data on the real to imaginary ratio and the dependence on the values assumed for b, σ_T and θ.	143
5.1	Asymptotic Behavior	191

LIST OF FIGURES

Figure		Page
1.1	Slope parameters for π^+p, K^+p, pp interactions approach the slope parameters for π^-p, K^-p, $\bar{p}p$ interactions. Figure taken from ref. 7.	10
2.1a	Schematic diagram of the N.A.L. Accelerator;	21
b	Location of experiments using the hydrogen jet target;	22
c	Schedules and allocations of the accelerator, the internal target and the experiments in the ITL.	23
2.2	Kinematics of $p + p \rightarrow X + p$.	25
2.3	Schematic diagram of rotating foil target.	29
2.4a	Schematic diagram of hydrogen gas target;	31
b	Hydrogen gas target located in the accelerator tunnel.	32
2.5	Timing of pulsed jet during beam acceleration cycle.	34
2.6	Various modes of operating with the gas jet.	35
2.7a,b	Geometry of the detector supporting carriage; (a) for diffraction peak data; (b) for real part data;	38
c	Schematic diagram of the configuration of the beam, target and detectors.	40
2.8	Schematic diagram indicating the relative thickness of the collimators, absorbers and detectors at various angles (diffraction peak data).	41
2.9a	Spectra of recoil particles from a carbon target. Arrows indicate the "position" of the "end of detector"; where arrow is not shown, the end of detector is beyond the right hand extreme of the histogram.	44
b	Spectra of recoils from a hydrogen gas target; the figure shows a superposition of "foreground" and "background" spectra.	45
2.10	Range-energy relations for silicon and copper.	47
2.11	Schematic diagram of electronic logic.	49

Figure		Page
2.12	Data acquisition on magnetic tape.	52
2.13a	Percentage dead time for diffraction peak data;	56
b	Percentage dead time for real part data.	57
3.1	Calibration of detectors for diffraction peak data.	65
3.2a	"MeV histograms" show clear elastic peaks, and background at the lower ends of the recoil energy spectra; 6.5 MeV (top) and 18 MeV (bottom) elastic peaks are shown;	66
b	"Envelopes" of the spectra shown in Fig.3.2a.	67
3.3	Examples of amplitude and differential cross section t-dependence.	73
3.4	Listing of fit of differential cross section from fitting program.	74
3.5	Nuclear correction and its t-dependence for the detector configuration of the diffraction peak data.	77
3.6	Kinematics for dissociated protons (N*).	79
3.7	Numerical correction due to diffraction dissociation events that must be subtracted from under the elastic peak.	81
3.8a	Differential cross section data (72 points);	84
b	Same as Fig. 3.8a but different incident energy (72 points).	85
3.9	Histogram of χ distribution indicating the slightly larger tails than for an expected Gaussian distribution (dots).	89
3.10	Slope parameter data, all 34 points. Data taken at two energies simultaneously, are connected by lines. The straight line is a single Regge pole fit; b_o=7.92 ± .29, α' = .303 ± .026.	91
3.11	Slope parameter data with pairs of points shifted to achieve a minimum χ^2 for a straight line fit; b_o = 8.03 ± .29, α' = .293 ± .026. The curved line indicates a parabolic fit over $\ln s$ (see Eq. 13).	92

Figure		Page
3.12	Differential cross section data points are shifted to 12 standard t values, one vlaue for each detector (a similar shift can be done for the same data, while defining a standard t value for each carriage position, for each detector); some data points are spread out to show structure (as in detectors 6, 8, 10, 11, 12), the rest of the data are spread out very little.	95
3.13	The slope of these differential cross sections is b_o. (a) The values represented in this differential cross section are the intercept values of the extrapolations of the lines in Fig. 3.12. (b) The same procedure as in (a) but with intercepts for the fixed t values per detector, per carriage position.	97
3.14	The slope of the lines drawn is α'. (a) The values represented form part of the Pomeranchuk trajectory and are obtained from the slopes of the lines drawn in Fig. 3.12. (b) The same procedure as in (a) but with slopes for fixed t values per detector, per carriage position.	98
3.15	Summary of data from one Regge pole fit. Error bars contain the one standard deviation ellipse. The relative fit parameters for the 4 different methods used in background subtraction are indicated in the lower left hand corner. The values should all be translated as shown by the arrow in order to obtain absolute parameters. (Note the consistency of the three sets of data analyzed in our experiment and indicated by the black dots.)	99
4.1a	At the top are shown the elastic peak spectrum (2.5 MeV foreground) and the "background" position histogram; below are shown the "background" position subtracted spectrum and the resulting error histogram;	105
b	The same as in Fig. 4.1a but different recoil energy (12 MeV);	106
c	The calibration of detectors for the real part data.	108
4.2	Projection of the interaction region onto the plane of the solid state detectors and the resultant spectrum.	110
4.3	Mass vs. channel for some of the larger $\|t\|$ detectors.	114

Figure		Page
4.4a	Inelastics (Δ(1236) and N*(1400)) mass distribution at 63 mrads and 350 GeV;	117
b	Inelastics (Δ(1236), N*(1400), N*(1520) and N*(1688)) mass distributions at 100 mrads and 350 GeV.	118
4.5a	At the top is the elastic peak spectrum after subtraction of inelastics (mass distribution which is shown at the bottom and is the sum of the distributions shown in Fig. 4.4a, taken with the appropriate relative amplitudes);	117
b	The same as in Fig. 4.5a, but data are at a different angle; 100 mrads;	118
c	Percentage of inelastic contributions at various incident energies.	120
4.6	Shift of data points due to macroscopic defect in detector 3. Observe the automatic increase of the error bars.	122
4.7a	Histogram of data (detector 3) in a case where an asymmetric elastic peak occurs (top) and χ deviations from fit (below);	123
b	Same as (a) but for a normal symmetric distribution; note the goodness of the fit, i.e., generally small χ.	
4.8	Jet width as obtained from fits of elastic peaks.	126
4.9	Examples of amplitude and differential cross section t-dependence.	129
4.10	Listing of fit of the differential cross section, with error matrix at the top.	131
4.11	Shape of χ^2 distribution in terms of an angular definition of the (detector's) carriage position.	133
4.12	Fringe magnetic field (in the accelerator tunnel) at various points along the ion guide. This field was measured outside the ion guide and as such is the upper limit on the field inside the ion guide, which, because of shielding effects is expected to be much smaller.	134
4.13a	Differential cross section data (70 points);	135
b	The same as (a) but different incident energy (60 points).	136

Figure		Page
4.14	Two dimensional plot of the differential cross section (with the (Coulomb amplitude)^2 removed).	138
4.15	See Figure 3.13 for explanatory notes.	139
4.16	See Figure 3.14 for explanatory notes.	140
4.17	Real to imaginary ratio data; observe the crossing of zero at about 300 GeV, as predicted from a rising total cross section.	141
4.18	Parametrizations of world data on the total cross sections for proton and antiproton scattering off protons. We used these parametrizations in our dispersion relation calculations.	147
4.19a	Results of dispersion relation (for pp) calculations using the total cross section parametrization of Leader and Maor;	148
b	Parametrization of Bartel and Diddens. (loc.ref.) The number labels on the various curves indicate the energy (in GeV) where the total cross section is assumed to stop rising.	
5.1	Ratio of the spin-dependent to the spin-independent amplitude, in the forward direction; figure taken from ref. 1.	154
5.2	Various models for fitting the energy dependence of the slope parameter. (In the case of Regge pole fits only data above ~10 GeV has been used.) There are three sets of data from our experiment. The most recent is indicated by II, while the data analyzed in this thesis is listed under PRESENT WORK.	157
5.3a,b,c	(a) The Chou-Yang fit of the differential cross section by the fourth power of the form factor; (b) and (c), the Durand-Lipes fit of ISR data (c), and the effects of different real parts (b); figures taken from ref. 8.	163
5.4	Diffraction dips observed in πp, pp and $\bar{p}p$ collisions; figure taken from ref. 9.	164
5.5	The opacity of the proton, $\sigma_{e\ell}/\sigma_T=1-\sigma_{incl}/\sigma_T$. Figure taken from ref. 13.	171

Figure		Page
5.6	The total elastic and inelastic overlap functions. The quantity $1/2\pi \ \tau_{inel}(x)$ is analogous to G(b,s) used in the text; figure taken from ref. 13.	172
5.7	Proton-proton differential cross sections with model fits; figures taken from ref. 14.	175
5.8	Total hadron-proton cross sections with model fits; figures taken from ref. 14.	177
5.9a	Predictions of the models by Cheng, Walker and Wu, and by Chan, Chen and Rarita for the real-to-imaginary ratio at high energies. Our data was not included in the fits, nevertheless our data agrees well with both predictions, in the N.A.L. energy range;	178
b	Predictions for the total cross sections by models of Cheng, Walker and Wu (CWW), and by Chan, Chen and Rarita (CCR). The parametrization of Leader and Maor (LM) is also indicated.	179

CHAPTER I

INTRODUCTION

1.1 Background

For many years it has been the prevalent belief among high energy physicists that the physics of strongly interacting elementary particles should exhibit asymptotic behavior at high energies.

In the sub-GeV energy region, threshold effects, due to the opening up of inelastic channels, spoil the picture of asymptopia. In the multi-GeV energy region, cross sections are dominated by resonance production; polarizations do not seem to approach any limit while changing their signs and angular distributions show unexpected dips. In general, at these low energies, there are many competing processes and a complete understanding on theoretical grounds is lacking.

However, the recent availability of particle energies of hundreds of GeV at the CERN Intersecting Storage Rings and the NAL accelerator, offers a glimpse at a possible asymptotic regime. Data obtained at these two laboratories has already shown the existence of some

important new effects and speculation about these effects is an ongoing effort on the part of many physicists. In this work we present some of the aspects of proton-proton forward elastic scattering data at high energies and analyze this data in the context of some of the more successful theoretical approaches.

1.2 Theoretical Concepts

In this section are recalled some useful concepts which allow an understanding of experimental results.

In classical physics, physical optics is an effective extension of electrodynamics in the case of short wavelengths, as compared to the characteristic sizes of the objects encountered. The analogy of a short de Broglie wavelength for matter waves, compared to the scattering object, allows the borrowing of ideas from optics into high energy physics. Indeed, in elementary particle scattering, hadrons are approximately 1 fermi in size, while the de Broglie wavelength $\lambda\!\!\!^{-}$, for a particle of momentum p is

$$\lambda\!\!\!^{-} = \frac{\hbar c}{p} = \frac{.2}{p} \text{ fermi},$$

where p is numerically expressed in GeV/c. In the

NAL-ISR energy region of hundreds of GeV, the optical concepts should therefore be applicable. The resultant theory is the background of the optical or diffraction model of high energy physics.

A convenient presentation of the problem occurs in impact parameter representation (b is the impact parameter). A partial wave expansion of the scattering amplitude f (for spinless particles) is

$$f = \frac{1}{2ip} \sum_{\ell=0}^{\infty} (2\ell + 1)\, P_\ell(z)(e^{2i\delta_\ell} - 1)$$

where δ_ℓ is the phase shift and z is the cosine of the forward scattering angle. The normalization, $d\sigma/d\Omega = |f|^2$, holds. For large p and z close to 1, a series of approximations ensues:

$$\begin{aligned}
(\ell + \tfrac{1}{2}) &\rightarrow bp \\
2\delta_\ell &\rightarrow \chi(b) \\
P_\ell(z) &\rightarrow J_o(\sqrt{-t}\, b) \\
\sum_\ell &\rightarrow p \int_o^\infty db \quad ,
\end{aligned}$$

where t is the 4-momentum transfer squared, $-t \approx (p\ \theta)^2$. Therefore the representation of the scattering amplitude from a partial wave expansion, becomes an integral over impact parameter b,

$$f(s,t) = i\,p \int_0^\infty J_0(\sqrt{-t}\ b)\ [1 - e^{i\chi(b)}]\,b\,db\ , \qquad (1)$$

where $e^{i\chi(b)} - 1 = \frac{i}{p}\int_0^\infty \sqrt{-t}\ d\sqrt{-t}\ \ J_0(\sqrt{-t}\ b) f(s,t)$ is the Fourier-Bessel transform of Eq. (1). In the case of potential scattering in classical optics, δ_ℓ, the phase shift, is a real number and therefore the incident wave is not depleted in intensity. In the case of high energy hadron scattering, many inelastic phenomena occur and the probability of finding the projectile with the incident energy after a collision, is less than unity; it follows that $\chi(b)$ can become complex, with a phase in the first quadrant and $|e^{i\chi(b)}| \leq 1$. In the case of a completely absorbing scatterer, the incident wave disappears and other inelastic channels emerge from the collision; then we have $\chi(b)$ purely imaginary and infinite. We have in such a case

$$1 - e^{i\chi(b)} = 1 \qquad b \leq R$$
$$1 - e^{i\chi(b)} = 0 \qquad b > R$$

where R is the radius of the scatterer. Integration of Eq. (1) results in

$$f(s,t) = i\,p\,R^2\ \frac{J_1(\sqrt{-t}\ R)}{\sqrt{-t}\ R}\ . \qquad (2)$$

This is the well known phenomenon of diffraction patterns from a black disk, called Fraunhofer diffraction in classical optics. It is notable that diffraction scattering in an optical model predicts a large diffraction peak and diffraction minima, which Eq. (2) can well reproduce. With the normalization used, the optical theorem reads, $\sigma_T = \frac{4\pi}{p} \operatorname{Im} f(s,o)$ (more will be said later about the optical theorem). Finally we obtain

$$\sigma_T = 2\pi R^2 \quad . \tag{3}$$

Equation (3) indicates that the total cross section is twice as large as the geometrical area of the scatterer. Integrating the $|\text{scattered amplitude}|^2$ in Eq. (2) over all momentum transfer space gives the elastic cross section, which is $\sigma_{e\ell} = \pi R^2$, or just half of the total cross section. This phenomenon is well recognized from physical optics. The ratio, $\sigma_{e\ell}/\sigma_T$ shall be called the opacity, and it appears that for maximum absorption, the opacity is a half. For more realistic cases of scatterers with "softer" edges than a black disk's, the opacity decreases from the one half maximum. What remains approximately the same, qualitatively, is the strong forward diffraction peak. For example, for a Gaussian distribution of the target in impact parameter space, the resulting differential

cross section is $d\sigma/dt \sim e^{-b|\sqrt{-t}|^2}$, where this is another Gaussian in momentum transfer space. The quantity b is here the diffraction peak slope parameter*.

Many models have followed along the optical approach to scattering. One notable contribution is that of Wu and Yang[1], who suggested a relation between the proton electromagnetic form factor and its hadronic matter distribution. This point of view allows the completely independent process of electromagnetic scattering of electrons on protons, to survey the proton hadronic structure. Following this line of thought Chou and Yang[2] have proposed an optical model. This topic is more fully treated in Chapter V.

For lack of knowledge of the strong interaction dynamics, the approach of S-matrix theory, in which one deals with relations between matrix elements, has been used. The fundamental property of the S-matrix, unitarity, leads directly to an important relation (in the forward direction), the optical theorem, which states that

$$\mathrm{Im}T(s,o) = s\sigma_T(s),$$

$$\left[\text{normalized } \frac{d\sigma(s,t)}{dt} = \frac{1}{16\pi s^2}\,|T(s,t)|^2\right]$$

---

*We shall use the notation of b for both impact parameter and slope parameter. Their respective dimensions are: fermi and $(\mathrm{GeV}/c)^{-2}$. No confusion should result from this mixed notation.

where s and t are the Mandelstam variables. This equation provides a relation between the total cross section (σ_T), which is a directly observable quantity, and the imaginary part of the forward scattering amplitude. This connection is invaluable in evaluating the real part of the forward amplitude, through dispersion relations; an example of such a calculation is found in Chapter IV.

In 1961, Froissart[3] first obtained a bound on the strong interaction size of the proton as a function of energy. This derivation was based on the assumptions that the nuclear scattering amplitude is analytic in t and that it is bounded by a polynomial in s. Later Martin[4] found it necessary to assume only microcausality and conservation of probability. The Froissart-Martin bound is

$$\sigma_T(s) < \frac{\pi}{m_\pi^2} \ln^2 s \ , \tag{4}$$

where m_π is the pion mass. An intuitive derivation of such a limit was given by Froissart through the following arguments.

From an impact parameter point of view, the angular momentum ℓ is related to the projectile (momentum q) to target distance by $\ell \sim qb$. An interaction will occur if the projectile comes close enough to the target to

exchange the lightest particle, a pion; thus an interaction occurs if $\ell \lesssim q\, b_o$, where $b_o = 1/\mu$ ($\mu = m_\pi$, mass of the pion). However, the Yukawa potential extends the range of the interaction by $\ln(qb_o)$ then the partial waves are unity for $\ell \lesssim qb_o \ln(qb_o)$ and zero otherwise (in the forward direction). Using the partial wave expansion

$\sigma_T = \frac{4\pi}{q^2} \sum_{\ell=0}^{\infty} (2\ell + 1)\mathrm{Im} f_\ell$ the Froissart bound is,

$\sigma_T \simeq \frac{4\pi}{\mu^2} \ln^2(s/\mu^2)$. The total cross section can then be interpreted to indicate the size of the proton, in which case we obtain a radius proportional to $\ln s$.

Recent ISR data have shown that the total proton-proton cross section rises; while a $\ln^2 s$ dependence works well, other parametrizations, such as $\sigma_T \sim \ln s$ are still possible. If the Froissart-Martin bound is saturated and the total cross section rises as fast as $\ln^2 s$, then this implies through unitarity on partial waves that the elastic cross section must obey a $\ln^2 s$ dependence, the ratio $\sigma_{e\ell}/\sigma_T \to 1/2$, and that the diffraction peak width of elastic scattering must shrink at least as fast as $\ln^{-2} s$. This width is the inverse of the slope parameter; that data is analyzed in Chapter III. Given that the observed shrinkage is less fast than perhaps even $\ln^{-1} s$, this behavior presents a problem. However, the currently available energies may not be asymptotic and yet larger energies

are necessary to exhibit the predicted behavior of the diffraction peak width.

At asymptotic energies, the Pomeranchuk theorem[5], which states that the particle-particle and antiparticle-particle cross sections approach each other asymptotically, should be satisfied. The basis of the theorem is s-channel unitarity and s-u channel crossing symmetry. Through the use of dispersion relations one proves that either the forward scattering amplitude is predominantly real, asymptotically, which is contrary to the physical intuition derived in an optical model context, or the particle and antiparticle cross sections are the same. This statement can be clarified by noting that the scattering amplitude becomes, asymptotically, in the forward direction

$$T(s,o) \rightarrow a + bs + is\sigma_T - s\frac{(\sigma_T - \bar{\sigma}_T)}{\pi} \ln s \qquad (5)$$

Another Pomeranchuk-like theorem[6] indicates that the ratio $\frac{d\sigma(pp)}{dt} / \frac{d\sigma(\bar{p}p)}{dt}$ goes to unity. As a consequence, the observed shrinking, in pp collisions, should also extend to $\bar{p}p$ collisions. This prediction may possibly be checked in the NAL-ISR energy range because the slope parameters for both pp and $\bar{p}p$ as well as πp and Kp collisions, are already very close (see Figure 1.1).

One of the most powerful theoretical techniques of

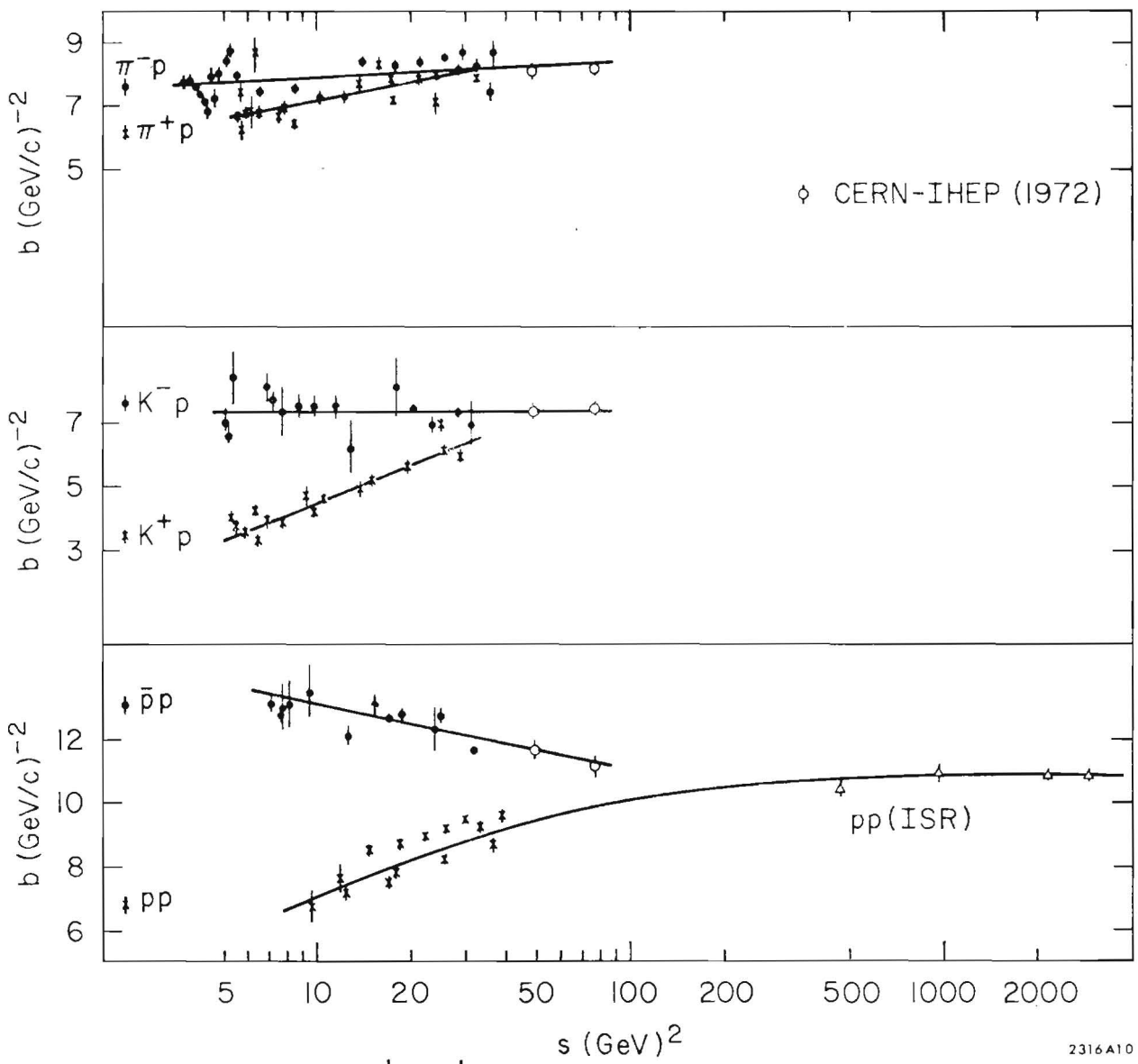

Figure 1.1 Slope parameters for π^+p, K^+p, pp interactions approach the slope parameters for π^-p, K^-p, $\bar{p}p$ interactions. Figure taken from ref. 7.

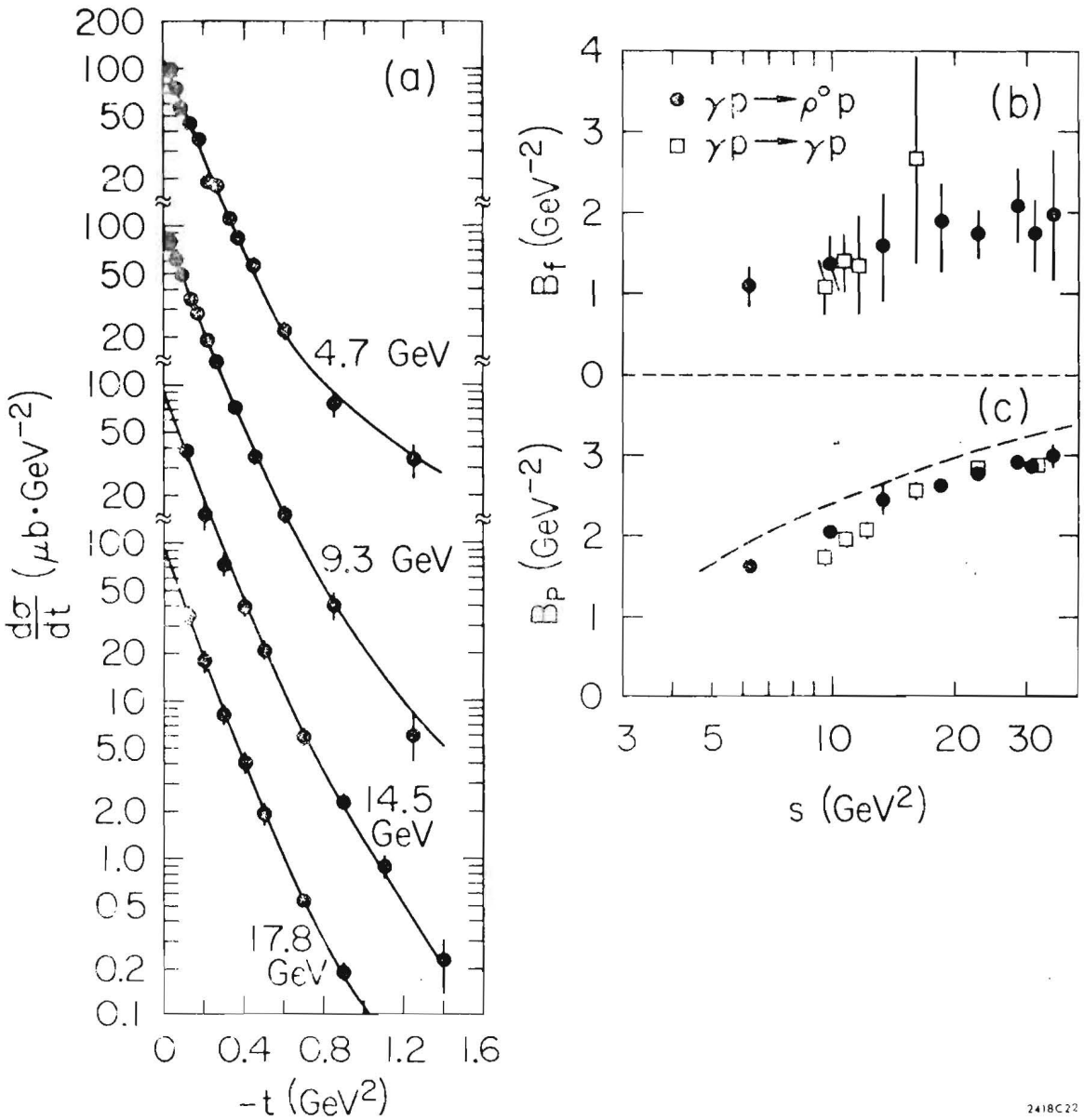
(a)
4.7 GeV
9.3 GeV
14.5 GeV
17.8 GeV
$\frac{d\sigma}{dt}$ (μb·GeV^{-2})
-t (GeV^2)
(b)
$\gamma p \rightarrow \rho^0 p$
$\gamma p \rightarrow \gamma p$
B_f (GeV^{-2})
(c)
B_p (GeV^{-2})
s (GeV^2)
2418C22

Fig. 21

high energy physics is that of dispersion relations. It has been shown that these follow rigorously form axiomatic field theory.[8] These relations connect the real and imaginary parts of the scattering amplitude. In a series of papers, Khuri and Kinoshita[9] established the necessity of using crossing symmetric forward scattering amplitudes; using analyticity and the assumption that the real part of the forward scattering amplitude is not dominant in the high energy limit (a result not required in field theory), they have established bounds on the real to imaginary ratio in accord with various asymptotic behaviors of the total cross section. In particular, (according to the optical theorem, $\mathrm{Im}T(s,o) = s\sigma_T(s)$), if the total cross section tends to a constant, the ratio $\rho \equiv \mathrm{Re}T(s,o)/\mathrm{Im}T(s,o)$ goes to zero from below, while if the Froissart bound is satisfied and $\sigma_T \sim \ln^2 s$, then ρ (crosses zero from the present negative values) tends to zero from above. This zero crossing property has been observed in this experiment, as explained in Chapter IV. In general, given the behavior $\sigma_T \sim \ln^\beta s$, then

$$\rho \sim \frac{\beta\pi}{2} (\ln s)^{-1} \quad . \tag{6}$$

The Feynman propagator for a spin zero particle is proportional to $(t - m^2)^{-1}$, where m is the mass of the particle. The one-particle-exchange model explains the features of scattering data at high energies through the dominance of single particle exchange graphs at low momentum transfer. In general, for any spin J and mass M_J, the exchange amplitude is proportional to $-[-s/s_o]^J/(t-M_J^2)$, in the large energy asymptotic limit. This functional form does not, however, give a satisfactory energy dependence for collisions of particles with spin of one, or greater. One remedy exists if we assume (empirical data and the Chew-Frautschi plot validate this assumption) that $M_J^2 = \mu^2(J - a)$ and coupling constants for all spins are the same; this reduces the summation over all particle spins, to the usual Regge pole elastic scattering amplitude,

$$T_{AB}(s,t) = - \beta_A(t)\ \beta_B(t) \cdot \frac{e^{-i\pi\alpha(t)} + 1}{\sin\pi\alpha(t)} \cdot (s/s_o)^{\alpha(t)} \tag{7}$$

This form shows factorization, with individual residues $\beta(t)$ for each scattering particle. The masses taken into account are either all odd spin or all even spin particles and lie on Regge trajectories. The description of the trajectory is contained in $\alpha(t) = \alpha(o) + \alpha' t$ and there could be more than one trajectory.

Some very important consequences result from the amplitude in Eq. (7). First at t = 0, the optical theorem gives,

$$\sigma_T^{AB}(s) = \beta_A(o)\ \beta_B(o)(s/s_o)^{\alpha(o)-1}, \qquad (8)$$

where $s_o = 1\ \mathrm{GeV}^2$. If the total cross section is to satisfy the Froissart bound, then $\alpha(o) \leqslant 1$. Because of the fact that all hadron total cross sections at high energies are relatively constant, a leading particle trajectory, the Pomeronchuk (or briefly, Pomeron) trajectory, has been assumed to give the dominant contribution to the cross sections and to have an intercept of one ($\alpha(o)=1$). Other trajectories with lower lying intercepts give a vanishing contribution with increasing energy and are believed to be responsible for the slowly decreasing total cross sections at energies below, say 50 GeV.

The dominant part of the scattering amplitude is imaginary as can be seen in Eq. (7), and the energy variation is,

$$\frac{d\sigma/dt}{d\sigma/dt|_o} = e^{\alpha' t \ln s} \left| \frac{\beta_A(t)\ \beta_B(t)}{\beta_A(o)\ \beta_B(o)} \right|^2, \qquad (9)$$

where, $\alpha(o) = 1$, has been assumed. This behavior exhibits a large forward peak which corresponds to the diffraction

peak of optical models. The forward peak shrinks with increasing energy as $\ln^{-1} s$. If the residues of the Regge poles, $\beta(t)$, are assumed exponential in t, then we obtain a slope parameter, $b(s) = 2(b_A + b_B + \alpha' \ln s)$, where $\beta_i(t) = \beta_i(o)e^{b_i t}$. The slope parameter b(s) is defined

$$\frac{d\sigma}{dt} = \left.\frac{d\sigma}{dt}\right|_o e^{b(s)t} . \tag{10}$$

Finally, Eq. (7) contains a prediction for the real-to-imaginary ratio of the forward scattering amplitude. In the small momentum transfer approximation, we have

$$\frac{\mathrm{Re}T(s,t)}{\mathrm{Im}T(s,t)} \cong \frac{\pi}{2} \alpha' t \quad . \tag{11}$$

The sign of the ratio is predicted to be negative and the ratio itself is energy independent. Of course a more complicated behavior for the scattering amplitude, involving other trajectories than the Pomeron, will contain some energy dependence.

The relative coupling constant of different trajectories are not known from theory. Therefore, data can be fit with a large or small number of parameters, as is suitable, or in taste. Furthermore, a theoretical specification of the exact behavior of the trajectories or residues as functions of t is lacking. This degree

of freedom allows elaborate, but sometimes little justified, complications to be introduced in comparison of theory with available data.

Other obstacles or opportunities, depending on the point of view, are that the couplings of exchanged trajectories can give a complicated structure for the scattering amplitude in the complex t plane, with cut, branch points and other singularities, which often elude mathematical tractability in terms of simple forms.

1.3 Experimental Confirmations

Recently, experiments at Serpukhov, N.A.L. and I.S.R. have produced a large amount of new and basic information about the structure of hadronic interacitons.

Whereas it was thought prior to the Serpukhov (1969) experiments that total cross sections will eventually reach asymptotic values from above, the new data show a remarkable increase in $\sigma_T^{K^+p}$. This slow increase, and the slow approach between $\sigma_T^{K^+p}$ and $\sigma_T^{K^-p}$ prompted theoretical speculations on the validity of the Pomeranchuk theorem. Mechanisms were invented in order to explain the data. Regge cuts were found to give a good description of the data and the asymptotic bounds were to be approached from below due to an interference between the Pomeron and cut

contributions. The new I.S.R. and N.A.L. data show an increase in all total cross sections (πp, Kp, pp) except for a possible minimum[10] in $\sigma_T^{\bar{p}p}$. It is therefore confirmed that all cross sections rise and the Pomeranchuk theorem is satisfied, at least locally in energy.

The pp cross section has been measured at the highest energies available (I.S.R. - 2000 GeV/c lab. momentum) and shows a most dramatic increase of about 15% from roughly 38.4 mb. The rate of increase is much smaller (~100 times) than the Froissart bound and as such only indicates that an asymptotic energy regime may not yet have been reached (note that the Froissart bound must not necessarily be satisfied).

Optical model ideas applied to hadronic interactions work satisfactorily, but are not very restrictive in their predictions. Given the freedom to choose an appropriate impact parameter structure for hadrons, the differential cross sections can be fit with good accuracy. Diffraction pattern minima can be reproduced. The most common necessary ingredients in these calculations, at least, are: the assumption of a Gaussian distribution of hadronic matter in impact parameter space and possibly the existence of a ring-like structure in addition to the Gaussian (which is probably responsible for the "break" in the pp differential cross section at $|t| \cong .15\ (\mathrm{GeV/c})^2$).

Valuable insight into the theoretical descriptions can be obtained from measurements of the pp differential cross section, which yield information regarding the slope parameter, b(s), and the real-to-imaginary ratio, $\rho(s)$. We have made these measurements, accurately, in the large energy range 40 to 400 GeV/c. A full description of the methods used appears in Chapters III and IV. Based on our data and other hadronic interactions information we offer conclusions in Chapter V.

References for Chapter I

1. T. T. Wu and C. N. Yang, Phys. Rev. 137, (1965) 708.
2. T. T. Chou and C. N. Yang, Phys. Rev. 170, (1968) 1591.
3. M. Froissart, Phys. Rev. 123, (1961) 1053.
4. A. Martin, Nuovo Cimento 42A, (1966) 930.
5. I. Ia. Pomeranchuk, Soviet Phys. JETP 34 (7), (1958) 499.
6. H. Cornille and A. Martin, Phys. Lett. 40B, (1972) 671.
7. D. W. G. S. Leith, SLAC-Pub-1263, (1973).
8. K. Hepp, Helv. Phys. Acta 37, (1964) 639.
9. N. N. Khuri and T. Kinoshita, Phys. Rev. 140, (1965) 706.
10. I-H. Chiang, private communication.

Among a number of useful books on the material presented here are:

- S. C. Frautschi, Regge Poles and S-Matrix Theory, W. A. Benjamin, New York, 1965;
- R. Omnès and M. Froissart, Mandelstam Theory and Regge Poles, W. A. Benjamin, New York 1963;
- M. Jacob and G. F. Chew, Strong Interaction Physics, W. A. Benjamin, New York, 1964;

- S. Gasiorowicz, Elementary Particle Physics, Wiley, New York, 1966;
- V. D. Barger and D. B. Cline, Phenomenological Theories of High Energy Scattering, W. A. Benjamin, 1969;
- D. Horn and F. Zachariasen, Hadron Physics at Very High Energies, W. A. Benjamin, New York, 1973.

CHAPTER II

EXPERIMENTAL TECHNIQUE

2.1 Overview

This experiment was performed at the National Accelerator Laboratory (N.A.L.) by a collaboration between the following institutions: The State Committee for Utilization of Atomic Energy of the U.S.S.R., The National Accelerator Laboratory, Rockefeller University and The University of Rochester. The experiment was the first to run at N.A.L. and in the early stages of accelerator turn-on it formed the nucleus for what eventually grew into a large scale operation, known today as the Internal Target Laboratory (I.T.L.). By the very nature of accelerator construction, an internal beam would exist before a suitably defined extracted beam was achieved and this motivated us to exploit the internal beam. The first internal beam was used at Serpukhov[1] in much the same way, by a group that later became part of our collaboration.

In Figure 2.1a we show a schematic diagram of the relative locations of major parts of the accelerator. Figure 2.1b shows schematically the present arrangement of different experiments located in the I.T.L., which utilize

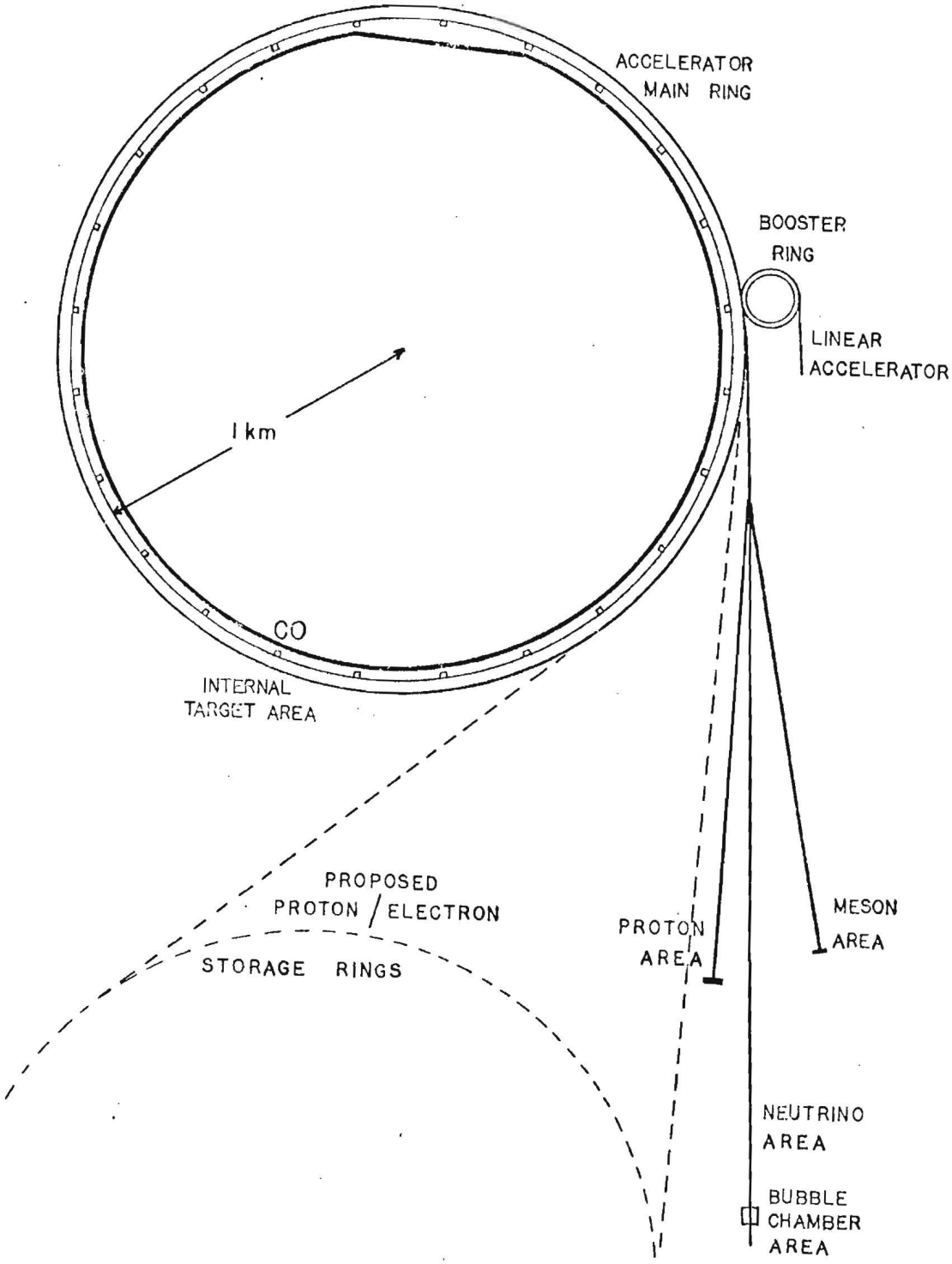

Figure 2.1a Schematic diagram of the N.A.L. Accelerator

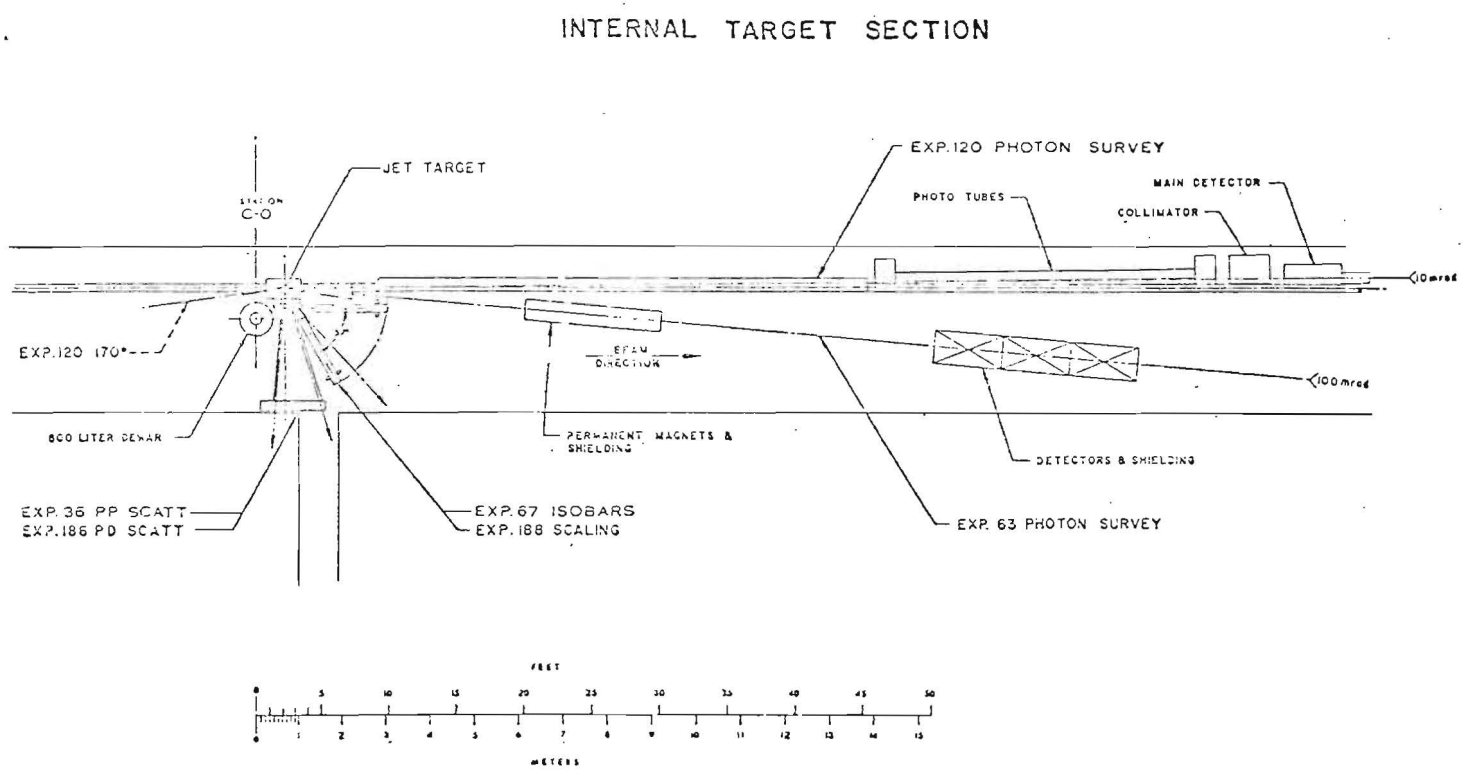

Figure 2.1b Location of experiments using the hydrogen jet target.

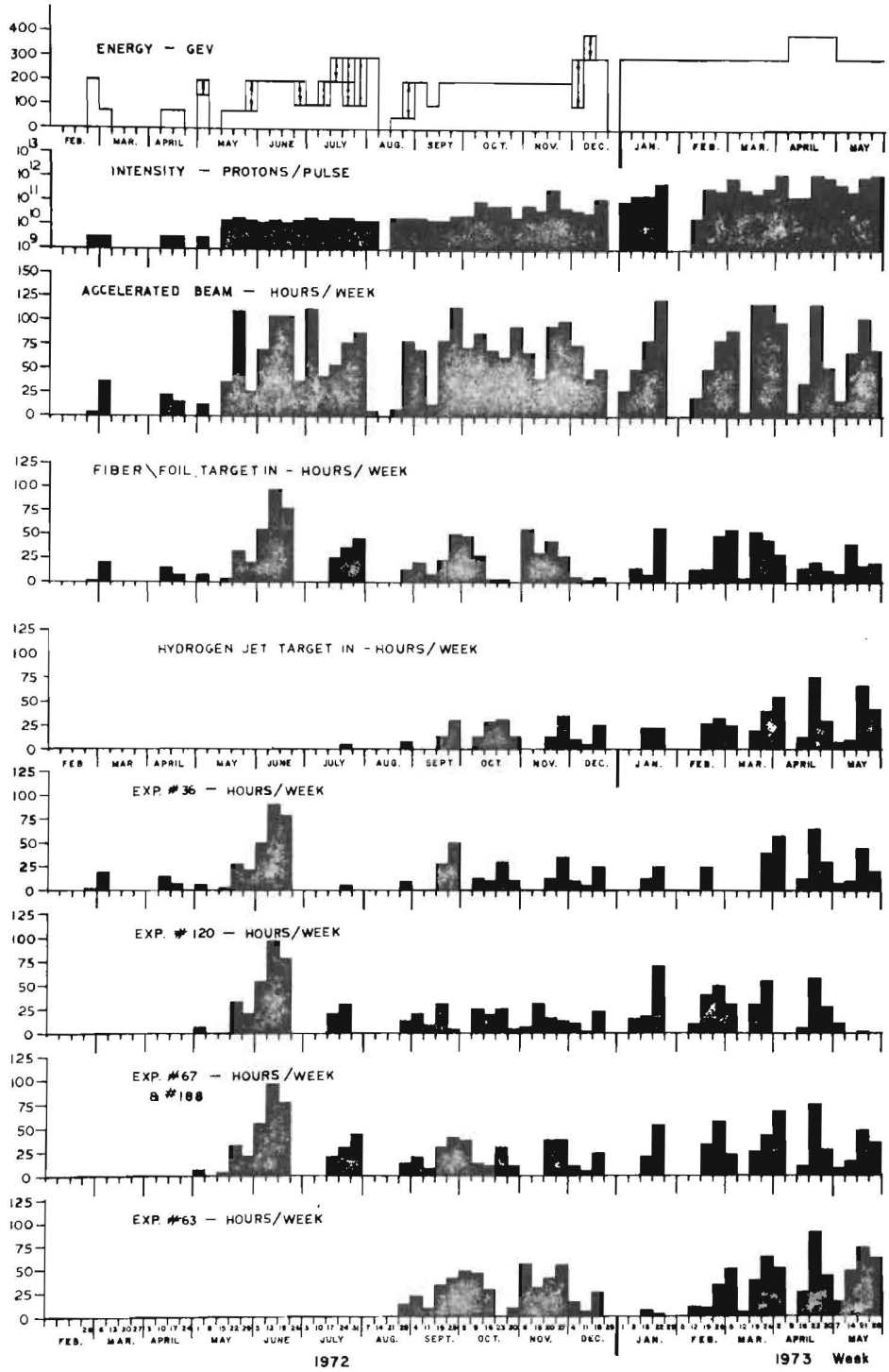

Figure 2.1c Schedules and allocations of the accelerator, the internal target and the experiments in the ITL.

the internal target. The usage of the internal target by May 1973, more than one year after beam was obtained at N.A.L. is shown in Figure 2.1c.

The major goals of the experiment were the study of:

a. the diffraction peak in proton-proton elastic collisions (at small momentum transfer),

b. the real part of the nuclear scattering amplitude,

c. the total cross section for pp,

d. low mass isobar excitation, in $pp \rightarrow N^*p$

To such ends it is sufficient to study the recoil proton in the reaction

(I) $p + p \rightarrow X + p$. (see Figure 2.2)

The scope of this writing is to analyze data obtained on the diffraction peak and the "real part", by use of a hydrogen jet target in the energy range 50-400 GeV.

2.2 Experimental Technique

The region of interest in the 4-momentum transfer squared, t, is $.001 \leq |t| \leq .2\ (\mathrm{GeV}/c)^2$. Simple kinematics leads us to the following relations:

$$|t| = 2m_p T \qquad (1)$$

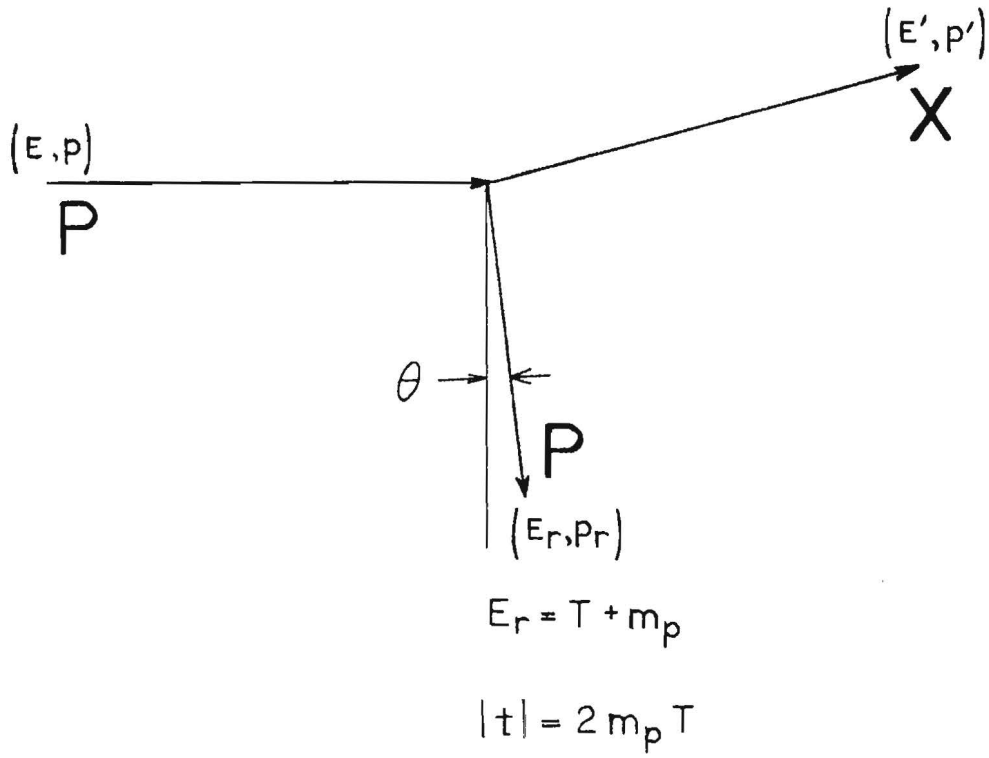

Figure 2.2 Kinematics of p + p → X + p.

$$|t| = \frac{4m_p^2 \beta^2 \sin^2\theta}{1 - \beta^2 \sin^2\theta} \qquad (2)^*$$

$$\frac{dt}{d\Omega} = \frac{\beta}{4\pi m_p^2} \sqrt{|t|} \; (|t| + 4m_p^2)^{3/2} \qquad (3)$$

where

t - 4-momentum transfer squared,

T - recoil proton kinetic energy,

m_p - proton mass,

θ - angle of recoil as measured at 90° from the incident beam direction,

β - center of mass velocity [is $P_o/(E_o + m_p) \approx 1$], ($p_o$, E_o refer to the incident particle).

From equation (2) we immediately note that at small angles of recoil, $0° \lesssim \theta \lesssim 12°$, the momentum transfer, t, depends only weakly on the incident energy, E_o, for $E_o >> m_p$. The approximate relation is

$$|t| \cong 4m_p^2 \beta^2 \sin^2\theta ,$$

while

$$\beta^2 = \left(\frac{P_o}{E_o + m_p}\right)^2$$
$$= \frac{E_o - m_p}{E_o + m_p} .$$

*Note that it is virtually impossible, in the N.A.L. internal beam, to look for forward recoils of the same t, because $|t| \cong p^2 \cdot \phi^2$, where ϕ is the forward recoil angle which is extremely small (at a minimum angle, ϕ, of .1mrad, that corresponds to a $|t|$ of 1.6×10^{-3} $(GeV/c)^2$ at 400 GeV, it is extremely difficult to measure the differential cross section; more accessible angles may be 2-5 mrads in the forward direction).

Therefore for incident energies larger than, say, 50 GeV, t does not vary by more than 4% for fixed angle. This property was both convenient in setting up our detectors, as well as an important and powerful asset for comparing data at different energies. Moreover, the use of an internal beam,equally accessible at all energies, makes the detection technique ideally suited for eliminating most energy dependent biases.

Target

From reaction (I) and the required range of t, we conclude that it is necessary to detect protons of kinetic energies 0.5-100 MeV. Therefore, a very low density target of small extent is required in order that multiple scattering and energy losses not destroy the recoil proton's initial momentum vector. Consequently, possible targets are of the following nature:

a. thin narrow film made of high ratio (hydrogen/other atoms),

b. contained hydrogen atmosphere of small extent ($\sim 1\ cm^3$),

c. same as (b), but gaseous higher Z materials.

Choice (a) is simply satisfied by use of a thin foil of polyethylene, $(CH_2)_n$, the highest density (hydrogen/other atoms) solid. It is, however, disadvantageous to

use $(CH_2)_n$ because the reaction $p + C \rightarrow p +$ "anything" contributes significant background to the reaction of interest, $p + p \rightarrow X + p$ (where X may also be p). It is also impossible to eliminate the problem of multiple scattering at very low $|t|$.

Choice (b) presents an apparent technical problem; how can a contained atmosphere of the necessary density $\sim 5 \times 10^{-7}$ gm/cm^3 of H_2 be exposed to an accelerator vacuum of 10^{-6}-10^{-7} torr, without destroying the latter? (The density of such a target is equivalent to a pressure of about 10 torr, at room temperature.) The solution is to make a supersonic gas jet of low temperature. Some of the technical details were investigated by the author[2]. Moreover, a Soviet team had an independent proposal for use of such a target[3]. It was decided in 1971 that the two groups should collaborate.

In the early stages of accelerator construction we decided, for reasons of simplicity and expedition, to use a polyethylene foil target. Figure 2.3 presents such a target schematically. The target was fixed on the rim of a rotating wheel and simply stretched by the centrifugal force. The small angle (20°) between the beam and the axis of rotation was a compromise between the requirements, that there be as little material as possible in the beam, and that the recoil particles also encounter

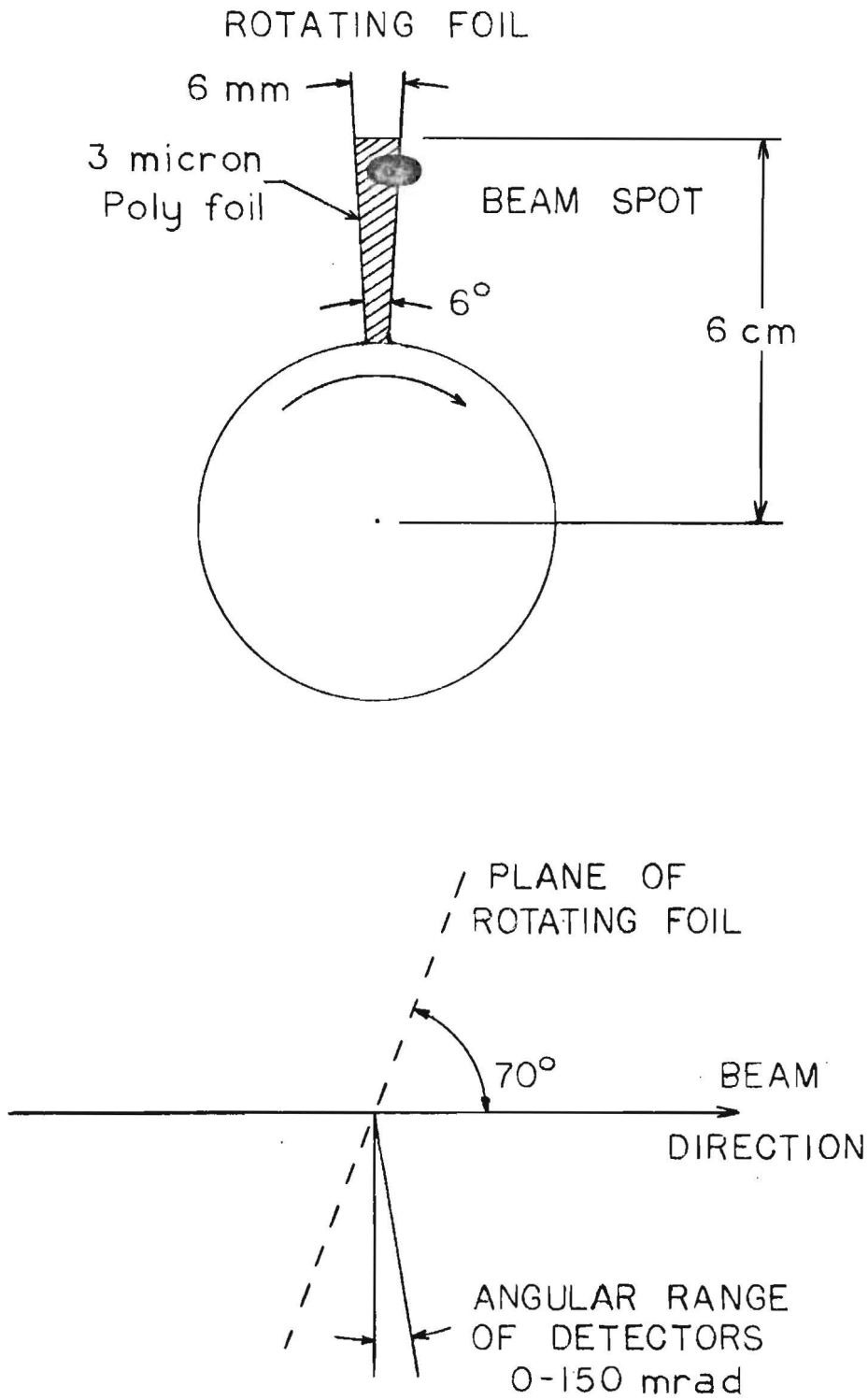

Figure 2.3 Schematic diagram of rotating foil target.

very little material. The $(CH_2)_n$ foil was cut radially in order to obtain a uniform interaction rate, independent of beam position. This is true as long as the period of radial motion of the beam is slow, as compared to the period of rotation of the target (60 cps.). The thickness of the foil was uniform to within 4%, and its dimensions were: length ~4 cm, width at the rim ~6 mm. The results obtained by use of such a target are given in reference (4). The beam intensity during this phase of the experiment was generally (2-4) $\times 10^{10}$ protons per pulse. Yet later, when the beam intensity increased to beyond 10^{11}ppp, the polyethylene foil would deteriorate rapidly and further acquisition of data under such circumstances was abandoned. The data was obtained in approximately 200 hours of beam time (May-June 1972),during which roughly 60 K elastic events were collected at 8 different energies ($25 \leq E_o \leq 200$ GeV). The luminosity was of the order of $6 \times 10^{34}/cm^2$ sec (instantaneous), but one must also take into account a duty factor of ~1/100. Roughly half of these events were used to obtain estimates of total cross sections.

The hydrogen gas target is shown schematically in Figure 2.4a. (Actual set-up is seen in Figure 2.4b.) The target was installed and became operational in the N.A.L. main ring during July 1972. Some of the specifications for our operating conditions were:

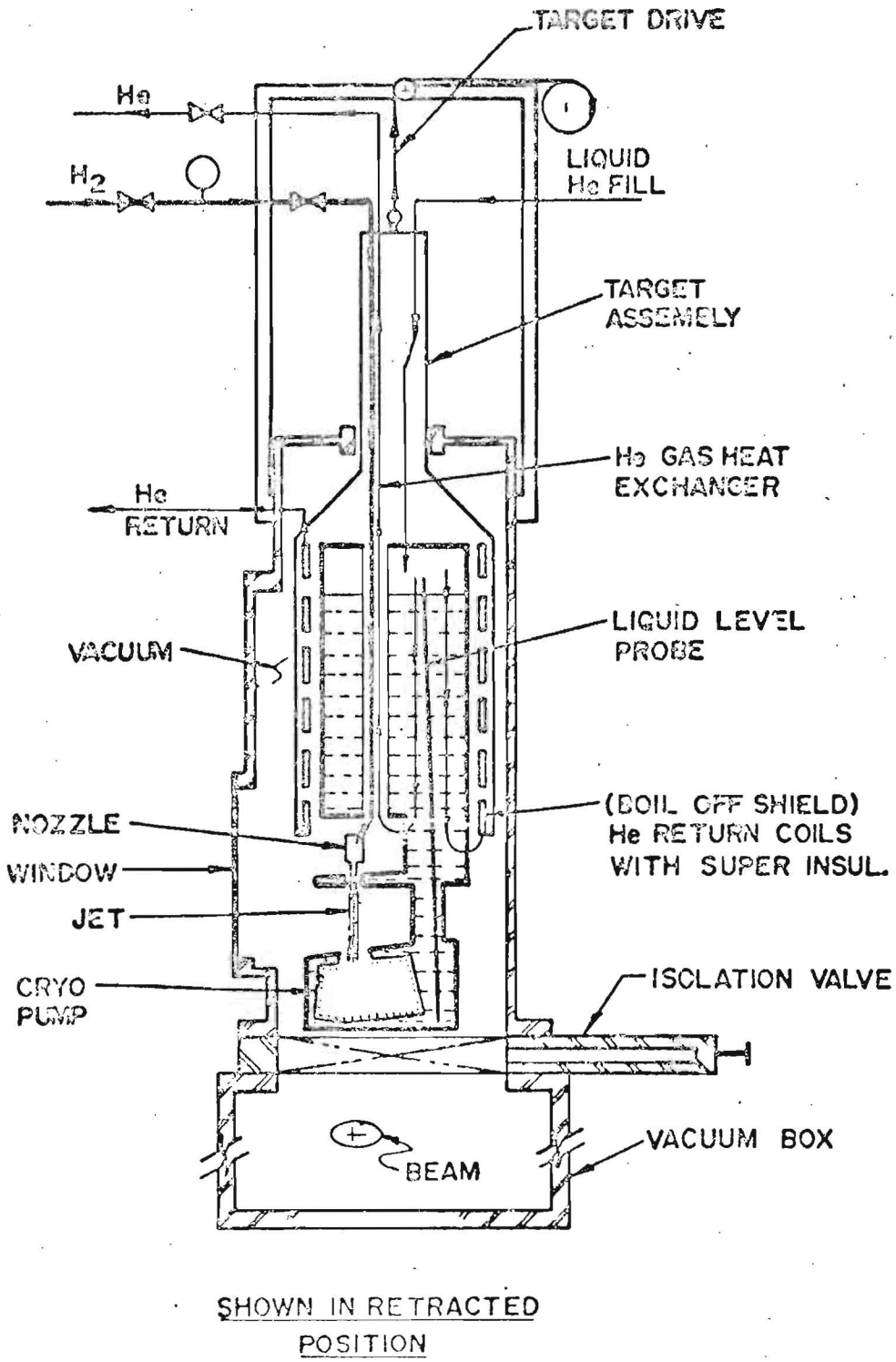

Figure 2.4a Schematic diagram of hydrogen gas target.

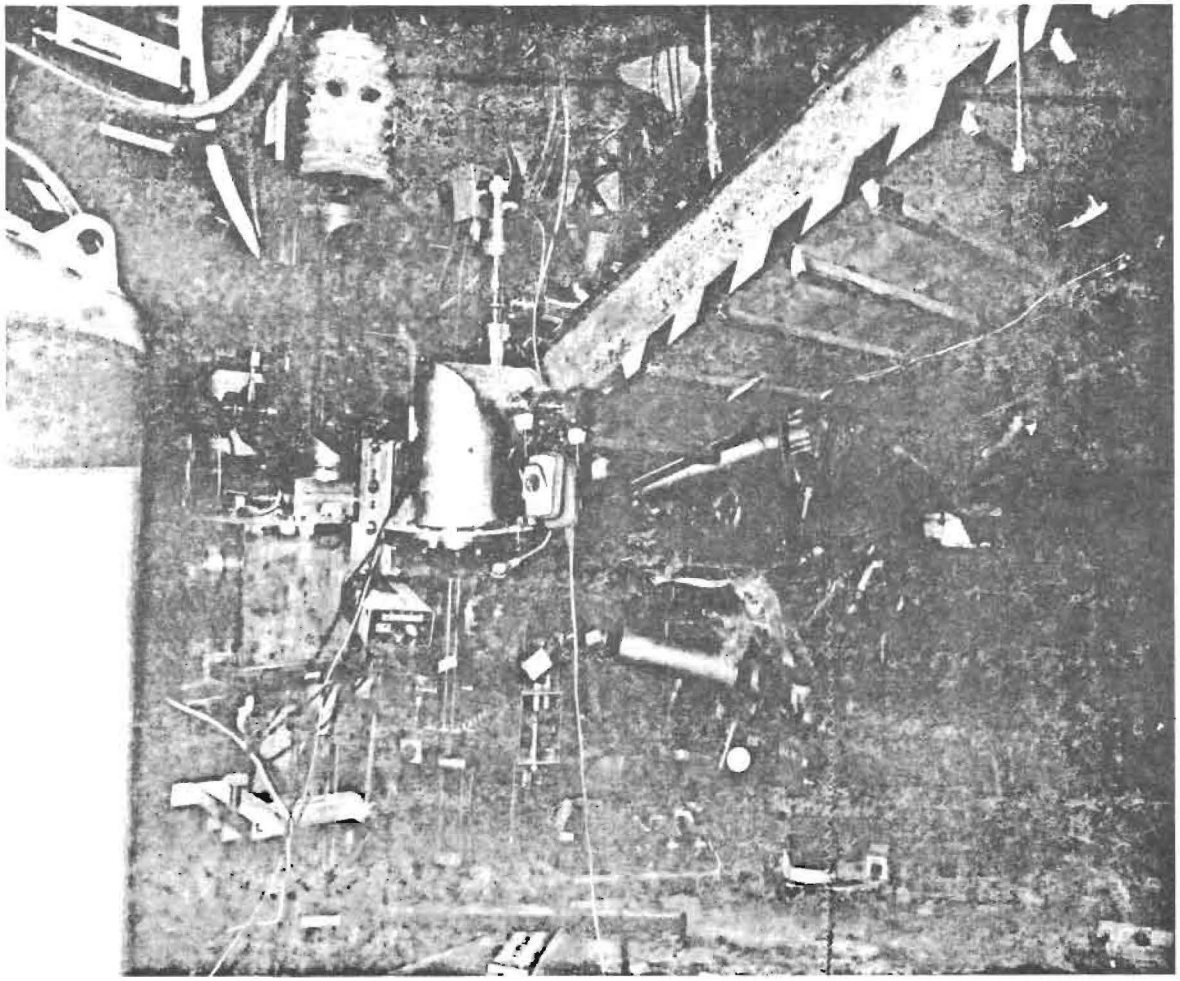

Figure 2.4b Hydrogen gas target located in the accelerator tunnel.

a.	width of hydrogen jet (FWHM)	12 mm
b.	nozzle to center-beam distance	15 mm
c.	pressure of injected H_2	25-60 psi
d.	temperature of gas, liquid or solid H_2 (most times gas-liquid mixture)	40°K
e.	density	3×10^{-7} gm/cm^2
f.	ambient vacuum in proximity of the target	10^{-5}-10^{-6} torr.
g.	duration of pulsed H_2 jet	~200 msec.
h.	sublimation period	40 minutes
i.	continuous operating period	2-4 hours

The target was pulsed at two different times in order to coincide with preselected energies during every acceleration cycle (see Figure 2.5). Approximately every 2½ hours, depending on operating conditions (Figure 2.6), the target would be remotely retracted from the beam line and warmed up in a sealed environment, so as to sublimate the frozen hydrogen. This procedure typically required 40 minutes, after which an already cooled target would be reinserted into the beam line for further pulsed operation. The operation of the target was controlled by monitoring the pressure and temperature at various points of the system, and also by the elastic scattering of the beam as revealed by the on-line data acquisition program.

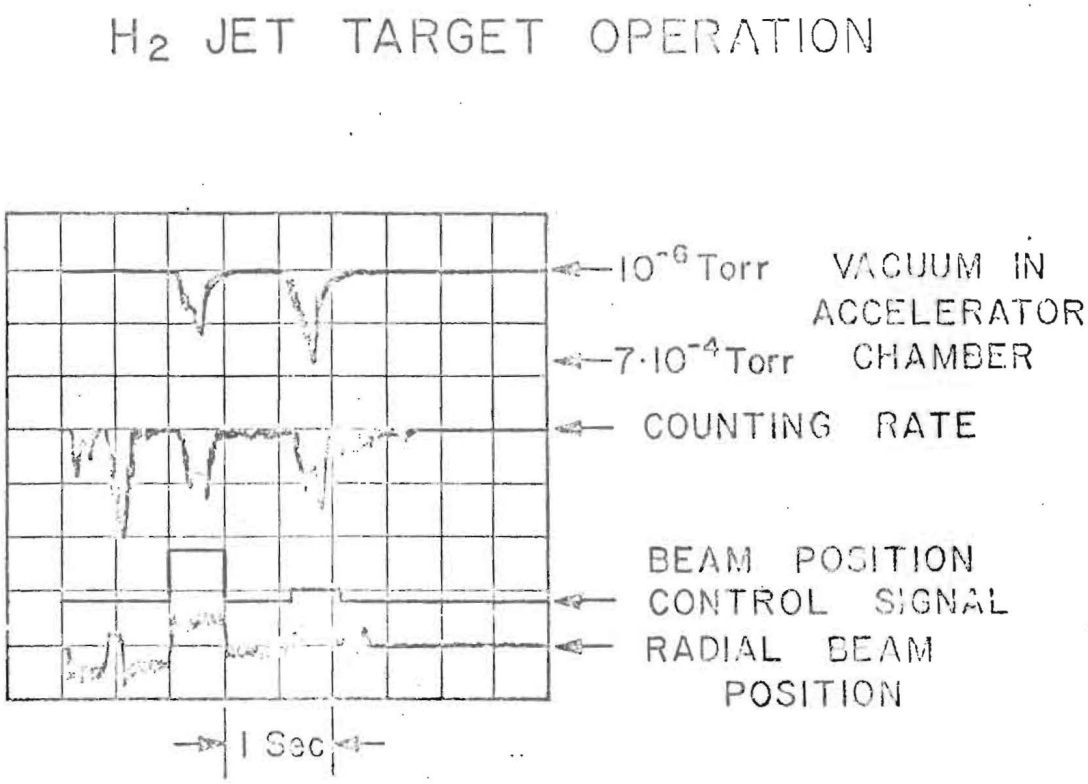

Figure 2.5 Timing of pulsed jet during beam acceleration cycle.

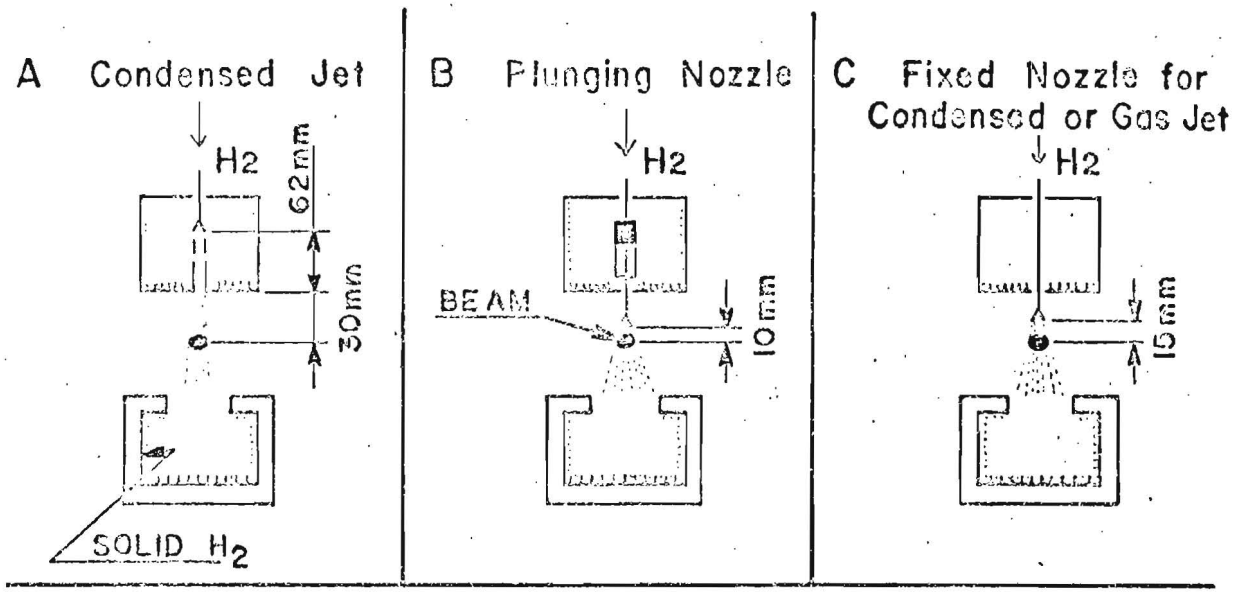

	A	B#	C
Distance from the Nozzle to Beam (mm)	30	10	15
Quantity of H_2 per Jet (cm^3)	60	130	90
Temperature H_2 before Nozzle (°k)	14÷20	45÷70	20÷23
Average Density of the Jet (g/cm^2)	$4\div5\times10^{-7}$	$1\div1.5\times10^{-7}$	$3\div5\times10^{-7}$
Width of the Jet (mm)	10÷12	10	12÷15

Quantity of Jets per Pulse: H_2 — 2
D_2 — 3÷4

Duration of the Jet Pulses ~ 250 msec.

For D_2 ≈ the same results.

Figure 2.6 Various modes of operating with the gas jet.

Beam

The accelerated beam was not under our control, however we were permitted to introduce local adjustments of the radial and vertical position ("beam bumps"), as required for a good interception of the target. Feedback circuits to the accelerator R.F. cavity permit adjustment of the beam radially ("radial bumps"). Operating mode B, shown in Figure 2.6, permits complete control over the interaction region. The average beam operating conditions for our experiment were:

a.	intensity	$(4\text{-}20)\times10^{11}$ ppp
b.	vertical size of beam at highest energies	~2-3 mm
c.	angular divergence as defined by straight section apertures	$\lesssim$.5 mrad.
d.	energy definition (2-3 data acquisition gates, each 15-20 GeV wide), from	50 to 400 GeV*
e.	rate of energy increase	100 GeV/sec*
f.	radial bumps of beam during pulsed jet	10 mm
g.	vertical correction of injection field	1 cm
h.	beam losses over acceleration cycle	$\lesssim$5%

The diameter of the N.A.L. main ring is 2 km (see Figure 2.1a), thus determining an orbit circulating period

*In the 400 GeV operation, the rate of energy increase for the last 100 GeV becomes parabolic, joining into the flat top. Saturation of magnets, orbit problems and electrical power network limitations make this mode of operation necessary.

of 20 μsec - i.e. 5×10^4 turns/sec for any one beam particle. During the "diffraction peak" phase of our experiment, the accelerated beam consisted of, from 1 to 3, injected beam bunches. In the latter stages the beam attained record intensities of 5×10^{12} ppp with as many as 11 beam bunches. Typically 4-6 beam bunches of moderate intensity $< 2 \times 10^{12}$ ppp, are close to the limit of the data rate that we can accept. This is due to an increase in accidentals, but mainly to a limit in event storage in the computer memory (24K words). For a high precision experiment such as ours, the accidental rate should not exceed 2%.

Detectors

The detector system used is shown schematically in Figure 2.7a,b. It consisted of a bank of solid state detectors mounted on a remotely operated movable carriage (platform). The solid state detectors ranged from .1 to 5 mm in thickness, and tungsten collimators of rectangular shape were used; the usable area was approximately 1 cm^2 for each detector. The movable carriage with the detectors was enclosed in an extension, connected directly to the accelerator main ring beam pipe and maintained at high vacuum. Vacuum gates were available for sectioning off the detector instrumentation in order to provide access and

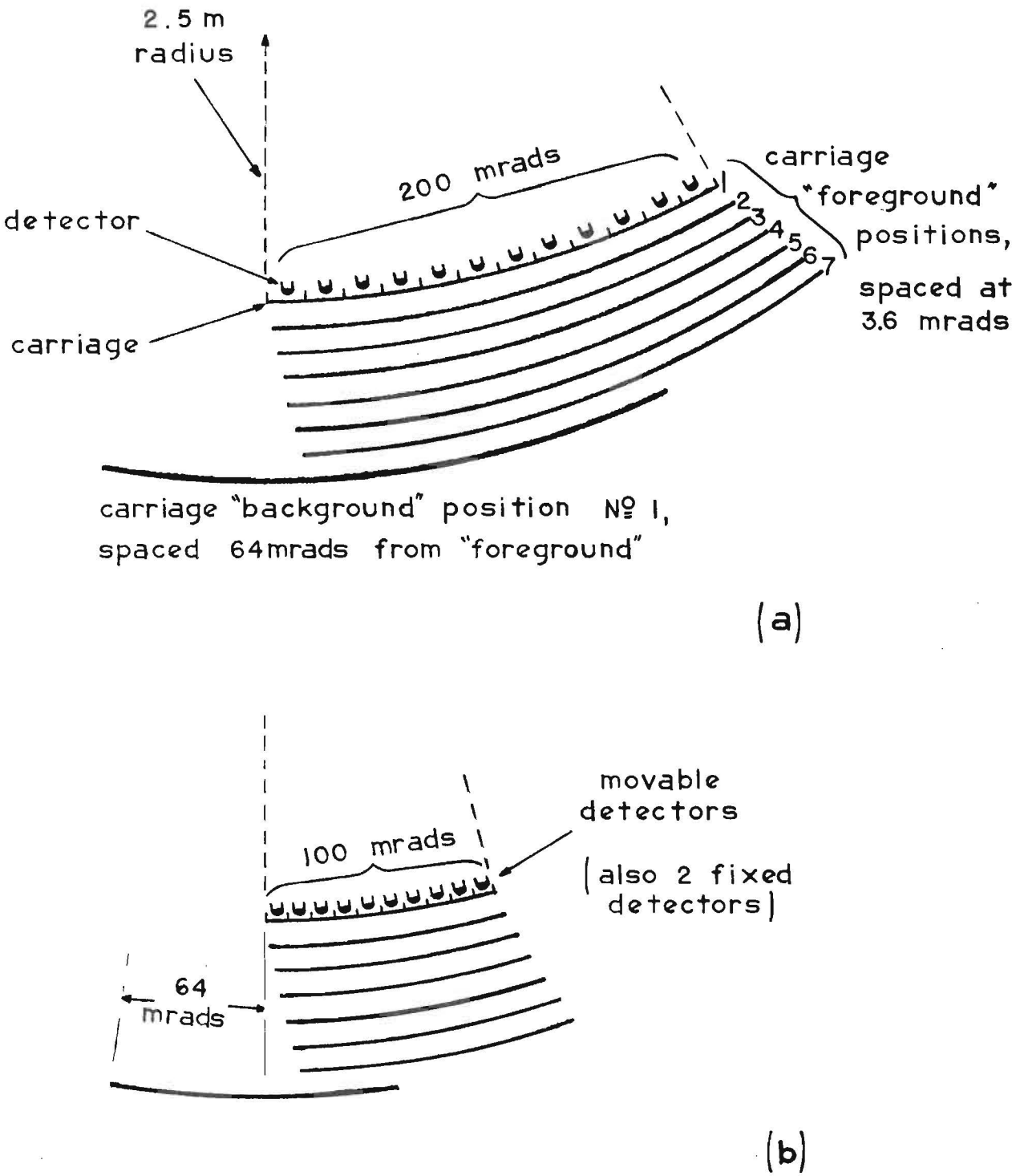

Figure 2.7a,b Geometry of the detector supporting carriage;

(a) for diffraction peak data; (b) for real part data.

guard against failures (see Figure 2.7c). The detectors were positioned on the arc of a circle centered on the target, at a distance of 2.48 m. The angular extent was roughly 10°. By moving the carriage, the full range of t, .001 - .18 $(GeV/c)^2$, could be covered. The geometry of the bank of solid state detectors is shown in Figure 2.8.

The solid state detectors were of the surface barrier type for the very low energy recoils, and lithium drifted type for the higher energy recoils. In order to protect the detectors against deposition of diffusion pump oil and other foreign matter, thin mylar films were used to cover the active surface (in cases where resolution would not be adversely affected).

The applied high voltage (field normal to active surface) that renders the detectors fully efficient is 200 - 250 volts/(mm of thickness). This applied voltage produces a quiescent leakage current (of a few $\mu A/cm^2$) within the detector. Improperly used detectors will exhibit considerably higher leakage currents; these detectors may adversely affect the linearity of the output signal with respect to particle energy. Detectors deteriorate due to radiation damage (primarily dislocations in the crystal lattice), or from contamination with oil or corrosive vapor impurities. Caution was exercised by keeping the

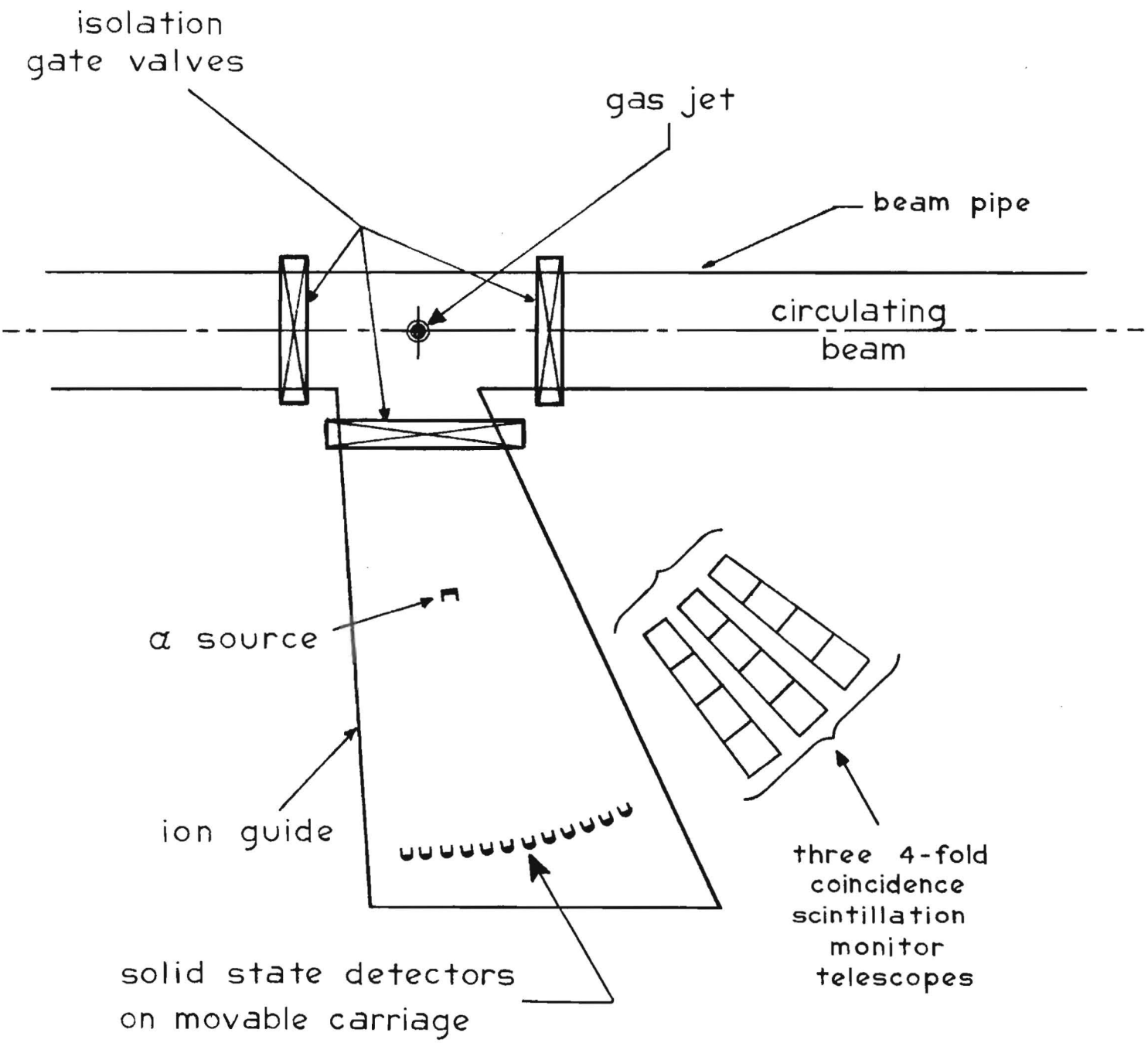

Figure 2.7c Schematic diagram of the configuration of the beam, target and detectors.

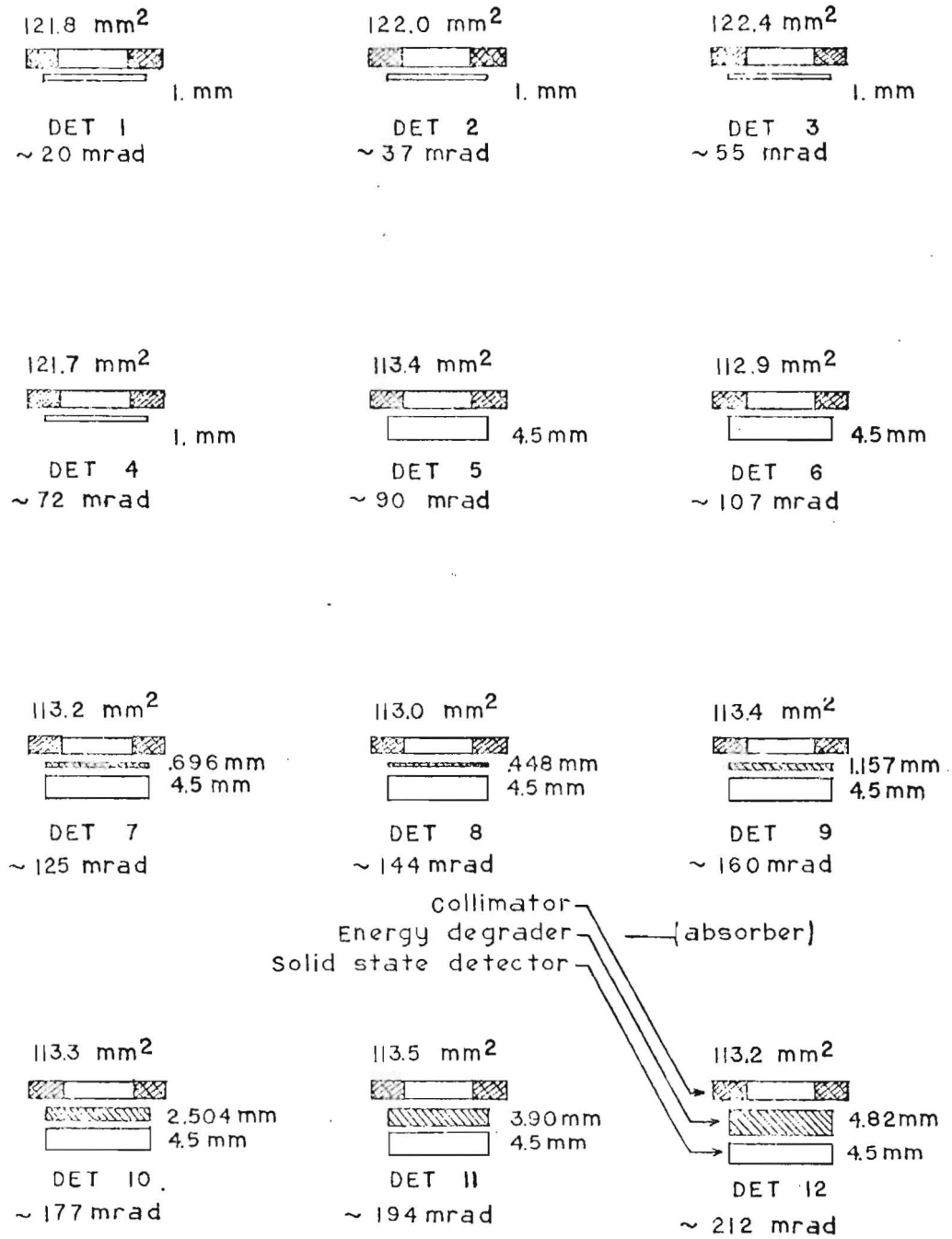

Figure 2.8 Schematic diagram indicating the relative thickness of the collimators, absorbers and detectors at various angles (diffraction peak data).

detectors in a clean environment and applying the high voltage gradually. The high voltage was turned off throughout inactive periods, to minimize radiation damage and protect the detectors against vacuum failures.

Detector Calibration

The following calibration procedure was devised and applied to each detector, individually, in order to relate pulse height energy to the recoil particles. A Ra^{220} α-source was mounted inside the ion guide, roughly 1 m away from the detectors, and was used to illuminate them. The signal obtained is a direct measure of the energy deposited by the α-particle stopping in the detector. Thereafter an extrapolation to all other energies (within the range of the detector) was obtained by making a linearity curve; this was achieved by sending a pulse (properly time shaped) of a given charge, through the preamplifier,to the detector and recording the output signal. By matching the input signal so that the output signal corresponds to the size of the signal obtained for the α-source, one has a complete signal vs. input energy relation. There are, however, at least two problems with the above procedure. Since the range of the α-particles within the silicon is only 28 μm ($\equiv$.028 mm, our detectors being .1-5 mm thick), the calibration procedure described does

not guarantee anything about depths larger than 28 μm. The calibration curve should, in principle, be obtained with sources of various discrete known energies, spanning the whole region of interest. Furthermore, the source should emit protons, to insure identical conditions for calibration and actual runs. In view of these requirements, extensive tests were done with a diffracted cyclotron beam at Princeton University[5]. The results indicated complete uniformity of the active layers, and in cases where results were doubtful, the particular detector was discarded. This gave us confidence in the validity of the α-source calibration procedure.

As part of the calibration procedure we also required that the detectors be fully depleted (i.e. have an appropriately high electric field throughout their active volume). This check was done by exposing the detectors to carbon filaments that were bombarded by the accelerated proton beam in the main ring. The carbon filament target was mounted by a technique similar to that of mounting $(CH_2)_n$ foils. The reaction p + C → "anything" has in its final state a few of the simple nuclei: $^1H_1$, $^2H_1$, $^3H_1$, as well as He, and others. The complexity of the reaction, and the wide distribution of Fermi motion momenta, produced a continuous spectrum of recoil particles in the kinematic region of our detectors (Figure 2.9). It was

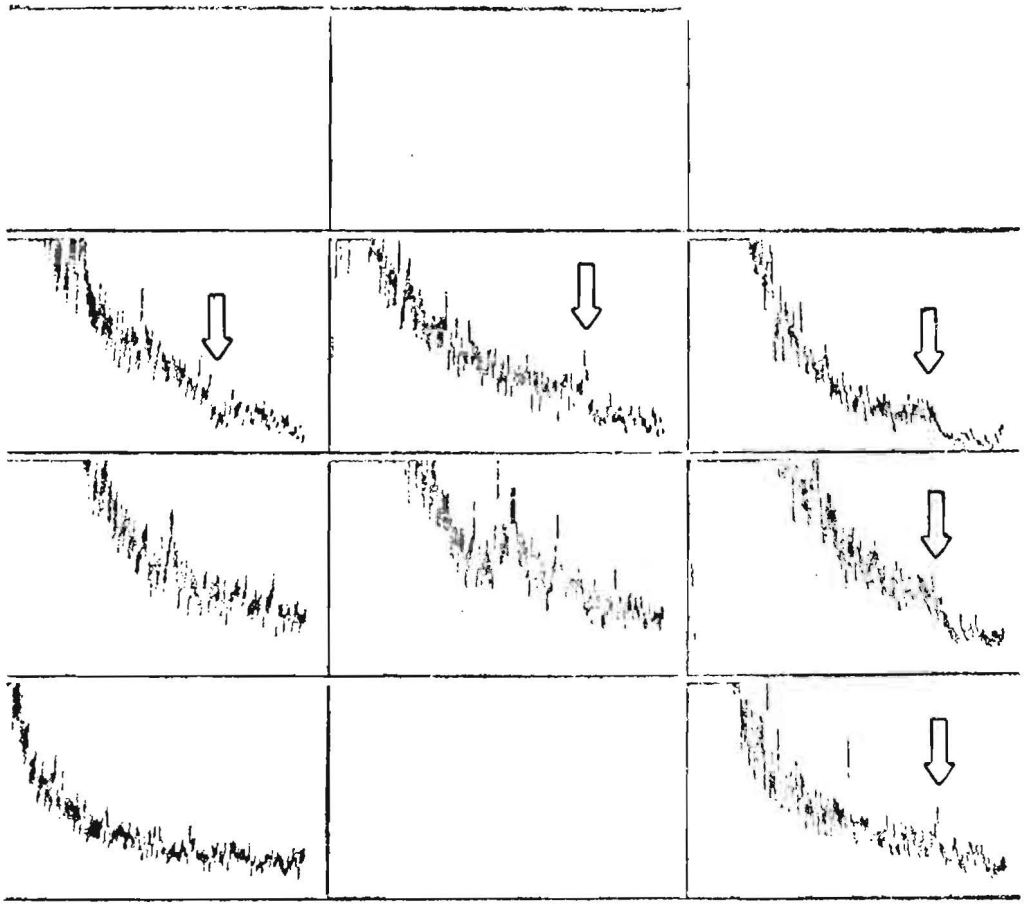

Figure 2.9a Spectra of recoil particles from a carbon target. Arrows indicate the "position" of the "end of detector"; where arrow is not shown, the end of detector is beyond the right hand extreme of the histogram.

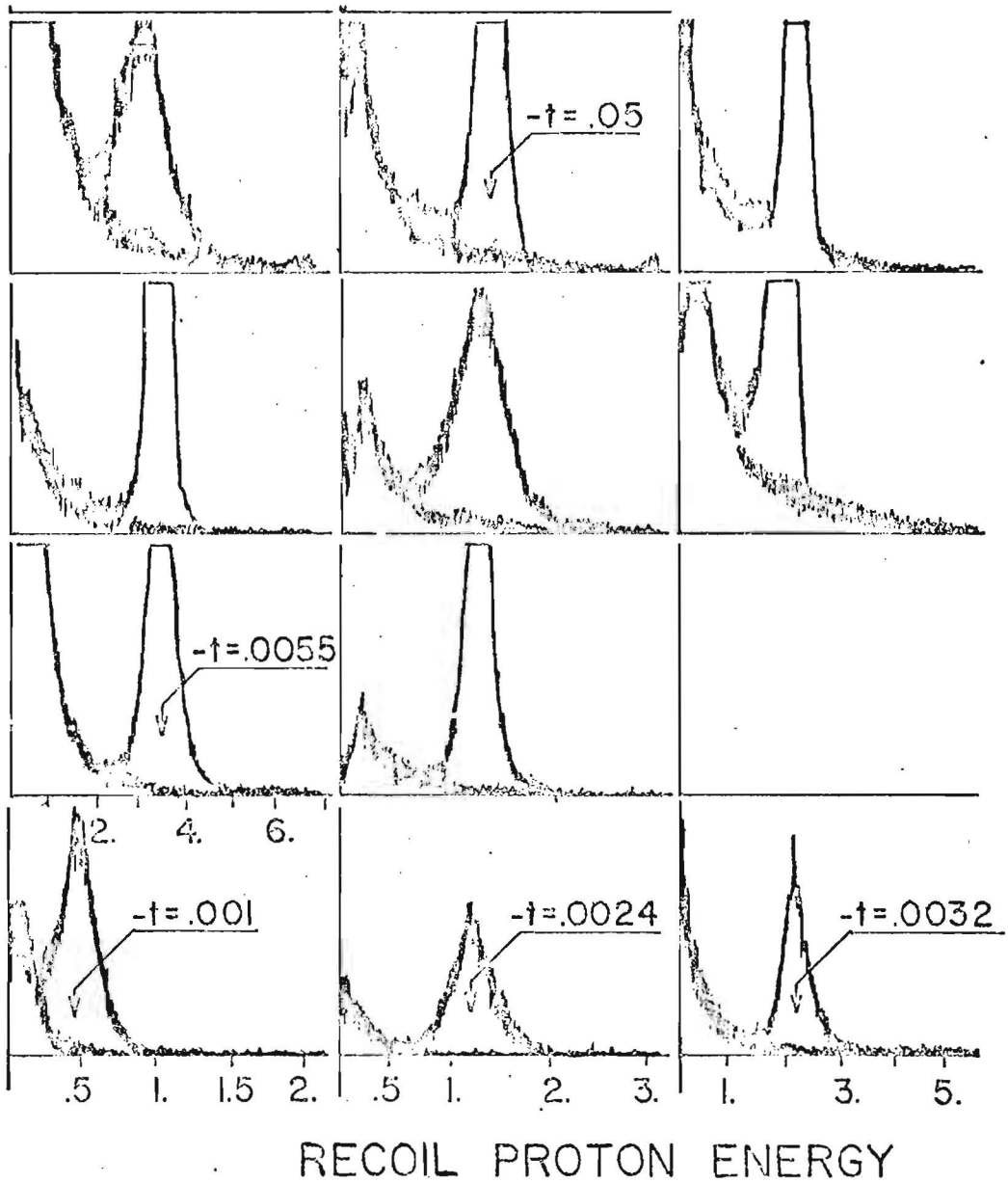

Figure 2.9b Spectra of recoils from a hydrogen gas target; the figure shows a superposition of "foreground" and "background" spectra.

determined that fully efficient detectors have a typical signature for the maximum range of particles stopping within the detectors. Higher energy particles traverse the detector and due to the shape of the range-energy curve, deposit less of their energy (dE/dx), than the "maximum range particle." If the typical "end of detector" signature has a large accumulation of counts, this indicates less than optimum efficiency.

Energy Degraders

Part of the experiment was devoted to the study of the diffraction peak in the region of $|t|$, .01 - .18 $(GeV/c)^2$. This corresponds to kinetic energies of ~5 - 90 MeV, whereas our detectors could stop only 30 MeV protons, i.e. 5 mm thick silicon detectors (see Figure 2.10). To extend the useful range of our detectors, "energy degraders" were used so as to reduce the effective incoming energy of the recoil protons. The degraders were used in two modes:

- either to reduce the protons' energy so that they would fully stop within the detectors,

or to significantly reduce the protons' energy but not to the point of stopping in the detector.

In the latter mode, the remaining energy after the protons passed through both the absorber (degrader) and the

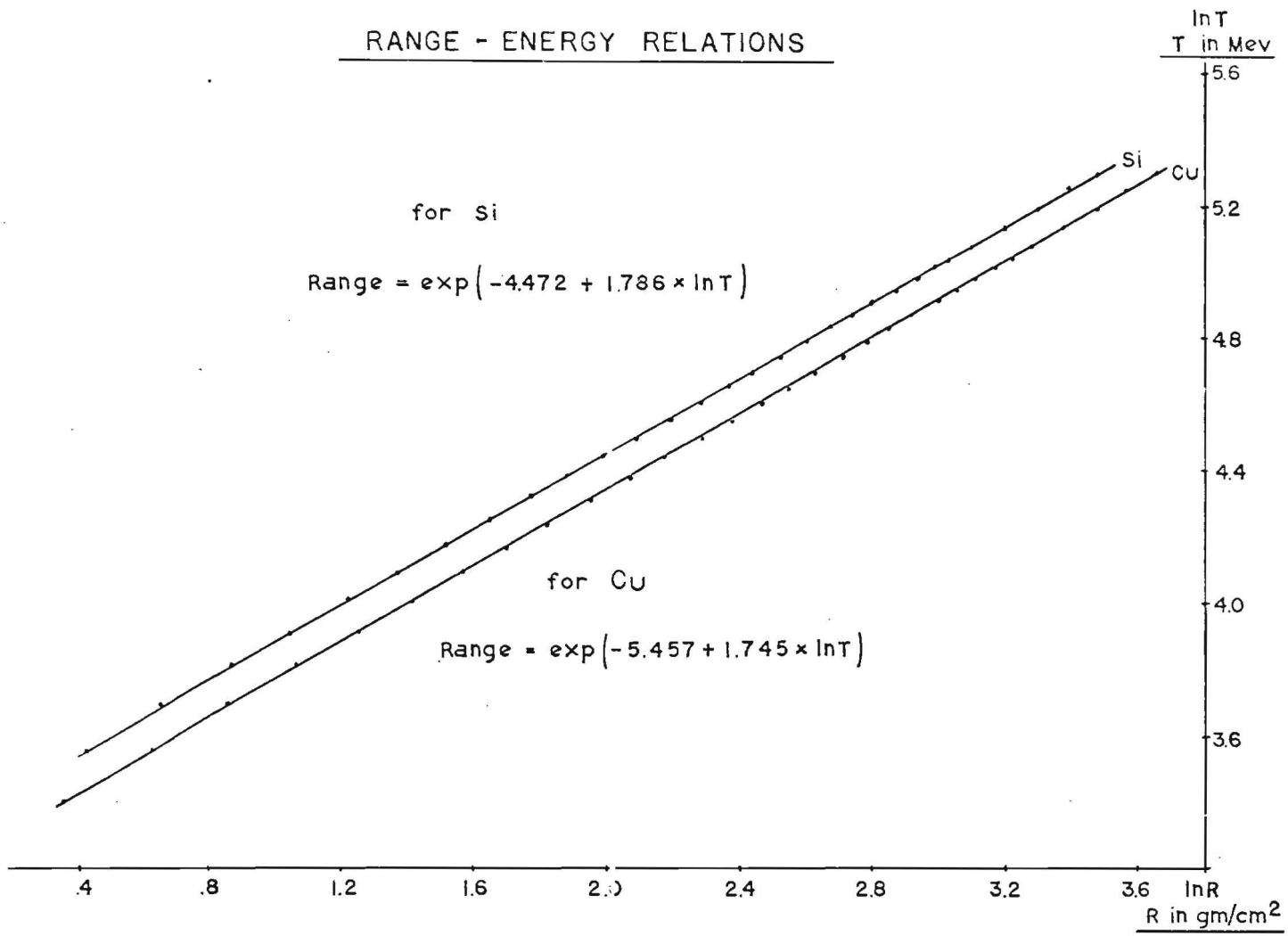

Figure 2.10 Range-energy relations for silicon and copper.

detector, was very small, and the energy deposition within the detector was increased. It is difficult to decide, under general conditions, which of the above two energy degrading modes is superior. The advantage of stopping protons within the detector is that no problem arises with nonuniformity in the thickness of active volume of the detector. However, enough material has to be used so that multiple scattering and nuclear interactions within the absorber become appreciable. Also the background subtraction from under, an originally narrow spectrum, becomes difficult, due to a broadened spectrum caused by straggling. The advantage of using absorbers with detectors in the dE/dx mode is that the signal moves out of the dE/dx background for fast particles, while multiple scattering and nuclear interactions are still kept in balance.

Electronics and On-line Operation

Twelve solid state detectors were used. Each was equipped with its own preamplifier, amplifier and analog to digital converter (ADC). Figure 2.11 is a schematic of the electronic logic. Pulses formed by the solid state detector (due to the passage of a charged particle), are amplified by the preamplifier, a short distance away from the detector (~2 feet). Then the signal is sent back to the bulk of the electronics. The purpose of the preamplifier is to minimize the capacitance in the solid

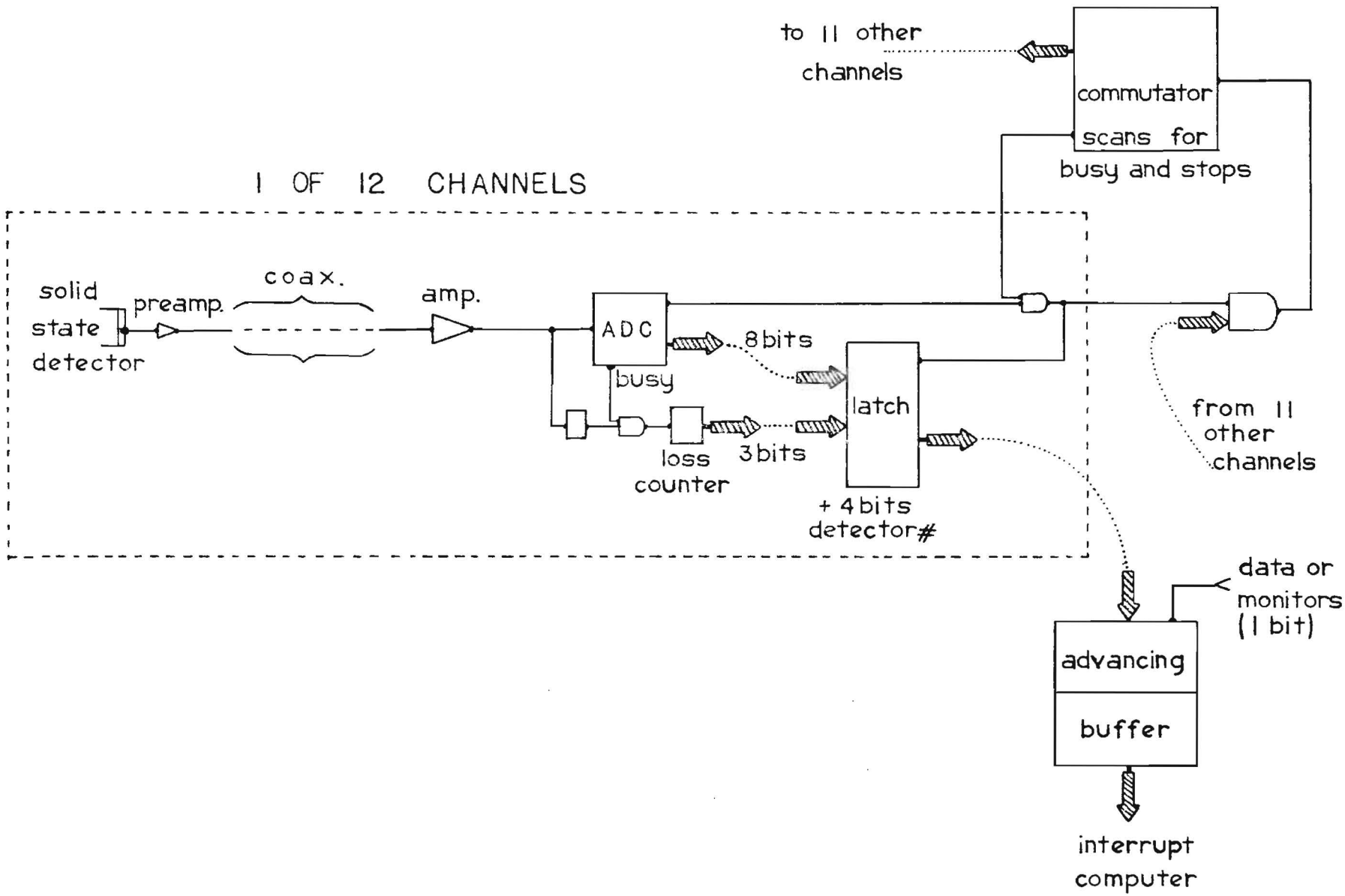

Figure 2.11 Schematic diagram of electronic logic.

state detector output line. It decouples the detector from the rest of the system and the amplifier signal is effectively not affected by the noise in the transmission line. The output of the preamp is amplified by the main amplifier to a working logic level. This output, in turn, is processed by an ADC which digitizes the pulse height. The solid state detector is a linear device, producing signals proportional to the energy deposited. Of course, the preamplifier, amplifier and ADC are all linear logic devices. The ADC contained a "loss-counter" which scaled the number of pulses received while the ADC was busy digitizing a signal. In the type of ADC used, the digitizing time is proportional to pulse height, up to a maximum of 6 μsec, for 256 channels; this corresponds to a scanning rate of 40 MHz. The detector rise time constant (including preamp. and amp.) was .8 μsec. The twelve solid state detector channels were input into a commutator which scanned sequentially at a 2 MHz rate through the channels. When an ADC-ready signal was detected, the output of that particular ADC was transferred to a dual buffer's first stage. [The output of an ADC consisted of: 8 bits digitized signal, 3 bits "loss-counter", 4 bits detector/number and 1 bit data <u>or</u> (monitor;gate number-time)]. The buffer would advance the data to the second stage while interrupting the

on-line PDP-11 computer. Meanwhile, any other ADC could have been independently acquiring and digitizing its data, while the commutator clock would scan sequentially for the next ADC-ready signal. As soon as the data of an ADC was transferred to its own buffered gate, an ADC reset signal would be generated. This allowed that particular channel to accept further signals.

Within the PDP-11, data from the ADC's and monitor was recorded and histogrammed. The main function of the on-line program was to store raw data on tape for further off-line processing. In core, a dual buffer was used for this purpose. Data filled one buffer before being dumped onto tape, while the other buffer was being accessed. The data on tape, consisted of sequences of blocks of data and a block of monitor and operating conditions (see Figure 2.12). The on-line program was histogramming the data on an interrupt basis, serving as an operations monitor.

Every pulsed jet duration of 200 msec was subdivided into 9 time intervals; typically, for 3-4 of these intervals, the jet was on. By acquiring data throughout all 9 time gates, one could estimate the origin and number of "background" events - events not associated with the target. This was a very useful on-line procedure for adjusting the jet and beam for an optimum signal to noise

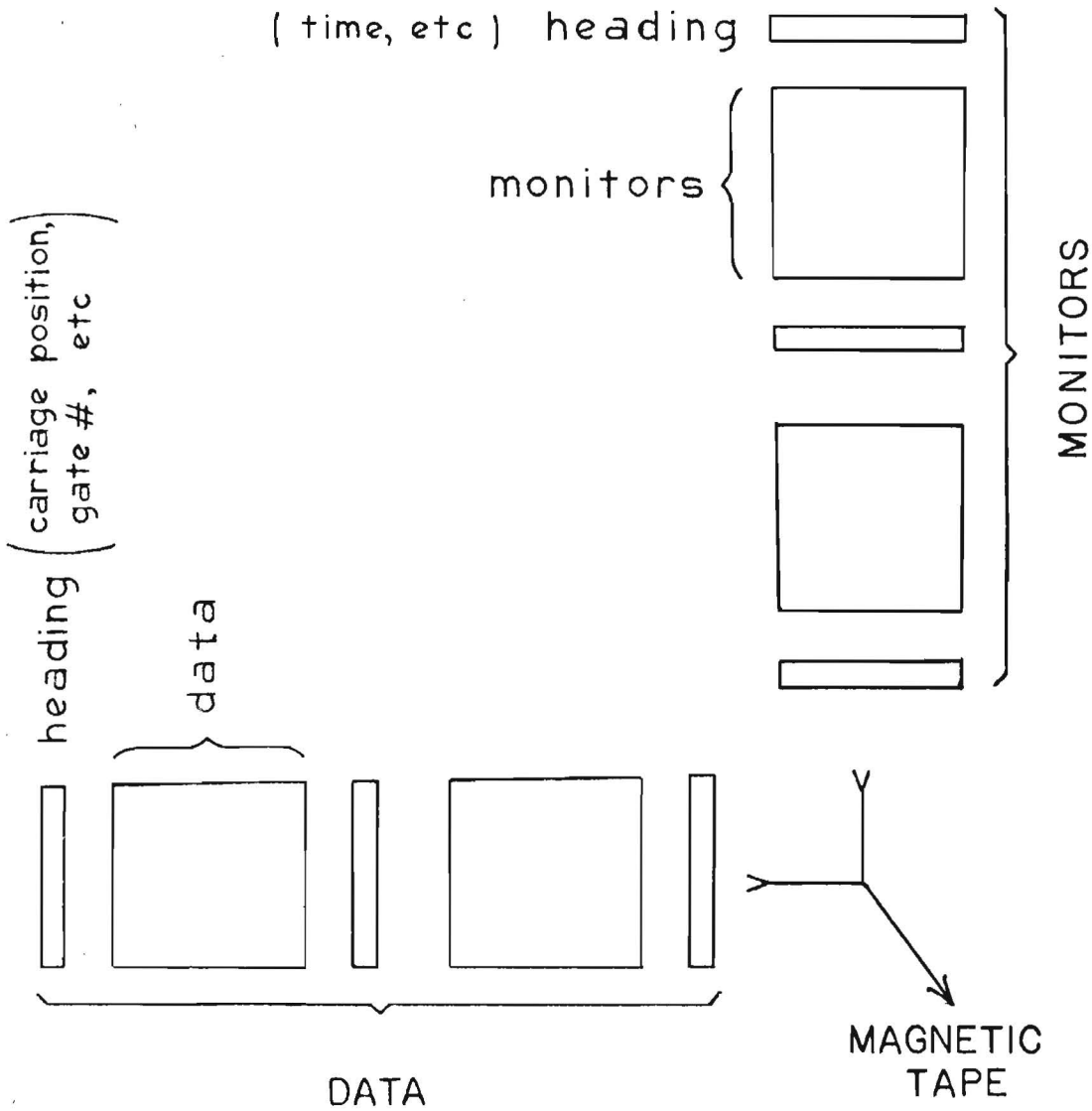

Figure 2.12 Data acquisition on magnetic tape.

ratio. Off-line data acquired just before, and just after the pulsing of the jet, were rejected, to reduce background.

Target saturation and the need for sublimating it were also determined from signal to noise ratios.

2.3 Background and Its Sources

It was found during our testing that background was roughly proportional to detector thickness, indicating a nonkinematic, target-independent source of such background. Relating this information with the fact that a significant column of residual gas diffuses upstream of the target, explains part of this problem. Therefore we tried to minimize background by optimizing the detector and absorber thickness. We also attacked the problem at its roots, by pumping faster the upstream region of the beam line, by installing partial collimators around the target, so that evaporates from the target could be better contained, and by sublimating the target cryopump whenever the background became appreciable. Usually, sublimation improved the situation. Another source of background was beam loss upstream of the target due to a small aperture in the orbit, and beam halo at low energies. To reduce this problem, we controlled the radial position of the beam during data taking.

Most of the background was determined to be not

target associated, and produced upstream of the target. Such background has a very weak kinematic dependence as a function of the angular position of the detectors (i.e. of carriage position). To take advantage of the situation, data was recorded in two different positions of the detector carriage. A so-called "foreground" position was obtained in the kinematic region of interest. Then, a "background" position was obtained by moving the carriage 64 mrads closer to low $|t|$. By this means, the elastic spectra in the detectors were shifted to much lower kinetic energies while the background (not target associated) remained the same. In most detectors the elastic spectrum was eliminated as the angular position was beyond 90° from the beam. In the rest, elastic spectra, in the "background" position, were far removed from the location of the elastic spectra in the "foreground" position.

The acquisition of the two spectra, "foreground" and "background", was accomplished by taking data in the ratio of 15 to 5 accelerator pulses, respectively. In order to be able to have a proper normalization of the two spectra, we used two solid state detectors in positions fixed in space. This procedure provides a direct relative monitor of the integrated luminosity for both the "foreground" and "background" spectra.

2.4 Data Analysis Problems

Given the stated beam and target conditions, one obtains a luminosity of 10^{34} events/cm^{2}sec and an event rate of 4×10^8 events/sec, for a 10^{12}ppp beam. Some two hundred beamtime hours were used to accumulate data in about 200 runs, totalling 6 million elastic events, for the diffraction peak analysis. Comparable quantities of data were obtained in the analysis of the "real part."

At this time we indicate some of the possible problems in data analysis, due to systematic errors.

a. Due to the finite ADC digitizing time, dead time effects were of the order of $\leq$2%, for the highest rates. Data were corrected by simply scaling up all events of the particular channel by the percentage dead time. This correction to the data was clearly defined and could not produce large systematic effects. The dead time correction itself was proportional to the event acquisition rate, as expected (see Figure 2.13).

b. Detection of recoil particles of energy larger than 30 MeV entails a correction in detection efficiency. Due to interactions in the absorber or the detector (charge exchange and plural nuclear collisions), a small fraction, typically $\leq$5% (for 60 MeV) of the recoil protons are shifted to lower energies. Thus they are effectively lost from their true elastic spectrum and an appropriate

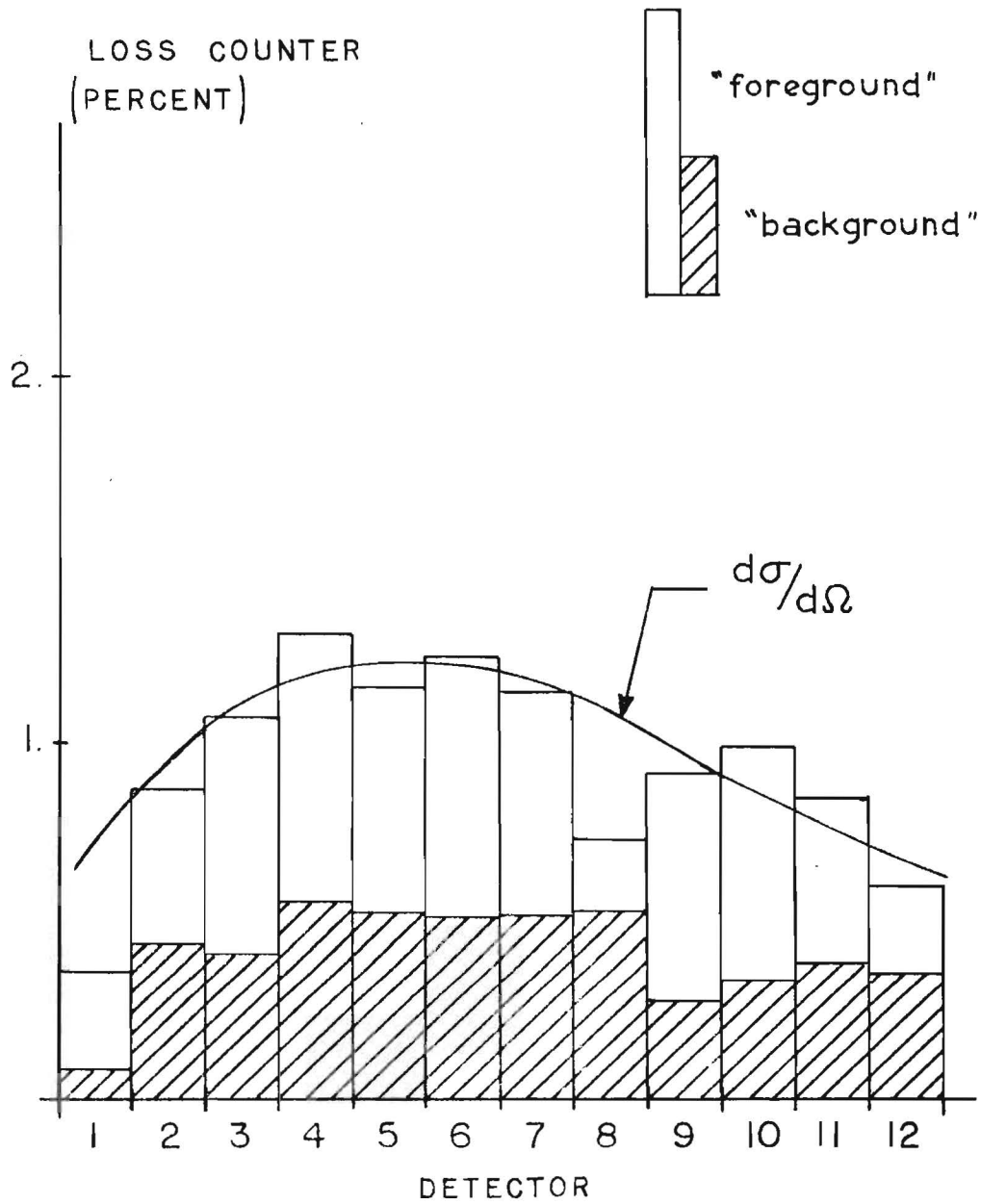

Figure 2.13a Percentage dead time for diffraction peak data.

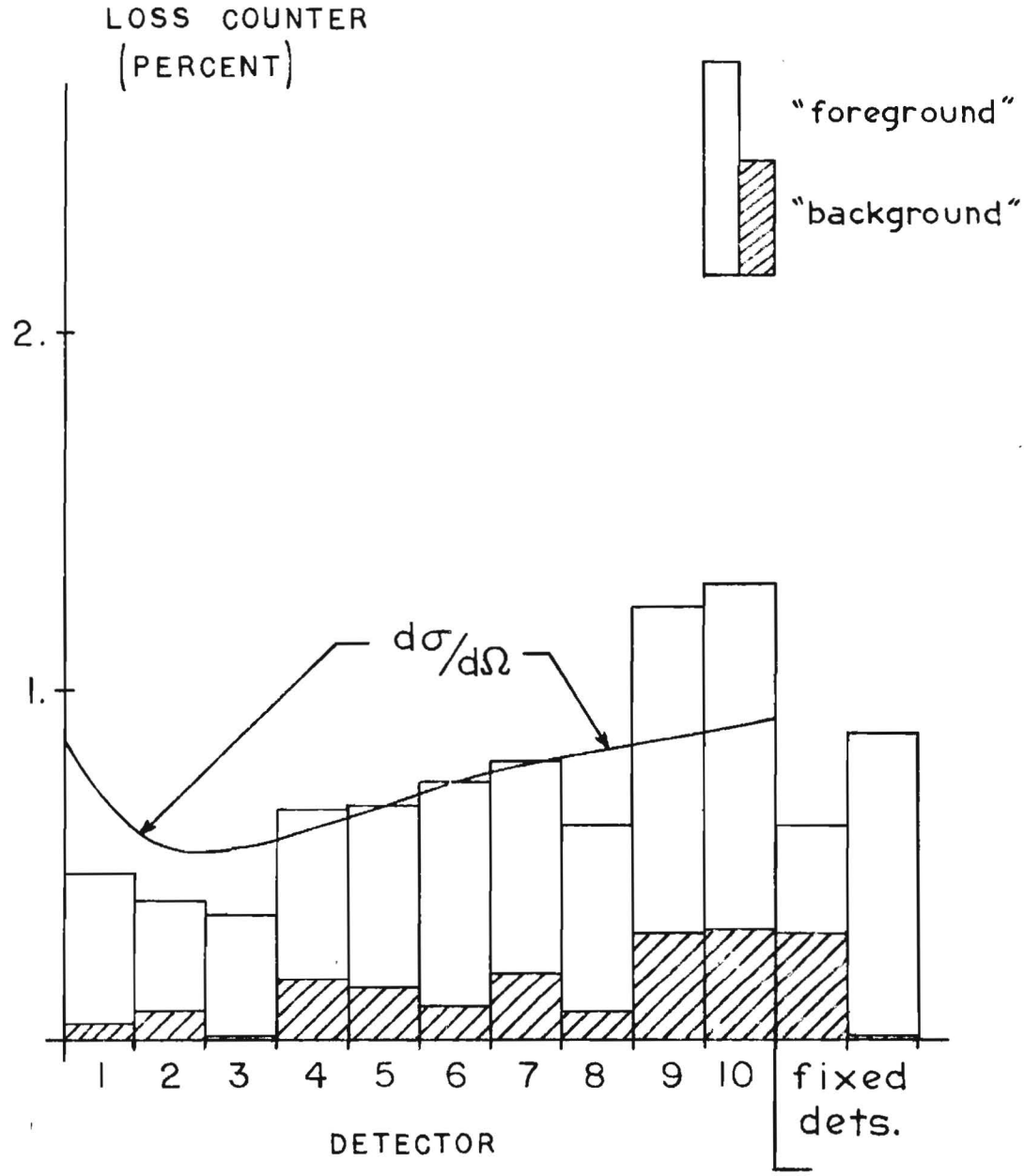

Figure 2.13b Percentage dead time for real part data.

correction must be applied. This correction, in turn, is known to an accuracy of (5-10)% of full value. It should be clarified that the correction is t-dependent in approximately monotonic fashion, and is only appreciable at $|t| > .06\ (\mathrm{GeV}/c)^2$, where it is roughly 1%, depending on absorber and detector thickness to some extent. The "real part" data did not require (much of) this correction ($\leq .6\%$). We call this correction a "nuclear correction."

c. A correction must be made to eliminate the tail of the inelastic contribution (from a reaction of the type $pp \rightarrow Xp$) to the elastic peak count. Since the mass resolution is linearly related to the recoil energy (inelastic collision kinematics differs from elastic kinematics) the correction is strongly t-dependent. This correction depends on incident energy as well, and was estimated by various methods as explained in the next two chapters. The correction is thought to be insignificant in the low $|t|$ range of the "real part" data ($\leq .02\ (\mathrm{GeV}/c)^2$).

d. Some geometric systematic errors could arise from wrong measurements of the target-to-detector distance, and wrong measurements of the detector collimator areas. We estimate that the first cause could systematically affect the results by less than .3%. The second error is estimated as less than 1% of the area of each collimator.

e. The effects of the energy dependent accelerator fringe field will be treated in the following chapters. They are believed, at this time, to be insignificant.

f. The resolution of the solid state detectors is typically 30 keV for a 15 MeV incident particle. We used ADC's which digitized signals to 8 bits (256 channels). No problem arises from detector resolution, but shifts of up to 3% in the measured energy of detected particles, are possible (deficient detector, or calibration). As a systematic error, these shifts manifest themselves when the recoil angles are evaluated from the data. The angular resolution of the system, given the available geometry (12 mm wide jet, 5 mm detector collimators, 2480 mm target to detector distance) was about 5 mrads. This, however, is not the limit for a more accurate knowledge of effective geometry, as explained in the chapter on the "real part."

g. Finally, in the analysis of the data, background subtractions using the "foreground" less "background" method, were estimated to introduce errors of $\lesssim$ 1%.

The systematic effects defined above will be discussed in detail in subsequent chapters.

References for Chapter II

1. G. G. Beznogikh et al., Phys. Lett. 30B, (1969) 274.
2. D. A. Gross and A. Melissinos, University of Rochester Report No. UR-875-365.
3. L. S. Zolin et al., JINR Preprint, P-13-3425 (1967); V. D. Bartenev et al., JINR Preprint P-13-6058 (1971); A joint paper authored by our whole group appears in: Advances in Cryogenic Engineering 18, (1973) 460.
4. V. D. Bartenev et al., Phys. Rev. Lett. 29, (1972) 1755.
5. The assistance of E. Cecil in these runs is appreciated.

CHAPTER III

ANALYSIS OF DIFFRACTION PEAK DATA

In this chapter we present an analysis of data obtained in the range of momentum transfer $.002 \leq |t| \leq .18$, which is part of the diffraction peak.

The data cover the incident energy range $40 \leq E \leq 400$ GeV, and were taken in runs at two energies simultaneously, during the acceleration cycle of the proton beam. This is an important point in the analysis, since, presumably, systematic errors for data taken at two energies with the same equipment (and same external conditions), are very similar. The measurement error is, practically s-independent, the main current interest being in the s-dependence of the diffraction slope b(s).

The elastic, spin-independent, differential cross section for nucleon-nucleon scattering is usually parametrized,

$$\frac{d\sigma}{dt} = \left.\frac{d\sigma}{dt}\right|_o e^{bt} \qquad \text{(assuming zero real part)}$$
$$= \frac{\sigma_T^2(s)}{16\pi} e^{b(s)t} \quad . \tag{1}$$

s is the center of mass energy squared.

It is true by definition, that,

$$\sigma_{el}(s) \leq \sigma_T(s) \quad . \tag{2}$$

From Eqs. 1 and 2 we get a lower limit on the elastic cross section upon integration over all t,

$$\sigma_T(s) \geq \sigma_{el}(s) \geq \int dt \, \frac{\sigma_T^2(s)}{16\pi} \, e^{b(s)t}$$

$$\geq \frac{\sigma_T^2(s)}{16\pi b(s)} \quad , \tag{3}$$

resulting in,

$$\sigma_T(s) \leq 16\pi b(s) \quad . \tag{4}$$

Since recent results indicate a rise in the total cross section, and a possible $\ln^2 s$ behavior, it is important to check the previous relation.

While the total cross section may be interpreted, in a geometrical way, as the area of the nucleon, in an optical model, b(s) may have a similar interpretation,

$$b(s) = R^2(s)/4 \quad , \tag{5}$$

where R(s) is the interaction radius of the nucleon.

The Regge theory predicts that the diffraction peak shrinks indefinitely with energy, meaning that b(s) grows with energy. The s-dependence according to Regge theory (single pole, no cuts) is,

$$b(s) = b_o + 2\alpha' \ln s. \qquad (6)$$

Recent results at the ISR indicate that there is a definite change in slope b(s) at about $|t| = .15$. This is one of the reasons for limiting ourselves to a region of $|t| \leq .18\ (\mathrm{GeV}/c)^2$. This experiment is less capable of distinguishing structure as a function of t, than might be required to see the "break." Finally, in the forward direction we should like to check whether the behavior e^{bt} continues, or whether there is yet another break at small $|t| \sim .01$ (or less).

3.1 Data Management

The on-line computer, a PDP-11, was programmed to buffer (2 buffers) events and periodically dump the buffers, alternately, onto magnetic tape. The tapes output by the PDP-11 were then read, interpreted and histogrammed by a PDP-10 computer. As each data acquisition gate was subdivided into 9 equal time intervals, separate histograms were obtained for different times, in the development of the pulsed jet.

Various monitors were employed in order to determine the relative quality of data in each time interval. Beam intensity and position, vacuum, temperature and pressure readings, gave us enough information about background and elastic events, to minimize the former by cuts on early and late time intervals. The remaining events were spread over a range where the increase of the primary beam energy was $\leq$ 20 GeV. These events (for the 3-4 intervals) were combined and constituted the main source of information at the averaged beam energy.

Detector calibrations, using a Ra α source (of 5.8 MeV), were obtained every few runs. The calibration constants were: the number of MeV per histogram channel and an offset of channels (Fig. 3.1). The implicit assumption was that detector response is linear with input signal (a fair assumption which was verified).

The finite rate of data acquisition by the computer and hardware, produced dead time effects. Data was corrected for the dead time which never amounted to more than 3% (see Fig. 2.13).

At this point the calibration information was introduced into the analysis and the spectra were printed in "MeV histograms" (Figure 3.2).

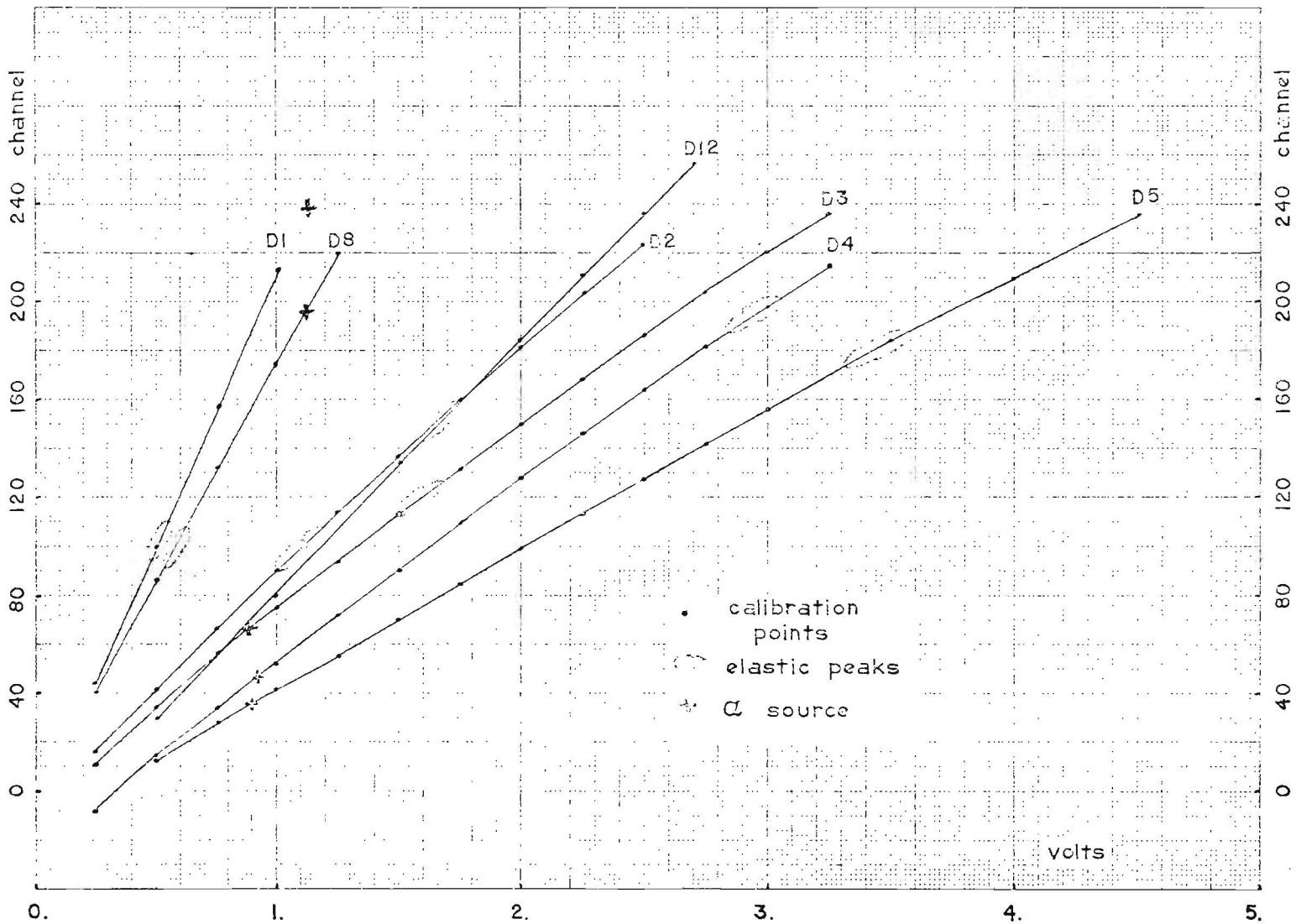

Figure 3.1 Calibration of detectors for diffraction peak data.

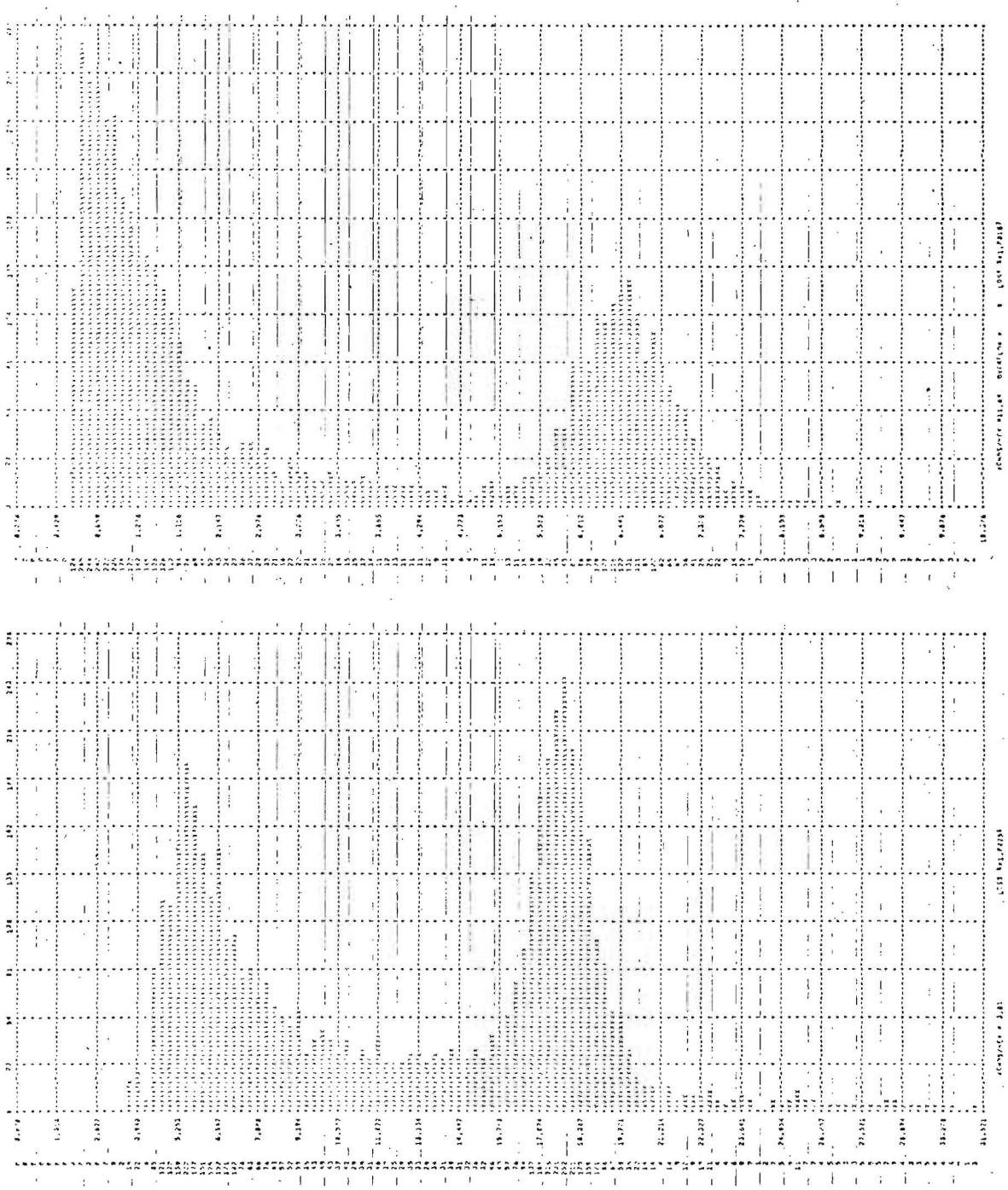

Figure 3.2a "MeV histograms" show clear elastic peaks, and background at the lower ends of the recoil energy spectra; 6.5 MeV (top) and 18 MeV (bottom) elastic peaks are shown.

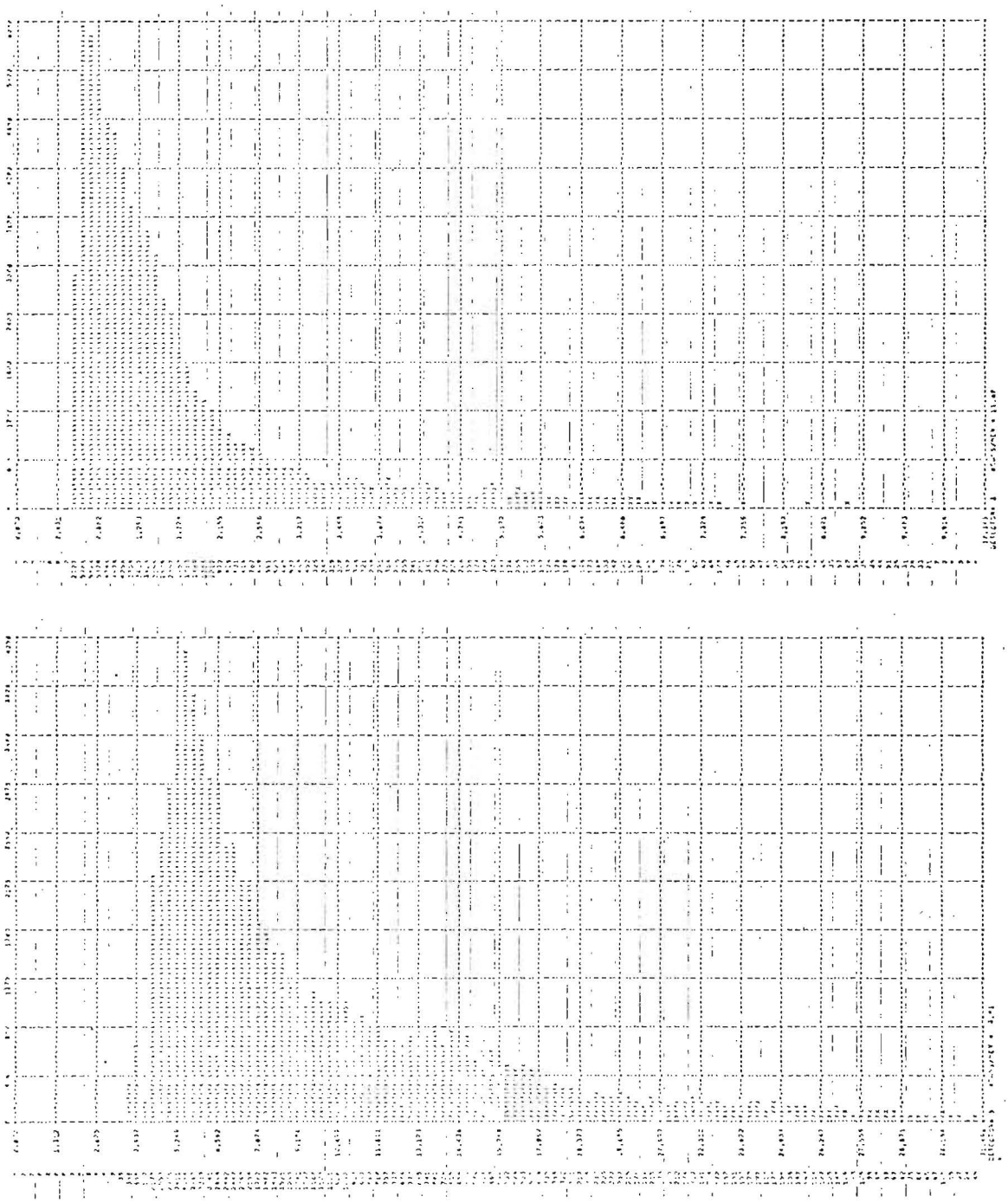

Figure 3.2b "Envelopes" of the spectra shown in Figure 3.2a.

3.2 Background Subtraction

Once the MeV histograms were formed, they sometimes showed evidence of substantial background under the elastic peak. We attribute this background primarily to "room background" (i.e. general radiation inside the accelerator tunnel), and to "tails" of the hydrogen jet (i.e. gas that originates from the gas jet but has diffused along the beam pipe). In order to minimize the latter background, we studied the thermodynamic conditions of the hydrogen jet, and concluded that best results are obtained with gas at a low input pressure (25-40 psi), at roughly 40°K.

We employed four different methods to subtract backgrounds:

a. two were based on MeV histograms as obtained after the procedures explained in the previous section,

b. the other two made use of "subtracted MeV histograms."

Subtracted MeV histograms were obtained by subtracting appropriate ratios (according to scintillation counter monitors) of "background" from "foreground" position histograms. This subtraction is, in first approximation, a subtraction of room background. What was left as background was attributed to part of the gas jet tails and to residual gases near the interaction region. An error of less than roughly 2% results. This subtraction procedure, broadly speaking, corresponds to an empty target subtraction.

The MeV histograms and the subtracted ones were studied, and individual limits were assigned for each elastic peak spectrum. The criterion for the limits was that most elastic events be contained within the limits. A simple fit to the peak was not always possible, because in some cases the elastic peak occurred in a region close to the end of the detector, resulting in an elastic spectrum which is very complicated and broad. In other cases minor defects in the large $|t|$ detectors would produce violent distortions. These limits, broadly speaking, correspond to cuts on the interaction region of the jet.

Each of the two histograms "MeV" and "subtracted" was further subjected to two types of background subtraction:

a. combining all spectra for one detector, less the elastic peaks, (the spectra are scaled to the same number of counts within a certain number of channels to either side of the elastic peak), one obtains, with few exceptions, a continuous and smooth histogram. The exceptions are those cases where one or two channel gaps are left. These are simply interpolated without any further problem. We shall call this background subtraction the "envelope method"*

* Note that this method is only allowed by the availability of the large kinematic range covered by the detectors from lowest to highest $|t|$ runs (i.e. the different carriage positions).

(the origin of the name being envelope, in reference to the smoothness of the resulting histogram);

b. interpolating between elastic peak limits with a straight line, one obtains a first order approximation to the background. This is obviously a very crude method, but, in effect, the result is quite similar to that of a simple fit. We call this the "interpolation method."

Each of the above two backgrounds was subtracted from the histogram. The result was the number of events in the elastic peak. We allowed an error of $\sqrt{(\text{histogram within limits} + (\text{background within limits})}$, on the elastic events. This is the minimum statistical error, assuming independence of background from elastic events. Overall we found relatively very little variation for the number of elastic events, due to limits placed on the elastic peak.

We give a systematic evaluation of the relative merits of the different background subtraction methods.

1) <u>Envelope on MeV histograms;</u> relatively large background allows good statistical evaluation. All runs at different kinematic positions are considered simultaneously, the envelope being an average and smooth background histogram (Fig. 3.2b). The justification for combining different kinematic positions is that most of the background is <u>not</u> kinematically dependent (room background).

2) Interpolation on MeV histograms; relatively good method for flat background. However this implies a limitation to low $|t|$. (This is an observation.)

3) Envelope on subtracted MeV histograms; difficult estimation of envelope because of lack of counts (due to subtraction), on either side of the elastic peak.

4) Interpolation on subtracted MeV histograms; little background is left after the foreground-background subtraction, therefore the method is quite good. However, the largest systematic error is that the ratio "foreground" to "background" is accounted for statistically, and may be fictitious, due to the basically different means by which it is obtained (scintillation counters at much higher t).

We are therefore prejudiced in favor of method 1. However, final results for the other three methods of background subtraction will also be presented.

3.3 Fitting the Slope and t Cuts

Background subtracted events do not represent a differential cross section. In order to do so, we have to express such events per unit solid angle. This is done by dividing the number of events by the area of the collimator for the detector[1]. We obtain $d\sigma/d\Omega$ from which

$$\frac{d\sigma}{dt} = \frac{d\sigma}{d\Omega} \cdot \frac{d\Omega}{dt} \qquad (7)$$

results. Figure 3.3 indicates the shape of $d\sigma/d\Omega$ and $d\sigma/dt$ at two energies. The curves for $dt/d\Omega$ (the acceptance), f_n^2, f_c^2, f_{intf} and $d\sigma/dt$ ($\rho = 0$), are also shown in Fig. 3.3.

Now we are ready to fit the differential cross section $d\sigma/dt$ for the forward diffraction peak, whose diffractive slope is b(s). Elastic scattering in the forward peak is usually expressed as e^{bt^2}. To do so we obtain the average number position for each detector. These angles are derived directly from the histograms. From the MeV histograms one obtains, according to the central value of the elastic peak, the average recoil energy of the target proton. When combined over all detectors (without absorbers), and carriage positions, these data produce a "grid" of angles. The average of all these angles gives a reliable absolute position in space, for the detectors on the carriage.

We choose not to normalize on the Coulomb amplitude, first, because the data do not extend to small enough $|t|$, ($t \geq .0018$), second, because the angles are easily available and to the accuracy required they are adequate. In Fig. 3.4 we show some examples of differential cross

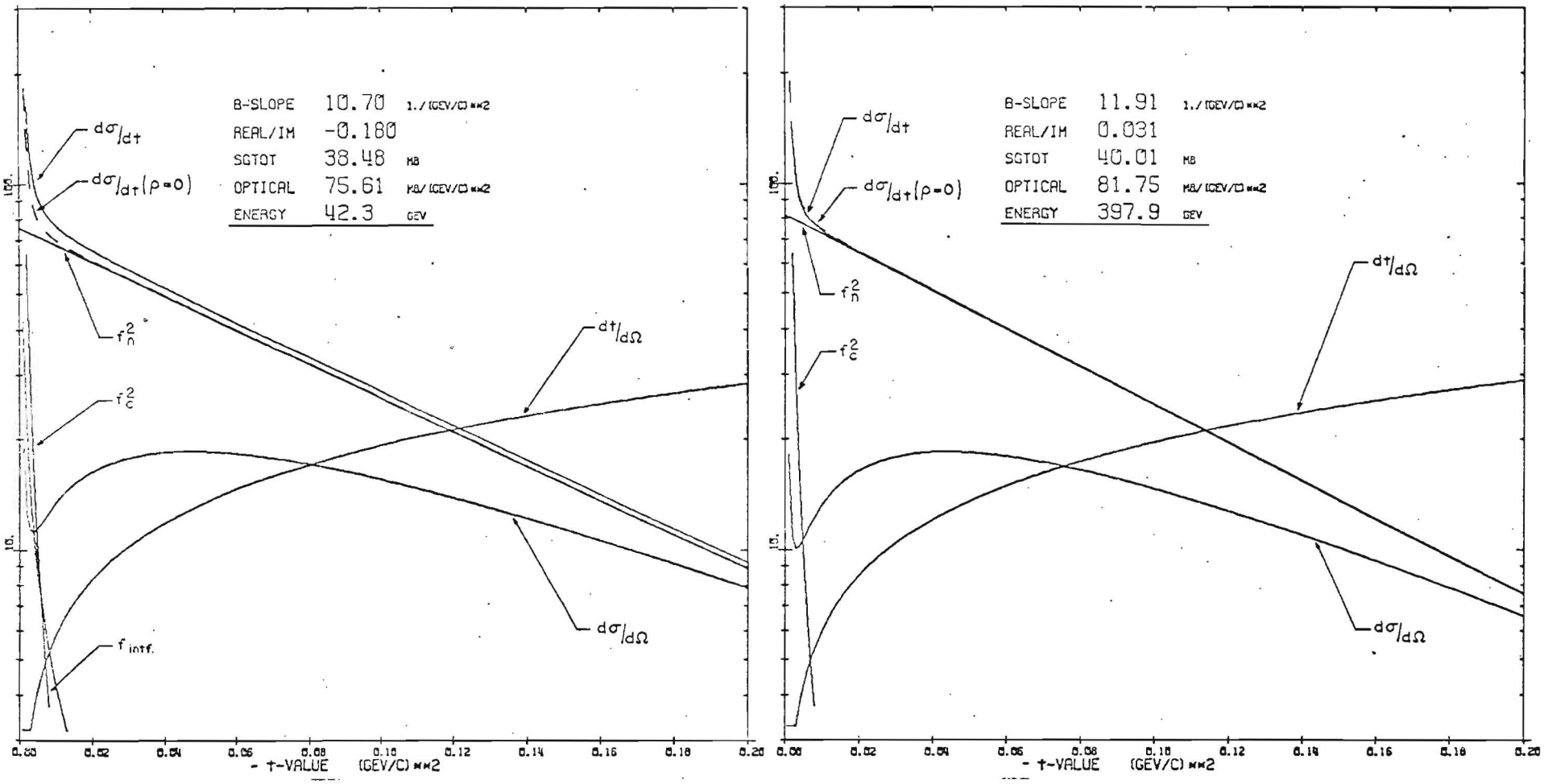

Figure 3.3 Examples of amplitude and differential cross section t-dependence.

	ENERGY	RUN	DET	POINT	PERROR	PERCENT	TPOINT	ANGLE	S-DEVS	CHISQR
1	129.5	3	11	13.118	0.726	0.251	0.15647	0.20929	2.049	4.197
2	129.5	4	11	13.251	0.983	0.256	0.15253	0.20571	1.144	1.309
3	129.5	5	11	12.572	0.794	0.261	0.14856	0.20414	-0.308	0.095
4	129.5	6	11	12.527	0.947	0.266	0.14464	0.20157	-0.889	0.790
5	129.5	1	10	13.697	0.821	0.284	0.13351	0.19373	-2.492	6.210
6	129.5	2	10	13.705	0.317	0.290	0.12991	0.19116	-2.514	6.320
7	129.5	3	10	14.244	0.854	0.297	0.12633	0.18859	-2.541	6.458
8	129.5	4	10	13.014	1.011	0.304	0.12265	0.18601	0.747	0.559
9	129.5	5	10	13.838	0.935	0.312	0.11940	0.18344	0.943	0.890
10	129.5	6	10	2[illegible].711	1.167	0.319	0.11601	0.18087	1.166	1.360
11	129.5	1	9	21.193	0.851	0.343	0.10572	0.17363	0.451	0.203
12	129.5	2	9	22.040	0.827	0.353	0.10253	0.17106	0.543	0.294
13	129.5	3	9	23.073	0.926	0.362	0.09936	0.16849	0.742	0.551
14	129.5	4	9	24.643	1.120	0.373	0.09728	0.16591	1.319	1.741
15	129.5	5	9	24.332	1.044	0.384	0.09423	0.16334	0.276	0.076
16	129.5	6	9	25.079	1.387	0.395	0.09124	0.16077	0.876	0.768
17	129.5	1	8	25.835	1.280	0.447	0.06014	0.15083	-1.838	3.378
18	129.5	2	8	26.[illegible]2	1.296	0.462	0.07740	0.14826	-0.312	0.097
19	129.5	3	8	27.172	1.418	0.478	0.07470	0.14569	-1.338	1.791
20	129.5	4	8	27.246	1.733	0.495	0.07204	0.14311	-2.067	4.273
21	129.5	5	8	3[illegible].492	1.843	0.514	0.06944	0.14054	-0.811	0.657
22	129.5	6	8	31.817	2.298	0.533	0.06690	0.13797	-0.496	0.246
23	129.5	1	7	37.287	1.196	0.615	[illegible]	0.12803	0.641	0.411
24	129.5	2	7	38.997	1.165	0.643	0.05573	0.12606	-0.489	0.239
25	129.5	3	7	39.170	1.323	0.671	0.05346	0.12349	0.496	0.246
26	129.5	4	7	41.089	1.659	0.703	0.05123	0.12091	2.904	8.431
27	129.5	5	7	39.524	1.511	0.736	0.04905	0.11834	-0.658	0.434
28	129.5	6	7	42.697	1.951	0.772	0.04693	0.11577	0.601	0.361
29	129.5	1	6	45.502	1.457	0.918	0.04013	0.10713	1.167	1.362
30	129.5	2	6	48.201	1.456	0.971	0.03822	0.10456	1.591	2.532
31	129.5	3	6	49.574	1.549	1.028	0.03635	0.10199	-1.489	2.217
32	129.5	4	6	46.699	1.941	1.091	0.03452	0.09941	-0.633	0.400
33	129.5	5	6	46.688	1.580	1.161	0.03275	0.09684	-1.220	1.488
34	129.5	6	6	48.756	2.291	1.238	0.03102	0.09427	-0.503	0.253
35	129.5	1	5	50.064	1.661	1.323	0.02936	0.09173	-0.492	0.242
36	129.5	2	5	50.312	1.652	1.418	0.02773	0.08916	-0.932	0.868
37	129.5	3	5	53.026	1.827	1.525	0.02615	0.08659	0.448	0.201
38	129.5	4	5	52.006	2.147	1.645	0.02461	0.08401	-0.805	0.648
39	129.5	5	5	53.851	2.191	1.781	0.02312	0.08144	-0.399	0.160
40	129.5	6	5	54.417	2.650	1.935	0.02168	0.07887	-0.447	0.200
41	129.5	1	4	55.496	1.833	2.259	0.01928	0.07439	-0.906	0.820
42	129.5	2	4	58.593	1.384	2.414	0.01796	0.07182	0.285	0.081
43	129.5	3	4	58.369	2.058	2.745	0.01670	0.06925	-0.261	0.068
44	129.5	4	4	58.396	2.482	3.091	0.01547	0.06667	-0.539	0.291
45	129.5	5	4	55.832	2.433	3.411	0.01430	0.06410	2.210	4.883
46	129.5	6	4	62.112	3.056	3.859	0.01317	0.06153	0.581	0.338
47	129.5	1	3	63.696	2.372	4.679	0.01152	0.05754	0.468	0.219
48	129.5	2	3	63.052	2.411	5.372	0.01051	0.05497	-0.094	0.009
49	129.5	3	3	67.276	2.793	6.225	0.00955	0.05240	1.978	3.912
50	129.5	1	1	67.169	2.676	7.229	0.00868	0.04996	0.966	0.934
51	129.5	4	3	64.496	3.401	7.293	0.00853	0.04982	-0.050	0.003
52	129.5	2	1	63.698	2.699	8.557	0.00781	0.04729	-0.581	0.338
53	129.5	5	3	65.758	3.214	9.639	0.00776	0.04725	0.140	0.019
54	129.5	3	1	63.472	3.032	10.259	0.00698	0.04462	-0.739	0.623
55	129.5	6	3	64.714	4.147	1[illegible].365	0.00694	0.04468	-0.294	0.087
56	129.5	4	1	63.171	3.830	12.488	0.00620	0.04224	-0.849	0.722
57	129.5	1	2	64.747	5.259	13.067	0.00565	0.04173	-0.568	0.322
58	129.5	5	1	67.195	4.[illegible]31	13.439	0.00547	0.03967	0.030	0.001
59	129.5	2	2	68.406	3.633	15.136	0.00533	0.03916	0.340	0.115
60	129.5	6	1	53.635	5.021	19.491	0.[illegible]478	0.03713	-1.663	2.766
61	129.5	3	2	73.134	4.450	20.400	0.00465	0.03659	0.554	0.307
62	129.5	4	2	65.703	5.834	26.381	0.00402	0.03401	-0.255	0.065
				4.269	-11.557	0.5	0.0[illegible]9	0.143	0.0	1.331

RUN	STANDR	CHISQR	SM/RUN
1	-2.602	14.101	445.095
2	-2.164	10.894	453.753
3	-[illegible].152	2[illegible].571	477.247
4	0.918	18.441	478.720
5	0.202	8.703	425.037
6	-1.[illegible]58	7.169	422.754

DET	STANDD	CHISQD	SM/DET
1	-2.887	5.384	383.339
2	0.071	0.810	269.990
3	2.147	4.248	390.973
4	1.370	6.482	359.795
5	-2.627	2.319	314.276
6	-1.087	8.252	251.520
7	3.494	10.121	239.714
8	-0.863	10.443	172.383
9	4.208	3.633	141.364
10	-4.690	21.796	97.869
11	1.996	6.391	51.468
12	0.0	0.0	0.0

Figure 3.4 Listing of fit of differential cross section from fitting program.

section data.*

The data are first cut on low and high t. This is done in order to compare our data more easily to the available world data, as well as to limit certain problems arising at the extremes. Stability of the data with cuts is important. Recognition of the "break" in the cross section at about .15 (in $|t|$), forces us to make a high $|t|$ cut.

The data exist in the form of runs; twelve detectors in one carriage position per run. There are, on the average, 6 runs with slightly shifted carriage positions. To combine the runs, we have to normalize the number of counts. The simplest and the adopted procedure was to minimize χ^2. It was found that the scintillation counters did not provide the necessary accuracy, and there were no fixed solid state detector monitors. Shifting certain detectors to one fixed t to simulate fixed detectors was an alternative that gave slightly higher χ^2.

The minimizing program** first cycled the data through to obtain approximate run normalizations. Secondly, a nuclear correction was applied. Thirdly, a Coulomb correction was applied in two passes, so as to have a good approximate run normalization, as well as a slope parameter during the second part. The last

*Note that this is data without any t cuts.

**Matrix inversion routine.

operation was a "3σ" (three standard deviation from fit) cut. The nuclear, Coulomb and "3σ" cut corrections are explained in the following three sections.

3.4 Nuclear and Inelastic Corrections

Throughout the four months, while we were acquiring data for the diffraction peak analysis, some of the mechanical problems encountered at this early stage of the experiment made it necessary for us to make some changes in the apparatus. The detector configuration was changed slightly four different times. The changes were undertaken in order to optimize the quality of the data. One typical configuration is shown schematically in Fig. 2.8.

The elastic spectrum (see Fig. 3.2) must be corrected for nuclear interactions, in which a fraction of elastic recoils actually deposits in the detector less than the kinematically predicted energy (this effect was explained in Chapter II). In order to account for the effect we must add back, to the elastic counts, the lost fraction. Figure 3.5 indicates the percentage correction, at various kinetic energies, by which one must scale up the elastic events. The procedure is quite simple if one works out the problem in terms of the ranges for the recoil particles. The range-energy relations for Si and Cu are given in Fig. 2.10. We shall follow through the correction for a detector (Si) with an absorber (Cu).

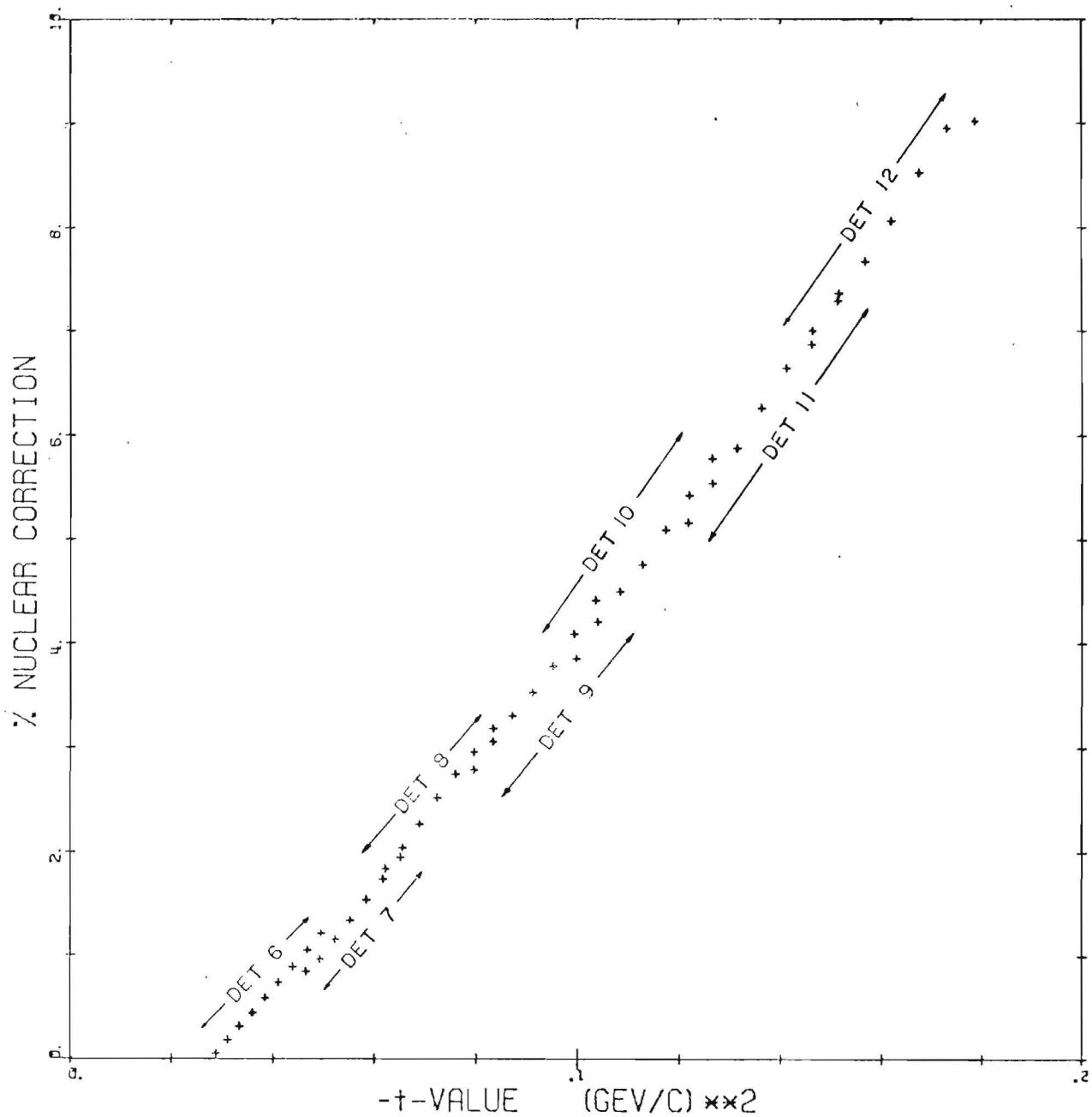

Figure 3.5 Nuclear correction and its t-dependence for the detector configuration of the diffraction peak data.

The range (gm/cm^2) of the particle in Cu, and the corresponding nuclear correction are obtained. For the particle coming out of the absorber, the thickness of the absorber (gm/cm^2) is subtracted from the range, and a "remainder" range equivalent of Cu is obtained. This remainder range is equivalent to the kinetic energy of the particle entering the Si detector. The nuclear correction for the absorber is the difference between the corrections for the full range and the remainder range. A similar procedure is followed through in the detector. The total nuclear correction is the sum of the corrections in the absorber and in the detector. It is estimated that this procedure is accurate to within (5-10)% of the magnitude of the correction. Of course such a correction cannot be s-dependent to first order.

Another important correction to be applied to the data is the inelastic correction. The forward recoil in the pp interaction has a probability of diffractive excitation; this is an inelastic process. The kinematics of the slow recoil for an inelastic process are distorted as compared to elastic scattering. Figure 3.6 shows the kinematics for various dissociated proton states (N*) for different incident beam energies. Note that at one angle (the position in space of one detector), the diffractive dissociation events produce a slower recoil proton; however, the higher the

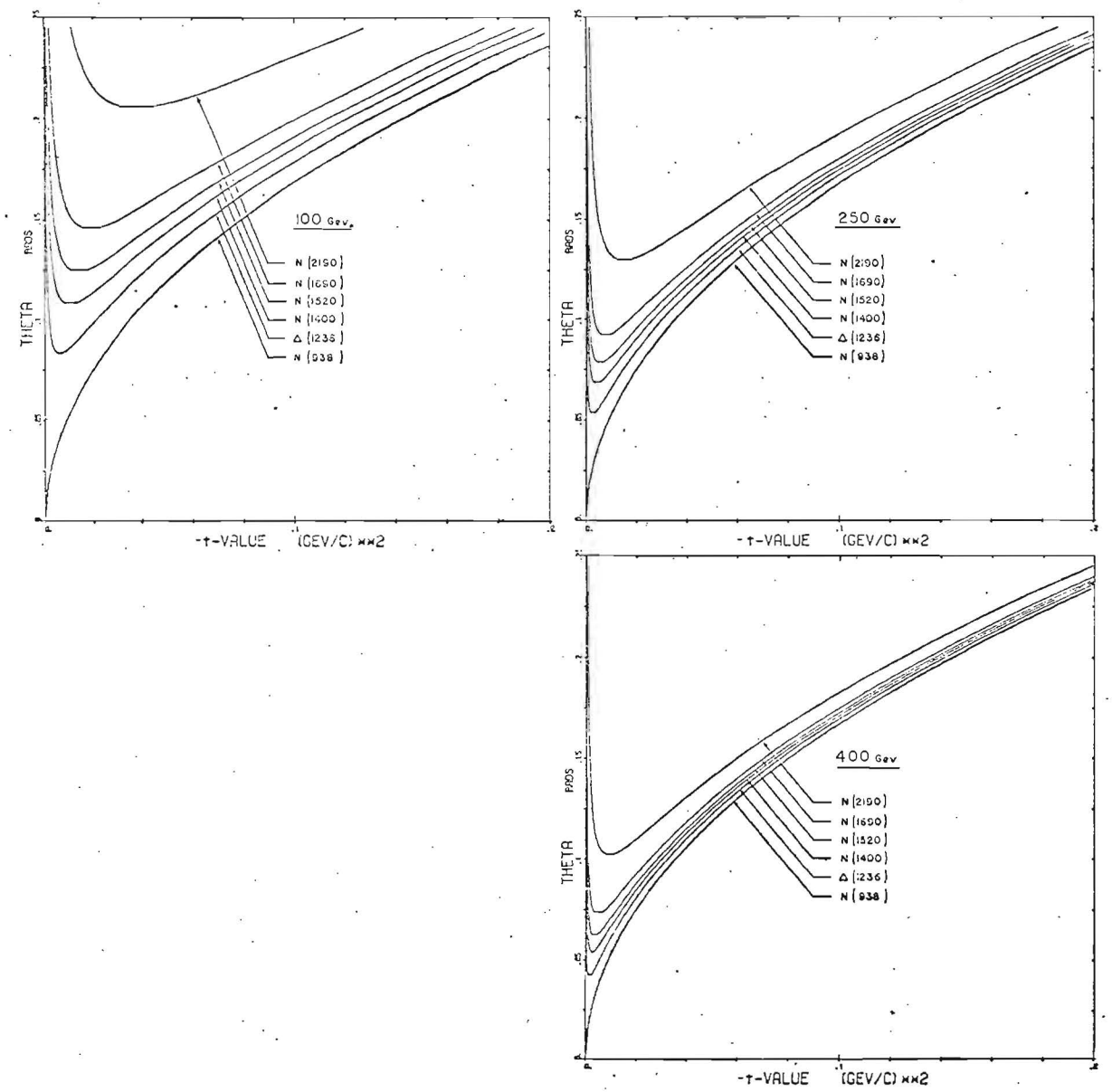

Figure 3.6 Kinematics for dissociated protons (N*).

incident beam energy, the smaller the gap between elastic and diffractive dissociation events. For a clean elastic count, inelastic events which would be found in the kinematic region of elastic peak, must be subtracted. In this chapter we merely present the numerical correction (see Fig. 3.7). A more detailed consideration of how one obtains these corrections, by a Monte Carlo type method, is left for the next chapter.

It is to be noted that, given the excellent resolution of solid state detectors (about 2 channels/1000 channels), it would not be too demanding to apply the corrections mentioned above, channel by channel. Firstly, however, there is no clearcut knowledge on the distribution of the nuclear correction[3]. Secondly, the complete histograms were not available, at this stage of the analysis, to allow a channel by channel correction. The corrections were therefore "bulk" corrections on background-subtracted numbers of events.

As a bulk correction, the nuclear correction is entirely satisfactory. The inelastic correction is somewhat uncertain, due to the specific background subtraction method and the lack of knowledge on dissociation data, at hundreds of GeV, in general. In any case the combination of background subtraction and inelastic correction, in the case of the diffraction peak data, is not rigorous.

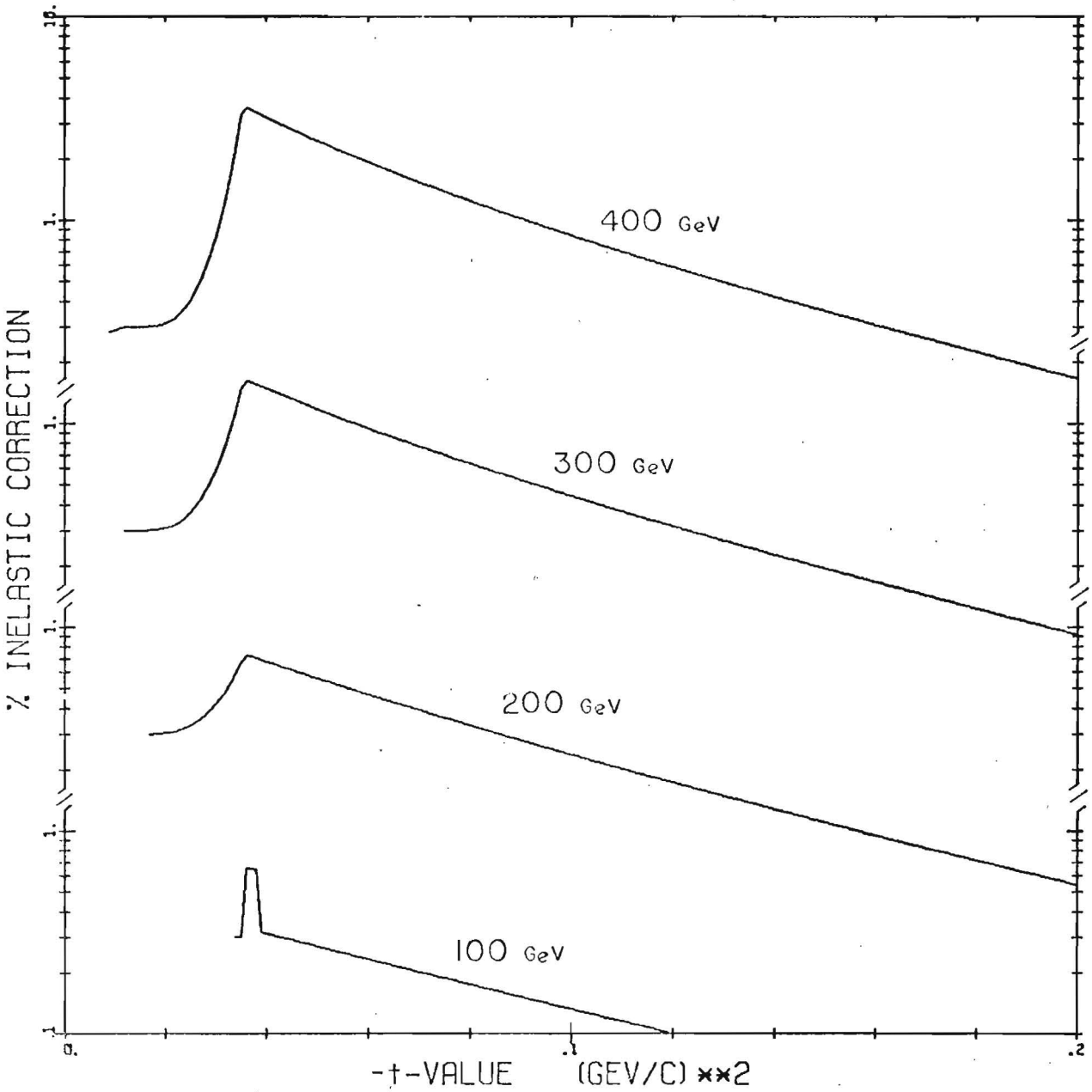

Figure 3.7 Numerical correction due to diffraction dissociation events that must be subtracted from under the elastic peak.

3.5 Coulomb Correction

The following is an expression for the pp differential cross section,

$$\frac{d\sigma}{dt} = \{f_n^2(1 + \rho^2) + f_c^2 + f_{intf}\} \qquad (8)$$

where f stands for an amplitude and the subscripts n, c, intf stand for nuclear, Coulomb and interference, respectively. Our task is to find the t-dependence of f_n^2, that is

$$f_n^2 = \{ \frac{d\sigma}{dt} - f_c^2 - f_{intf}\} / (1 + \rho^2) \qquad (9)$$

where

$f_c = - 2 \frac{\alpha}{\beta} [F(t)]^2 \sqrt{10\pi} / |t|$,

$f_{intf} = 2 \cdot f_c \cdot f_n \cdot [\rho + \frac{\alpha}{\beta} (\ln|\frac{t_o}{t}| - .5772)]$ (ref. 4),

$F(t)$ - proton form factor

σ_T - total pp cross section ($\sigma_T \cong 38.4 + .49[\ln(s/122)]^2$,*

ρ - the ratio of the real to the imaginary parts of the nuclear amplitude ($\rho \cong -.598 + .095 \cdot \ln(s)$)*,

t_o - approximately .09,

α - the fine structure constant ($\cong 1./137.4$),

β - the velocity of the beam proton.

---

*Parametrizations of world data.

Some examples of data at different energies are shown in Fig. 3.8. Clearly working in a range of $|t| \geq .002$, where $|f_c| \cong |f_n|$, one can safely do the subtraction in Eq. (9) by choosing some approximate form for $f_n^2 \sim e^{bt}$ where b is known roughly, i.e., $10 < b < 12$ $(\mathrm{GeV}/c)^{-2}$. Then b is obtained accurately from the χ^2 minimizing routine. Table 3.1 shows the distribution with t of percentage (Coulomb) corrections, for three different energies.

An indication of the systematic effects of the Coulomb correction is given in Table 3.2, where the changes in b, with respect to ρ, σ_T and θ ($\frac{\Delta b}{\Delta \rho}$, $\frac{\Delta b}{\Delta \sigma_T}$ and $\frac{\Delta b}{\Delta \theta}$ respectively) are given (the change in θ is given in mrads). Also in Table 3.2, are given the final results for the slope parameter b(s).

3.6 "3σ" Cuts

Throughout the analysis we found a fraction of ~2.5% of data points, which were situated outside the three-standard deviation region. Such points should occur only in ~.27% of all cases. Naturally, the points, with large deviations from the fit, contribute abundantly to the χ^2.

The large deviation of points from the fit can be justified by: ineffective operation of the particular detector channel, voltage line fluctuations, detector noises, etc. These are systematic causes which we tried hard to

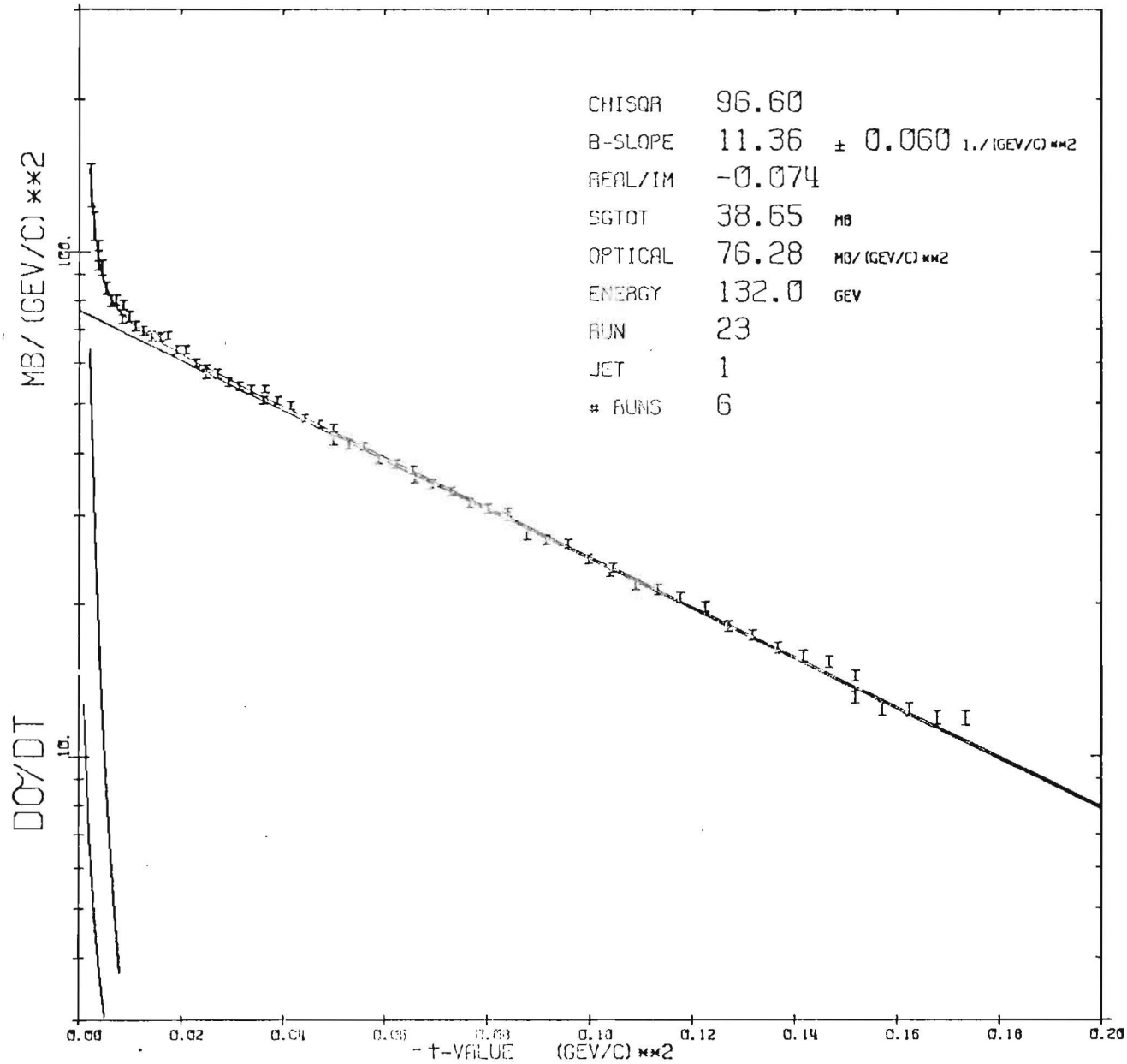

Figure 3.8a Differential cross section data (72 points).

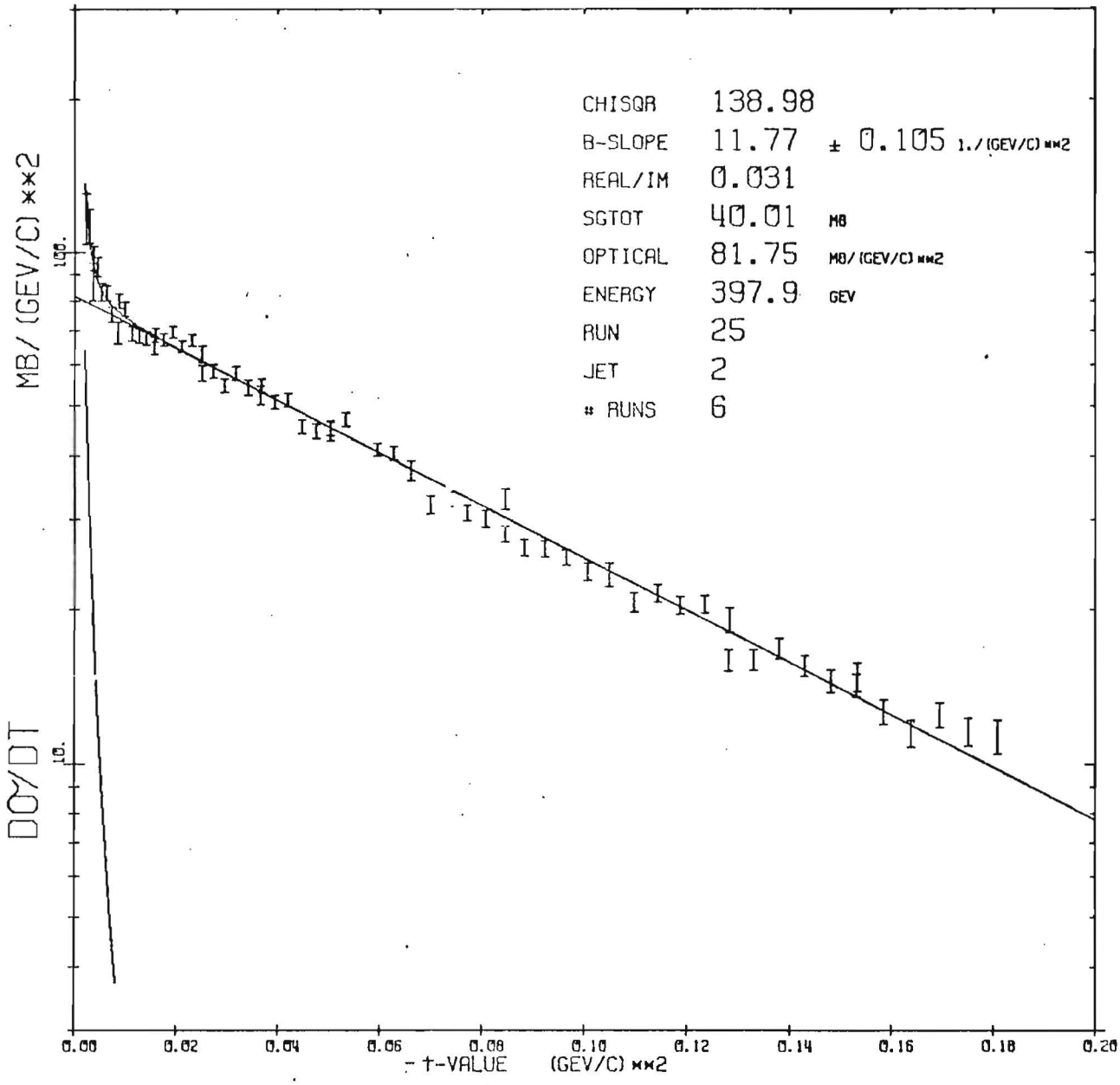

Figure 3.8b Same as Figure 3.8a but different incident energy (72 points).

	ENERGY= 50.0 BSLOPE= 10.77 SCTOT= 38.43 ALPHA= -0.170			ENERGY= 150.0 BSLOPE= 11.37 SCTOT= 38.75 ALPHA= -0.070			ENERGY= 400.0 BSLOPE= 11.91 SCTOT= 40.02 ALPHA= 0.019		
T	DS/DT	FN2 %	CORR.	DS/DT	FN2 %	CORR.	DS/DT	FN2 %	CORR.
3.392D-04	2437.74	75.40	96.82	2244.05	76.63	96.57	2142.62	81.73	96.18
6.182D-04	814.69	75.17	90.51	735.72	76.38	89.57	690.64	81.45	88.20
9.803D-04	384.39	74.88	79.96	342.22	76.06	77.67	317.98	81.09	74.49
1.426D-03	230.33	74.52	66.71	204.06	75.67	62.74	189.76	80.65	57.49
1.954D-03	163.32	74.10	53.32	145.96	75.20	47.98	136.49	80.12	41.27
2.566D-03	129.81	73.61	41.65	116.53	74.67	35.61	111.14	79.52	28.62
3.261D-03	111.16	73.06	32.37	100.98	74.06	26.24	97.71	78.85	19.28
4.040D-03	99.81	72.45	25.31	91.59	73.39	19.47	89.90	78.09	13.10
4.902D-03	92.38	71.78	20.05	85.57	72.66	14.67	84.94	77.27	9.00
5.848D-03	87.16	71.06	16.12	81.38	71.86	11.26	81.52	76.38	6.28
6.877D-03	83.26	70.27	13.16	78.25	71.01	8.31	78.95	75.41	4.44
7.990D-03	80.19	69.44	10.91	75.76	70.09	7.02	76.87	74.39	3.19
9.187D-03	77.65	68.55	9.17	73.66	69.12	5.70	75.07	73.30	2.33
1.047D-02	75.45	67.61	7.81	71.80	68.10	4.70	73.44	72.15	1.71
1.183D-02	73.49	66.62	6.72	70.10	67.02	3.93	71.89	70.95	1.28
1.328D-02	71.68	65.59	5.85	68.60	65.90	3.33	70.39	69.70	0.96
1.481D-02	69.98	64.52	5.13	66.96	64.73	2.86	68.92	68.39	0.72
1.643D-02	68.34	63.40	4.54	65.45	63.52	2.48	67.44	67.04	0.55
1.813D-02	66.76	62.25	4.05	63.96	62.27	2.17	65.95	65.65	0.42
1.992D-02	65.20	61.07	3.63	62.43	60.99	1.91	64.45	64.22	0.32
2.179D-02	63.67	59.85	3.28	61.00	59.67	1.70	62.94	62.76	0.25
2.375D-02	62.14	58.60	2.98	59.52	58.32	1.52	61.40	61.26	0.19
2.579D-02	60.63	57.33	2.72	58.03	56.95	1.37	59.85	59.74	0.14
2.792D-02	59.12	56.03	2.49	56.53	55.56	1.25	58.28	58.20	0.11
3.014D-02	57.61	54.71	2.29	55.03	54.14	1.13	56.70	56.63	0.08
3.244D-02	56.10	53.37	2.11	53.52	52.71	1.04	55.10	55.05	0.06
3.482D-02	54.59	52.02	1.96	52.01	51.26	0.96	53.50	53.46	0.04
3.729D-02	53.08	50.65	1.82	50.49	49.80	0.88	51.89	51.85	0.03
3.985D-02	51.57	49.27	1.69	48.98	48.34	0.82	50.27	50.24	0.02
4.250D-02	50.07	47.89	1.58	47.46	46.87	0.76	48.65	48.63	0.01

Table 3.1 Percentage contribution of the (Coulomb amplitude)^2 to the differential cross section; various t values and incident energies.

	ENERGY	S	B	DB	STATISTICAL RHO= REAL/IM	SGTOT	DB/DRHO	DB/DSGTOT	DB/DTHETA	DB
1	42.3	81.1	10.27	0.14	-0.180	38.48	1.8	0.020	-0.199	0.17
2	43.0	82.5	10.43	0.14	-0.179	38.48	2.1	0.022	0.011	0.14
3	43.7	83.8	10.84	0.15	-0.177	38.47	2.5	0.028	-0.186	0.18
4	62.2	118.5	11.13	0.17	-0.144	38.40	5.3	0.033	-0.203	0.23
5	70.9	134.8	11.31	0.26	-0.132	38.40	2.7	0.024	-0.194	0.29
6	74.7	141.9	10.76	0.14	-0.127	38.41	3.3	0.032	-0.210	0.19
7	81.8	155.3	11.07	0.07	-0.119	38.43	2.5	0.024	-0.113	0.10
8	93.9	178.0	10.72	0.15	-0.106	38.47	2.8	0.022	-0.186	0.18
9	104.0	196.9	11.21	0.10	-0.096	38.51	3.5	0.030	-0.196	0.16
10	107.4	203.3	11.25	0.10	-0.093	38.53	3.2	0.027	-0.185	0.15
11	108.8	205.9	11.19	0.12	-0.092	38.53	2.8	0.023	-0.194	0.17
12	122.4	231.4	11.00	0.13	-0.081	38.60	2.8	0.020	-0.221	0.18
13	126.3	238.8	11.55	0.10	-0.078	38.62	4.2	0.034	-0.223	0.17
14	129.5	244.8	11.64	0.17	-0.075	38.64	3.6	0.030	-0.266	0.23
15	132.0	249.5	11.18	0.08	-0.074	38.65	3.0	0.026	-0.190	0.14
16	136.0	257.0	11.45	0.12	-0.071	38.67	3.4	0.027	-0.204	0.17
17	150.5	284.2	11.09	0.14	-0.061	38.75	2.8	0.019	-0.219	0.12
18	150.6	284.4	11.39	0.08	-0.061	38.75	3.2	0.025	-0.130	0.12
19	151.1	285.3	11.80	0.09	-0.061	38.75	4.4	0.037	-0.263	0.18
20	153.9	290.6	11.59	0.08	-0.059	38.77	3.0	0.023	-0.320	0.19
21	157.4	297.1	11.32	0.15	-0.057	38.79	2.4	0.016	-0.150	0.17
22	171.4	323.4	11.18	0.13	-0.049	38.87	3.2	0.020	-0.231	0.18
23	195.5	368.6	11.91	0.18	-0.037	39.00	3.9	0.028	-0.258	0.23
24	204.4	385.3	11.83	0.07	-0.032	39.05	3.1	0.019	-0.219	0.14
25	217.0	409.0	11.39	0.10	-0.027	39.12	3.3	0.021	-0.001	0.12
26	226.7	427.2	11.58	0.09	-0.023	39.17	4.0	0.033	-0.187	0.16
27	241.5	454.9	11.59	0.09	-0.017	39.25	3.9	0.030	-0.202	0.15
28	248.9	468.8	12.21	0.10	-0.014	39.29	5.2	0.038	-0.231	0.19
29	254.4	479.1	11.23	0.14	-0.012	39.32	2.8	0.014	-0.175	0.17
30	268.2	505.0	11.65	0.10	-0.007	39.39	4.9	0.034	-0.290	0.20
31	278.5	524.4	11.45	0.08	-0.003	39.44	-5.6	0.119	-0.009	0.15
32	279.4	526.1	11.85	0.07	-0.003	39.45	4.0	0.099	-0.213	0.16
33	297.2	559.5	11.52	0.12	0.003	39.54	21.9	0.023	-0.252	0.47
34	397.9	748.4	11.77	0.14	0.031	40.01	3.5	0.020	-0.119	0.17

Table 3.2 Final data on the slope parameter and the dependence on the values assumed for ρ, σ_T and θ.

avoid. When one detector channel worked improperly, it did not necessarily appear to malfunction (being independent of the rest of the channels). Voltage line fluctuations due to accelerator cycle and extreme temperature conditions were also found to cause malfunction in some channels. Detector noise is a far worse problem, as it is quite erratic and is often caused by ground loops and voltage surges. Persistent noise was spotted and the problem corrected before further data acquisition.

A priori it is never safe to eliminate "bad" data, but we found the procedure necessary and justified.[5] It should be stressed that only 2.5% of the data was thrown out and this procedure usually reduced χ^2/(degree of freedom) by about one quarter. A histogram of the χ distribution indicates the magnitude of the problem (see Fig. 3.9).

Generally, χ^2's were found to be about 1.5 per degree of freedom after this last correction.

3.7 Fits to Single Regge Pole, with No Cuts

Elastic scattering, according to Regge theory, can be parametrized as

$$\frac{d\sigma}{dt} = F(t) \quad e^{2[\alpha_P(t) - 1]\ln(s/s_o)} , \qquad (10)$$

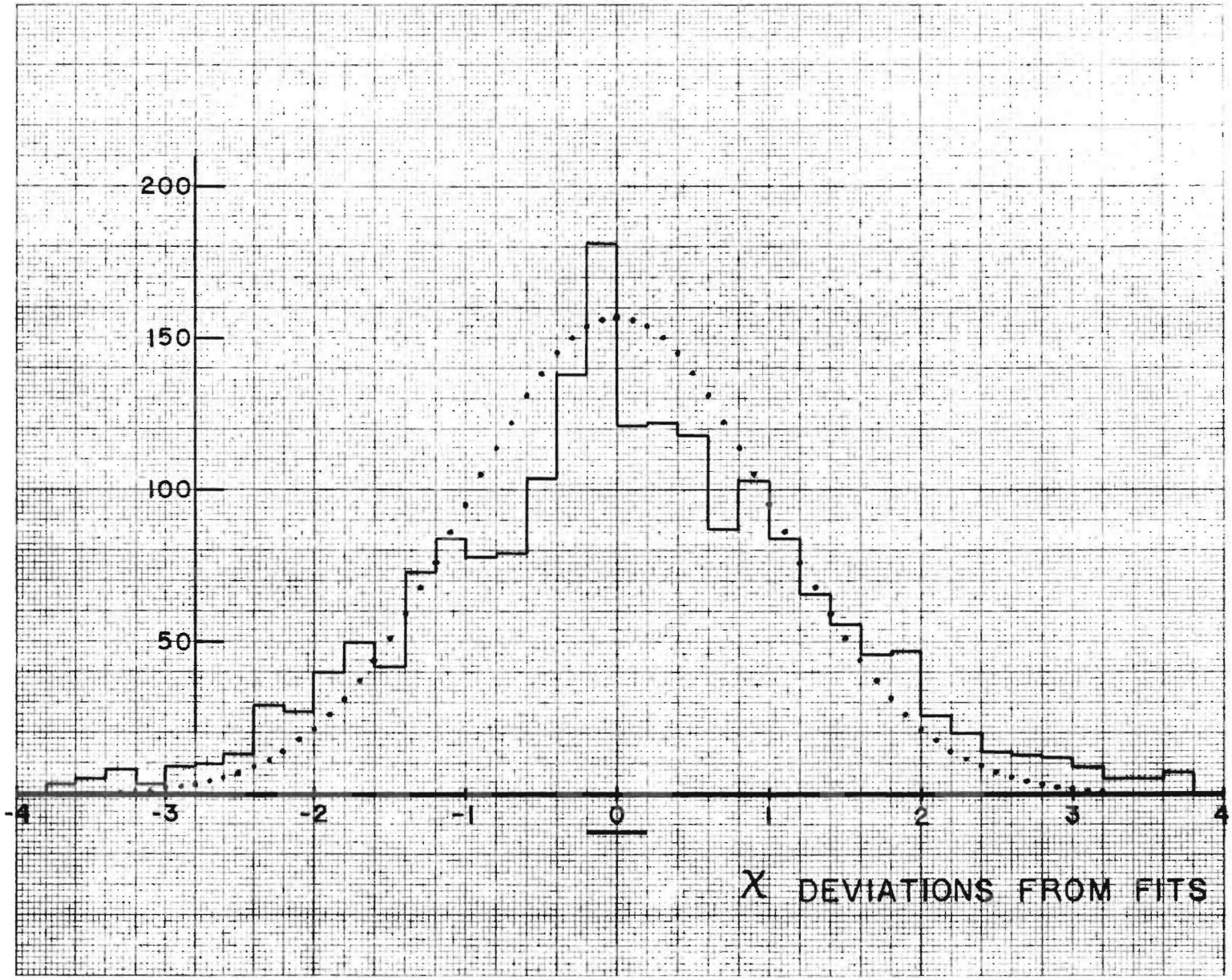

Figure 3.9 Histogram of χ distribution indicating the slightly larger tails than for an expected Gaussian distribution (dots).

where $\alpha_P(t) = \alpha_o + \alpha' t$ $(= 1 + \alpha' t)$ describes the Pomeranchuk trajectory. If we let $F(t) = e^{-b_o t}$ and $s_o = 1\ \mathrm{GeV}^2$, then $\frac{d\sigma}{dt} \sim e^{b(s)t}$, where

$$b(s) = b_o + 2\alpha' \ln s \tag{11}$$

where b_o and α' are as yet undetermined constants. In the previous sections we have fit the differential cross section for the slope parameter b(s). Now we can find α', the slope of the Pomeranchuk trajectory. Figure 3.10 indicates the slope parameter data (note the range of t for which the fit applies).

The remainder of this section is devoted to various attempts made to determine the magnitude of the systematic problems.

If we believe that data acquired simultaneously at two energies is more consistent (various mechanical conditions being the same) than data obtained in separate runs, then we can shift, pairwise, all data points for b(s), such that we minimize a straight line fit for χ^2 in Eq. (11) (see Fig. 3.11). Presumably, this procedure gives us a more reliable value for α', and as b_o is of no intrinsic physical interest, there is no loss of information. In fact, the stability of α' in this procedure is desirable, and is an important criterion for deciding on a proper set of data

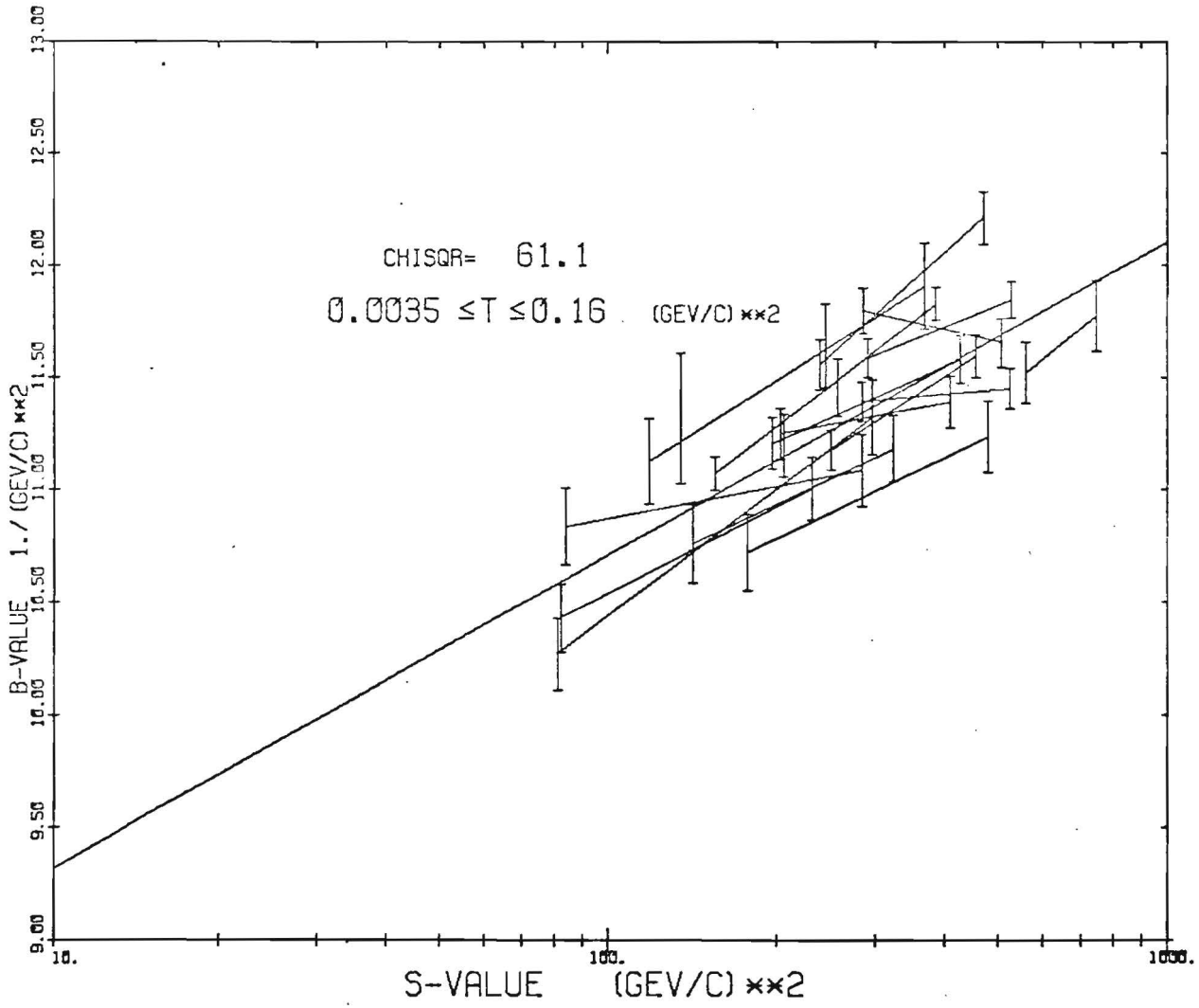

Figure 3.10 Slope parameter data, all 34 points. Data taken at two energies simultaneously, are connected by lines. The straight line is a single Regge pole fit; $b_o = 7.92 \pm .29$, $\alpha' = .303 \pm .026$.

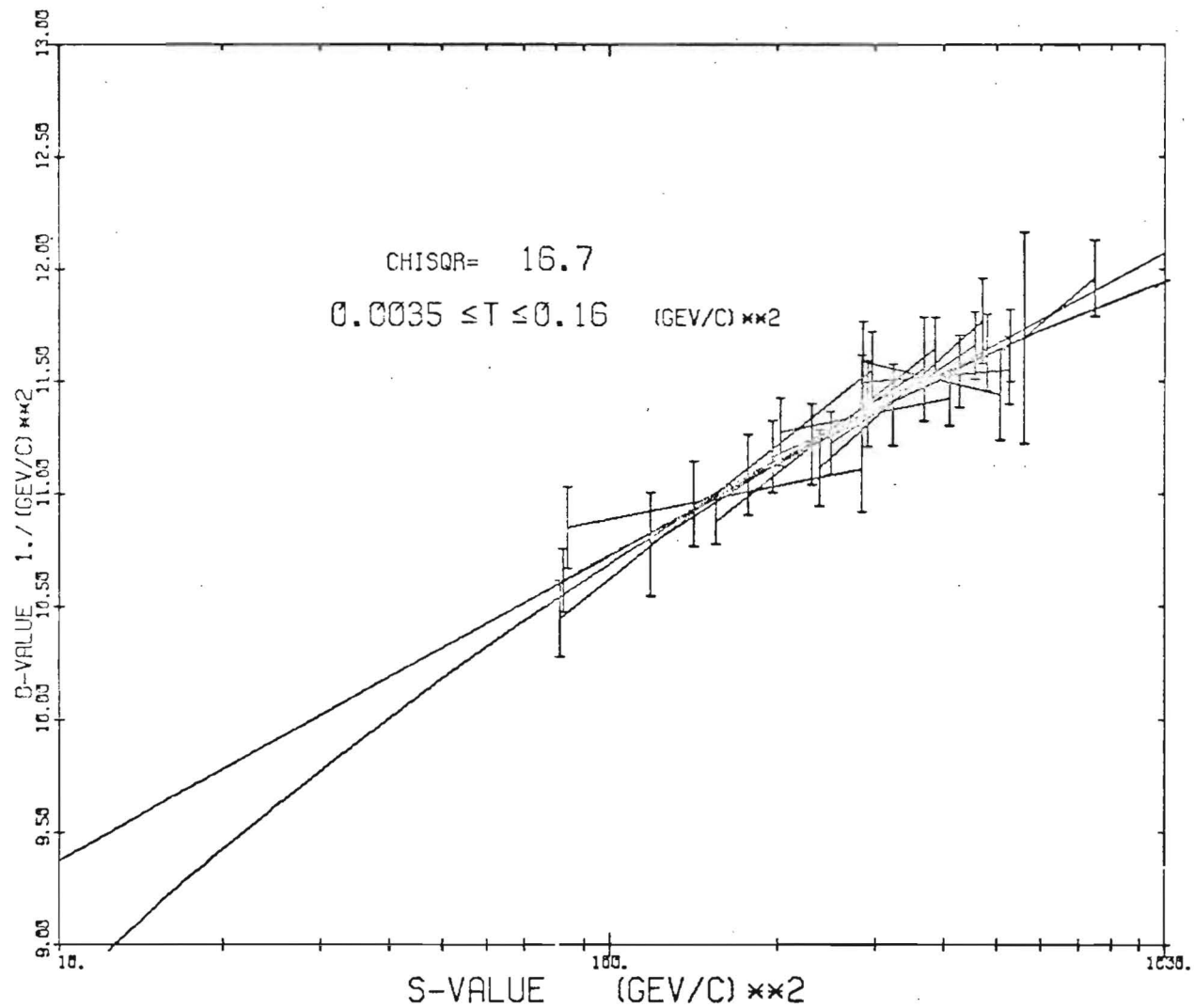

Figure 3.11 Slope parameter data with pairs of points shifted to achieve a minimum χ^2 for a straight line fit; $b_o = 8.03 \pm .29$, $\alpha' = .293 \pm .026$. The curved line indicates a parabolic fit over $\ln s$ (see Eq. 13).

points. We regard various cuts in the range of t as intrinsically different, primarily because our detector system is not continuous and hence somewhat non-uniform, in what concerns systematic errors. Indeed, the large "dynamic range" of the apparatus, $.0015 \leq |t| \leq .18$ $(\mathrm{GeV}/c)^2$, must be adjusted. Experience with detector performance indicates that the most stable cut is $.0035 \leq |t| \leq .16$. For this cut we obtain $\alpha' = .293 \pm .026$ (χ^2/degree of freedom = .60)*. Further cuts on pairs of data points, to eliminate runs, for which α' diverges from the average, do not seem justified (although they may produce χ^2/degree of freedom $\simeq .25$), because these cuts shift the average α' by less than one standard deviation.

Cuts on data, at this point, are also unwarranted because Eq. (10) is not necessarily correct. Firstly, we may parametrize

$$\frac{d\sigma}{dt} = \left.\frac{d\sigma}{dt}\right|_o e^{bt + ct^2} \tag{12}$$

which can be derived, for example, from an uncorrelated jet model[6]. Whereas, usually c in Eq. (12) is found to be $0 \leq c \leq .04\ b^2$ (positive), we find an average (for all incident energies, 40 to 400 GeV) of $.03 \leq (-c/b^2) \leq .08$ with an error of about $.10\ b^2$ for the value of c (note,

*The χ^2 degree of freedom for unshifted pairs of points is 2.2.

that $|ct^2/bt|$ at our highest $|t|$ of .18 is only about .07). Secondly, even though the form e^{bt} may be a good fit, b(s) may have a variation other than given in Eq. (11), perhaps

$$b(s) = b_o + b_1 \ln s + b_2 \ln^2 s \qquad (13)$$

as may be required if the total cross section really rises as fast as $\ln^2 s$, indefinitely. For the range $.0035 \leq |t| \leq .16$, we obtain,

$$b(s) = (6.52 \pm 2.33) + (1.28 \pm .86)\ln s - (.064 \pm .079)\ln^2 s$$
$$\delta\langle b_0 b_1\rangle = -2.0 \qquad \delta\langle b_0 b_2\rangle = .18 \qquad \delta\langle b_1 b_2\rangle = -.068$$

for the range of energies 40 to 400 GeV (χ^2/degree of freedom is .59).

Another procedure of studying systematic errors, also of use in representing the Pomeranchuk trajectory, is to reduce all data points for the differential cross section, to standard t values (either one value per detector - i.e., 12 standard t values, or one value per detector for each carriage position - i.e., some 80 standard t values). This operation is done by shifting points along the differential cross section, according to the slope parameter b, up to the appropriate t value. Figure 3.12 shows the 12 standard t values of the detectors, along the s-axis. From Eq. (10) one gets, using $d\sigma(s)/dt\big|_o = \frac{\sigma_T^2(s)}{16\pi} \sim s^{2(\alpha_P(o)-1)}$

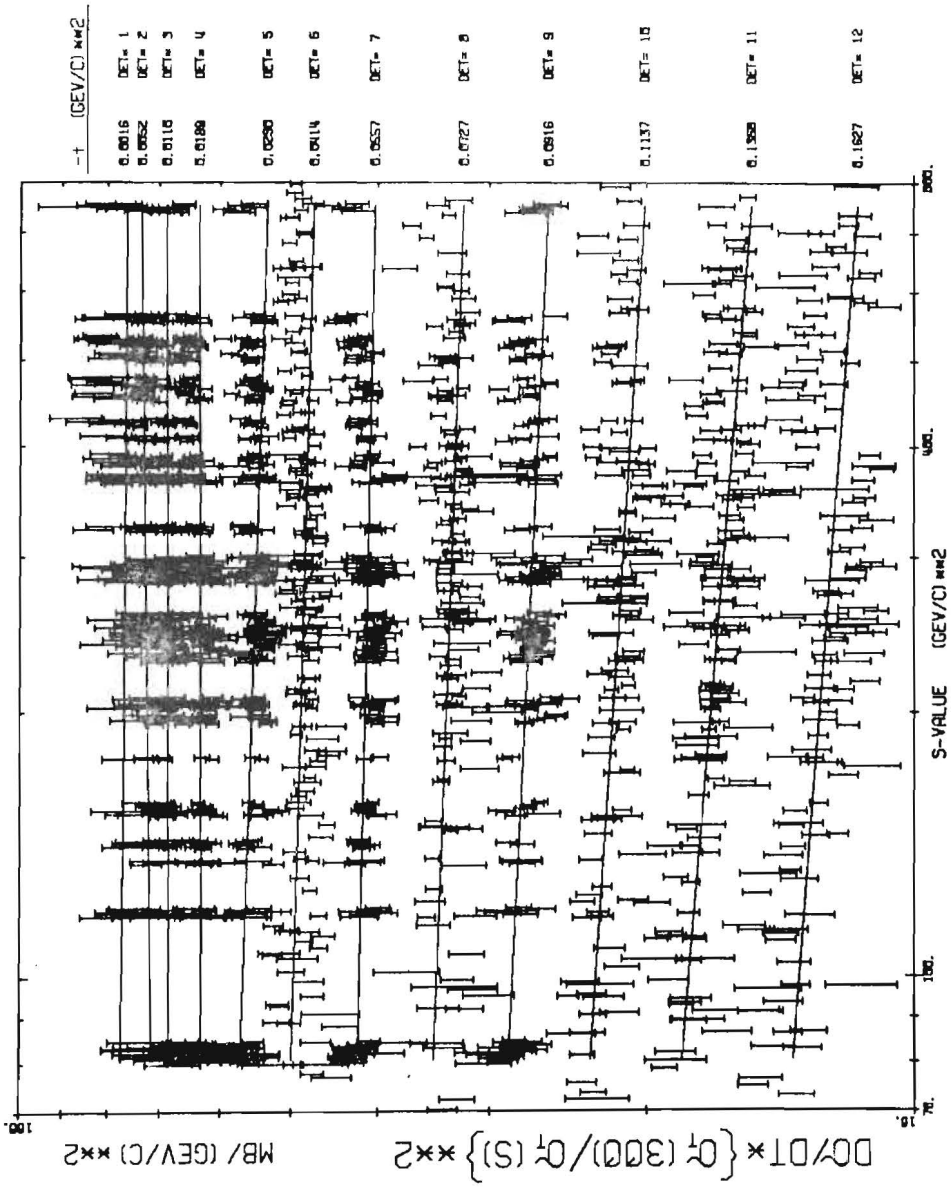

Figure 3.12 Differential cross section data points are shifted to 12 standard t value, one value for each detector (a similar shift can be done for the same data, while defining a standard t value for each carriage position, for each detector); some data points are spread out to show structure (as in detectors 6, 8, 10, 11,12), the rest of the data are spread out very little.

$$\ln[\{\frac{d\sigma}{dt} \cdot 16\pi\} \cdot \frac{\sigma_T^2(300)}{\sigma_T^2\ (s)}] = b_o t + 2\alpha' t \ln s \qquad (14)$$

where the quantity 300 in $\sigma_T^2(300)$ is some arbitrary center of mass energy squared. Fits were made for a linear polynomial in $\ln s$. A curious, but obviously justifiable fact is that χ^2 grows with t, from about .37/degree of freedom (124 points), to about 3.4/degree of freedom (141 points). The quantities α' and b_o are of interest, since they are the Pomeranchuk trajectory slope and diffraction slope intercept (b_o), respectively. Figures 3.13 and 3.14 show the data. We point out that the advantage of this procedure of fitting the data, is that most systematic problems associated with particular detectors are removed. Indeed, most t-cuts produce results with parameters in close agreement. The preferred t-cut $.0035 \leq |t| \leq .16\ (\mathrm{GeV/c})^2$ gives (χ^2/degree of freedom 2.1 statistical errors only) $\alpha' = .299 \pm .016$ and $b_o = 8.02 \pm .18$.[7]

A concise compendium of world data on the values of α' and b_o is shown in Fig. 3.15. In the same figure are included the results of fits to our data, treated by means of the other background subtraction methods.

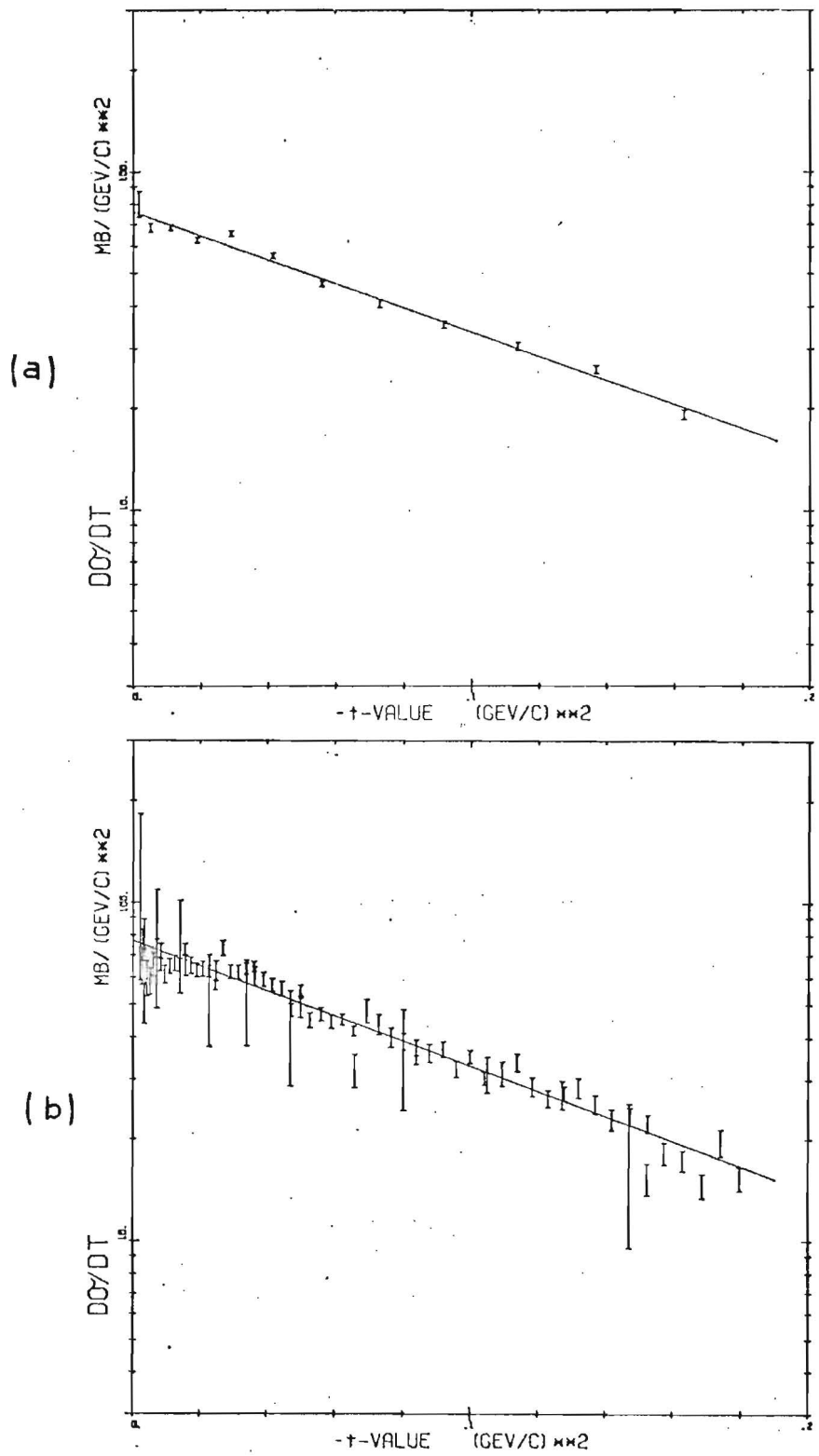

Figure 3.13 The slope of these differential cross sections is b_o. (a) The values represented in this differential cross section are the intercept values of the extrapolations of the lines in Fig. 3.12. (b) The same procedure as in (a) but with intercepts for the fixed t values per detector, per carriage position.

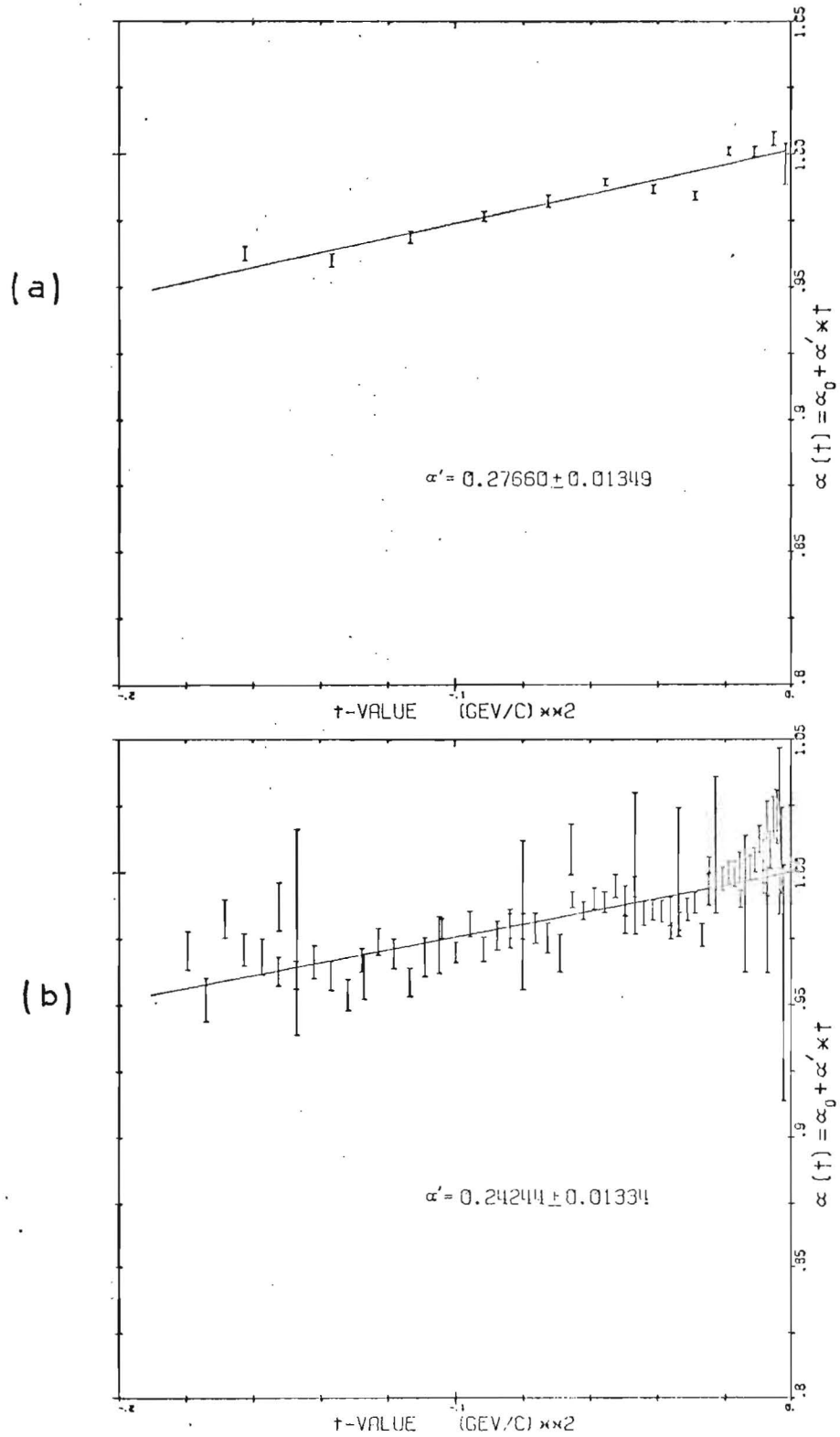

Figure 3.14 The slope of the lines drawn is α'. (a) The values represented form part of the Pomeranchuk trajectory and are obtained from the slopes of the lines drawn in Fig. 3.12. (b) The same procedure as in (a) but with slopes for fixed t values per detector, per carriage position.

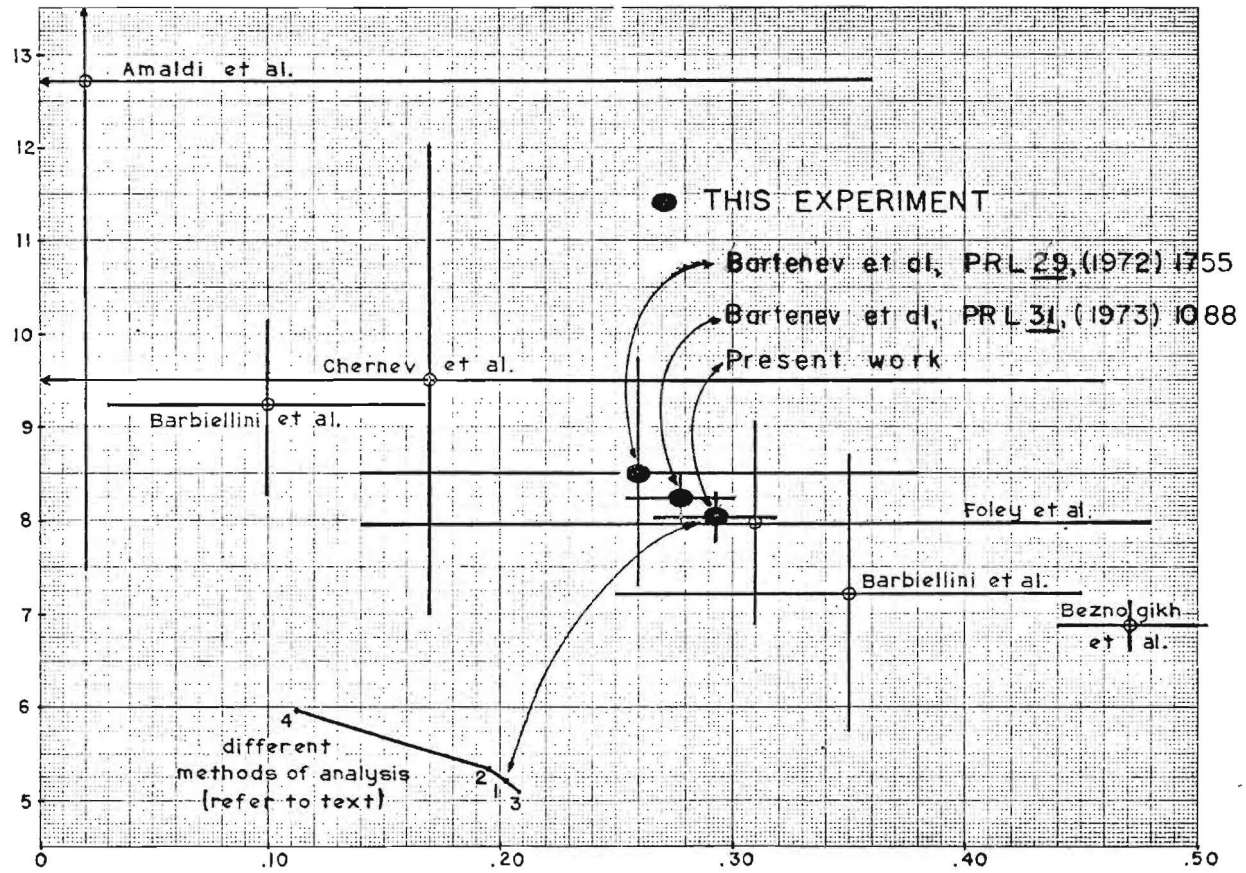

Figure 3.15 Summary of data from one Regge pole fit. Error bars contain the one standard deviation ellipse. The relative fit parameters for the 4 different methods used in background subtraction are indicated in the lower left hand corner. The values should all be translated as shown by the arrow in order to obtain absolute parameters. (Note the consistency of the three sets of data analyzed in our experiment and indicated by the black dots.)

References for Chapter III

1. This procedure applies simply because all detectors are equally spaced from the target; $\Delta\Omega = 2\pi\ \Delta\phi\Delta\cos\theta$, where $\Delta\phi \sim .004$ and $\Delta\theta \sim .004$.

2. This parametrization is suggested mainly by the Regge pole theory; see for example, K. J. Foley et al., Phys. Rev. Lett. 11, (1963) 425.

3. Some information on the nuclear correction is contained in: D. F. Measday and C. Richard-Serre, CERN Report No. CERN 69-17, 1969 (unpublished); we also found it useful to consult: C. F. Williamson, J.-P. Boujot and J. Picard, Rapport CEA-R 3042, and the Ortec Corp. Instruction Manual for Surface Barrier Detectors, in connection with range-energy relations in silicon.

4. This form for the interference term was derived by; G. B. West and D. R. Yennie, Phys. Rev. 172, (1968) 1413; the nonrelativistic, potential model was solved by; H. A. Bethe, Ann. Phys. (N.Y.) 3, (1958) 190.

5. Some statistical ideas are presented in: J. Topping, Errors of Observation and Their Treatment, (Chapman and Hall Limited, London, 1962); Y. Beers, Introduction to the Theory of Error, (Addison-Wesley, Reading, Mass. 1957); within these texts can be found criteria for rejecting invalid data, as for example, p. 23 of Beers.

6. L. Van Hove, Rev. Mod. Phys. 36, (1964) 655.

7. A publication by our group on a different set of data gives very similar results and these results shall be used in the next chapter. V. D. Bartenev et al., Phys. Rev. Lett. 31, (1973) 1088 reports $b_o = 8.23 \pm .27$ and $\alpha' = .278 \pm .024$ $(GeV/c)^{-2}$.

CHAPTER IV

ANALYSIS OF REAL PART DATA

The rise of the total nucleon-nucleon cross section is currently of great interest. Various models have been proposed to explain the need for a rising total cross section[1]. In this chapter we establish the s-dependence of the real part of the nuclear scattering amplitude, which is intimately related to the total cross section through dispersion relations. The data is in excellent agreement with results for higher energies at the I.S.R.

We assume that in the forward direction, a good parametrization for the nuclear amplitude is still e^{bt}, at least down to $|t| \sim .001$ $(GeV/c)^2$, which is well within the Coulomb region. Since the Coulomb amplitude is basically real, while the larger part of the nuclear amplitude is imaginary, the interference of these two amplitudes in the region $|t| \lesssim .005$, will provide a measure of the real part. The effect on the differential cross section will be small, (because the nuclear amplitude is primarily imaginary) making the measurement difficult.

Various phase shifts of the nuclear, as well as Coulomb amplitudes, have been calculated theoretically by Bethe and by West and Yennie, as well as others[2]. It is

extremely difficult to experimentally distinguish between the former two theoretical predictions, which differ by a phase shift angle of about,

$$\Delta\phi = \phi_{West-Yennie} - \phi_{Bethe} \simeq .006 \qquad (1)$$

at very small $|t| \sim .002$, without much of a t-dependence. We chose to work with the calculation of West and Yennie, which is entirely relativistic. Consequently, we must remember possible uncertainties in the real part coming strictly from theory (order .006), when we give our results. However this uncertainty is well contained within our errors, which are of the order of .01 (i.e. insertion of the Bethe phase shift into the analysis will produce a shift of the data, down, by about .006 in $\rho(s)$.)

4.1 Data Management

Data handling, from on line bits to off line histograms, proceeded in the same way as for the diffraction peak data, including the dead time correction, which did not exceed 1.5% (see Fig. 2.13). It should be emphasized, that data relating to the real part was taken throughout runs that lasted a total of two weeks and all equipment was unchanged. This presents a great advantage as

compared to the data on the diffraction peak, which were acquired in four months of running time with various modifications of equipment.

In the case of the real part data, two detectors were used at fixed positions in space, in order to monitor the counts for "foreground" and "background" positions, as well as for different carriage position runs. Some spectra for fixed, as well as movable detectors, are shown in Fig.4.1a,b. One may see in Fig. 4.1 the size of backgrounds to be subtracted under the elastic peaks. Our procedure was to use the data in the "background" position of detectors to approximate "empty target" data, as discussed in the previous chapter. The subtracted ratios of "foreground" to "background" position histograms, were obtained by using the two fixed position detector elastic counts. The subtraction was done channel by channel. This result provided the primary set of data. Residual backgrounds due to tails of the gas jet, inelastic excitation and imperfect empty target subtraction, were then handled on the University of Rochester IBM 360-65 computer.

The calibration of detectors,(i.e., response vs. channel), was fit to a second order polynomial for a more accurate physical interpretation for each histogram channel (256 channels-full histogram), than in the case of the diffraction peak data. On the average, the quadratic term gave

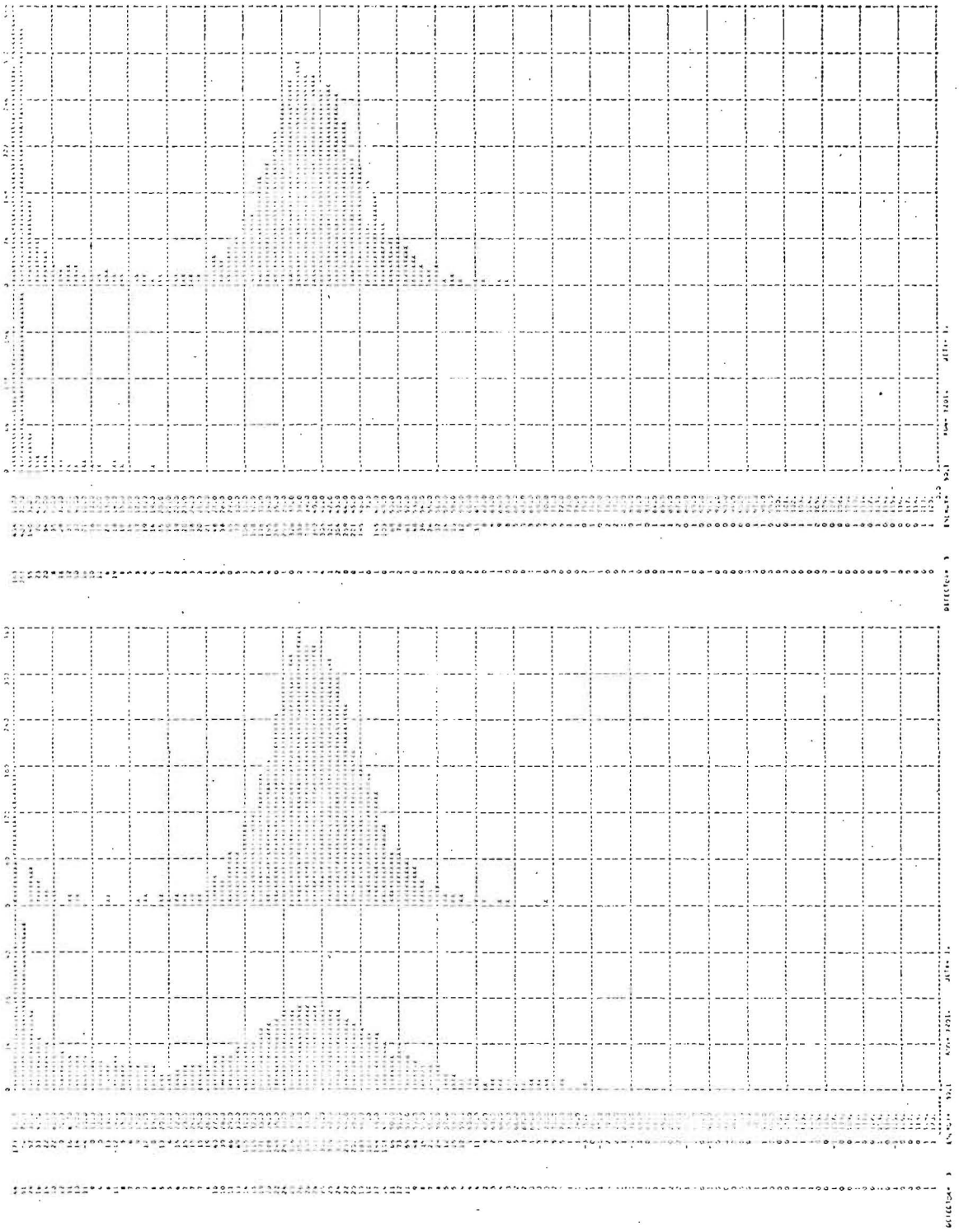

Figure 4.1a At the top are shown the elastic peak spectrum (2.5 MeV foreground) and the "background" position histogram; below are shown the "background" position subtracted spectrum and the resulting error histogram.

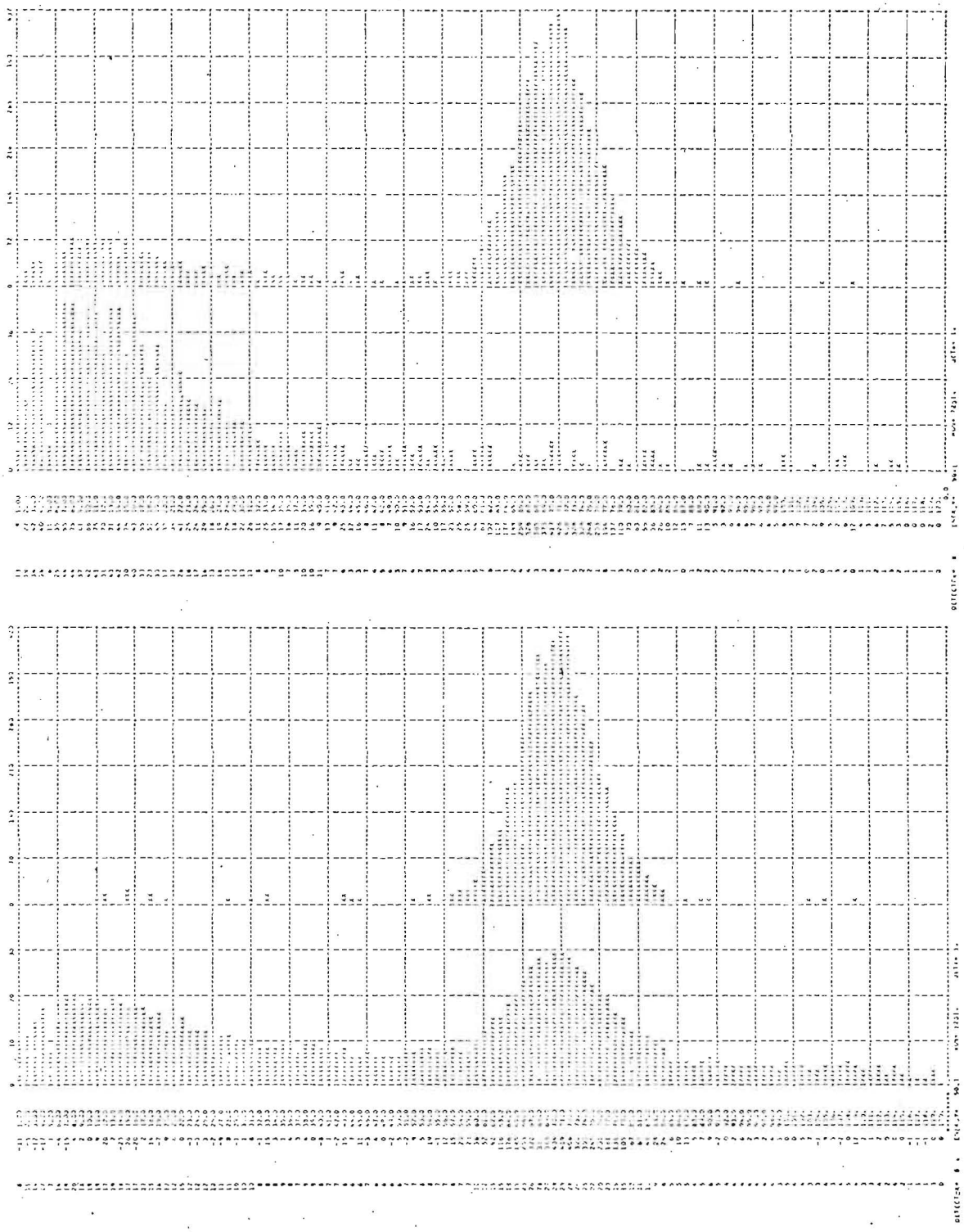

Figure 4.1b The same as in Fig. 4.1a but different recoil energy (12 MeV).

less than a 10% deviation from linearity around the elastic peak. This exact nature of the calibrated histogram channel is very important, as can be seen in the following sections. These calibrations are shown in Fig. 4.1c.

4.2 Background Subtraction

In general, a certain distribution of target material, totally contained in the beam, will be reflected in the spectrum of elastic recoils, at a particular detector (angle). We must however, unfold the dependence of the differential cross section, $d\sigma/d\Omega$ on the angle. This statement is the basis of our analysis for subtracting the residual background, (the background left after the "empty target" subtraction).

The theoretical particle density of an accelerator beam is a two-dimensional Gaussian in space. While the three-dimensional flow of gas dynamics is very complex, enough evidence exists[3], to allow us to approximate the hydrogen jet by a two-dimensional Gaussian as well. It is easily proved that the interaction of 2 two-dimensional Gaussian beams, at right angles is a 3D Gaussian.

$$e^{-x^2/a-y^2/b} \; e^{-y^2/c-z^2/d} = e^{-x^2/a-y^2(1/b+1/c)-z^2/d} \tag{2}$$

(provided the beam axes intersect). This is the rough

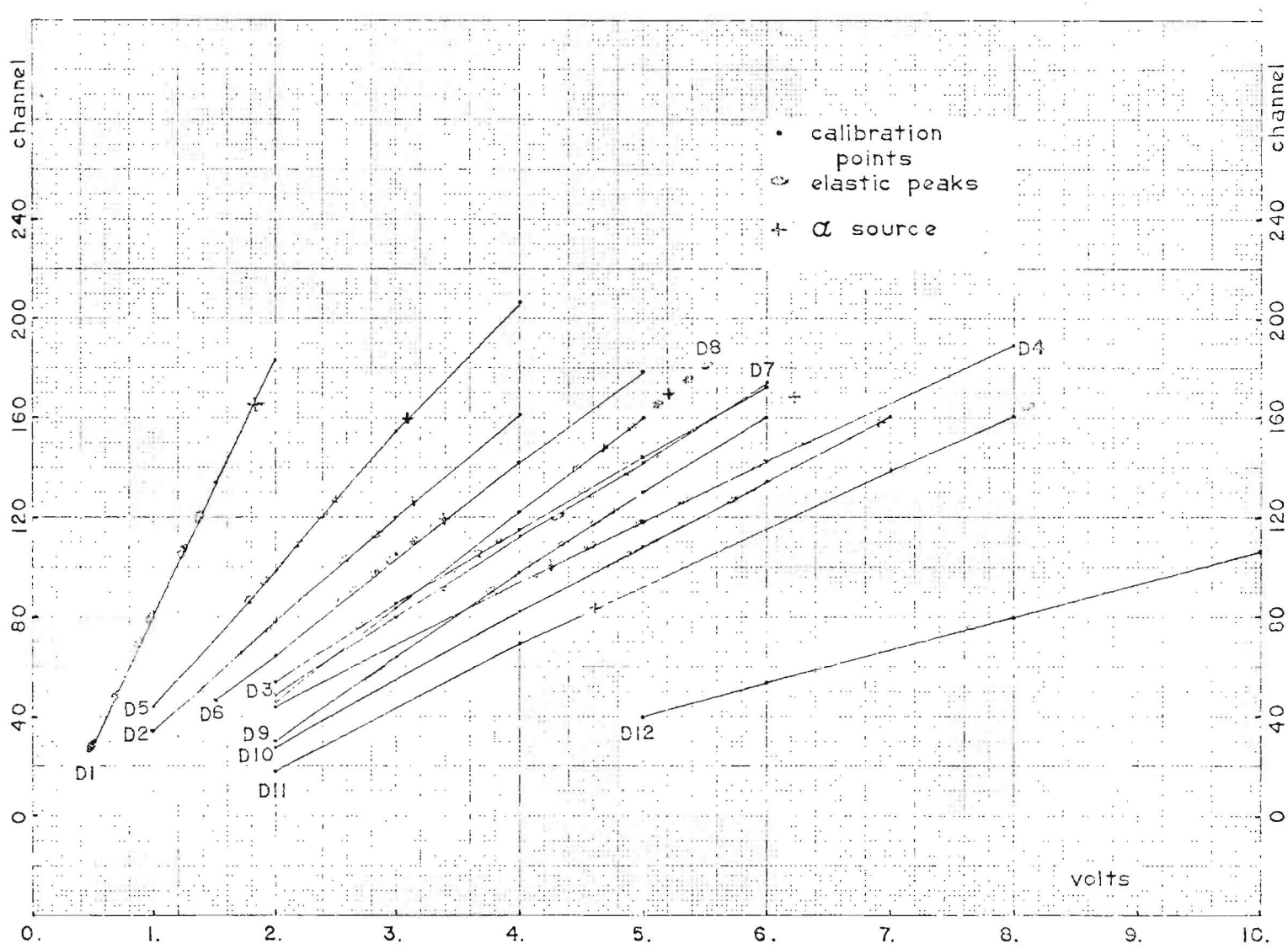

Figure 4.1c The calibration of detectors for the real part data.

density of the beam-target interaction region. The projection of the latter onto a far-away plane, along one dimension gives a 2D Gaussian. The only relevant dimension is, however, the one along the accelerator beam, as different points on it appear at different angles in the detector plane (see Fig. 4.2). Finally we project the height of the "interaction region" and obtain a 1D Gaussian. Apart from the modulating effect of the differential cross section $d\sigma/d\Omega$, which is a function of the recoil angle, the observed spectrum should be an exact image of the linear density of the interaction region. This is the programme of our analysis. Of course having collimated the detectors with other than rectangular collimators (actually, shape of a racetrack) changes the observed spectrum slightly. The important fact is that we make a uniform model for the shape of the observed distributions in all detectors. This shape should be identical for all detectors (due to their small angular extent, first to last, 5°, all being close to 90°) if plotted in recoil particle momentum space (the angle of recoil away from 90° is approximately proportional to the recoil momentum). However, we do not choose to impose identical common parameters for the shape of the distribution in all detectors, because the detector system is not continuous and every detector acts independently of the rest.

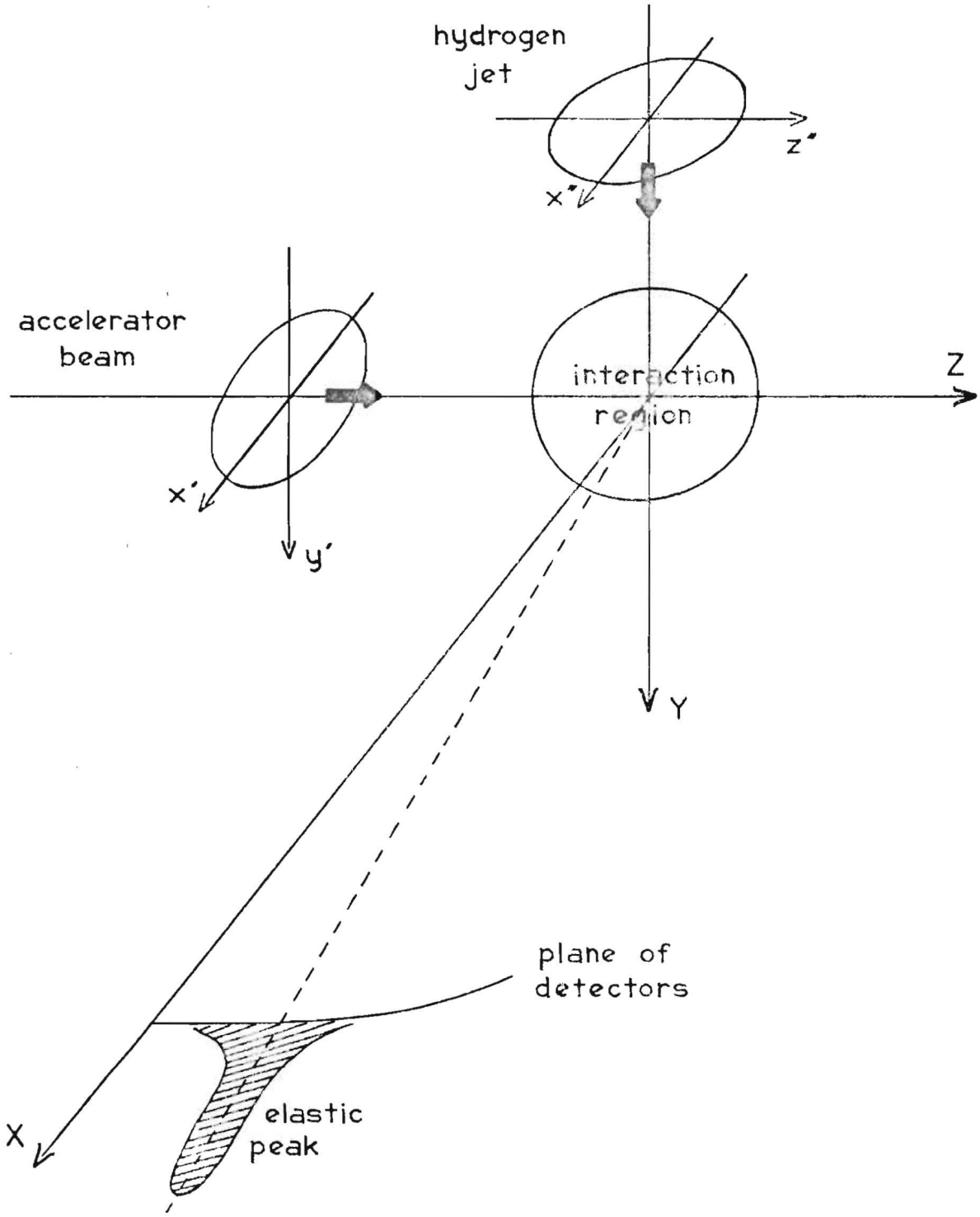

Figure 4.2 Projection of the interaction region unto the plane of the solid state detectors and the resultant spectrum.

The data were analyzed at one primary beam energy, detector by detector. A rough description of the analysis program follows. Data are read from disk. According to detector calibration, each channel in the histogram is assigned a value of momentum transfer, t. A search proceeds for a rough center of the elastic peak, and limits are placed at channels corresponding to one quarter full center channel count. The logarithms of histogram values, channel by channel, are used in a matrix inversion fit routine for a second order polynomial. A change of variables at this point obtains the standard parameters for a Gaussian distribution (N, t_c, σ), where

$$g(t) = N\, e^{-(t - t_c)^2/2\sigma^2} . \qquad (3)$$

(Note space is momentum transfer, t.)

This fit is particularly accurate in finding t_c, the center value with an error much smaller than a channel ($\lesssim .3\%$). A good approximation of N and σ is also obtained. That we do not choose to use the area of the Gaussian as the number of events, is for the following reasons:

a. inelastic data were not subtracted before the fit,

b. only approximate limits were placed on the elastic peak before the fit,

c. according to previous arguments, the distribution

fitted should not be a Gaussian in t space, nor has the differential cross section been divided out before the fit.

This indicates the logic of the further analysis steps.

Inelastic kinematics give us:

$$\Delta + T = \beta \sin\theta \, (T^2 + 2mT)^{1/2} \tag{4}$$

where

$$\Delta \equiv (M^2 - m^2)/2(E + m), \tag{5}$$

M being an excited mass (m is proton mass, m_p). From Eq. 4.4, one obtains a channel by channel formula for mass, after having computed $|t|$ (= 2mT).

$$M^2 = m^2 + \frac{s|t|}{2m^2} \{-1 + \beta\sin\theta(1 + \frac{4m^2}{t})^{1/2}\}^* \tag{6}$$

which is exact. The elastic peak mass, m_p, is then adjusted to the correct value by scaling the whole histogram appropriately. Usual deviations do not amount to more than 40 MeV/c^2 from the proton mass. To get a picture of what masses correspond to a particular channel

---

*Note: for $t=t_{el}$, $M^2=m^2$; for $|t|>|t_{el}|$, $M^2<m^2$; for $|t|<|t_{el}|$, $M^2>m^2$.

for some of the larger $|t|$ detectors, at an incident energy of 350 GeV, we refer to Fig. 4.3. Note that channels are indicated on the abscissa, mass on the ordinate. The Jacobian peaks, i.e. largest mass producible at one angle (for incident energy), are approximately at 1/4 t of elastic peak. Clearly, t = 0 is off into "negative channel" numbers (this is due to the use of a discriminator against low signals). We have chosen to consider five inelastic mass contributions to diffractive excitations: $\Delta(1236)$, N(1400), N(1520), M(1688) and N(2190). See Table 4.1[4] for a list of optical points, cross sections, mass widths and diffractive slopes for each mass.

In Appendix A we refer to a simple method of estimating inelastic cross sections from the data presented here (energy subtraction method).

A Breit-Wigner distribution is formed channel by channel for each of the above masses, according to their mass width. The amount of inelastics is obtained relative to the number of elastic events, as follows:

$$N_{inel} = N_{el} \cdot \frac{d\sigma/d\Omega \,|\, inel}{d\sigma/d\Omega \,|\, el} \tag{7}$$

$$N_{el} \cdot \frac{d\sigma/dt \,|\, inel}{d\sigma/dt \,|\, el} \cdot R \,, \tag{8}$$

where N_{el} and N_{inel} are total numbers of events (elastic

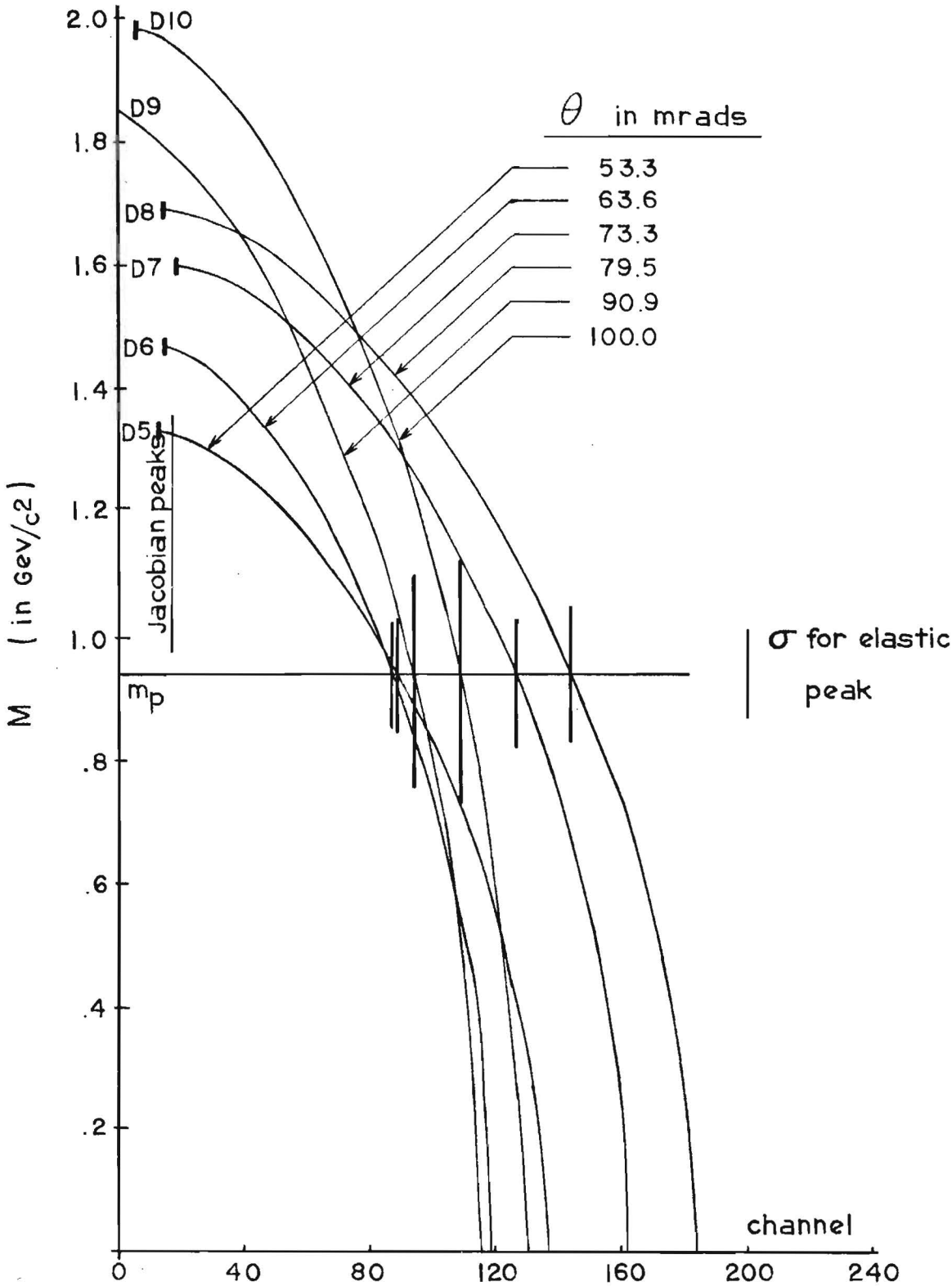

Figure 4.3 Mass vs. channel for some of the larger $|t|$ detectors.

Table 4.1

Data on dissociated protons. Taken from ref. 4

Particle (mass)	I (J^P)	Full width (MeV)	$d\sigma/dt\|_o$ mb/(GeV/c)^2	$\delta\{d\sigma/dt\|_o\}$ mb/(GeV/c)^2	Slope b (GeV/c)$^{-2}$	δb (GeV/c)$^{-2}$
$\Delta(1236)$	$\frac{3}{2}$ $(\frac{3}{2}^+)$	115	.18	.05	6.4	.8
N(1400)	$\frac{1}{2}$ $(\frac{1}{2}^+)$	200	11.6	4.2	24.2	2.5
N(1520)	$\frac{1}{2}$ $(\frac{3}{2}^-)$	130	.91	.19	4.84	.24
N(1688)	$\frac{1}{2}$ $(\frac{5}{2}^+)$	150	2.35	.36	5.12	.08
N(2190)	$\frac{1}{2}$ $(\frac{7}{2}^-)$	300	.16	.05	3.01	.17

and inelastic, respectively). The factor R is given by the ratio $(B \equiv \beta_{cm}\sin\theta)$:

$$R \equiv \frac{dt/d\Omega|\text{inel}}{dt/d\Omega|\text{el}} \tag{9}$$

$$= \frac{2mB \pm \dfrac{(m-\Delta)^2(1+B^2)-m^2(1-B^2)}{\sqrt{(m-\Delta)^2 - m^2(1-B^2)}}}{4mB}$$

(at fixed angle), (10)

from kinematics. The differential cross sections $d\sigma/dt|\text{inel}$ are:

$$\left.\frac{d\sigma}{dt}\right|^{\text{inel}}(t) = \left.\frac{d\sigma}{dt}\right|^{\text{inel}}_{t=0} \cdot \frac{1}{2} \cdot e^{b_{\text{inel}}t}, \tag{11}$$

The factor of $\frac{1}{2}$ comes from the probability of excitation of either forward or recoil (beam or target) proton. We now form the inelastic contribution channel by channel

$$N_{\text{inel}}(t) = \frac{N_{\text{el}} \cdot R}{\left.\frac{d\sigma}{dt}\right|^{\text{el}}_{t=0} e^{b_{\text{el}}\bar{t}_{\text{el}}}} \cdot \left.\frac{d\sigma}{dt}\right|^{\text{inel}}_{t=0} e^{b_{\text{inel}}t_{\text{inel}}} \tag{12}$$

where $N_{\text{inel}}(t)$, t_{inel}, $\bar{t}_{\text{el}}$ are inelastic events at t_{inel} with an elastic peak at an average $\bar{t}_{\text{el}}$. We show some of the distributions of the inelastics in Fig. 4.4 and the inelastics and (elastics less inelastics) in Fig. 4.5. In Fig. 4.4 relative production amplitudes between inelastics are unity. In Fig. 4.5 the inelastic counts are

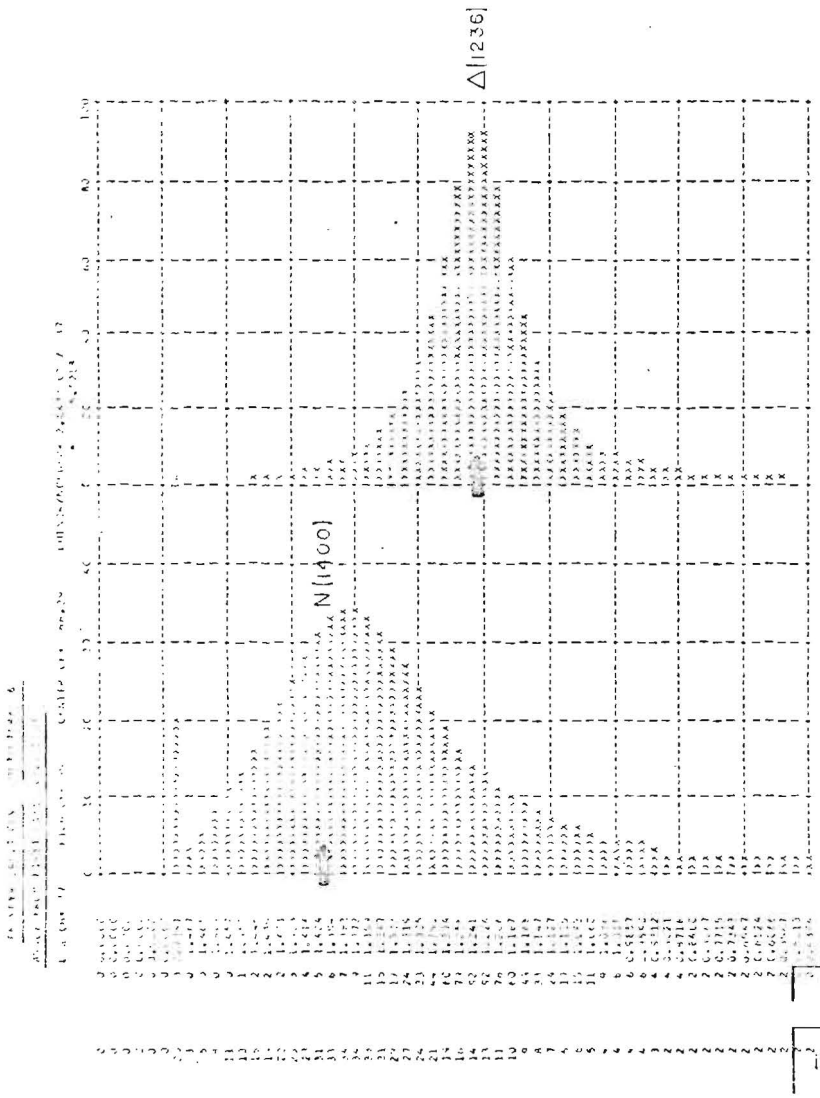

Figure 4.4a Inelastics (Δ(1236) and N*(1400)) mass distribution at 63 mrads and 350 GeV.

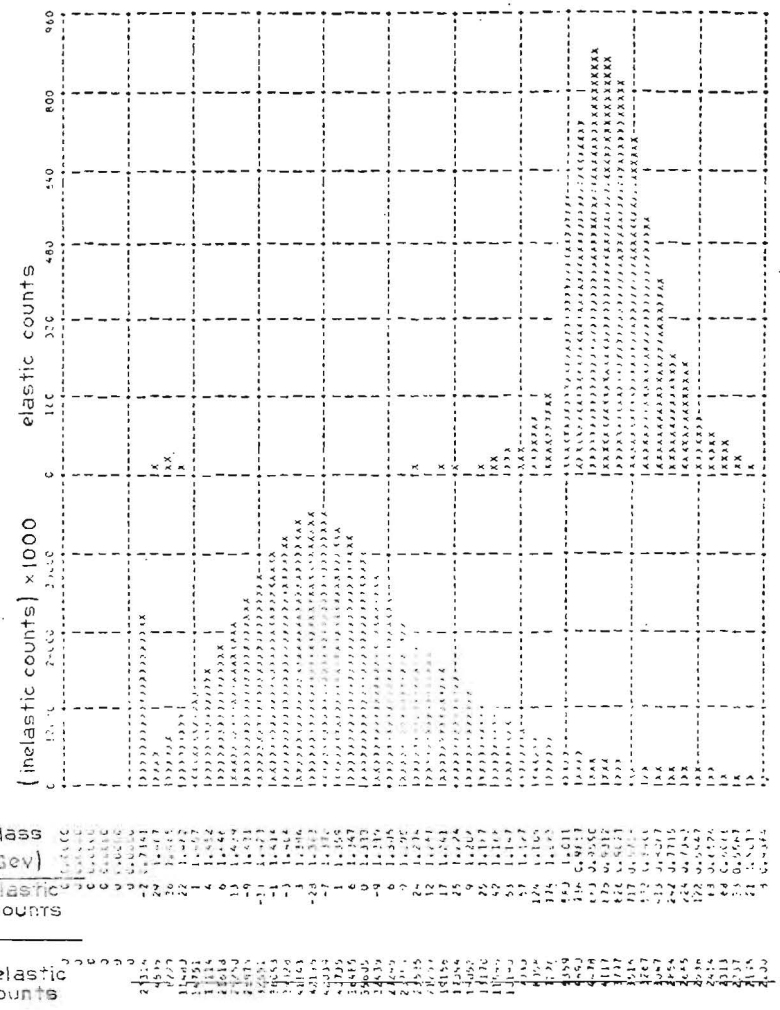

Figure 4.5a At the top is the elastic peak spectrum after subtraction of inelastics (mass distribution which is shown at the bottom and is the sum of the distributions shown in Fig. 4.4(a) taken with the appropriate relative amplitudes).

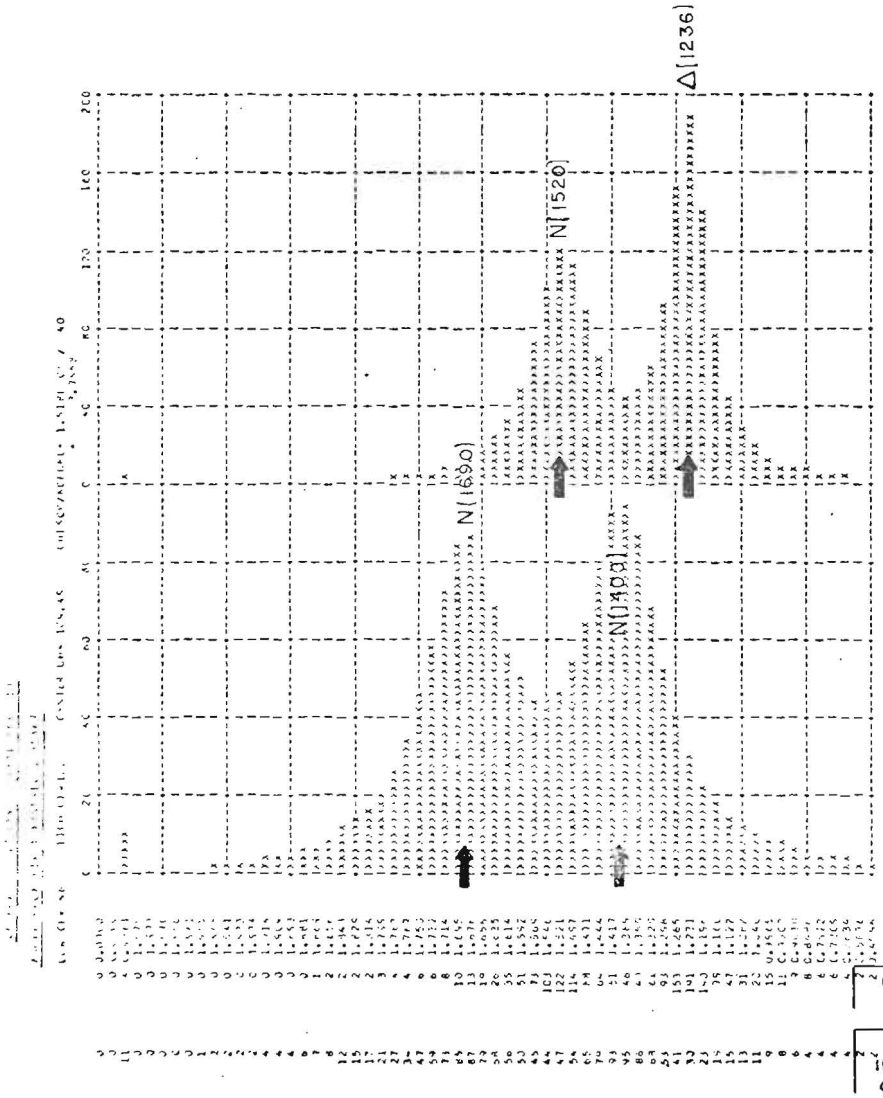

Figure 4.4b Inelastics (Δ(1236), N*(1400), N*(1520) and N*(1688)) mass distributions at 100 mrads and 350 GeV.

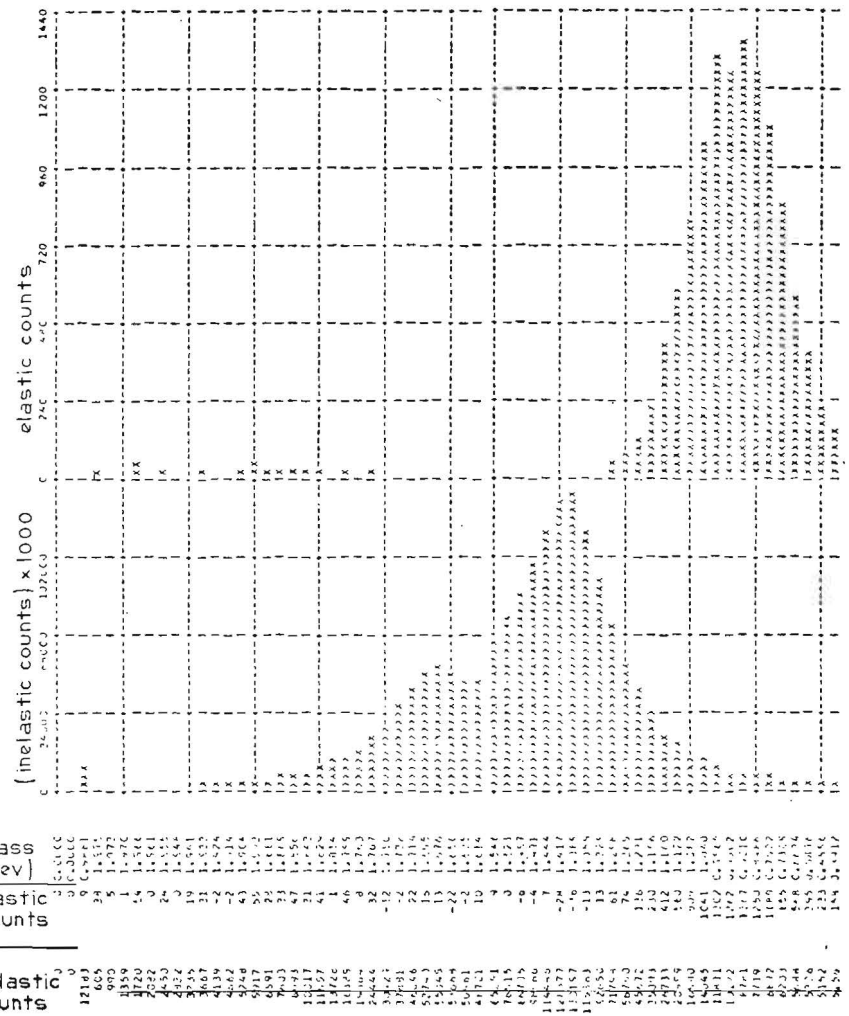

Figure 4.5b The same as in Fig. 4.5a, but data are at a different angle; 100 mrads.

multiplied by 1000. The percentage of inelastic contributions are printed out (also Fig.4.5c). As can be seen in Fig.4.5 there is practically no background left on either side of the elastic peak. However, in order to account for possible contributions from residual gas near the jet, we simply interpolate and subtract this background. This contribution is also shown in Fig. 4.5. It is actually very small at all times, but subsequent fits are vastly improved by lack of these tails. The percentage was generally $\leq$ 1% and never $\leq$ -.3%, giving good agreement with some kind of residual background.

Finally,the histogram is divided, channel by channel, by the differential cross section $d\sigma/d\Omega$ (the parameters used in this expression appear in Table 4.3). This is done relative to the center channel of the elastic peak. The result is a "flat" distribution (these are still elastic peaks however) in recoil momentum space. (The linear density shape of the interaction region.) We do this because the differential cross section, $d\sigma/dt$, changes very rapidly in the Coulomb region which we are trying to measure. Instead, of the 4-momentum transfer squared scale, t, we define, channel by channel, the recoil 3-momentum transfer scale, p_r. Limits are placed on the elastic peak at 3 standard deviations of the Gaussian from the previous fit. These limits are very much

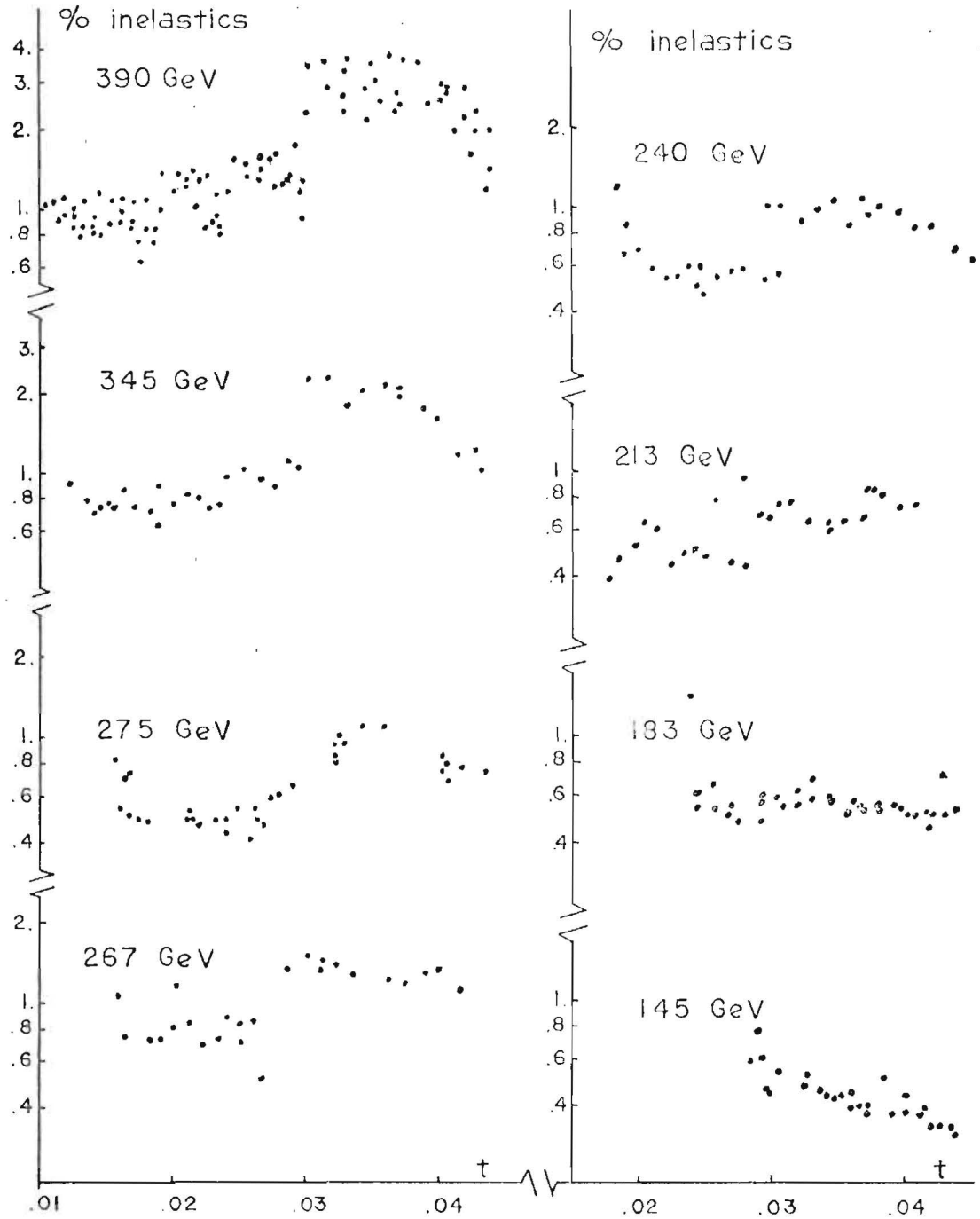

Figure 4.5c Percentage of inelastic contributions at various incident energies.

independent of the procedures before the Gaussian fit.

The CERN minimization routine, MINUITS, has been optimized for use in the "large production" fits that were undertaken. Very strict convergence criteria were required, as this is the closest guarantee of proper error analysis by the subroutine MIGRAD (with gradients). Adequate testing was done in all circumstances to warrant reliable operation of the routine (routine MIMOS was found to be too time consuming). The need for the generalized minimization routine MINUITS, arose out of the introduction of an extra modulating parameter in the Gaussian shape. The minimization function was (distorted Gaussian):

$$dg(p) = N\, e^{-(p-p_c)^2/2\sigma^2} \cdot \{1 + (p-p_c)^2 \cdot W\}, \qquad (13)$$

where the term $(p-p_c)^2 W$ is modulating the Gaussian distribution. This symmetric term, in addition to the symmetric Gaussian shape,could not well accomodate any asymmetric distribution, but was found to satisfactorily increase the overall error on the number of events, in such anomalous cases (see Fig. 4.6). Large effects of this variety occurred on few occasions and mainly in detector 3. Generally, the extra term was found to significantly improve χ^2. We present in Fig. 4.7 histograms of the events, and channel by channel standard deviations from the fit

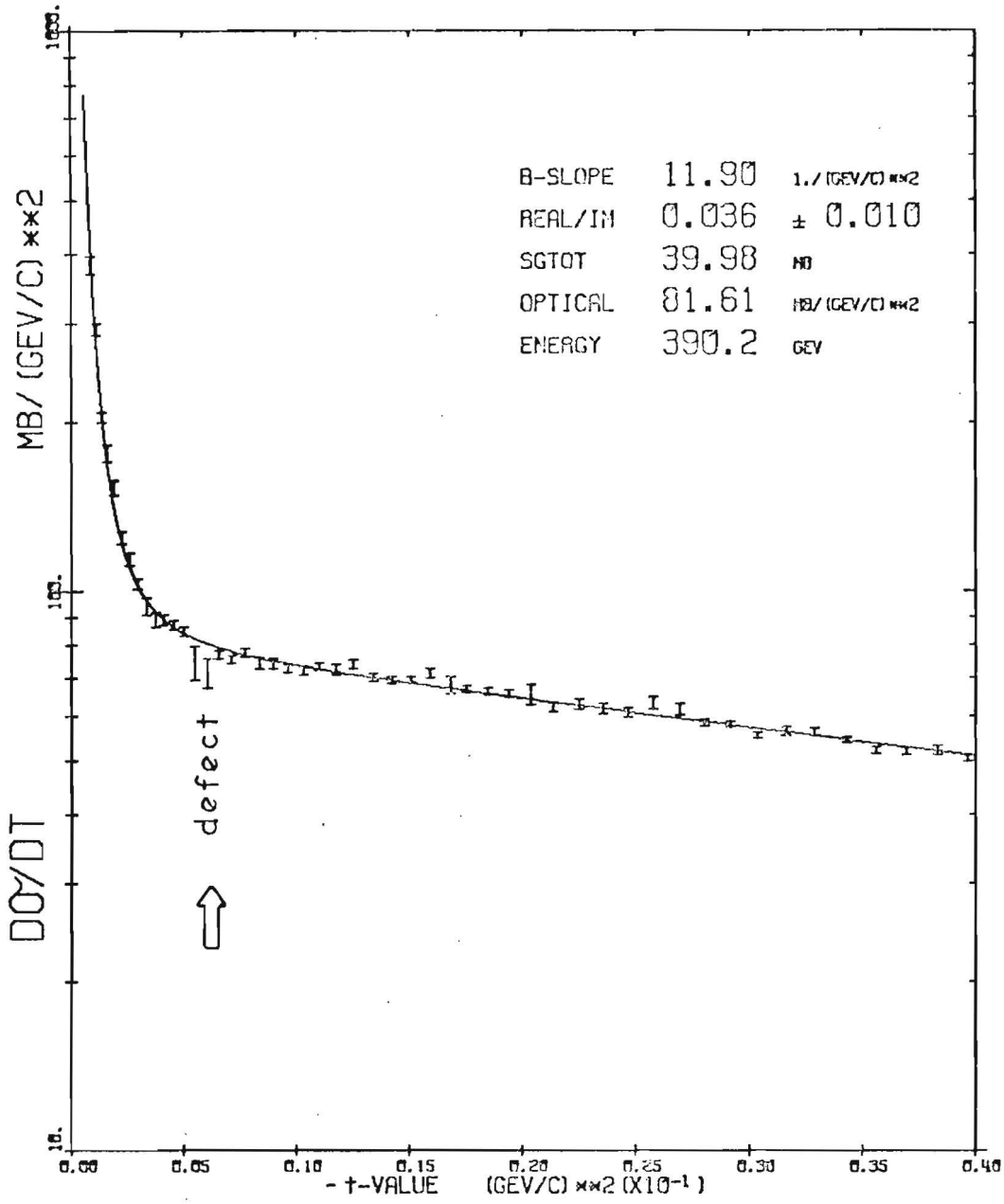

Figure 4.6 Shift of data points due to macroscopic defect in detector 3. Observe the automatic increase of the error bars.

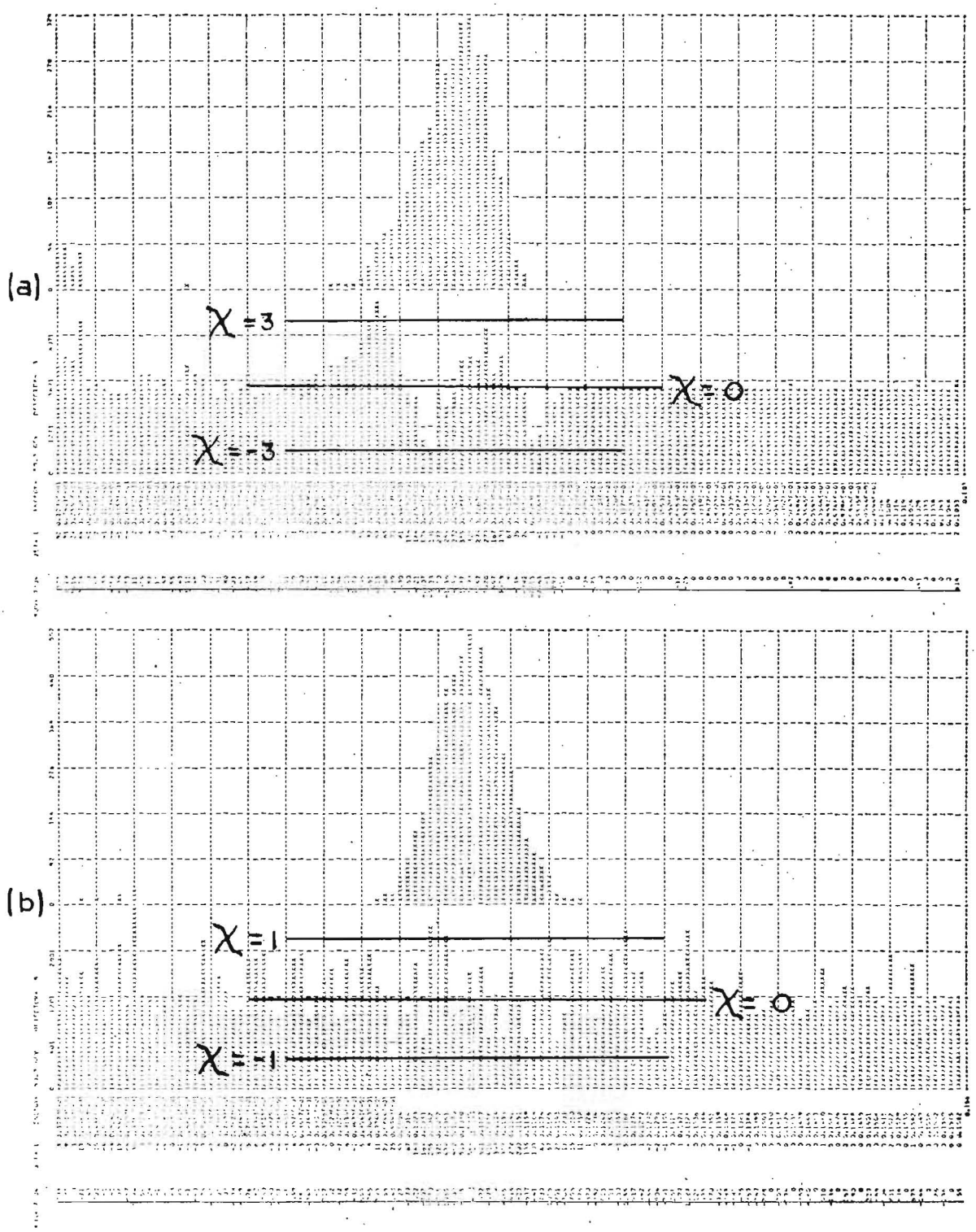

Figure 4.7 (a) Histogram of data (detector 3) in a case where an asymmetric elastic peak occurs (top) and χ deviations from fit (below). (b) Same as (a) but for a normal symmetric distribution; note the goodness of the fit, i.e., generally small χ.

given by Eq. 4.13; χ-distributions are also shown. In Table 4.2 are given indications of the χ^2/(degree of freedom) in the above fits, along with the percentage contribution of the terms $(p-p_c)^2W$, inelastics and background contributions. From the above procedures, one obtains the physical width in space for the gas jet and this is also listed in Table 4.2. The behavior of the jet width with t is also shown (for a typical run) in Fig. 4.8. Detectors 9 and 10 indicate an appreciably larger jet width. This is in part due to the larger collimator sizes on these detectors (i.e. also wider). Detector 8, having had the smallest collimator, also indicates the smallest jet width. The dominant contribution to the apparent jet width is, however, not the collimator size, <1 cm wide, while the full width at one standard deviation for the jet is more than 1 cm.

At this point we recreate the data by multiplying back by $d\sigma/d\Omega$, channel by channel (where the differential cross section is the same one "taken out" as explained on page 119, with parameters appearing in Table 4.3). We repeat the process, for the fitted form of Eq. 4-13, with the parameters (N, p_c, σ, W) obtained above (the distorted Gaussian shape is reduced to a differential cross section spectrum for each detector). Three standard deviations of data (3σ of histograms on either side of p_c), as well

Table 4.2 Contributions due to inelastics, background and the term $(p-p_c)^2 W$, along with χ^2/(degree of freedom) for each detector (50 and 350 GeV).

	LOW ENERGY JET = 50 GEV								HIGH ENERGY JET = 350 GEV							
DET	# INEL HIST	# INEL EL	# BACKG EL	# WIDTH TERM	# DWIDTH TERM	JET WIDTH	DJET WIDTH	CHI2 DFD	# INEL HIST	# INEL EL	# BACKG EL	# WIDTH TERM	# DWIDTH TERM	JET WIDTH	DJET WIDTH	CHI2 DFD
1	0.000	0.000	0.089	5.48E-06	9.562	1.188	13.154	1.087	0.000	0.000	-0.109	2.09E-06	13.011	1.133	13.625	1.006
2	0.000	0.000	0.485	-3.06E-08	6.937	1.151	7.329	1.041	0.000	0.000	0.481	2.31E-05	9.374	1.147	9.873	0.855
3	0.000	0.000	0.709	-2.48E-08	3.796	1.152	4.121	1.466	0.000	0.000	0.687	-3.88E-08	5.116	1.070	5.457	1.330
4	0.000	0.000	0.941	-3.24E-07	3.176	1.243	3.465	2.073	0.000	0.000	1.233	1.00E-07	4.848	1.210	5.161	1.587
5	0.000	0.000	0.875	2.73E-07	3.612	1.238	3.830	1.343	0.107	0.021	0.718	-6.01E-07	4.966	1.202	5.213	1.474
6	0.000	0.000	0.592	4.48E-06	2.951	1.233	3.153	1.402	5.721	0.732	0.764	2.88E-08	2.728	1.160	3.031	2.743
7	0.000	0.000	0.354	3.81E-09	2.938	1.256	3.136	1.827	6.590	0.902	0.629	-2.95E-08	4.320	1.186	4.540	1.711
8	0.000	0.000	0.929	1.67E-09	4.595	1.232	4.888	1.266	8.155	1.020	0.942	1.56E-05	5.740	1.166	5.929	1.717
9	0.000	0.000	0.971	5.98E-07	4.878	1.497	5.041	1.310	8.017	2.298	0.793	-2.09E-06	6.369	1.463	6.561	1.769
10	0.000	0.000	0.535	-2.52E-07	3.930	1.435	4.076	1.944	7.827	2.084	0.517	1.13E-05	3.660	1.384	3.846	2.346
1	0.000	0.000	0.307	5.77E-06	8.494	1.165	8.917	1.049	0.000	0.000	0.108	-2.73E-05	9.489	1.160	9.970	0.727
2	0.000	0.000	0.337	-2.28E-07	8.097	1.177	8.488	0.915	0.000	0.000	0.164	-7.89E-07	5.812	1.135	6.464	0.893
3	0.000	0.000	0.492	-2.01E-07	3.613	1.150	3.969	1.398	0.000	0.000	0.577	2.05E-05	5.384	1.101	5.688	1.013
4	0.000	0.000	0.729	7.67E-09	4.446	1.228	4.731	1.232	0.099	0.020	0.398	1.64E-08	5.648	1.217	5.925	1.578
5	0.000	0.000	0.477	4.73E-07	3.186	1.219	3.438	2.091	0.110	0.023	0.637	-3.59E-08	3.723	1.190	4.006	1.791
6	0.000	0.000	0.256	-1.59E-06	3.265	1.217	3.483	1.524	5.813	0.745	0.399	-2.38E-05	3.720	1.160	3.954	1.806
7	0.000	0.000	0.415	-2.79E-08	3.613	1.214	3.828	2.221	6.590	0.775	0.335	6.35E-02	2.765	1.140	2.781	2.659
8	0.000	0.000	0.777	-5.67E-08	4.129	1.199	4.435	1.595	8.153	1.010	0.477	-1.62E-05	4.695	1.102	5.046	1.377
9	0.000	0.000	0.688	-3.16E-06	6.057	1.463	6.243	1.671	7.986	2.298	0.799	1.75E 01	6.558	1.245	3.775	1.328
10	0.000	0.000	0.073	-3.08E-06	3.564	1.395	3.711	2.599	7.825	1.736	0.740	1.11E-06	3.696	1.298	3.682	2.539
1	0.000	0.000	0.277	3.70E-10	6.284	1.150	5.616	0.985	0.000	0.000	0.324	1.62E 00	54.723	1.093	52.724	0.951
2	0.000	0.000	0.419	2.91E-07	5.458	1.108	5.847	1.347	0.000	0.000	1.053	-3.31E-05	6.445	1.067	7.009	1.018
3	0.000	0.000	0.215	-1.23E-05	9.575	1.079	9.836	1.489	0.000	0.000	0.283	5.75E 00	10.132	0.976	7.924	1.183
4	0.000	0.000	0.664	2.57E-06	3.639	1.171	3.888	1.805	0.100	0.017	0.608	3.51E-06	6.256	1.126	6.511	1.403
5	0.000	0.000	0.507	-1.84E-07	3.998	1.195	4.225	1.473	12.230	2.221	0.799	2.00E-06	5.015	1.144	5.249	1.286
6	0.000	0.000	0.062	-1.44E-05	4.090	1.187	4.271	1.508	6.524	0.845	0.091	1.03E-03	3.289	1.137	3.490	1.705
7	0.000	0.000	0.137	8.25E-06	3.372	1.172	3.568	1.902	6.559	0.827	0.191	1.12E-05	3.101	1.094	3.334	2.517
8	0.000	0.000	0.384	1.54E-05	3.987	1.124	4.286	1.646	8.132	0.946	0.506	-1.46E-07	3.924	1.073	4.271	1.501
9	0.000	0.000	0.771	-3.47E-07	3.647	1.418	3.814	2.753	7.984	1.748	0.255	1.54E-08	5.720	1.393	5.899	2.323
10	0.000	0.000	0.246	2.06E-06	3.768	1.300	3.910	2.286	7.751	1.584	0.070	-2.12E-05	4.904	1.229	5.007	2.018
1	0.000	0.000	0.271	4.39E-05	9.520	1.039	9.858	0.996	0.000	0.000	0.314	-1.90E-06	6.207	0.979	6.716	0.993
2	0.000	0.000	1.782	1.61E-06	6.165	1.091	6.594	1.028	0.000	0.000	0.506	4.79E-07	5.942	1.005	6.782	1.010
3	0.000	0.000	0.104	4.97E 01	7.031	0.563	1.974	5.196	0.000	0.000	0.201	4.99E 01	9.251	0.493	2.704	4.880
4	0.000	0.000	0.825	1.61E-05	8.858	1.142	9.135	2.049	0.103	0.015	0.965	8.55E-06	4.670	1.090	5.022	1.583
5	0.000	0.000	0.568	-3.77E-06	5.948	1.145	6.161	1.212	6.175	0.912	0.450	-5.59E-05	5.005	1.082	5.354	1.044
6	0.000	0.000	0.012	1.45E-06	4.300	1.110	4.495	1.381	6.536	0.741	0.157	6.71E-08	5.552	1.043	5.764	1.491
7	0.000	0.000	0.146	8.16E 00	6.698	0.994	4.805	2.178	8.429	0.803	-0.049	3.27E-06	6.250	0.994	6.511	2.721
8	0.000	0.000	0.483	7.33E-07	7.089	1.040	7.393	1.417	8.139	0.881	0.816	-1.39E-01	0.991	1.027	1.530	1.951
9	0.000	0.000	0.856	7.57E 00	8.293	1.259	6.274	2.209	7.922	2.055	0.814	3.25E-07	10.018	1.337	10.283	0.965
10	0.000	0.000	0.153	-1.11E-06	8.554	1.224	8.764	1.965	7.782	1.161	-0.337	4.79E-06	3.831	1.122	4.060	3.467
1	0.000	0.000	1.312	-2.47E-05	8.552	1.071	8.853	0.790	0.000	0.000	0.000	1.60E-06	4.062	1.051	4.602	1.060
2	0.000	0.000	1.009	-3.41E-05	9.340	1.129	9.720	1.085	0.000	0.000	1.126	1.06E-06	6.643	1.096	7.239	1.111
3	0.000	0.000	0.005	2.77E 01	6.355	0.869	2.535	1.580	0.000	0.000	-0.133	-1.34E 01	1.389	1.158	3.185	2.567
4	0.000	0.000	0.437	1.04E-07	8.606	1.228	8.884	2.219	0.107	0.020	0.281	-4.80E-06	5.124	1.236	5.430	1.939
5	0.000	0.000	0.217	5.91E-07	4.089	1.189	4.323	1.313	5.582	0.786	0.138	2.29E-05	29.232	1.149	29.878	1.342
6	0.000	0.000	0.136	1.46E 01	5.827	0.939	3.353	2.453	6.576	0.693	0.330	2.15E 01	5.390	0.802	2.580	4.368
7	0.000	0.000	-0.101	1.23E 01	5.113	0.885	3.115	3.402	8.145	0.727	0.171	5.45E-06	11.972	0.938	12.239	4.038
8	0.000	0.000	0.060	1.72E-07	4.786	1.114	5.064	1.056	8.076	1.106	-0.034	3.32E-05	9.844	1.083	10.189	1.268
9	0.000	0.000	0.499	-7.62E-07	5.830	1.390	6.017	2.837	7.829	2.174	0.864	-2.61E-07	8.992	1.340	9.235	1.516
10	0.000	0.000	0.048	5.26E-06	3.658	1.164	3.828	2.832	7.819	1.236	0.314	2.03E-05	3.867	1.054	4.068	2.554
1	0.000	0.000	0.000	-9.63E-06	2.893	0.998	3.195	1.117	0.000	0.000	0.000	-5.93E-07	4.663	0.965	5.038	0.964
2	0.000	0.000	0.908	-3.65E-07	4.260	1.015	4.629	1.397	0.000	0.000	1.307	-4.61E-06	6.375	0.970	6.629	1.139
3	0.000	0.000	0.031	3.34E 01	5.839	0.634	1.493	6.699	0.000	0.000	0.059	-1.40E 01	1.486	0.854	3.684	7.728
4	0.000	0.000	0.328	1.04E-05	4.251	1.130	4.448	3.173	0.108	0.017	0.326	8.96E-07	10.761	1.080	11.056	1.952
5	0.000	0.000	0.006	1.46E-05	5.488	1.095	5.657	2.282	5.623	0.617	0.191	6.40E-05	10.943	1.006	11.250	3.039
6	0.000	0.000	0.048	8.38E 00	5.369	0.847	3.808	6.553	6.580	0.489	0.208	9.57E 00	6.533	0.757	4.488	8.014
7	0.000	0.000	0.041	1.67E-05	8.813	0.871	8.991	6.927	8.137	0.613	0.151	-6.29E-06	7.797	0.820	7.991	7.638
8	0.000	0.000	-0.316	1.39E-05	4.099	1.012	4.329	1.336	8.098	0.744	-0.016	3.30E-06	4.232	0.936	4.563	2.235
9	0.000	0.000	0.215	1.33E 01	5.279	1.216	3.322	4.603	7.849	1.798	0.583	1.36E-06	6.132	1.247	6.321	2.093
10	0.000	0.000	0.077	1.87E-06	4.284	1.033	4.405	3.579	7.681	0.941	0.247	-1.66E-05	4.434	0.930	4.606	5.013

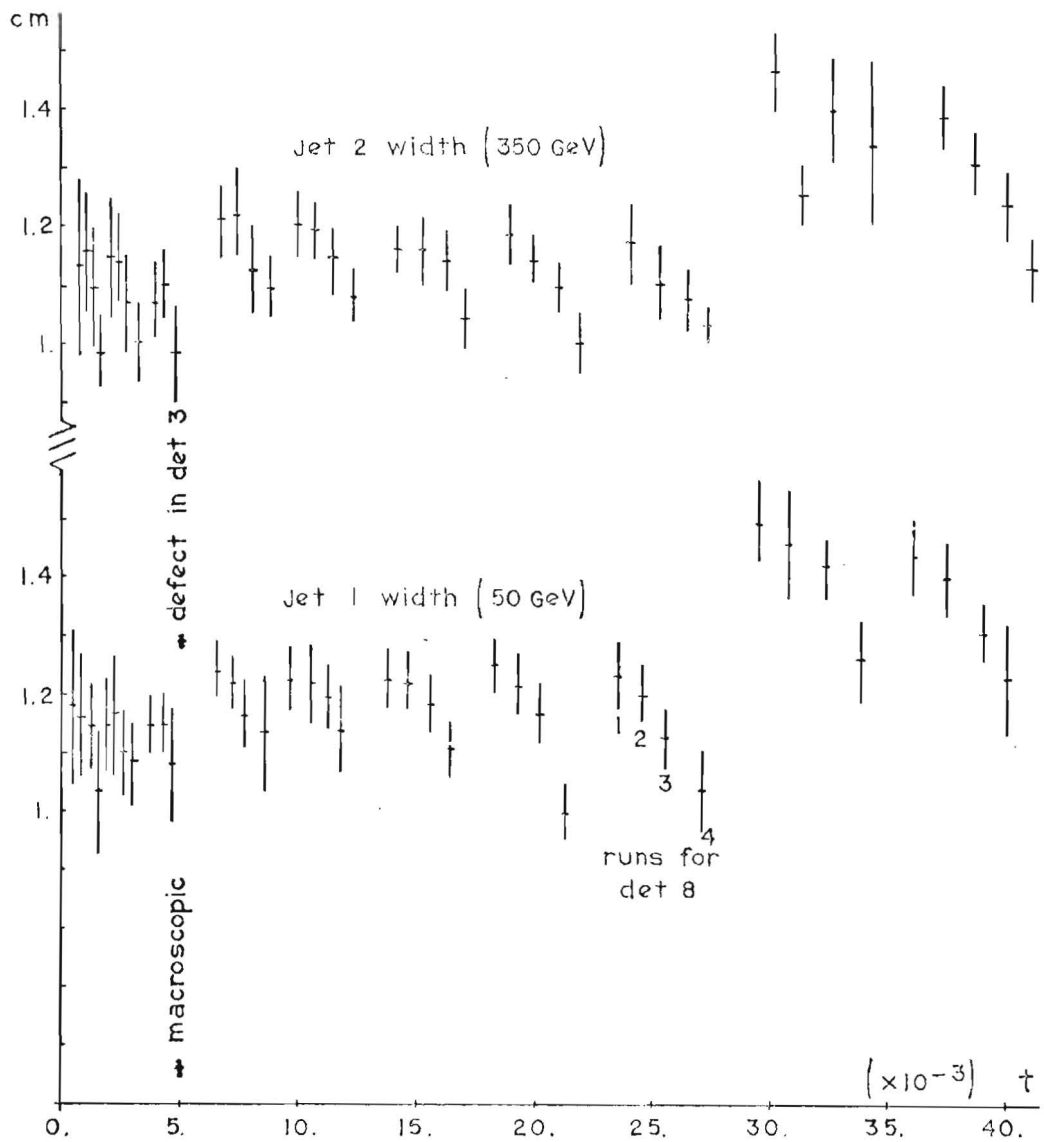

Figure 4.8 Jet width as obtained from fits of elastic peaks.

as fit (distorted Gaussian converted to a differential cross section spectrum) were summed. These two quantities represent the final differential values at an average value of t (i.e.for one detector), for two basically different means of evaluation (i.e. counting the spectrum between certain channels and summing a function - distorted Gaussian - between the same channels, respectively).

The operations outlined above were done detector by detector, run by run, for all energies. In dealing with differential cross sections which involve the relatively recently obtained quantities b, ρ,σ, we used the following approximate parametrizations, which, for the purposes of this analysis are totally adequate (see Table 4.3).

Table 4.3

$b(s) = 7.7 + 2. \times .3415 \times \ln s$	(all energies)
$\rho(s) = -.55 + .1 \times \ln E$	($E < 250$ GeV)
$\rho(s) = -.24 + .0435 \times \ln E$	($E > 250$ GeV)
$\sigma(s) = 38.44$	($50 < E < 188$ GeV)
$\sigma(s) = 38.4 + .9 \times \ln(E/93.83)$	($E > 188$ GeV)

This is our method of background subtraction. In the sense that residual backgrounds found are small, we believe that the inelastic contributions subtracted are handled reasonably, and the parameters used,adequately describe diffractive excitation. In the

next section is presented a complete analysis of further fits of the differential cross section, to obtain the ratio of the real to imaginary parts of the nuclear amplitude.

4.3 Fits of Differential Cross Section

The number of events extracted from the histograms is used in fits for the differential cross section formula,

$$\frac{d\sigma}{dt}(s,t) = K\{f_n^2(s,t)(1 + \rho^2(s)) + f_c^2(s,t) + f_{intf}(s,t)\} \text{ (ref.2)} \quad (14)$$

where

$$f_n(s,t) = \sqrt{\frac{\sigma_T^2(s)}{16\pi}}\; e^{1/2\, b(s)t} \quad ,$$

$$f_c(s,t) = -\,2\,\frac{\alpha}{\beta(s)}\,\{F(t)\}^2\,\sqrt{10\pi}/|t| \quad ,$$

$$f_{intf}(s,t) = 2\cdot f_n(s,t)\cdot f_c(s,t)\cdot[\rho(s) + \frac{\alpha}{\beta(s)}\,(\ln\frac{1.}{b(s)|t|} - .5772)],$$

$$F(t) = \frac{1}{(1+|t|/.71)^2} \text{ is the proton form factor.}$$

The amplitudes and cross sections are shown in Fig. 4.9.

The fit to the data was accomplished by the minimization routine MINUITS. The data were read in from disk, one energy at a time. The differential cross section $d\sigma/d\Omega$ was formed by a division of events by detector area. Then $d\sigma/dt$ was obtained by multiplying by $d\Omega/dt$. We used

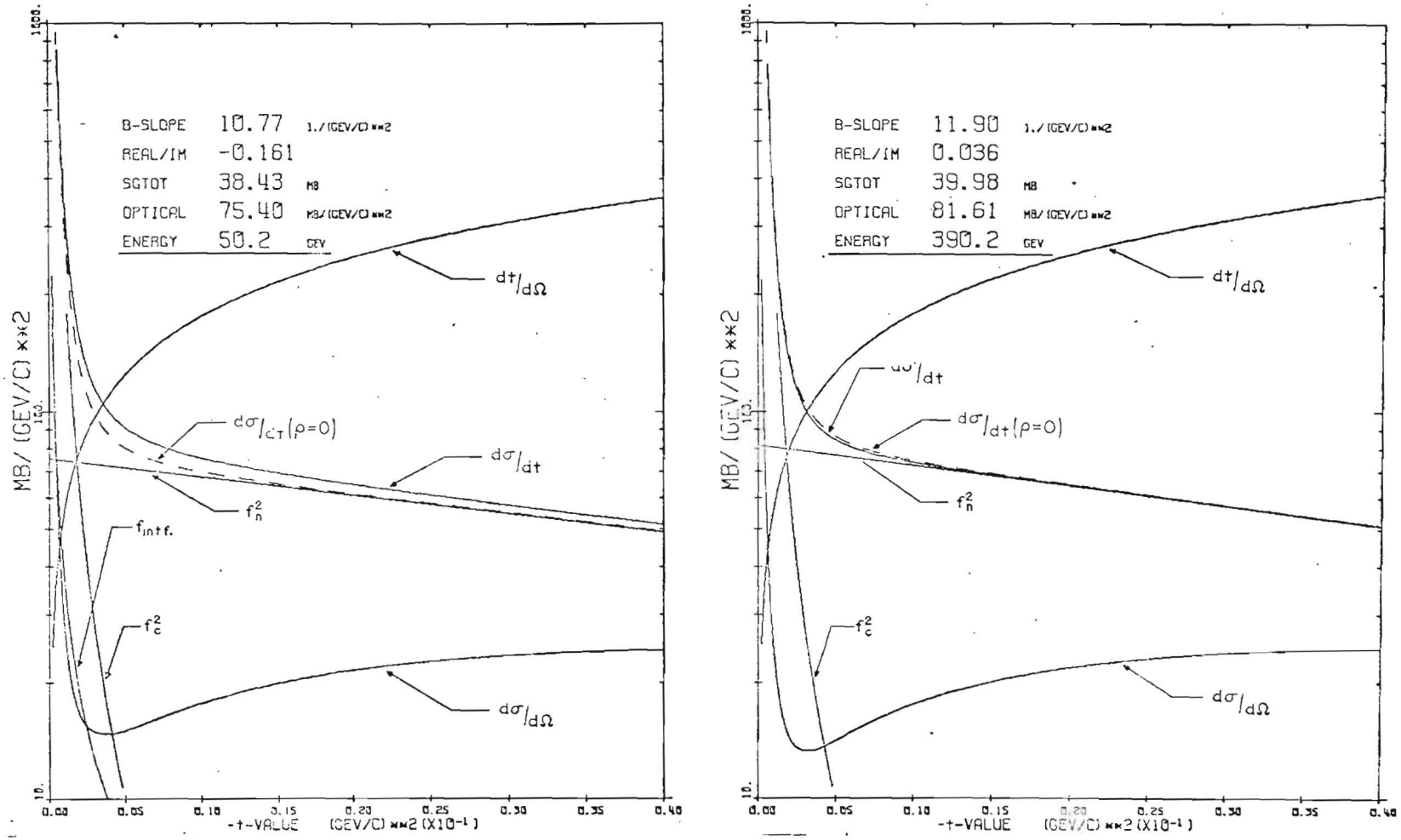

Figure 4.9 Examples of amplitude and differential cross section t-dependence.

parametrizations taken from published results for b(s) and $\sigma_T(s)$:

$$b(s) = 8.23 + 2 \cdot .278 \cdot \ln(s) \qquad \text{(ref. 5)}$$

and

$$\sigma_T(s) = 38.4 + .49 \cdot [\ln(s/122)]^2 \qquad \text{(ref. 6)}$$

Attempts to determine the t-scale, by using the angles obtained in fitting the elastic peaks, proved less successful than a normalization on the Coulomb amplitude. We therefore used the latter method, which involves the minimization of χ^2 for different angular ranges of the detector system.

The various runs at one incident energy, were combined to make up some 50-70 points of the differential cross section; this combination was also performed by a χ^2 minimizing process. The alternative of using the fixed detectors as normalization factors, invariably gave a much larger χ^2 (about 1.3-1.5 times larger).

The actual minimizing process was initiated by subroutine TAUROS (in MINUITS) and subsequently taken over into MIGRAD (with gradients). Very strict convergence criteria were required, so as to insure proper error analysis. We present in Fig. 4.10 a typical fit listing which indicates $d\sigma/dt$, points and errors, $|t|$, χ and the

```
EXT.COV.          INTERNAL COVARIANCE MATRIX//.
  9.399720-01 K     6.480-06
 -4.317360-02 ρb    1.160-05  1.830-05
 -2.427590-01       9.440-07  1.660-06  1.960-07
  1.553720 00  σ   -1.690-06 -2.070-06 -1.940-07  4.780-07
EXT.COV.          EXTERNAL COVARIANCE MATRIX//.
  1.652520-02 K     7.620-03
 -4.317360-03 ρb    3.540-03  1.830-03
 -2.373320-04       3.080-02  1.740-02  2.310-01
  1.355930-04  σ   -4.780-01 -2.130-01 -1.690 00  3.060 01

KOD= 7200    JET=-2    ENERGY= 346.6 GEV    # RUNS=  6
FIT DIFFERENTIAL CROSS SECTION FOR b SLOPE AND REAL/IM ALPHA AND TOTAL XSECTION
```

JET	DSDT-TH	FDIAT	ERROR	ROC-CORR	T-VALUE	ANGLE	S-DEV	CHISQR
1	397.57021	426.47607	11.85274	0.0	0.00068	15.83832	2.43675	5.94749
1	280.63287	305.67139	8.51647	0.0	0.00110	17.68666	2.91066	8.47192
1	212.33396	213.21471	10.64928	0.0	0.00134	19.53384	0.08505	0.00723
1	169.91015	166.19247	9.03606	0.0	0.00163	21.38295	-0.45284	0.72734
1	142.59942	138.54689	3.44668	0.0	0.00189	23.23109	-1.16359	1.35394
1	124.26571	125.64106	2.83330	0.0	0.00220	25.07905	0.48543	0.23564
2	122.41237	132.83989	3.65770	0.0	0.00225	25.31208	2.85384	8.12730
2	110.32374	109.33499	3.14000	0.0	0.00259	27.15304	-0.32035	0.10651
2	101.71365	101.51158	2.74462	0.0	0.00295	29.00781	-0.07364	0.03542
2	94.40557	97.46530	9.06209	0.0	0.00334	30.85548	0.07396	0.45422
2	90.67943	90.55312	2.58678	0.0	0.00375	32.70315	-0.04535	0.00206
2	87.02576	88.13002	2.27908	0.0	0.00419	34.55059	0.48276	0.23306
3	87.69114	87.53404	1.94544	0.0	0.00413	34.17910	-0.08075	0.00652
3	84.63312	85.22311	1.90653	0.0	0.00455	36.02656	0.28009	0.07845
3	82.26116	82.49838	2.72099	0.0	0.00503	37.87380	0.07983	0.00637
3	80.30423	79.89320	4.23159	0.0	0.00553	39.72091	-1.04241	1.08681
3	78.64354	77.20042	5.16397	0.0	0.00606	41.56798	-0.27962	0.07819
3	77.21719	73.30670	3.95557	0.0	0.00661	43.41481	-0.98860	0.97734
4	77.36584	76.32591	1.41891	0.0	0.00555	43.20452	-0.73573	0.54129
4	76.16367	75.77739	1.42219	0.0	0.00712	45.05132	-0.22731	0.05167
4	74.56588	73.20263	1.31622	0.0	0.00772	46.89787	-1.27669	1.61312
4	73.55431	72.32948	1.53112	0.0	0.00834	48.74424	-0.72191	0.52116
4	72.97921	72.84144	1.39193	0.0	0.00899	50.59057	-0.07024	0.00493
4	72.08117	73.44965	1.23241	0.0	0.00966	52.43661	1.05885	1.12117
5	72.14268	70.90477	1.27212	0.0	0.00961	52.30699	-0.97311	0.94694
5	71.28496	71.66403	1.27723	0.0	0.01030	54.15297	0.45338	0.20555
5	70.45232	69.11730	1.25637	0.0	0.01102	55.99866	-1.12249	1.25979
5	69.05649	69.35449	1.20642	0.0	0.01176	57.84417	-0.19383	0.03757
5	68.07415	71.31636	1.26395	0.0	0.01252	59.68958	1.65556	2.74087
5	65.10163	69.22318	1.17173	0.0	0.01331	61.53468	0.95458	0.91122
6	68.02156	67.69752	1.14855	0.0	0.01340	61.72711	-0.26178	0.07540
6	67.25727	67.27475	1.15430	0.0	0.01421	63.57266	0.01514	0.00023
6	66.45725	67.40143	1.09173	0.0	0.01505	65.41673	0.82821	0.68592
6	65.73903	67.46073	1.30128	0.0	0.01592	67.25115	1.27696	1.63064
6	64.98873	65.31599	2.03630	0.0	0.01681	69.10546	0.16304	0.02658
6	64.22100	63.58084	1.79040	0.0	0.01772	70.94942	-0.35755	0.12764
7	64.39056	63.02191	1.65155	0.0	0.01751	70.53835	-1.30155	1.69404
7	63.62891	64.17567	1.08234	0.0	0.01845	72.38222	0.50516	0.25519
7	62.86415	63.85161	1.03598	0.0	0.01940	74.22575	0.96224	0.92590
7	62.09562	63.43480	1.23533	0.0	0.02038	76.06902	1.11104	1.23441
7	61.32298	61.65586	1.08417	0.0	0.02139	77.91213	0.34404	0.11836
7	60.54576	58.12239	0.55509	0.0	0.02242	79.75488	-2.53731	6.43792
8	60.45444	60.27219	1.59147	0.0	0.02253	79.94706	-0.12080	0.01459
8	59.68225	59.47673	1.51356	0.0	0.02359	81.78961	-0.13578	0.01844
8	58.87952	59.49268	1.49475	0.0	0.02467	83.63178	0.37915	0.14375
8	58.10431	58.45314	1.64158	-0.02641	0.02577	85.47366	0.21645	0.04685
8	57.30970	57.95602	1.51163	0.17953	0.02691	87.31534	0.43484	0.18909
8	56.52397	57.52013	1.42290	0.28698	0.02808	89.15763	0.71062	0.50498
9	56.55776	55.74152	0.83604	0.0	0.02800	89.76758	0.23176	0.05371
9	55.74429	55.17494	1.49734	0.12792	0.02918	90.90868	0.22903	0.05245
9	54.93723	55.08946	0.79117	0.26954	0.03039	92.74937	0.19241	0.03702
9	54.12636	54.05863	0.76758	0.36543	0.03162	94.58974	0.50854	0.25861
9	53.31369	53.40150	0.84436	0.43391	0.03287	96.42969	0.10429	0.01088
9	52.49755	53.12207	0.76546	0.61102	0.03415	98.26961	0.81161	0.65871
10	52.39450	51.29325	0.73955	0.32829	0.03431	98.50158	-1.48084	2.19289
10	51.57035	50.65753	0.74796	0.48993	0.03562	100.34102	-0.92054	0.84739
10	50.73567	49.95865	0.73611	0.51557	0.03695	102.18062	-1.12904	1.27474
10	49.93433	50.67778	0.85087	0.58855	0.03831	104.01867	0.87376	0.76345
10	49.11178	48.37613	0.79195	0.54542	0.03969	105.85706	-0.57936	0.33566
10	48.28874	49.03356	0.80535	0.52240	0.04109	107.69499	1.03518	1.07160

NORM	DNORM	BSLOPE	CB	ALPHA	DALPHA	SGTOT	DSGTOT	CHISQR
1.041541	0.067301	11.472024	0.480859	0.010854	0.042770	39.315026	1.376997	45.132766

JET	SUM CHI O	SUM CHISQ O	RNFDG	RUN	SUM CHI R	SUM CHISQ R
1	-1.9950	2.3242	99.9772	1	-1.8920	13.6567
2	3.5522	8.9256	100.0023	2	-0.1272	1.6159
3	-2.3315	2.2355	99.8779	3	-1.0683	5.9593
4	-1.5504	3.8523	99.9610	4	1.8497	6.7009
5	0.7742	6.1019	99.9510	5	0.5836	4.8606
6	1.3440	2.5506	99.9714	6	1.6956	12.2795
7	-0.7164	10.0658				
8	1.1849	0.9177				
9	2.5776	1.0714				
10	-2.2023	0.4857				

CONSTANT CHISQR	ALPHA	BSLOPE	SGTOT	NTAU	NMIG
0	0.0	0.120705	0.054355	33	12

Figure 4.10 Listing of fit of the differential cross section, with error matrix at the top.

various parameters obtained, K, ρ, b, σ_T, χ^2, etc. At the top is indicated the covariance matrix. At the bottom, the various deviations and χ^2 per detector and per run, are presented as well. Options were available for constraining variables and fitting any, or all, of K, ρ, b, σ_T and run normalizations.

The proper angle definition was obtained by repeated fits with a shifted angular scale to the detectors (Fig. 4.11). We also provided a scale distortion option, which would act in such a manner, as to simulate the angular deviations produced by a fringe magnetic field in the accelerator tunnel. Estimates of the field were read with pulsing magnets, but without any beam (see Fig. 4.12), i.e., reading at 400 GeV.

All the fits described above were undertaken one (beam) energy at a time. However, we also used all data within the same fit to parametrize the differential cross section in the s-t plane. The advantages of such a procedure are, that subsequent analysis for s-dependence is reduced, and all data are treated equally. However, some instabilities (due to systematic effects that are s-dependent) spoil the quality of such a fit.

The differential cross section data for some energies are shown in Fig. 4.13. There is no cut on the data in this figure, but the data used in the actual fits were limited to $|t| \geq .0011\ (\mathrm{GeV}/c)^2$, because at lower $|t|$

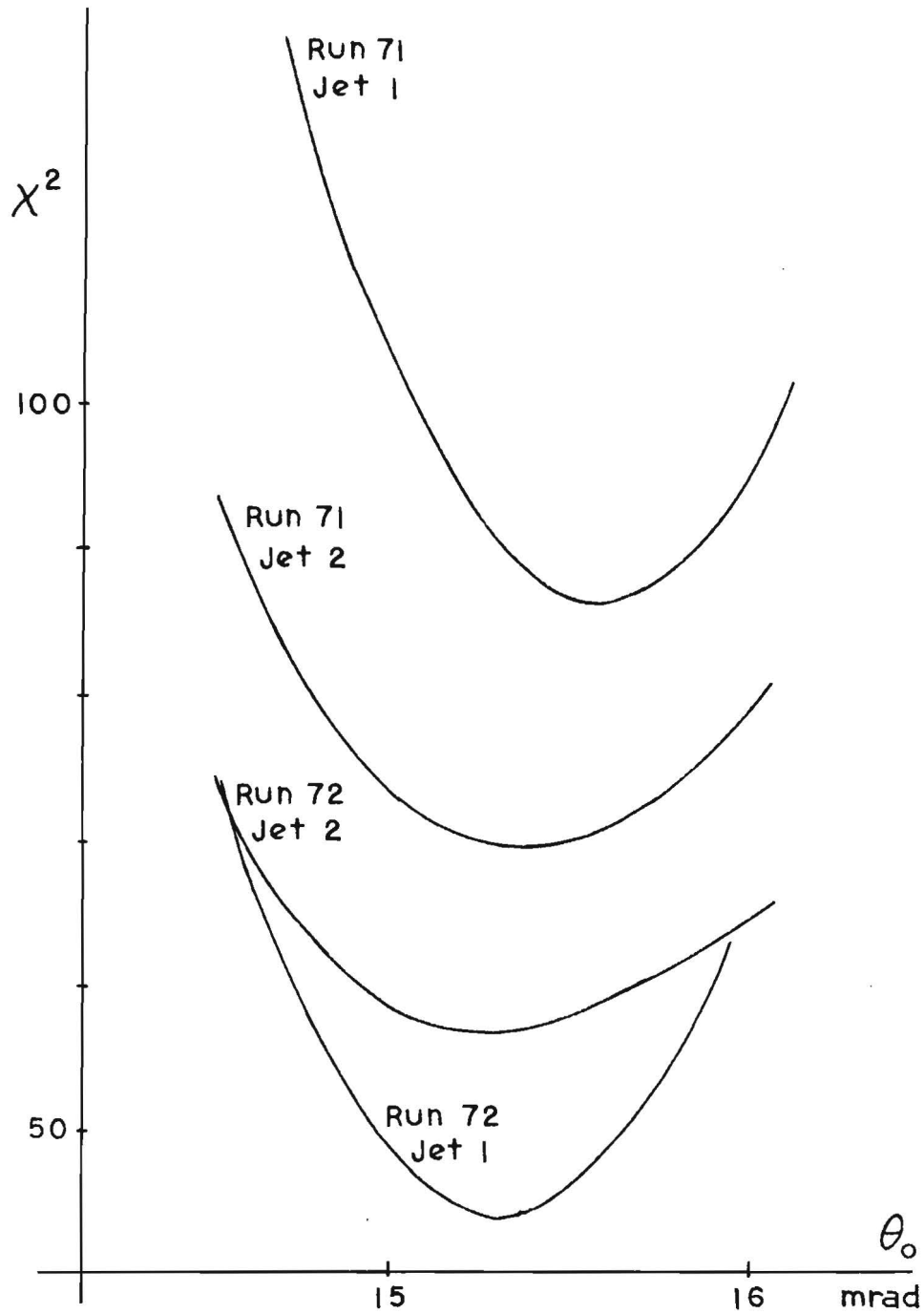

Figure 4.11 Shape of χ^2 distribution in terms of an angular definition of the (detector's) carriage position.

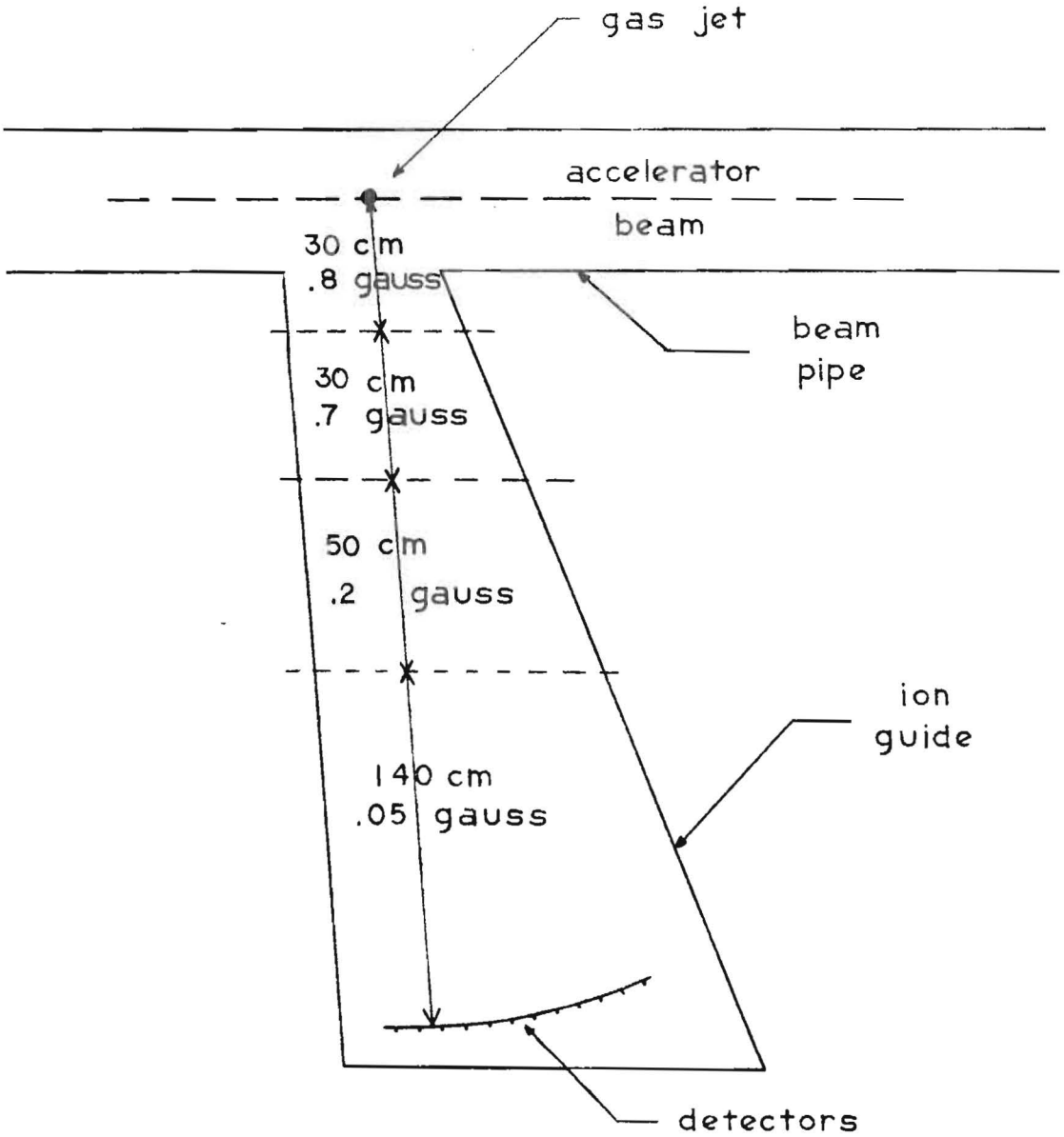

Figure 4.12 Fringe magnetic field (in the accelerator tunnel) at various points along the ion guide. This field was measured outside the ion guide and as such is the upper limit on the field inside the ion guide, which, because of shielding effects is expected to be much smaller.

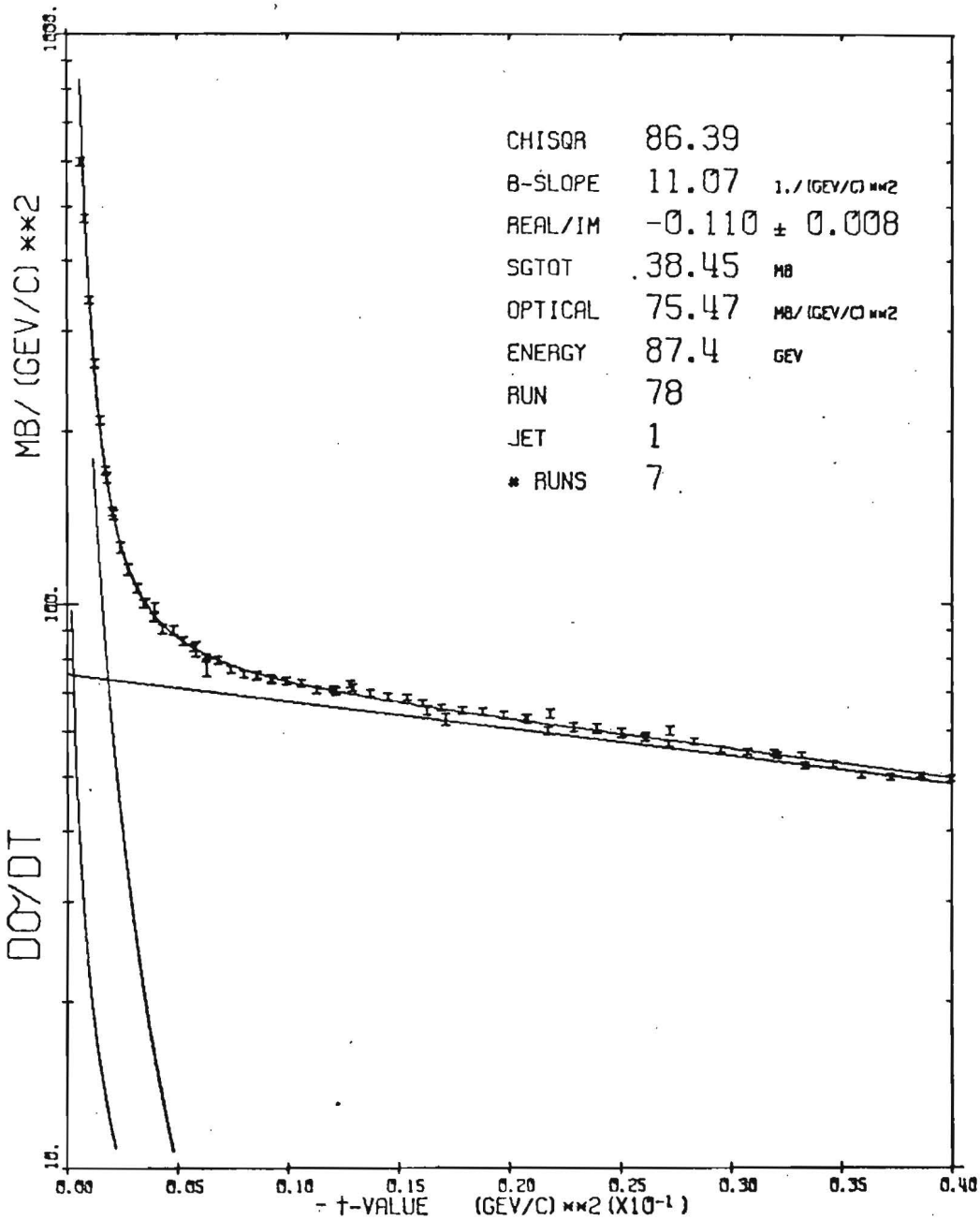

Figure 4.13a Differential cross section data (70 points).

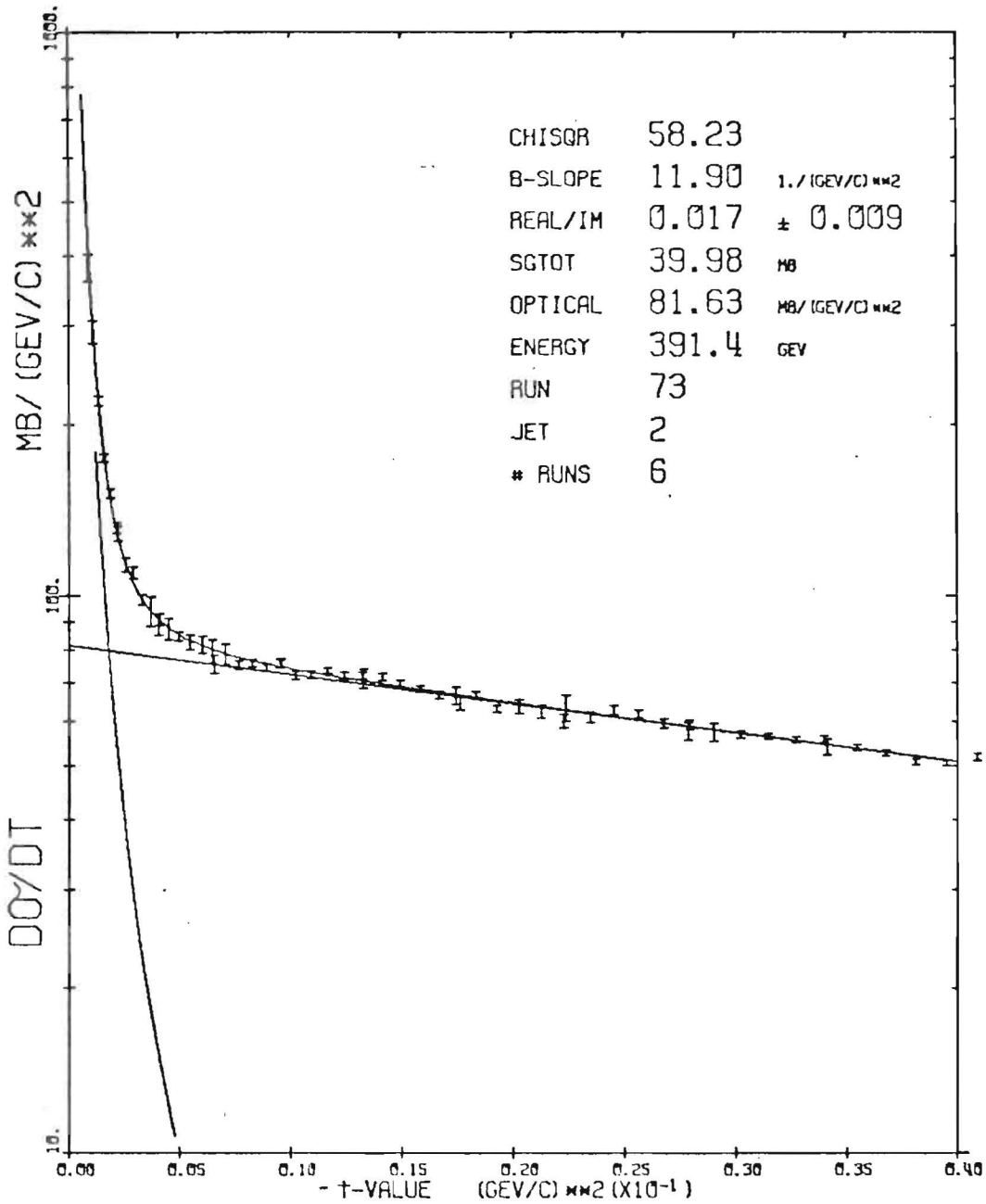

Figure 4.13b The same as Fig. 4.13a, but different incident energy (60 points).

values the background extraction procedure begins to fail (mainly because the histogram is cut off by a discriminator). In Fig. 4.14 are shown all data at all energies, simultaneously. In this particular figure the Coulomb contribution to the differential cross section has been removed (i.e.f_c^2), in order to emphasize the behavior of the interference term (the part that deviates from a straight-line nuclear cross section) with energy. Note the clear and gradual change of the interference term from constructive to destructive interference (positive to negative). (Results similar to the "fixed t" analysis of the last chapter are shown in Figs. 4.15 and 4.16. These results were obtained for purposes of testing the quality of the data.)

4.4 Results and t-Cuts

The stability of the values of $\rho(s)$ obtained was checked by forming various t-cuts at low $|t|$, and cuts on detectors 9 and 10 at high $|t|$. The most reasonable cut we find is $|t| \geq .0011\ (\mathrm{GeV}/c)^2$, with all detectors included (see Fig. 4.17).

In the process of extracting the number of events from histograms, we fit the elastic peak to approximate the peak shape. The number of events taken, was the integral of the function fitted to the peak, between certain limits. We also counted the corresponding number of events

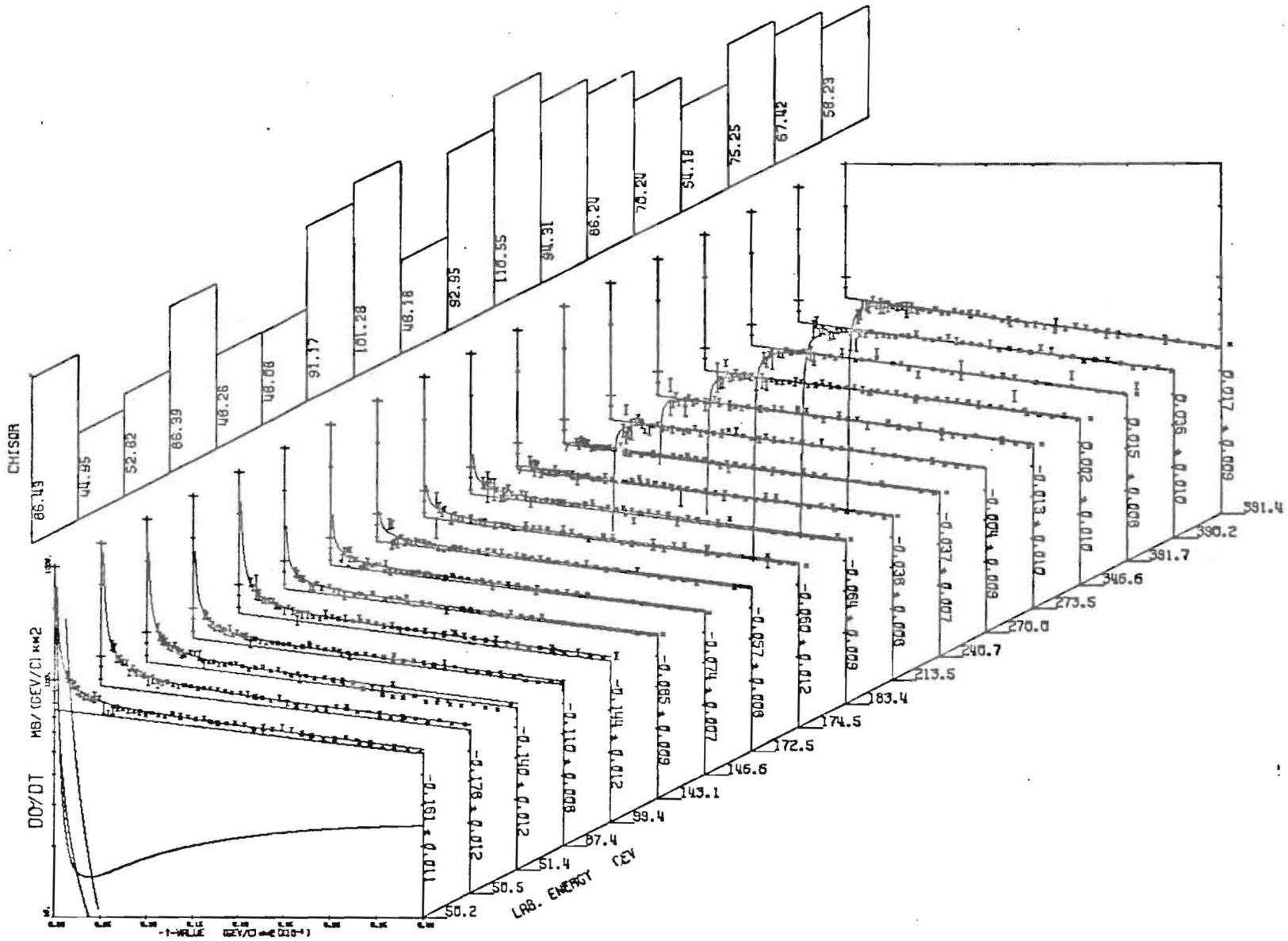

Figure 4.14 Two dimensional plot of the differential cross section (with the (Coulomb amplitude)^2 removed).

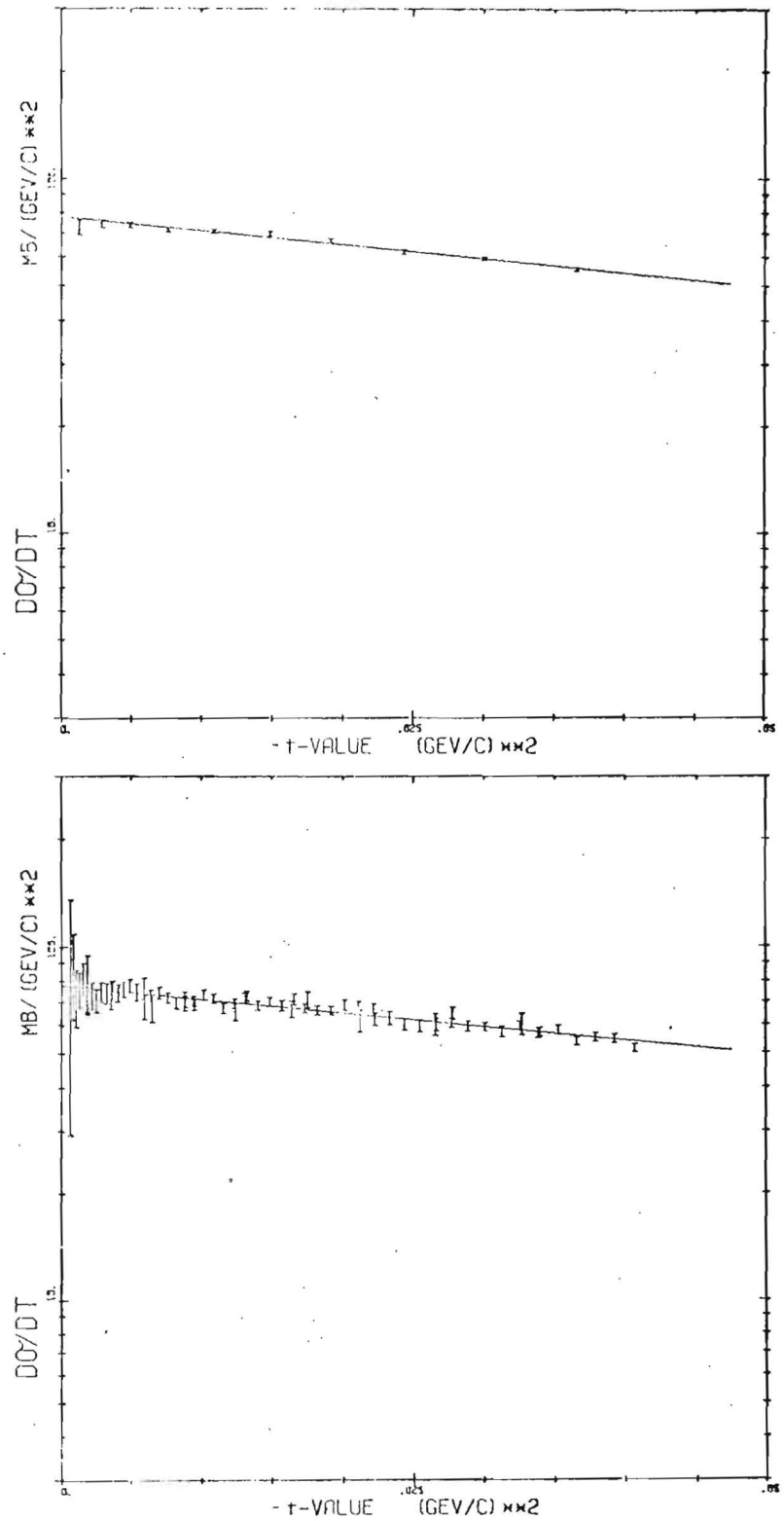

Figure 4.15 See Figure 3.13 for explanatory notes.

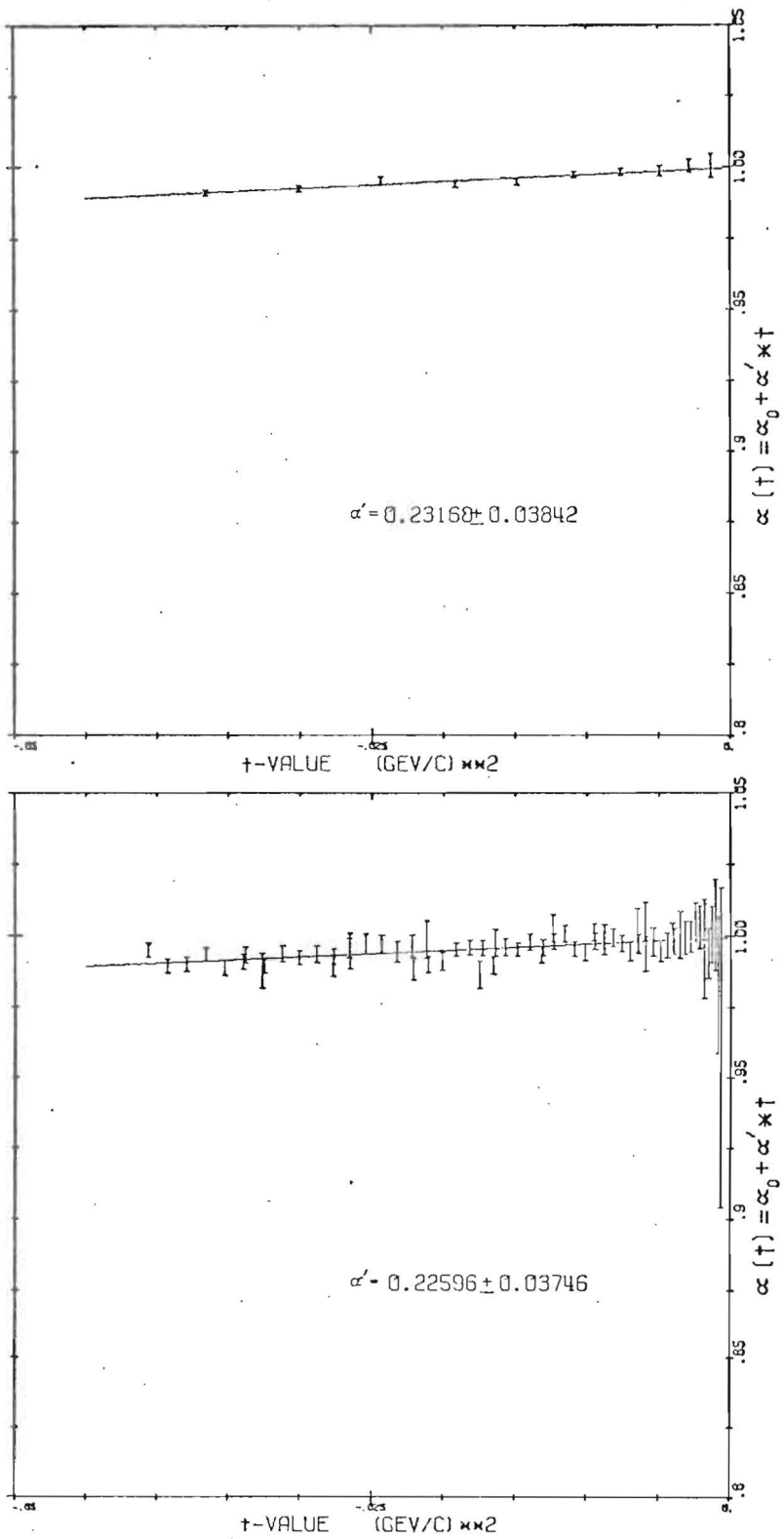

Figure 4.16 See Figure 3.14 for explanatory notes.

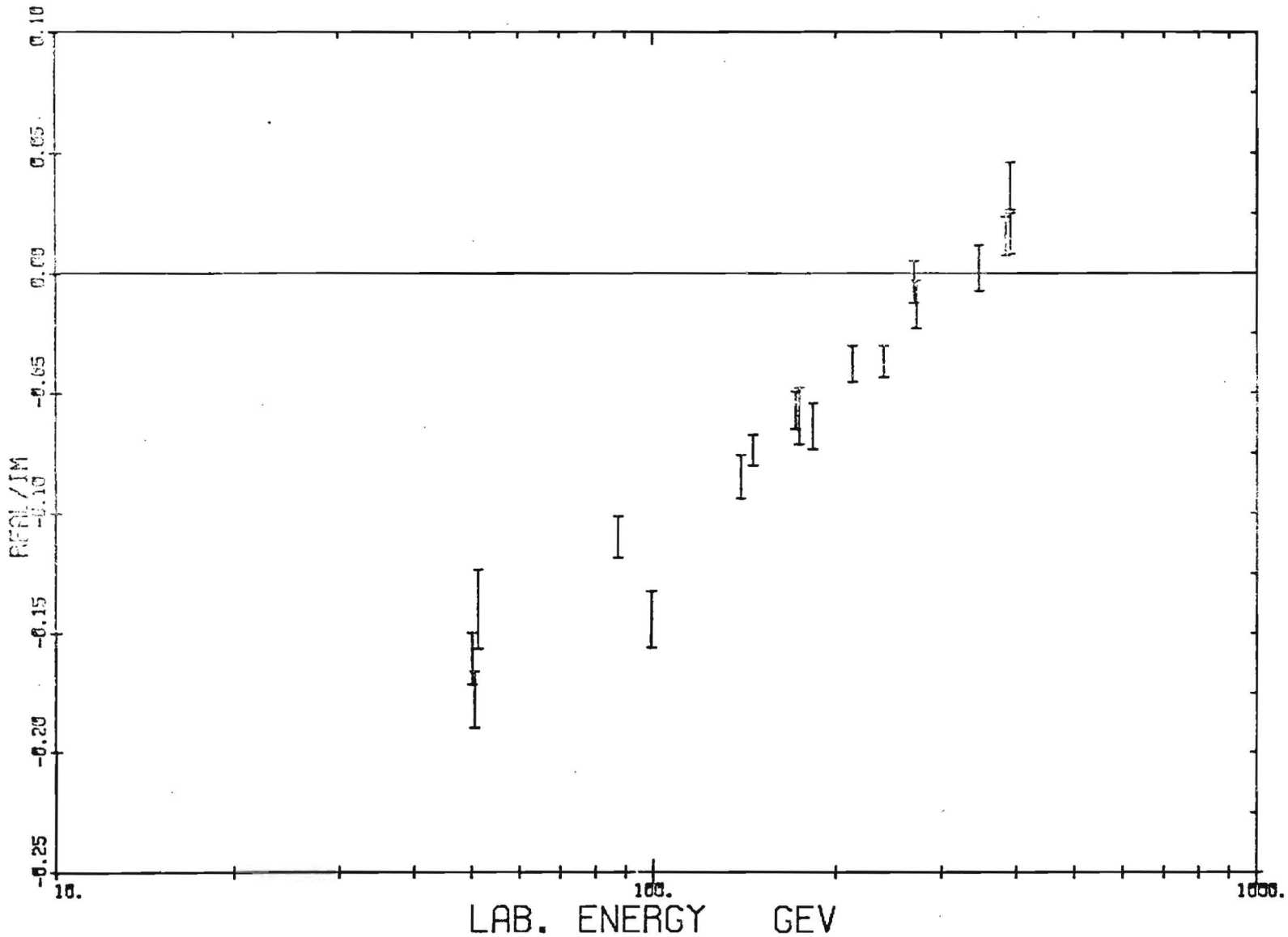

Figure 4.17 Real to imaginary ratio data; observe the crossing of zero at about 300 GeV, as predicted from a rising total cross section.

in the histograms, between the same limits. We have thus two methods of background subtraction. Therefore it is quite legitimate to evaluate the differential cross section with each of the two sets of elastic peak counts. The procedure of background subtraction is most uncertain at very low $|t|$, where some of the histograms still contained background (even after our attempts at removing it), or else the elastic peak did not fully exist in the histogram. This is the reason for a cut at $|t| < .0011$. It is therefore important to compare results of fits for the two different counting methods. We find that simple counting of the histograms consistently gives $\rho(s)$ smaller by about .02, which is about 1.5 standard deviations on ρ. This situation occurs because improper background has been subtracted at low $|t|$, (too little) and we estimate therefore that .02 is the size of our possible systematic error, with a lower limit for our data derived from this simple counting method.

The final value for $\rho(s)$ at various energies are given in Table 4.4. In Table 4.4 we present various gradients of $\rho(s)$. It is important to note that $\partial\rho/\partial\sigma_T$ from the differential cross section is <u>negative</u> ($\partial\rho/\partial\sigma_T<0$). This fact will be used in the next section to strengthen the impact of results on $\rho(s)$.

	ENERGY	S	RHO= REAL/IM	STATISTICAL DRHO	B	SGTOT	DRHO/DB	DRHO/Dσ	DRHO/Dθ	DRHO	MAGNETIC FIELD CORRECTION *
1	50.2	96.0	-0.161	0.011	10.77	38.43	0.058	-0.030	-0.038	0.016	-0.002
2	50.5	96.5	-0.178	0.012	10.77	38.43	0.062	-0.033	-0.045	0.018	-0.002
3	51.4	98.2	-0.140	0.012	10.78	38.42	0.042	-0.035	-0.066	0.019	-0.002
4	87.4	165.8	-0.110	0.008	11.07	38.45	0.043	-0.030	-0.038	0.013	-0.003
5	99.4	188.3	-0.144	0.012	11.14	38.49	0.050	-0.031	-0.045	0.017	-0.003
6	143.1	270.3	-0.085	0.009	11.34	38.71	0.045	-0.029	-0.045	0.015	-0.005
7	146.6	276.9	-0.074	0.007	11.36	38.73	0.039	-0.027	-0.034	0.011	-0.004
8	172.5	325.5	-0.057	0.008	11.45	38.87	0.035	-0.025	-0.049	0.014	-0.012
9	174.5	329.2	-0.060	0.012	11.45	38.88	0.047	-0.026	-0.040	0.016	-0.006
10	183.4	345.9	-0.064	0.009	11.48	38.93	0.041	-0.025	-0.032	0.013	-0.005
11	213.5	402.4	-0.038	0.008	11.56	39.10	0.039	-0.024	-0.033	0.012	-0.005
12	240.7	453.4	-0.037	0.007	11.63	39.24	0.038	-0.024	-0.029	0.010	-0.006
13	270.0	508.4	-0.004	0.009	11.69	39.40	-0.000	-0.021	-0.051	0.013	-0.018
14	273.5	515.0	-0.013	0.010	11.70	39.42	0.038	-0.025	-0.039	0.014	-0.009
15	346.6	652.2	0.002	0.010	11.83	39.78	0.042	-0.019	-0.022	0.012	-0.014
16	390.2	734.0	0.036	0.010	11.90	39.98	0.037	-0.019	-0.035	0.013	-0.028
17	391.4	736.2	0.016	0.009	11.90	39.98	0.037	-0.023	-0.034	0.012	-0.012
18	391.7	736.8	0.015	0.008	11.90	39.98	0.040	-0.022	-0.035	0.012	-0.011

Table 4.4 Final data on the real to imaginary ratio and the dependence on the values assumed for b, σ_T and θ.

*The last column indicates a possible maximum shift in the data, if the accelerator fringe field is used. However, the actual shift is much less, corresponding to much smaller fields than indicated in Figure 4.12 (which was measured outside the ion guide).

4.5 A Dispersion Relation Calculation

In the interest of knowing the probable behavior of the total cross section at energies higher than current accelerators can produce, we have made a dispersion relation calculation (modeled by the one of Bartel and Diddens[7]) to compare the values predicted by it with our data.

The basic properties of the scattering amplitude assumed are: analyticity, unitarity and crossing symmetry. Given these properties and using the Cauchy relation

$$\mathrm{Re}\ f(q) = \frac{1}{2\pi} \oint \frac{\mathrm{Im}\ f(q')}{q' - q}\, dq' \ , \tag{15}$$

one can produce a singly subtracted forward dispersion relation for the real part of the scattering amplitude. Neglecting the proton mass (m), compared to the energies ($E > 50$ GeV) that interest us, we have

$$\mathrm{Re}A(E) = \text{constant} + \frac{m}{8\pi^2} E \int_m^\infty dE' \left[\frac{\sigma_T(E')}{E' - E} - \frac{\bar{\sigma}_T(E')}{E' + E}\right] \tag{16}$$

where σ_T and $\bar{\sigma}_T$ are total cross sections for pp and $\bar{p}p$, respectively. In the process of the calculation, we have used the optical theorem which states that

$$\mathrm{Im}\ A(E) = \frac{pm}{8\pi}\, \sigma_T(E) \ . \tag{17}$$

We have evaluated the integral at energies from 25 to 10^6 GeV by numerical integration (Gaussian), using various parametrizations of σ_T and $\bar{\sigma}_T$ to estimate the high energy behavior of the total cross section.[8] First, we reintegrated the fitted cross sections given by Bartel and Diddens with (their parametrization)

$$\sigma_T^{\pm} = \sigma_1 E^{-\alpha_1} \mp \sigma_2 E^{-\alpha_2} + \sigma_o[1 + C \ln^2(E/m)] \qquad (18)$$

where

$\sigma_1 = 42.67 \pm 56$ mb $\qquad \alpha_1 = .450 \pm .009$

$\sigma_2 = 27.80 \pm 1.21$ mb $\qquad \alpha_2 = .602 \pm .014$

$\sigma_o = 30.60 \pm .22$ mb $\qquad C = .00654 \pm .00012$

The + and - signs in Eq. (18) refer to σ_T and $\bar{\sigma}_T$, respectively. Then we used a slightly different parametrization of the total cross section[6] but kept the same difference $\bar{\sigma}_T - \sigma_T$ as used in Eq. (18). Both parametrizations assume saturation of the Froissart bound at high energy, however with different coefficients in front of the $\ln^2 s$ terms. We also used parametrizations (as initially used by Bartel and Diddens), in which we assume the behavior of the total cross sections as given in Eq. (18) up to a certain energy; from there on we assume a flat cross section to infinity

(this is a non-smooth function for the σ_T and $\bar{\sigma}_T$, but it is a close enough approximation for some models which predict cross sections that flatten out eventually). The rising shape of the cross sections in different parametrizations is shown in Fig. 4.18.

Once numerical integration was completed, we evaluated the subtraction constant in Eq.(16). This constant is due to residues given by poles and the contribution of the integral in the complicated region around $|E| \lesssim m$. To find the constant, we forced agreement between our data for the real part and the integration values (effectively a one parameter fit). The results of the dispersion relation calculation are presented in Fig. 4.19.

We are now reminded that $\frac{\partial \rho(s)}{\partial \sigma_T(s)}$ is negative in the fit of the differential cross section. But from a dispersion relation point of view, the derivative is positive; we may therefore safely assume that since $\rho(s)$ crosses zero at about 300 GeV, the calculation suggests strongly a rising cross section, at least to a few thousand GeV. That is, the dispersion relations indicate what happens to $\rho(s)$ when the total cross section rises. But if we chose not to believe the rise in σ_T and used, for example, a flat total cross section input into the differential cross section fit (say σ_T = 38.4 mb), then from our data alone, we should get an even higher $\rho(s)$, which would be in total disagreement with numerical results of dispersion relations.

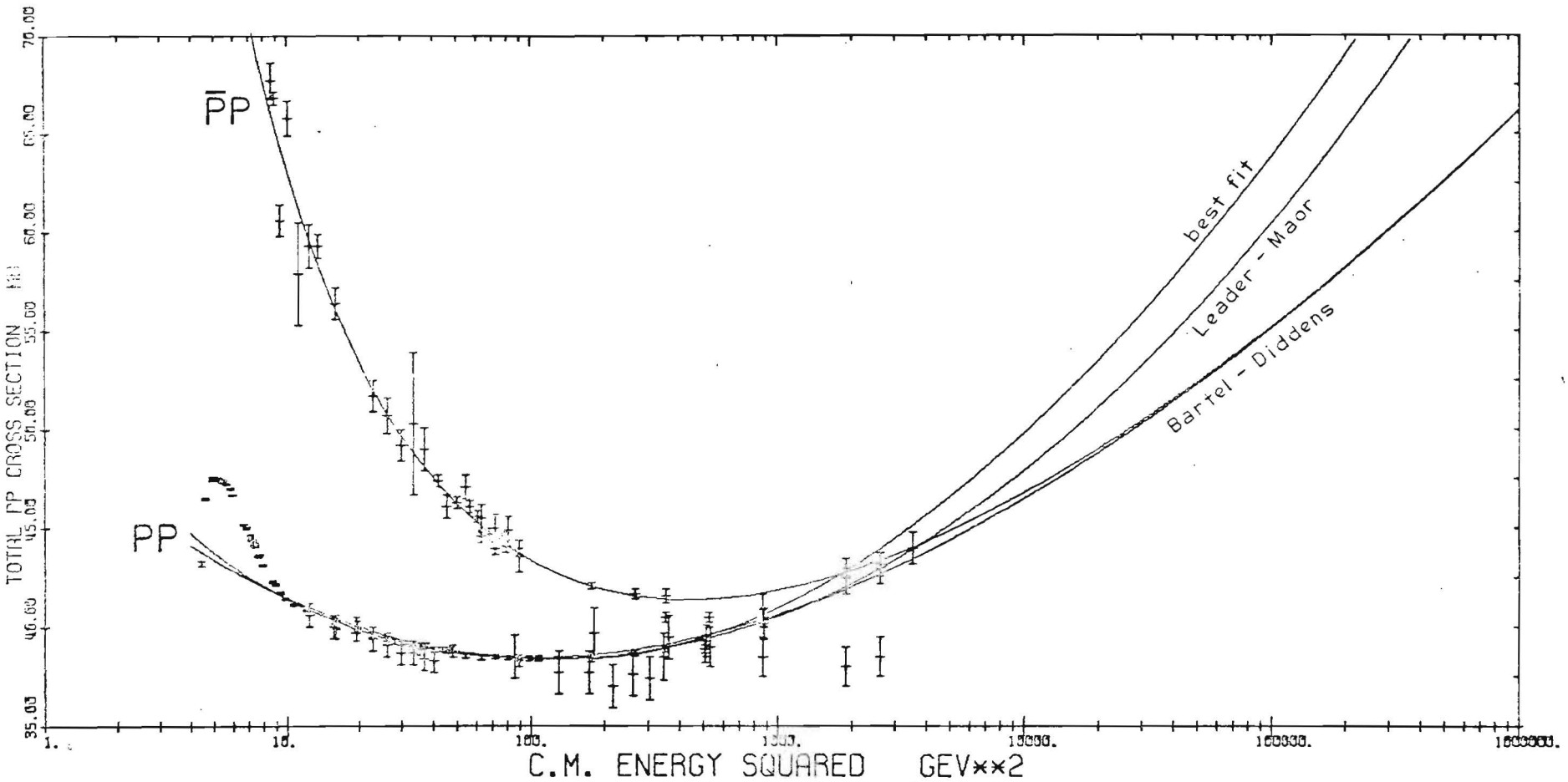

Figure 4.18 Parametrizations of world data on the total cross sections for proton and anti-proton scattering off protons. We used these parametrizations in our dispersion relation calculations.

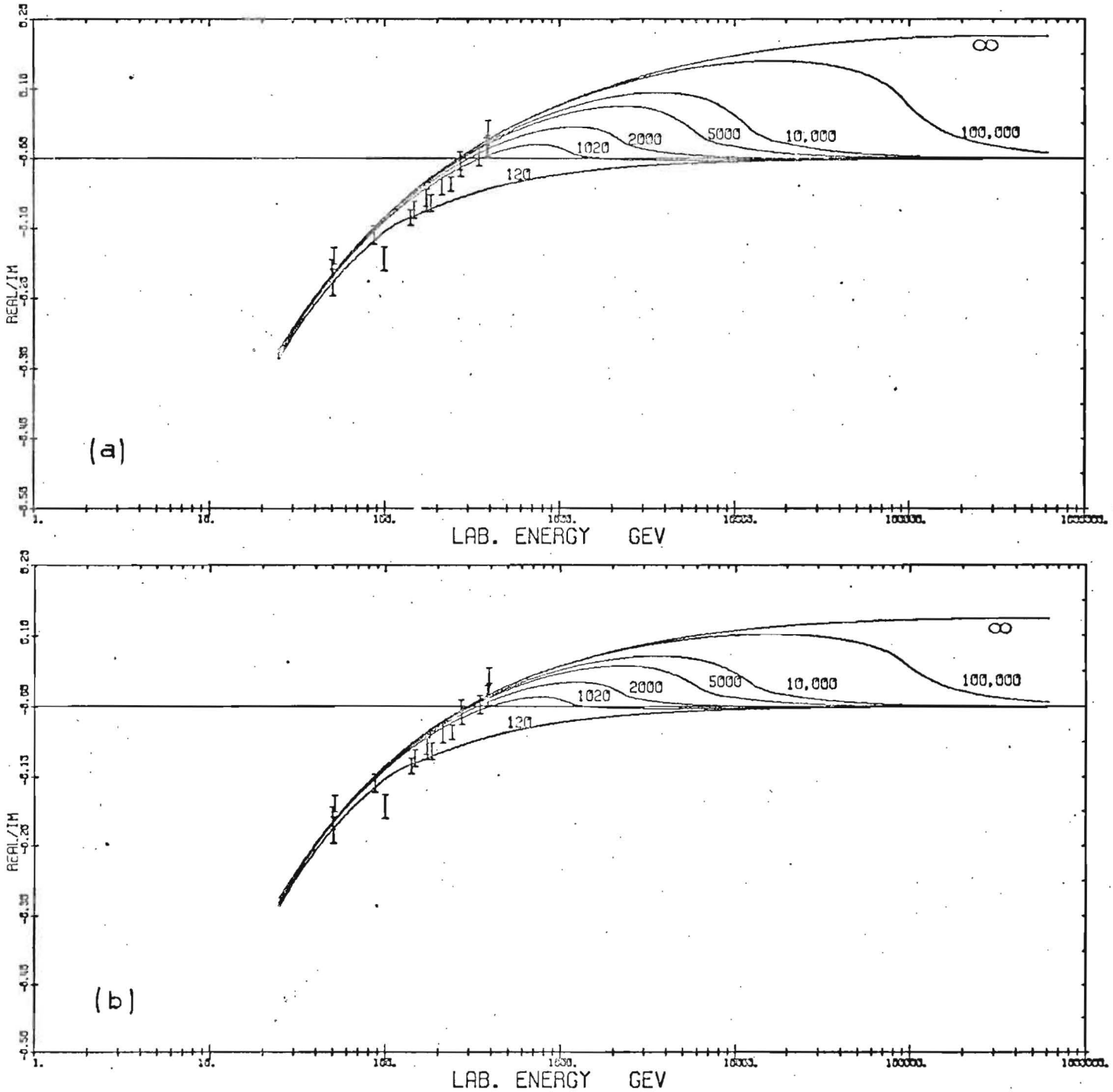

Figure 4.19 (a) Results of dispersion relation (for pp) calculations using the total cross section parametrization of Leader and Maor; (b) parametrization of Bartel and Diddens. (loc. ref.) The number labels on the various curves indicate the energy (in GeV) where the total cross section is assumed to stop rising.

References for Chapter IV

1. H. Cheng, J.K. Walker and T. T. Wu, preprint submitted to the XVI Intern. Conf. on High-Energy Physics, Chicago 1972; this model proposes an indefinitely rising total cross section. V. Barger and R. J. N. Phillips, Phys. Rev. Lett. 24, (1969) 291; this model proposes a rising total cross section to some asymptotic limit by use of Regge cuts.
2. H. A. Bethe, Ann. Phys. (N.Y.) 3, (1958) 190; G. B. West and D. R. Yennie, Phys. Rev. 172, (1968) 1413.
3. D. A. Gross and A. Melissinos, University of Rochester UR-875-365; (see Appendix IV therein).
4. R. M. Edelstein et al., Phys. Rev. D5, (1972) 1073; J. V. Allaby et al., Nucl. Phys. B52 (1973) 316; our Table 4.1 is taken from Table V of Allaby et al.
5. See ref. 7 of Chapter III.
6. E. Leader and U. Maor, Phys. Lett. 43B, (1973) 505.
7. W. Bartel and A. N. Diddens, CERN, NP Internal Report 73-4 (1973); a calculation similar to the one made by Bartel and Diddens, was made by Kroll: P. Kroll, Institut für Theoretische Kernphysik der Universität Karlsruhe preprint, TKP 6/73; other relevant articles are: P. Söding, Phys. Lett. 8, (1964) 285; M. L. Goldberger, Y. Nambu and R.Oehme, Ann. Phys. (N.Y.) 2 (1957) 226; I. I. Levintov, Phys. Lett. 7, (1963) 41; I. I. Levintov and G. M. Adelson-Velsky, Phys. Lett. 13, (1964) 185; C. Bourrely and J. Fischer, CERN TH.1652 (1973).

8. Reference 6, Leader and Maor; ref. 7, Bartel and Diddens; a fit reported by U. Amaldi et al., preprint, January 1973 [$\sigma = 38.4 + .9\ (\ell n[s/s_o])^{1.8}$]; throughout we have kept the difference $\bar{\sigma} - \sigma$ equal to that of Bartel and Diddens.

CHAPTER V

CONCLUSIONS

In this concluding chapter we are concerned with applying the data to various models for elastic scattering. The postulates of Quantum Field Theory are checked by means of comparison of the data with the bounds implied by the theory. Finally, since we have available data at very high energies, some of the predicted asymptotic behaviors of quantities of physical interest, are enumerated in a succinct form; this is done in order to distinguish between the available models and offer an indication of what particular aspects of high energy phenomena to check in the future.

5.1 Spin Effects in Proton-Proton Forward Elastic Scattering

The analysis undertaken in the last two chapters assumes that spin effects are negligible in small angle proton-proton elastic scattering. The nuclear elastic scattering amplitude is mainly imaginary. The real part of the forward amplitude is, however, quite small and

therefore to evaluate it we must be sure that no large effects will be felt due to the, presumably also small, spin-dependent part of the amplitude. Analysis of a considerable amount of experimental data was performed by Bourrely, Soffer and Wray[1] to obtain the magnitude of the spin-dependent term in the scattering amplitude.

Bourrely et al. parametrize the nuclear scattering amplitude with three* out of the usual five amplitudes. These two missing nuclear amplitudes are eliminated through angular momentum conservation and in effect the magnitude of the spin-dependent term is contained in the second term of

$$\frac{d\sigma^N}{dt} = \frac{\sigma_T^2}{16\pi} \quad (1 + \rho^2)\{e^{b_1 t} + \beta^2 \; e^{b_2 t}\},$$

where

$$\frac{d\sigma}{dt} = \frac{d\sigma^N}{dt} + \frac{d\sigma^C}{dt} + \frac{d\sigma^{intf}}{dt}$$

and N, C and intf stand for nuclear, Coulomb and interference. A full parametrization of the Coulomb amplitude is the, quite complicated, full expression given in ref. 1. Finally, using the spin-independent part of the Coulomb scattering amplitude a^C, we have

---

* Triplet, singlet and spin flip amplitudes.

$$\frac{d\sigma^{intf}}{dt} = \frac{\sigma_T a^C}{2k} [\rho \cos \delta + \sin \delta] e^{b_1 t/2}$$

where

$$\delta = \frac{\alpha(s - 2m^2)}{\sqrt{s(s - 4m^2)}} \ \ell n \frac{-1.12}{a^2 t}$$

using k as c.m. momentum and a = 1 fermi. The expression for δ is the Bethe phase factor.

Data spanning the energy range 8 to 500 GeV is used in the fits (from Dubna, P.S., Serpukhov, N.A.L. and I.S.R.). In most cases the authors did not fit for σ_T and b (which was taken to be $b = b_1 = b_2$ for the calculation), but fixed both these quantities at the appropriate values. They then proceeded to find ρ and β. Two iterated fits were done, one in which β was fixed at zero value and one which allowed it to float. The two fits were in very good agreement for the value of ρ at all energies and gave an average contribution of β = 11% spin-dependent part in the scattering amplitude, or roughly 1% in the differential cross section. Figure 5.1 gives their results on the spin parameter β (where our data are shown as solid triangles). The scatter of points in the graph is rather large, but in general the effect is small. It is therefore safe according to these authors to proceed with a spin-independent analysis even at the smallest $|t|$ values, where data currently exists.

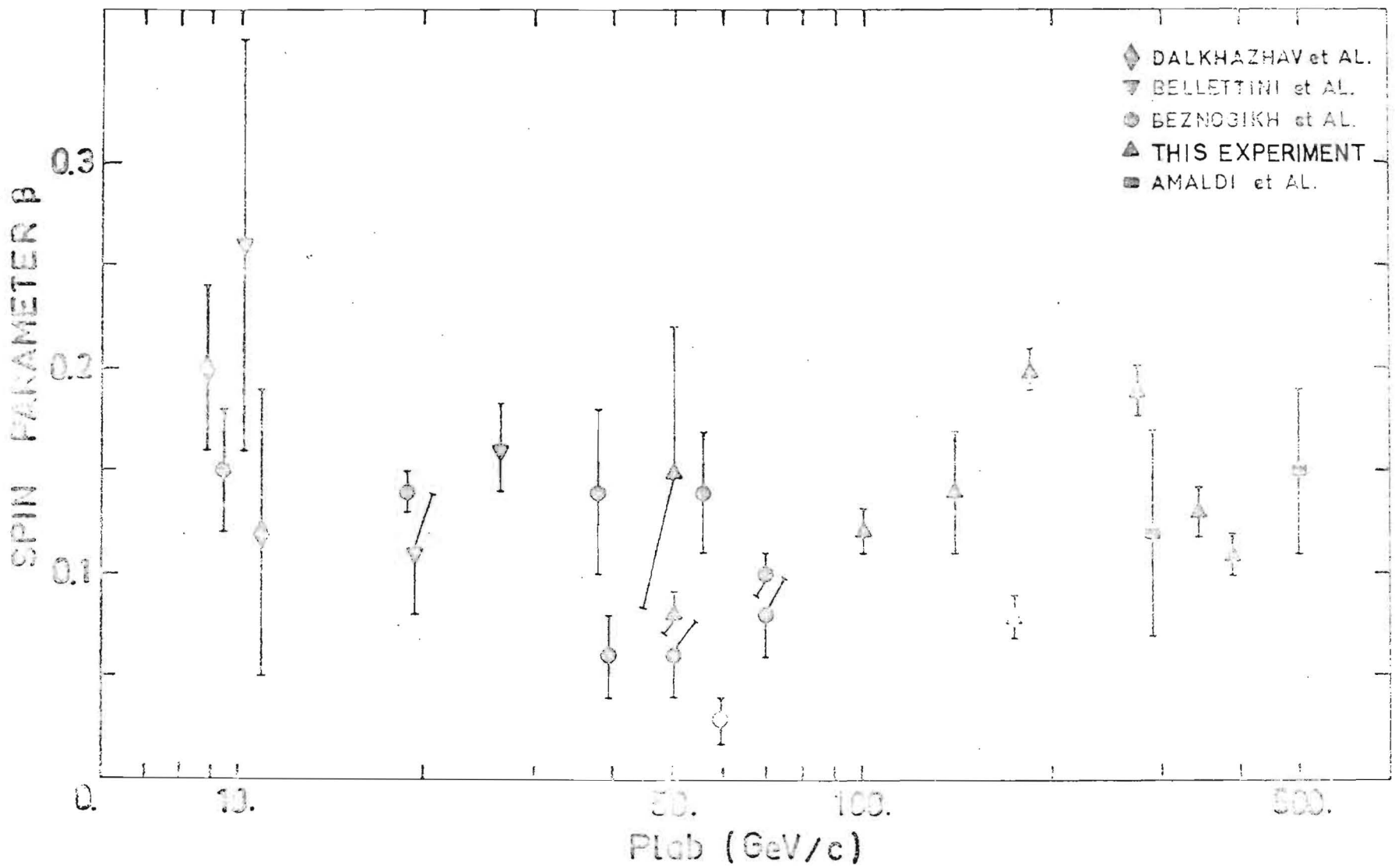

Figure 5.1 Ratio of the spin-dependent to the spin-independent amplitude, in the forward direction; figure taken from ref. 1.

5.2 Various Models for the Slope Parameter b

We now mention some theoretical models for the energy dependence of the slope parameter b. The model of Krisch[2] is based on a geometrical picture of a Lorentz contracted spherical proton. Krisch represents the proton "interaction probability density", ρ_{int}, as $\rho_{int} = B\, e^{-\frac{1}{2}[(R_\perp/A)^2 + (\gamma R_{11}/A)^2]}$, where the transverse and longitudinal directions are separately indicated. The spherical distribution of the proton, in its own frame, is Gaussian. The usual procedure of Fourier transforming an impact parameter amplitude (which is proportional to ρ_{int}) produces the elastic cross section in momentum transfer space,

$$\frac{d\sigma}{dt} = \left.\frac{d\sigma}{dt}\right|_o e^{-A^2[p_\perp^2 + p_{11}^2/\gamma^2]}$$

and if this cross section is represented in terms of $p_\perp^2$ only*,

$$\frac{d\sigma}{dt} = \left.\frac{d\sigma}{dt}\right|_o e^{-A^2\beta^2 p_\perp^2 - A^2M^2}$$

This equation is identified with $\frac{d\sigma}{dt} = \left.\frac{d\sigma}{dt}\right|_o e^{-b|t|}$ and we obtain the energy dependence of b in this model,

$$b = A^2\beta^2 \equiv A^2(1 - \frac{1}{\gamma^2})$$

---

*The factor $e^{-A^2M^2}$ (where M is the proton mass) can be absorbed in $\left.\frac{d\sigma}{dt}\right|_o$.

where β is the center of mass velocity of the protons.

Two distinct regions of momentum transfer must be considered[3]: one $|t| \lesssim .15$ and the other $|t| \gtrsim .15$. The location of the "break" in the differential cross section forces this issue. The data are shown in Fig. 5.2, where the two regions of t are fit by different b(s):

$$b(s) = 11.61\ \beta^2 \qquad t \gtrsim .1$$

$$b(s) = 11.13\ \beta^2 \qquad t \lesssim .1\ ^*$$

Our data are shown by the crosses and while they qualitatively agree with the curve for small $|t|$, a quantitative fit fails.

It is important to note that this simple geometrical picture can fit all data over a large range of energies. Part of the discrepancy between the fit and the data may be due to systematic errors arising from the combination of data from several different experiments. The most critical test of this model lies in the high energy region where the model predicts a flat b. Present indications tend to show that the model fails in this respect.

Following the line of a group-theoretical approach, Leader and Pennington[4] have obtained, from the symmetry properties of the scattering amplitude, an expression for the amplitude itself. The analysis applies to any

*Based on all data used; see ref. 24.

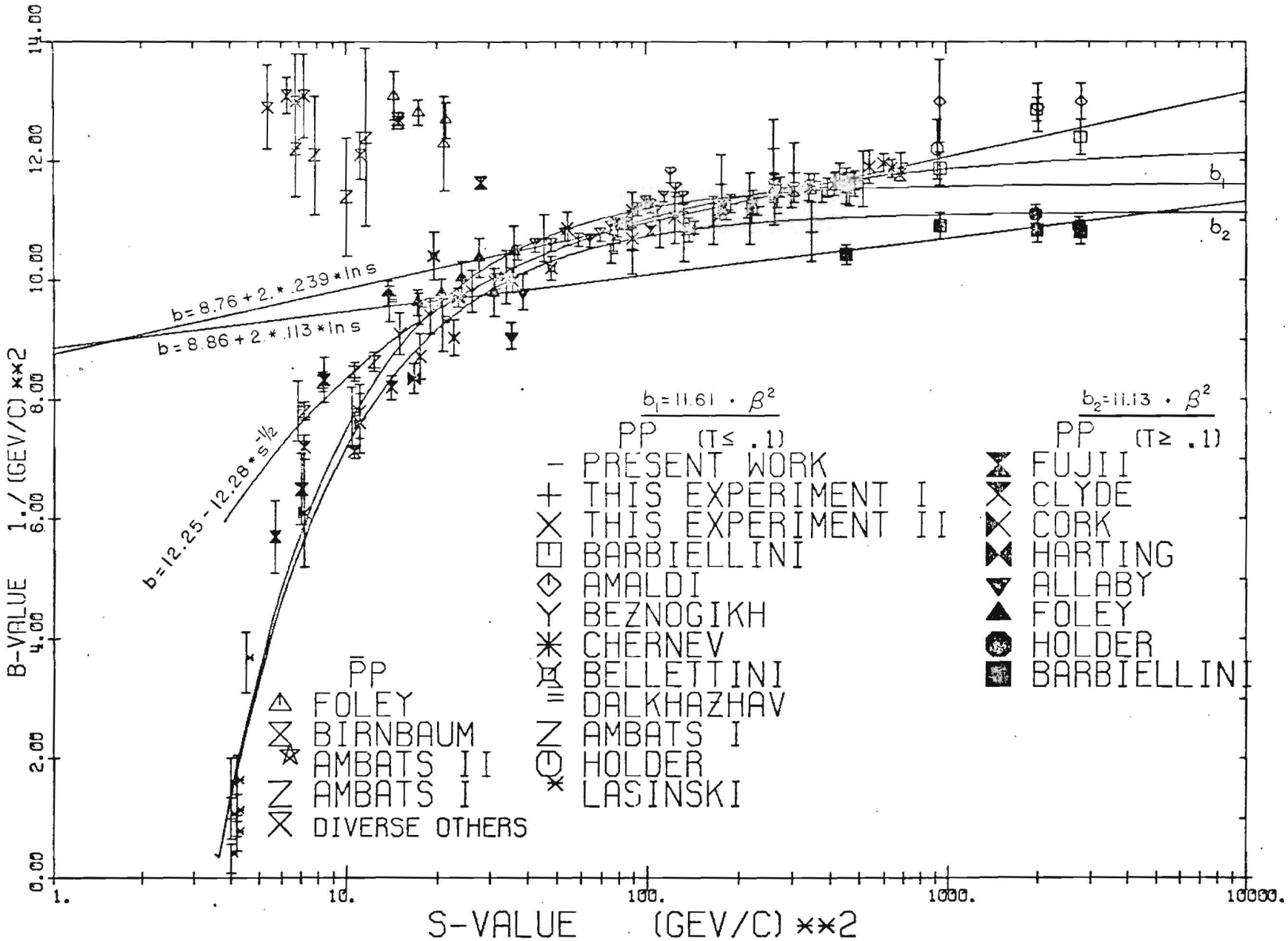

Figure 5.2 Various models for fitting the energy dependence of the slope parameter. (In the case of Regge pole fits only data above ~10 GeV has been used.) There are three sets of data from our experiment. The most recent is indicated by II, while the data analyzed in this thesis is listed under PRESENT WORK.

interacting particles and the resulting differential cross section depends essentially only on the masses involved and on the parametrization of the diffractive peak slope. This is given by

$$\frac{d\sigma}{dt} = \left.\frac{d\sigma}{dt}\right|_o e^{b(s)t}$$

where

$$b(s) = \beta_o[1 - \frac{2(M^2 + m^2)}{s} + \frac{(M^2 - m^2)^2}{s^2}]$$

for the reaction $m + M \rightarrow m + M$. In the case of the proton-proton interaction $b(s) \rightarrow \beta_o[1 - \frac{4m^2}{s}]$ (see Fig. 5.2). A fit to the data yields $\beta_o \sim 11.5\ (\mathrm{GeV/c})^{-2}$ and a good qualitative fit of data at all energies. This approach misses badly in the case of πp and $\bar{p}p$ scattering, which do not show shrinkage. Note that this model is in agreement with the simple geometrical interpretation of the hadronic interactions (Krisch).

Barshay and Chao[5] represent distributions in the transverse momenta of final particles as proportional to $e^{-\lambda(m^2 + p_\perp^2)^{1/2}}$ where $p_\perp$ is the transverse momentum (they call $\sqrt{m^2 + p_\perp^2}$ the "longitudinal mass"). In seeking a covariant representation of the longitudinal mass, they used Leader and Pennington's analysis and found that

$$\frac{d\sigma}{dt} = \left.\frac{d\sigma}{dt}\right|_o e^{bm} e^{-b(m^2 + n^2)^{1/2}} \tag{1}$$

where

$$n^2 = \frac{tu}{s} = -t\left(1 + \frac{t}{s - 4m^2}\right)\left(1 - \frac{4m^2}{s}\right) = p_\perp^2\left(1 - \frac{4m^2}{s}\right) .$$

Thus for small $|t|$ values they get,

$$\frac{d\sigma}{dt} = \left.\frac{d\sigma}{dt}\right|_o e^{-bn^2/2m} = \left.\frac{d\sigma}{dt}\right|_o e^{-b/2m\left(1 - \frac{4m^2}{s}\right)p_\perp^2}$$

The approximate slope parameter $b(s) = \frac{b}{2m}\left(1 - \frac{4m^2}{s}\right)$ gives again a fairly good fit for all pp slope data, but only qualitatively.

None of the above three models incorporates a rising total cross section. However, the Barshay and Chao Eq. (1) integrated over $p_\perp$ yields,

$$\sigma_{e\ell} \simeq \frac{\sigma_T^2}{16\pi} e^{bm} \int_o^\infty e^{-b(m^2 + p_\perp^2)^{1/2}} dp_\perp^2$$

$$= \sigma_T^2(1 + bm)/8\pi b^2$$

This is a relation for σ_T in terms of $\sigma_{e\ell}$ and b. Using extrapolated values of $\sigma_{e\ell}$ and b at 500 GeV, their

expression gives the observed ISR cross section.

5.3 Chou-Wu-Yang Hypotheses

Wu and Yang[6] have speculated on the possibility that the hadron-hadron differential cross sections have certain symmetries as $s \to \infty$. They argued that the exponential damping of the elastic differential cross section as $e^{-p_\perp/.15}$ (at large $p_\perp$) is a very strong dependence and is probably due to the difficulty in emitting the nucleon coherently at large angle, due to the possibility of break up. This property should be true for all hadrons and Wu and Yang proceeded to predict that whether the interaction is $NN \to NN$ or $NN \to \pi D$ or $\pi N \to \pi N$ where N, D and π stand for nucleon, deuteron and pion, respectively, the differential cross sections for these reactions approach common limits as $s \to \infty$ (regardless of whether N is a p or an n). In the same spirit they found that the ep interaction amplitude should be proportional to the square root of the pp interaction amplitude, because the electron (point particle) cannot break up, but can easily absorb large momentum transfers in the reaction. They therefore suggested that

$$\frac{d\sigma(pp \to pp)}{dt} = \text{constant} \cdot G^4(q^2) \qquad (2)$$

where $G(q^2)$ is the electromagnetic form factor of the proton, as obtained in ep collisions.

Chou and Yang[7] later identified the charge distribution (form factor) of the proton with the hadronic matter in the proton. Using the assumption that differential cross sections tend to a finite limit as $s \to \infty$, Chou and Yang proceed to find a model in which such an asymptotic description exists.

In the eikonal formalism with spin-independent amplitudes normalized by $\frac{d\sigma}{dt} = \pi\ |a|^2$ where

$$a = \lambda\!\!\!^{-2} \sum_{\ell} (2\ell + 1) P_{\ell}(\cos\theta) \frac{1}{2}(1 - S)$$

is the partial wave expansion of the amplitude, we can get at large energies, $P_{\ell}(\cos\theta) \to J_o(b\sqrt{-t})$ where b is the impact parameter, $b = \lambda\!\!\!^{-}(\ell + \frac{1}{2})$. If an asymptotic limit exists for the differential cross section, then $S = S(b)$ is only a function of impact parameter (and S is the S-matrix). For large numbers of partial waves the summation becomes an integral,

$$\begin{aligned} a(t) &\to \int_0^{\infty} [1 - S(b)]\ J_o(b\sqrt{-t})\, b\,db \\ &\equiv \frac{1}{2\pi} \int_0^{\infty} [1 - S(b)] \int_0^{2\pi} e^{ib\sqrt{-t}\cos\phi}\, d\phi\, b\,db \\ &= \frac{1}{2\pi} \iint [1 - S(b)] e^{i\underline{q}\cdot\underline{b}} d^2b\ , \end{aligned} \tag{3}$$

where $q^2 \equiv -t$.

This last expression is simply a Fourier transform. Then Chou and Yang obtained the properties of the Fourier transform which they equated with a multiple scattering expansion of the form found in Glauber theory.

An inverse Fourier transform of Eq. (3) is used to describe the distribution of hadronic matter in the proton. This is found to be close to Gaussian. One can also get the exact nature of the proton form factor by calculations involving the whole series of multiple scattering terms if one assumes the validity of Eq. (2).

However, the form of Eq. (2) does not provide for any diffraction pattern, namely zeros in the differential cross section. Durand and Lipes[8], have used an impact parameter S-matrix for elastic scattering. An interaction density, based on the hadronic matter distribution (assumed the electromagnetic form factor) is formed. The Born approximation in the eikonal expansion of the amplitude used to evaluate the differential cross section is just that of Eq. (2), but a more exact treatment yields the necessary zeros in $d\sigma/dt$. The result is an asymptotic differential cross section which fits the data reasonably well (see Fig. 5.3).

The diffraction minimum recently observed at the ISR (see Fig. 5.4) in the pp collision, is analogous to

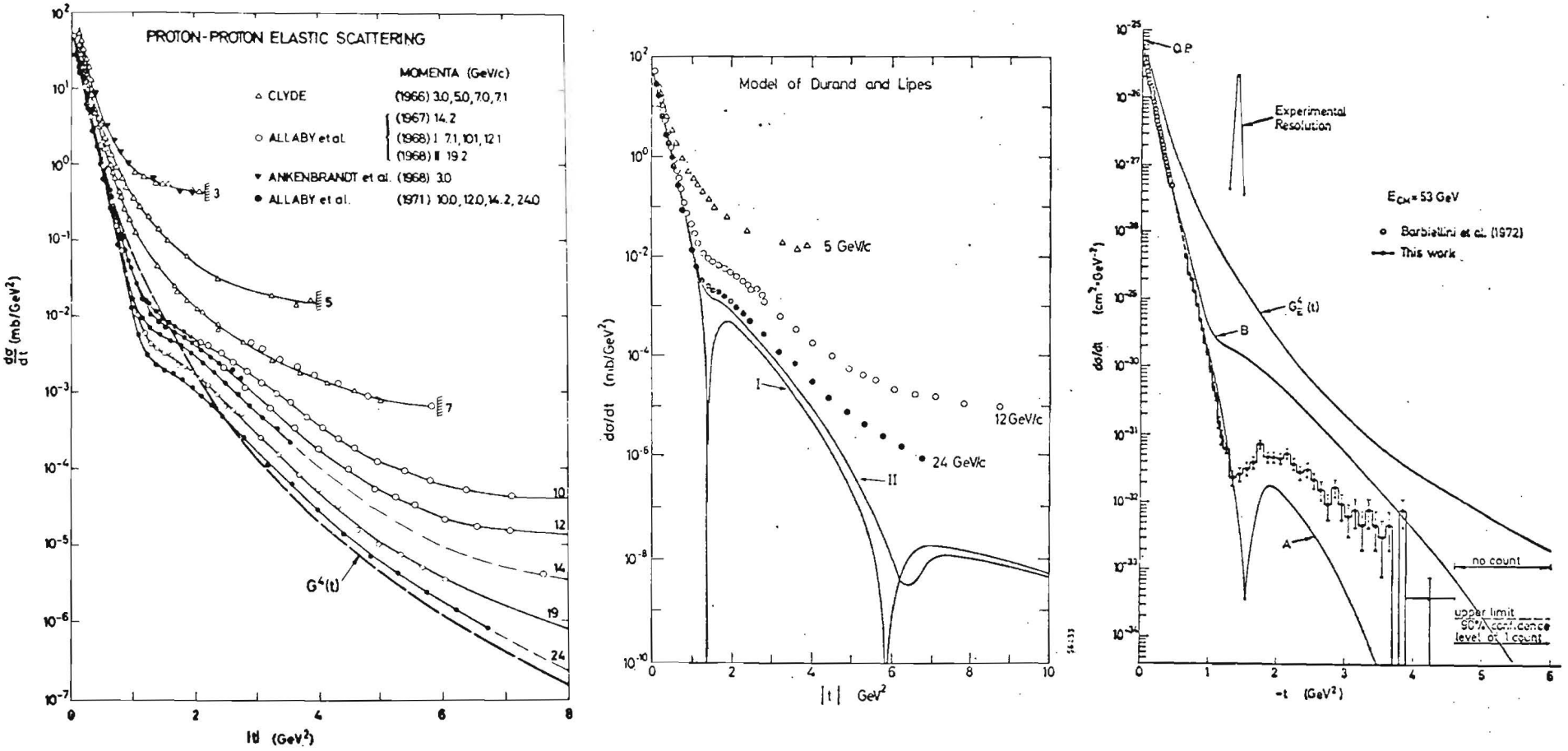

a) b) c)

Figure 5.3 (a) The Chou-Yang fit of the differential cross section by the fourth power of the form factor; (b) and (c), the Durand-Lipes fit of ISR data (c), and the effects of different real parts (b); figures taken from ref. 8.

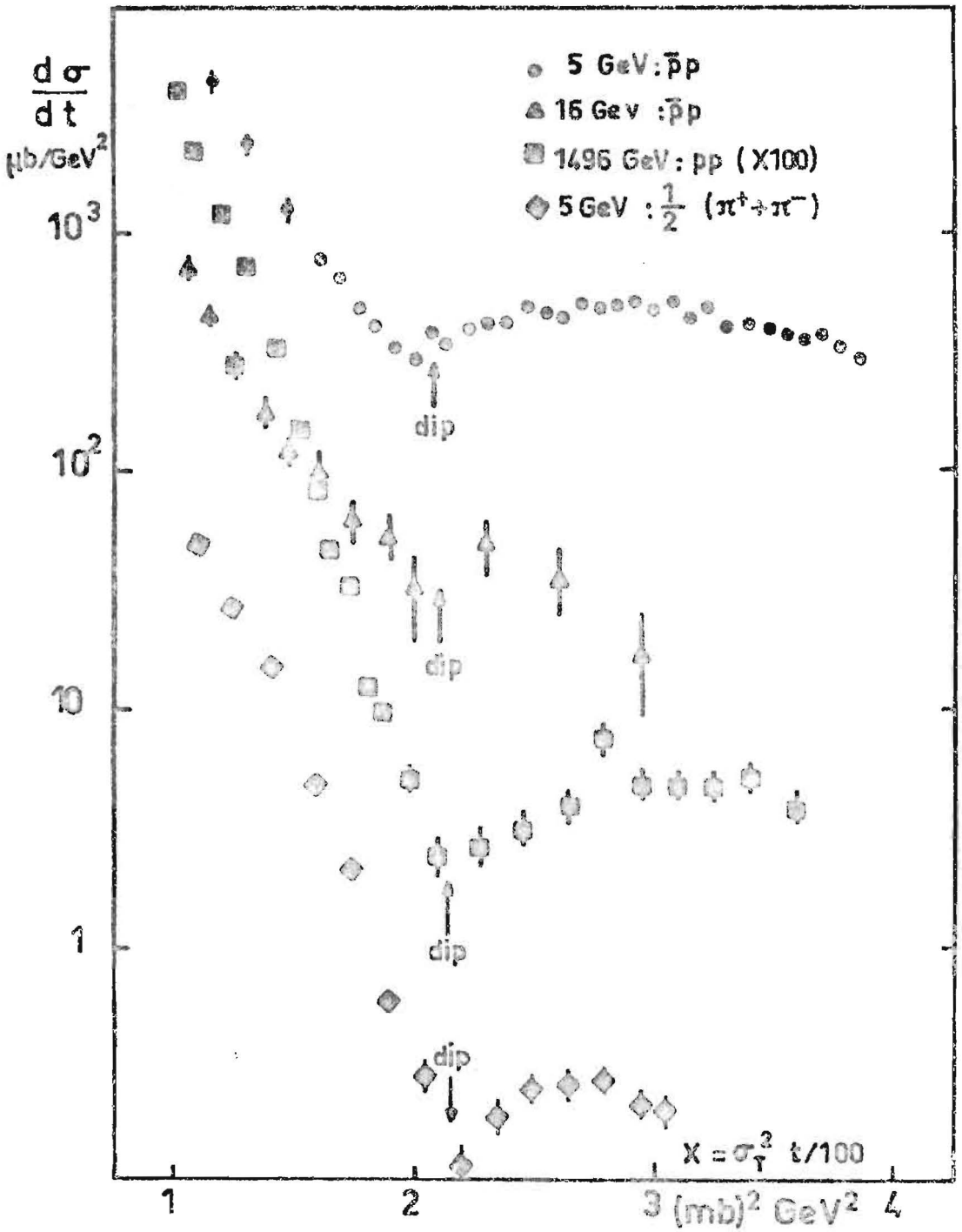

Figure 5.4 Diffraction dips observed in πp, pp and $\bar{p}p$ collisions; figure taken from ref. 9.

the diffraction minima in πp, Kp and pp collisions at various other values of t. If the matter distribution in impact space b is a Gaussian, $\mathrm{Im}f(b) = e^{-b^2/4A}$, then the Fourier transform is $\mathrm{Im}f(t) \sim A\, e^{At}$ but this distribution does not contain a diffraction peak zero. Similarly, if we assume that the proton is a black disk in impact parameter space we get (optical model)

$$\mathrm{Im}f(t) \simeq R^2 \frac{J_1(R\sqrt{-t})}{(R\sqrt{-t})}$$

and at small $|t|$ we have $\mathrm{Im}f(t) \to R^2\, e^{R^2 t/8}$ or a slope parameter, $b = R^2/4$. But there is no zero at the observed values! Tran Thanh Van[9] has chosen a modified Gaussian in impact parameter $\mathrm{Im}f(b) = e^{-b^2/4A}\, I_o(\frac{b}{bo})$ where $I_o(x)$ is the Hankel function and $x \to 0$, $I_o(x) \to e^{x^2/4}$, while for $x \to \infty$, $I_o(x) \to e^x$. The amplitude in momentum transfer space is $\mathrm{Im}f(t) \sim e^{At}\, Jo(\frac{A\sqrt{-t}}{2b_o})$ which has just the right zero as in pp scattering. His arguments indicate that a quantity $\sigma_T^2 t_{dip}$ should be a universal value for hadron interactions. Thus πp, Kp, pp and $\bar{p}p$ all satisfy the relation

$$\sigma_T^2\, t_{dip} = \text{constant} \quad .$$

The data are shown in Fig. 5.4 and the location of the dip is remarkably stable. The meaning and dimensions of $\sigma_T^2\ t_{dip}$ are however more obscure.

5.4 Elastic Scattering and σ_T Models

Recent ISR data have shown a remarkable increase in σ_T. This data admits many parametric interpretations, but one good set of parameters that continue to describe even low energy data down to 4 GeV is given by Leader and Maor[10]. They have,

$$\sigma_T = 38.4 + .49\ \ln^2 (s/122) \ .$$

According to this parametrization they form (from the optical theorem)

$$\mathrm{Im} f(s,o) \simeq 38.4 + .49s\ \ln^2 (s/122)$$

where the normalization is

$$\frac{d\sigma}{dt} = \frac{1}{s^2}\ |f(s,t)|^2 \qquad (4)$$

Going further they form at any t value

$$f(s,t) = i\ s\,[Ce^{\frac{1}{2}\beta_o t} + D\ell n^2(s/s_o)e^{\frac{1}{2}b_o t\ \ell n^2(s/s_o)}], \qquad (5)$$

with β_o and b_o constants. The second term dominates in the region $|t| \leq \ell n\ \ell n\ s/\ell n^2 s$ but otherwise the first term is most important. Using the fact that the slope, past the "break" at $|t| \simeq .15$, tends to a constant, they define $\beta_o = 10.8$. Furthermore, they use $b_o = 5.0\ (\mathrm{GeV}/c)^{-2}$. From Eqs. (4) and (5) one gets the logarithmic slope $b(s,t)$. The important fact is that there is no distinct break in $d\sigma/dt$ but a continuous increase in the value of $b(s,t)$ at low $|t|$ for values of s larger than s = 100.

The predictions of such a model are:

(a) Apparent "break" moves to lower $|t|$ as s increases.

(b) $b(s,o) \underset{s\to\infty}{\simeq} \ell n^2 s$; therefore extrapolation to t = 0 should be done very carefully. However, for $s \lesssim 750\ \mathrm{GeV}^2$ (as in our data) the error should be much less than 1%.

(c) $\sigma_T \sim \ell n^2 s$ and $\sigma_{el} \sim \ell n^2 s$.

(d) the term $e^{\frac{1}{2}\beta_o t}$ can be replaced with $e^{\frac{1}{2}\beta_o n^2}$ (ref. 4) in order to be compatible with lower energy slopes. Our data are not at large enough s to test these predictions.

In general, there is a correlation between a growing σ_T and the break at $|t| \simeq .15$. This correlation is

largely model independent.

Barshay and Rostokin[11] make use of the rising total pp cross section to form the scattering amplitude

$$F(s,t) = N\left[\frac{A}{f(s)} + \frac{1}{\frac{4m_\pi^2}{g(s)} - t}\right] e^{bt} \qquad (6)$$

with $\frac{d\sigma}{dt} = \pi\ |F(s,t)|^2$ and $s_o = 2810\ \mathrm{GeV}^2$ where $f(s) = 1 + \alpha\ \ell n(s/s_o)$ and $g(s) \simeq 1 + .2\ \ell n(s/s_o)$. The first term is a simple exponential; the second, is a pole-like contribution. The parametrization $F(s,t)$ works well to represent the break; this parametrization gives a continuously changing slope below $|t| \simeq .2$ and of course the total cross section is also well represented, asymptotically. In an eikonal formulation, $F(s,t)$ can be given by

$$F(s,t) \simeq \int_0^\infty bdb\ J_o(b\sqrt{-t})(1 - e^{-\delta(s,b)}) \qquad (7)$$

where $1 - e^{-\delta}$ is an overlap function. The Bessel inverted Eq. (7) gives (as $s \to \infty$)

$$1 - e^{-\delta(s,b)} \to C_1(s)\ e^{-b^2/2R_1^2} + C_2\ K_o(b/R_2(s))$$

with

$$C_1(s) = C_1/(1 + \alpha \ln(s/s_o)$$

$$R_1 = \sqrt{2b}$$

$$R_2(s) \simeq (1 + .2 \ln(s/s_o)/2m_\pi$$

The overlap function corresponds to two regions:

- one fixed radius R_1 = .6 fermi with decreasing strength of interaction
- interaction is approximately constant, but the radius increases logarithmically.

5.5 Shadow Scattering Approach

Diffraction scattering is thought of in the sense that the observed elastic scattering results from the shadow of all other scattering (inelastic). Direct channel unitarity being applicable, one obtains a relation between the total and inelastic differential cross sections[12] and the scattering problem takes on a simple form in impact parameter space. The formation of a Gaussian inelastic differential cross section

$$\frac{d\sigma_{in}}{d\underline{b}^2} \equiv G(b,s) \qquad (8)$$

(where $\underline{b}$ is the two-dimensional impact parameter vector) is phenomenologically motivated by the observation that the proton opacity (the ratio σ_{el}/σ_T) is approximately constant and just below the van Hove limit of .185 (see Fig. 5.5). Various other opacities are obtained according to the assumed shape and structure of the proton. Thus a proton that resembles a black disc (giving complete absorption) yields an opacity of one half, while an opacity of one quarter is derived from a diffraction peak exponential in t. Data do not warrant the selection of any but a Gaussian inelastic overlap function, G(b,s), at least in the energy range $40 < p_{lab} < 1500$ GeV/c. Slight modifications of the overlap function in order to better fit the observed differential cross sections indicate the possible existence of an effect, such that the edges of the proton are slightly more pronounced than those of a Gaussian shape.

In the shadow approach, the relation between the total, elastic and inelastic differential cross sections is

$$\frac{d\sigma_T}{d\underline{b}^2} = \frac{d\sigma_{el}}{d\underline{b}^2} + \frac{d\sigma_{in}}{d\underline{b}^2} \quad .$$

The shapes of the cross secitons $\frac{d\sigma_T}{d\underline{b}^2}$ and $\frac{d\sigma_{el}}{d\underline{b}^2}$ are given as (see Fig. 5.6)

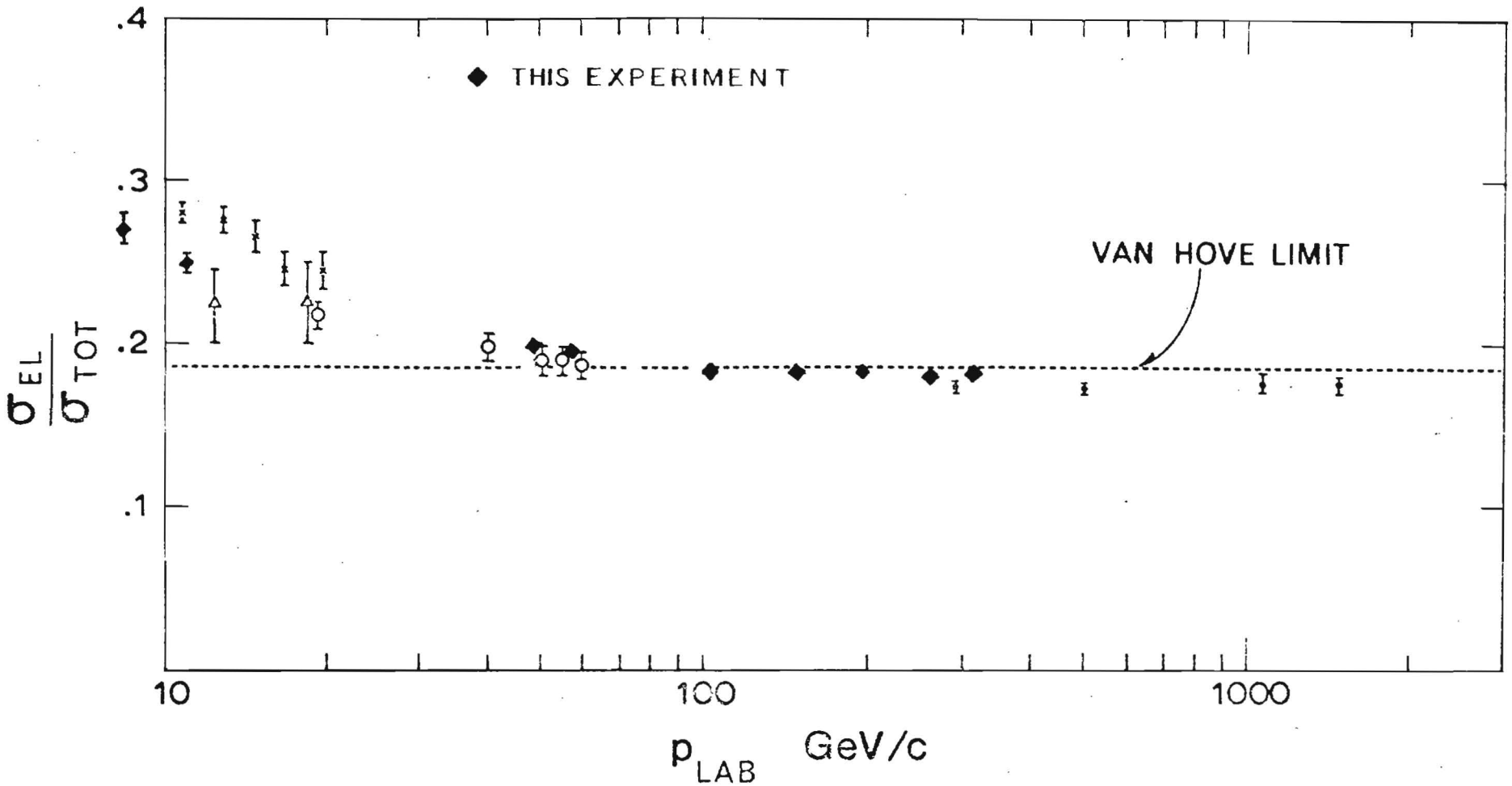

Figure 5.5 The opacity of the proton, $\sigma_{e\ell}/\sigma_T = 1 - \sigma_{incl}/\sigma_T$. Figure taken from ref. 13.

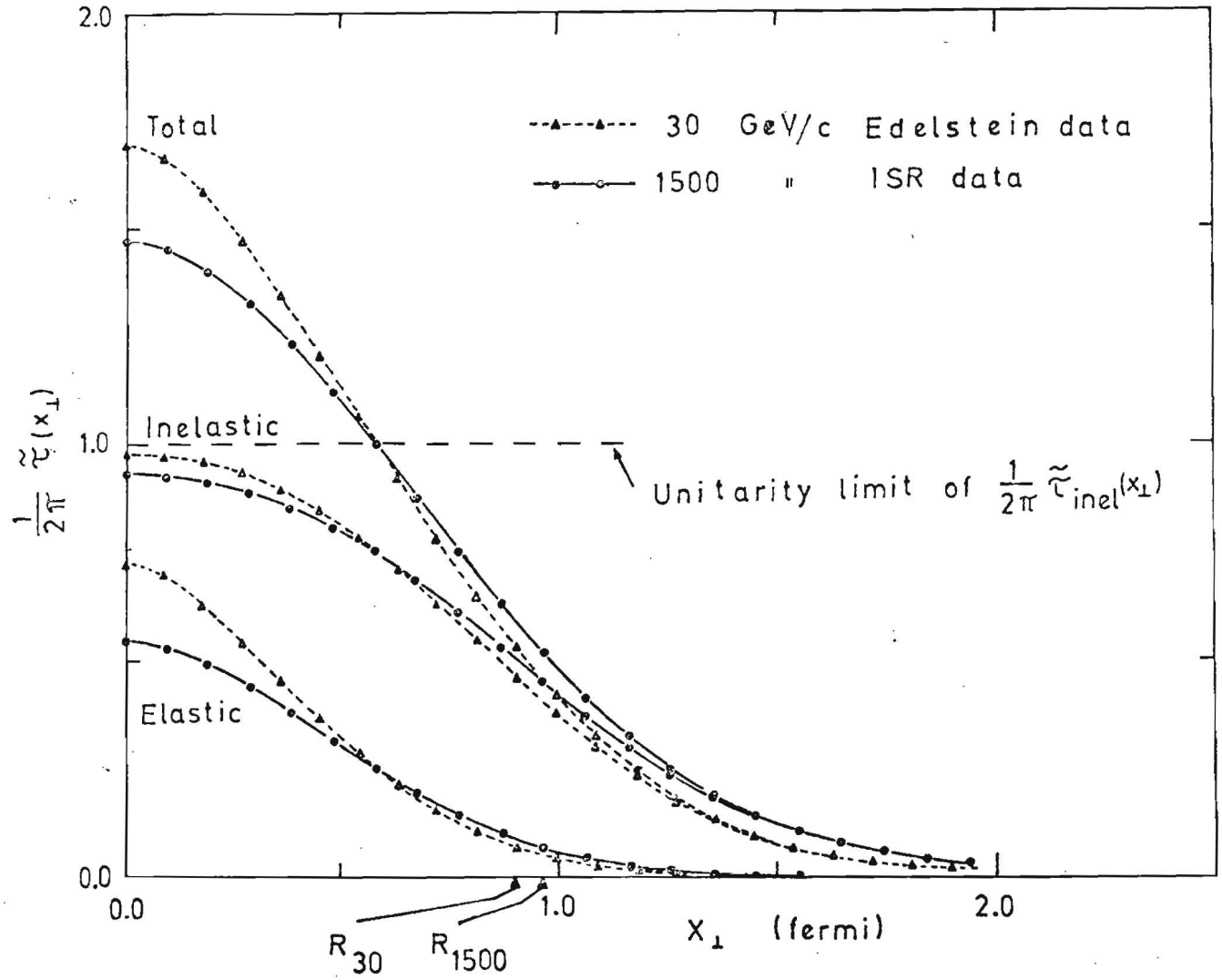

Figure 5.6 The total elastic and inelastic overlap functions. The quantity $\frac{1}{2\pi}\tau_{inel}(x\ )$ is analogous to G(b,s) used in the text; figure taken from ref. 13.

$$\frac{d\sigma_T}{d\underline{b}^2} = 2(1 - \sqrt{1 - G(b,s)}) \tag{9}$$

$$\frac{d\sigma_{el}}{d\underline{b}^2} = (1 - \sqrt{1 - G(b,s)})^2 \ . \tag{10}$$

The respective differential cross sections in momentum transfer space, t, are obtained by the Fourier-transforms of Eqs. 8, 9 and 10.

Calculations[13] in the spirit of the shadow approach reproduce the data on the differential cross section very well. Dips in $d\sigma/dt$ are fit satisfactorily, but the size of the minima is determined by the real part of the scattering amplitude, which the models do not predict. Depending on the choice for an inelastic overlap function G(b,s), the small $|t|$ break can be predicted; the break essentially is the result of peripheral scattering from the larger edge of the proton than might be found in a Gaussian overlap function.

The van Hove limit cannot be indefinitely satisfied if σ_T grows as $\ell n^2 s$ in which case the opacity tends to one half. The model of Cheng, Walker and Wu[14], which was developed before the I.S.R. data on the rising σ_T were obtained, predicts both the rise in σ_T and the asymptotic limit $\sigma_{el}/\sigma_T = 1/2$. This model is a phenomenological

description, based on Quantum Electrodynamics, of the field theory of massive photons. Aided by relativistic Lorentz contraction, the authors are able to sum all the graphs contributing to the scattering amplitude and obtain an effective coupling constant for hadron dynamics. As a result of the model two distinct regions of interaction are discerned in the proton. A black core, whose radius grows as $\ln s$, is completely absorbing for the incoming wave and contributes the dominant part of elastic scattering. A grey fringe, whose width is constant but whose radius grows as $\ln s$, is attributed the bulk of diffractive inelastic processes.

As a consequence of the growing radius, the total cross section grows asymptotically as fast as $\ln^2 s$. Due to the two distinct regions a break in the differential cross section is predicted (independent of parameters) at about $|t| = .15\ (\mathrm{GeV}/c)^2$. Diffraction pattern dips are also predicted (see Fig. 5.7) (but the locations are input). The slope parameter, b, is predicted to exhibit the indefinite shrinkage of the diffraction peak and as a result the diffraction dips are predicted to move in toward $t = 0$.

The model makes use of all πp, Kp, pp and $\bar{p}p$ information to adjust its rather large number of parameters (fourteen). All total cross sections (πp, Kp, pp, $\bar{p}p$)

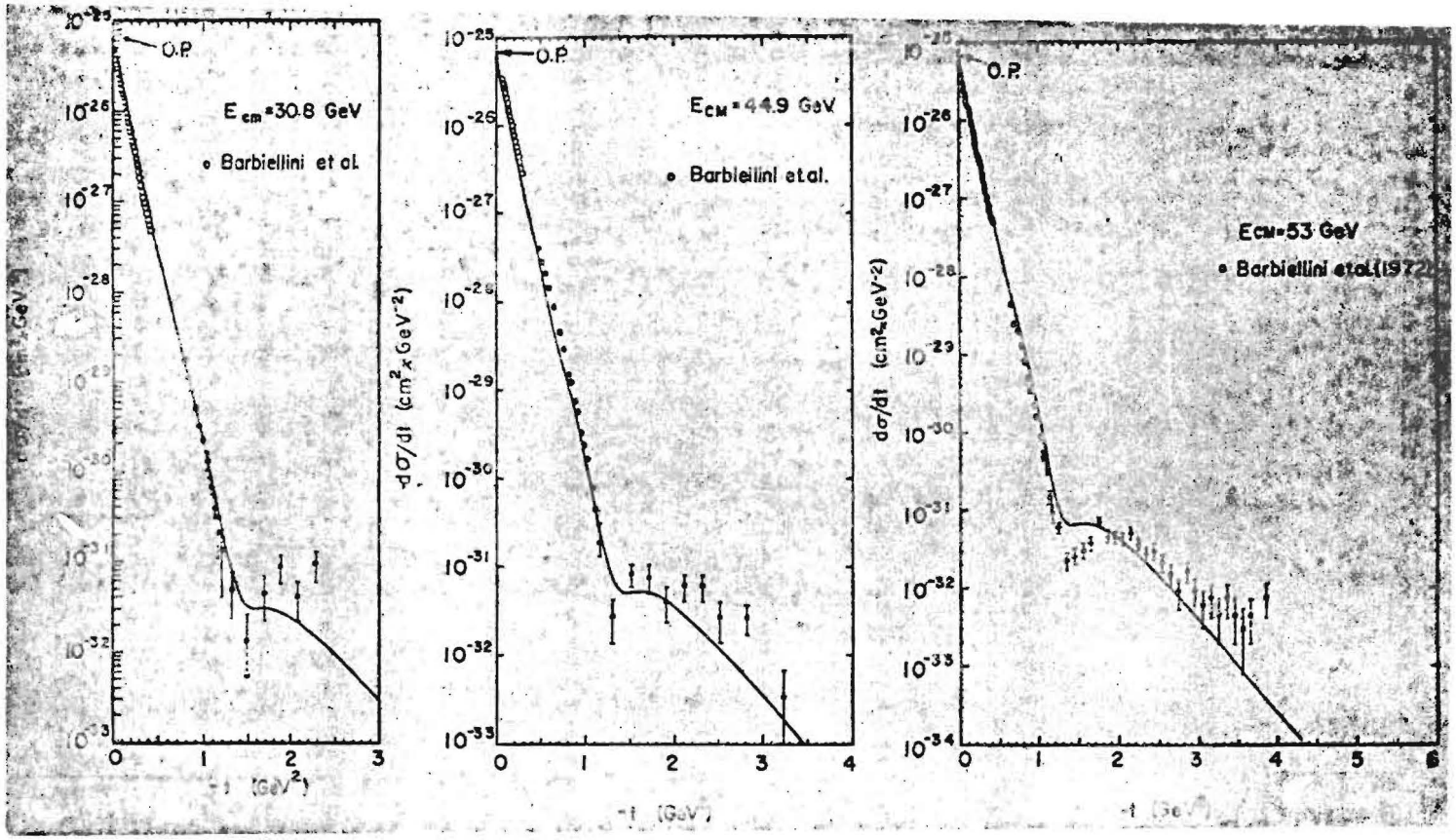

Figure 5.7 Proton-proton differential cross sections with model fits; figures taken from ref. 14.

are predicted to rise (see Fig. 5.8). Predictions on the real to imaginary ratio are given in Fig. 5.9, with a possible maximum at 10^4 - 10^5 GeV.

From the point of view of the experimentalist, the drawback of the model of Cheng, Walker and Wu is that the asymptotic behavior predicted is reached very, very slowly.

5.6 Regge Models

The Regge description of particle scattering is attractive, useful and extremely varied in its particular applications[15]. We have already described an analysis of data in Chapters III and IV in terms of the single Regge pole exchange. Further comparisons of data with Regge models based on multiple poles, Regge cuts and complex poles are given below.

The simplest extension of the single Regge pole exchange, which is postulated to be the Pomeranchuk pole, is the introduction of other poles[16]. In pp scattering P' and ω are the usual additional poles. While the Pomeranchuk pole can account for a constant asymptotic cross section, the P' and ω poles can account for the energy dependence observed at the usual machine energies (especially the falling σ_T in $\bar{p}p$ which is assumed to be

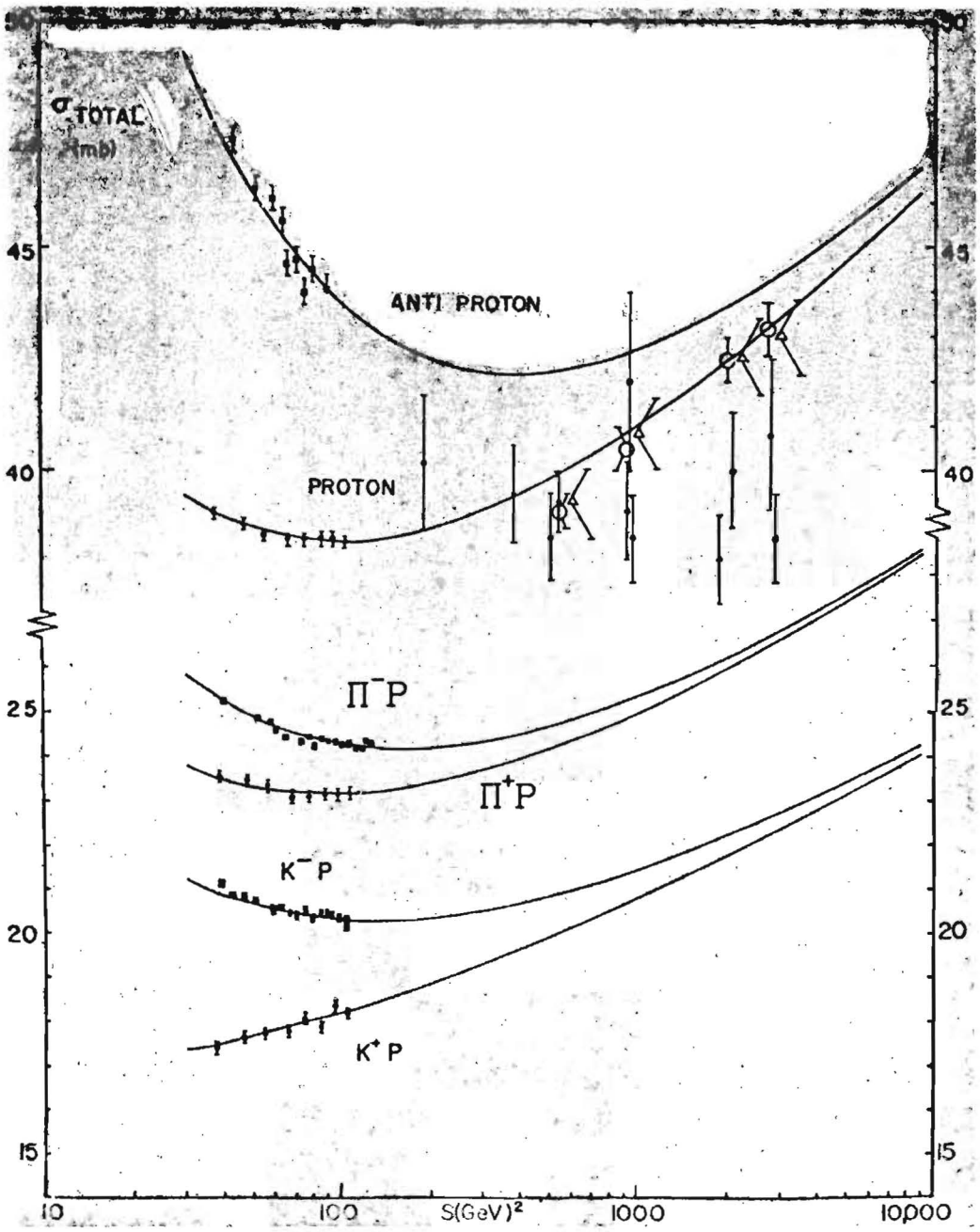

Figure 5.8 Total hadron-proton cross sections with model fits; figures taken from ref. 14.

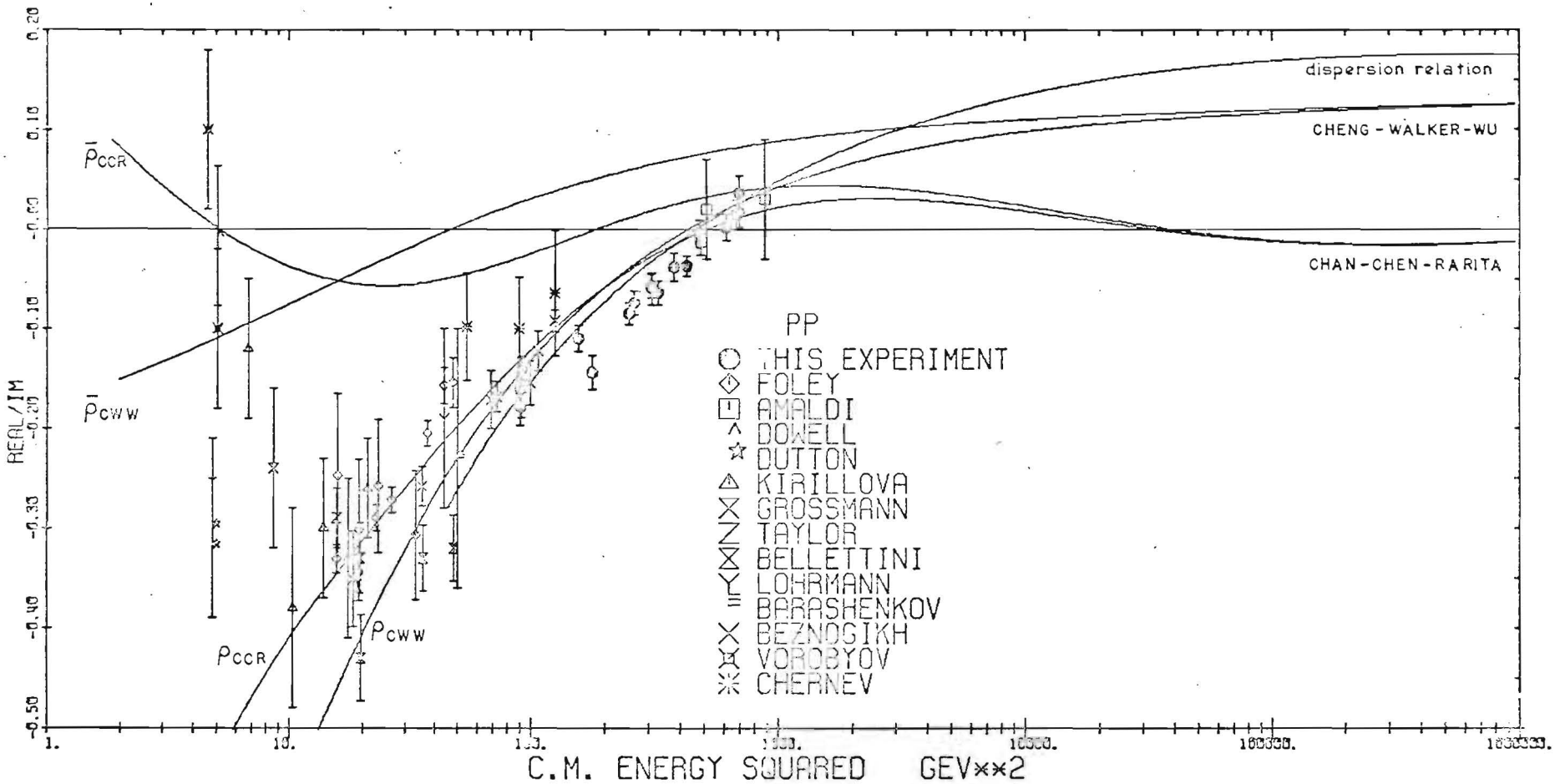

Figure 5.9a Predictions of the models by Cheng, Walker and Wu, and by Chan, Chen and Rarita for the real-to-imaginary ratio at high energies. Our data was not included in the fits, nevertheless our data agrees well with both predictions, in the N.A.L. energy range.

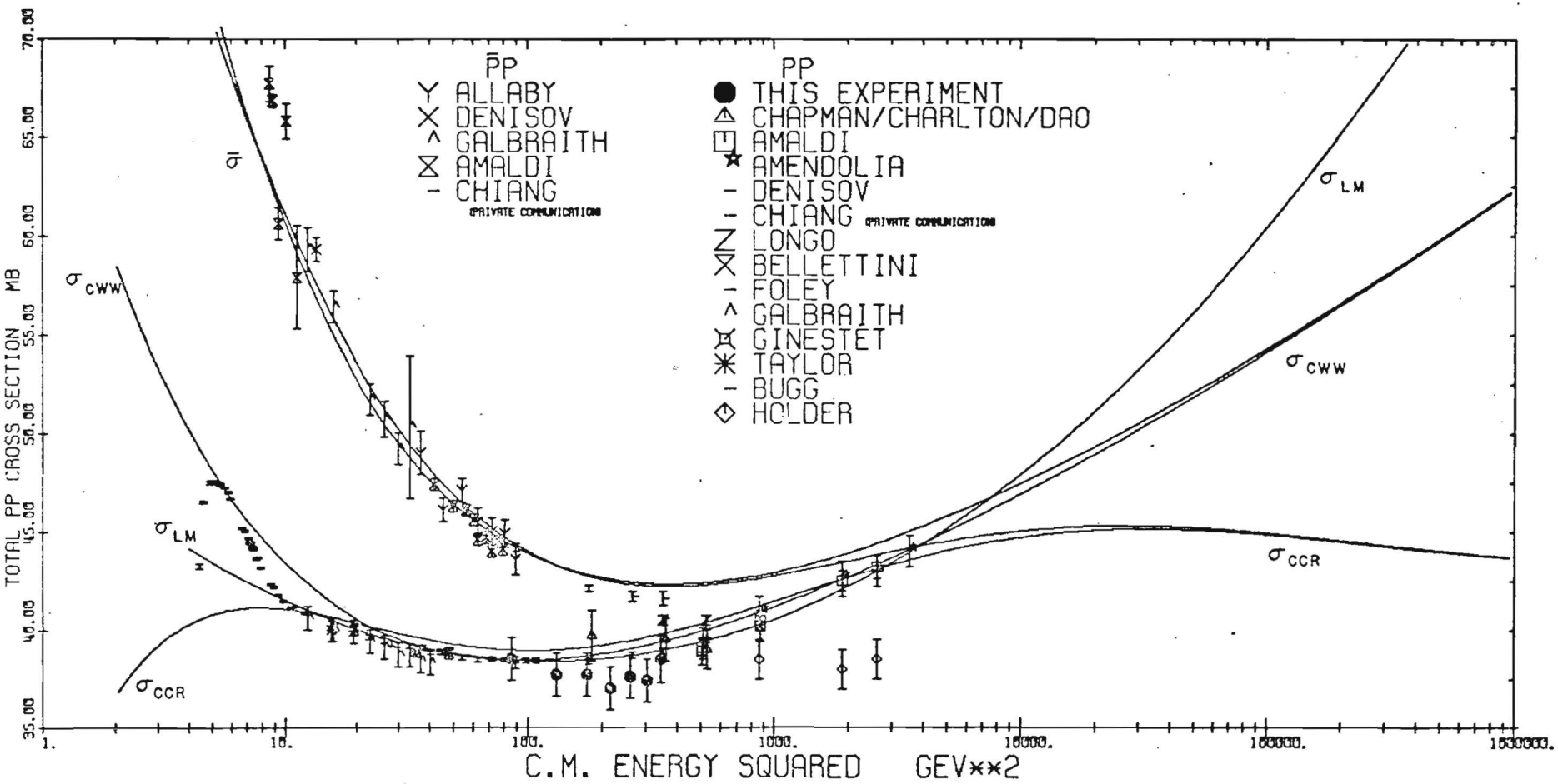

Figure 5.9b Predictions for the total cross sections by models of Cheng, Walker and Wu (CWW), and by Chan, Chen and Rarita (CCR). The parametrization of Leader and Maor (LM) is also indicated.

an interference between P' and ω poles). Recall that the Pomeranchuk trajectory has a postulated intercept of 1 in the Chew-Frautschi plot, but all the other trajectories are below the Pomeron in the $t < 0$ region. The usual intercepts from fits or assumptions are $\alpha_{P'}(o) \cong \alpha_{\omega}(o) \cong 1/2$. Therefore the total cross sections can be expressed as $\sigma_T(s) = a \cdot s^{\alpha_P(o)-1} + bs^{-1/2}$ where the a is the residue of the Pomeranchuk pole. Clearly such a behavior is in contradiction with the now known data on σ_T at the ISR, NAL and Serpukhov. The introduction of more poles will not improve the situation, but can be regarded as somewhat successful at least at low energies, (say $\lesssim$ 20 GeV) where most cross sections are still falling with energy*.

The next step in complexity is to assume the contribution of cuts[17]. Cuts are generated by the simultaneous exchange of two Regge trajectories and are known from Regge theory to obey the following relation

$$\alpha_{cut}(t) = \alpha_1(t/4) + \alpha_2(t/4) - 1$$

where $\alpha_1(t)$ and $\alpha_2(t)$ are the descriptions of the colliding Regge trajectories. The amplitude obtained

*Except possibly for K^+p which is exotic and non-Pomeron poles are assumed to cancel their imaginary contributions to the scattering amplitude; and pp, in which dual quark diagrams are impossible without exotic intermediate states.

from vacuum cuts (exchange of the Pomeranchuk or vacuum trajectory with other lower trajectories) is of the form

$$f \cong ia - \frac{i\gamma_c}{\ln^{\nu}(-is/s_o)} + \text{(lower lying Regge poles)}.$$

The first term is the Pomeron contribution; the second term is the cut. It should be noted that the cut term is very slowly changing due to the $\ln s$ denominator and is falling. This term then provides the necessary interference at lower energies ($s \simeq 100\ \mathrm{GeV}^2$) where the all hadron-hadron cross sections have a minimum. The cut term slowly disappears at higher energies (as do the other pole terms) and what is left is the Pomeranchuk contribution which is a plateau somewhere above current cross sections. This behavior is not in disagreement with total cross section data and was specifically introduced to account for Serpukhov K^-p (then $\sigma_T K^+p$ was predicted to rise) in order to avoid a possible violation of the Pomeranchuk theorem.

The elastic differential cross section data from Serpukhov, NAL and ISR are shown in Fig. 5.2. The obvious disagreement between the single Regge pole description of the slope parameter, $b(s) = b_o + 2\alpha'\ln s$ and the data, motivated Barger, Geer and Phillips[18] to introduce a phenomenologically suggested dependence,

$$b(s) = b_o + b_1 s^{-1/2}$$

They have succeeded in providing an explanation for this behavior by the interference between a non-shrinking Pomeranchuk term and other Regge poles. The data may well fit such a dependence but mention must be made that different systematic errors in the Serpukhov data and the NAL data produce different slopes in the (50-70) GeV region. Nevertheless the continuously changing slope of the effective one pole trajectory is rather well reproduced (beyond 10 GeV) and an asymptotic slope parameter is predicted. The $\bar{p}p$ data seem to already have reached such a value (approximately 12.7 $(\mathrm{GeV}/c)^{-2}$).

The possible oscillatory behavior of the total cross sections as a function of energy motivated Chew and Snider[19] to consider a model which involves complex Regge poles. More recently Chan, Chen and Rarita[20] have considered a specific introduction of the poles P, P', and ω plus a pair of complex poles (for the pp and $\bar{p}p$ data). The parametrization of the cross section and the real to imaginary part is given as:

$$\sigma_T^{PP} = C_P[1 + 2|\beta_c|s^{\alpha_R - 1}\cos(\alpha_I \ln s + \underline{|\beta_c}) + \beta_{P'}s^{\alpha_{P'} - 1} + \beta_\omega s^{\alpha_\omega - 1}]$$

$$\rho^{PP} = C_P[-2|\beta_c||\cot\tfrac{1}{2}\pi\alpha_c|s^{\alpha_R - 1}\cos(\alpha_I \ln s + \underline{|\beta_c} + \underline{|\cot\tfrac{1}{2}\pi\alpha_c})$$

$$-\cot(\tfrac{1}{2}\pi\alpha_{P'})\beta_{P'}s^{\alpha_{P'} - 1} + \tan(\tfrac{1}{2}\pi\alpha_\omega)\beta_\omega s^{\alpha_\omega - 1}]/\sigma_T^{PP}$$

the β's are the residues of the c, P, P' and ω. $\lfloor\beta_c$ is the phase of β_c and $\alpha_P = 1$ is assumed. While there are 9 free parameters, the model has been very successful with pp and $\bar{p}p$ data, but also allows extension to other particle data and other physical parameters such as: slope parameters and pion multiplicities. Damped oscillations in all these physical parameters are predicted (due to the ℓns phase of the cosine terms). The total cross section σ_T is predicted to have a maximum at $s = 3 \times 10^4$ GeV^2. The ratio ρ has the same periodic variation in ℓns but the phase is about 1/4 cycle ahead of the phase for σ_T and it has possibly a maximum at $s = 1000\text{-}2000$ GeV^2. Optimistically, this prediction can be tested on present machines even though it is difficult to measure ρ at the highest ISR energies; more accurate data at NAL seems a possible alternative. The future experimental confirmation about the oscillatory behavior would be strong evidence for the complex Regge poles. Figure 5.9 shows the data and the fits (our data, shown by the crosses, is not included in the ρ fit, although they seem nevertheless to be in accord with the model).

5.7 Bounds from Quantum Field Theory

High energy theorems in the form of bounds[21] can be derived using the following properties of the scattering amplitudes:

1. analyticity
2. unitarity
3. polynomial boundedness of the amplitude $F(s,t)$ at fixed t as $s \to \infty$.

Special theorems, such as the Pomeranchuk theorem are derived using extra assumptions. Alternatives to the Pomeranchuk theorem are also available.

The Pomeranchuk theorem states that the ratio of the cross sections (total and diffractive) for particle and antiparticle collisions with the target goes to unity as the energy diverges. Certainly current data have not yet reached the stage of high enough energy to check the theorem, but the cross sections for particles and antiparticles are approaching slowly. There does not seem to be justified yet the assumption that the Pomeranchuk theorem may be violated in the situation in which σ_T and $\bar{\sigma}_T$ approach different constants at high energy. If such a violation occurred, then from dispersion relations one could predict that the ratio, ρ, would increase as the logarithm of the c.m. energy. From our results such a

behavior is denied. However, such a point of view is completely contrary to the prevailing intuitive picture that at high energies, the elastic scattering is a consequence of absorption.

a) Forward Scattering Theorems

The Froissart bound for the total cross section states that the maximum rate of growth in $\sigma_T(s) \leq \frac{\pi}{\mu^2} \ln^2(s/s_o)$ where s_o is some unknown constant and μ is the pion mass. The coefficient π/μ^2 is about 60 mb and therefore this bound is far from violated even if the rate of growth is $\ln^2(s/s_o)$ at current energies; the coefficient that comes from data is about .2 to 1 mb and $\sigma_T(s) \leq \frac{\pi}{\mu^2} \ln^2(s/s_o)$ is satisfied. If the scattering amplitude is normalized as $\frac{d\sigma}{dt} = \frac{|F(s,t)|^2}{16\pi s^2}$ the optical theorem (spin-independent amplitude) gives $\mathrm{Im}F(s,o) = s\sigma_T(s)$. Together with the previous bound on $\sigma_T(s)$ and the tendency to zero of the ratio $\rho = \mathrm{Re}F(s,o)/\mathrm{Im}F(s,o)$, we get $|F(s,o)| \leq \frac{\pi}{\mu^2} s\ln^2(s/s_o)$.

We have

$$\left.\frac{d\sigma_{el}(s)}{dt}\right|_{t=0} = \frac{\sigma_T^2(1+\rho^2)}{16\pi} \sim \frac{\sigma_T^2}{16\pi} \quad . \tag{11}$$

There is an upper bound on the previous relation, as follows:

$$\left.\frac{d\sigma_{el}(s)}{dt}\right|_{t=0} \leq \frac{1}{16\mu^2}\, \ell n^2(s/s_o)\ \sigma_{el}(s) \qquad (12)$$

Using Eqs. (11) and (12) we obtain $\sigma_T^2(s) \leq \frac{\pi}{\mu^2}\, \ell n^2(s/s_o)\sigma_{el}(s)$. But we know from the data that the opacity σ_{el}/σ_T is finite and quite stable at about .185 (van Hove limit), therefore the relation approachs, in form, the Froissart bound, which is satisfied ($6\ \sigma_T(s) \lesssim 60\ \ell n^2(s/s_o)$).

The real to imaginary ratio is also bounded as in

$$|\mathrm{ReF}(s,o)/\mathrm{ImF}(s,o)| \leq \frac{\pi}{\mu^2}\ \ell n(s/s_o)\ \sigma_{el}^{1/2}/\sigma_T$$

If we put in the numbers the right side becomes about $4\ \ell n(s/s_o)$ numerically, while the left side is of the order of 10%. Similarly a weaker bound is

$$|\mathrm{ReF}(s,o)/\mathrm{ImF}(s,o)| \leq \frac{\pi}{\mu^2}\ \ell n(s/s_o)/\sigma_{el}^{1/2}$$

in which case the right side is numerically about $25\ell ns/s_o$.

b) <u>Diffraction Peak Bounds</u>

The logarithmic derivative of the forward scattering amplitude has both a lower and an upper bound. We have

$$\frac{1}{2}\, b(s) \equiv \left[\frac{d}{dt}\, \ell n|F(s,t)|\ \right]\Big|_{t=0} \leq c\ \sigma_{el}^{1/2}(s)\ \frac{s\ell n^3(s/s_o)}{|F(s,o)|}$$

We use the optical theorem and get

$$\frac{1}{2}\, b(s) \leq c\sigma_{el}^{1/2}(s)\ \frac{s\ell n^3(s/s_o)}{s\sigma_T(s)} = c(\sigma_{el}/\sigma_T)^{1/2}\ \frac{\ell n^3(s/s_o)}{\sigma_T^{1/2}}$$

or

$$\frac{1}{2}\, b(s) \leq .4c\ \frac{\ell n^3(s/s_o)}{\sigma_T^{1/2}}$$

Even if the total cross section were to rise as $\ell n^2 s$, still the bound would not be reached at present rates of increase in b(s), because b(s) seems to grow at most as fast as ℓns. Asymptotically, however, b(s) will have to grow as fast as $\ell n^2 s$ if unitarity is not to be violated. Recall that in models like the one of Leader and Maor, where b(s) actually has a t dependence at low $|t|$, the bound may soon be reached (at a few TeV).

On the lower bound we know that

$$b(s) \geq \frac{1}{18}[\sigma_T^2/\ \pi\sigma_{el} - 1/k^2]$$

where k is the c.m. momentum. Putting in the proper

numbers we have

$$b(s) \simeq 5 \text{ mb} \gtrsim \frac{1}{18}\left[\frac{(40)^2}{\pi \cdot 6} - \frac{1}{k^2}\right]$$

The relation is satisfied even for $k = \infty$; then the right side equals about 4 mb. The question again becomes an asymptotic one; will b(s) increase fast enough to allow the σ_T^2/σ_{el} to be smaller than b(s) itself?

c) Fixed t bounds

One relation required for the elastic differential cross section at any $t < 0$ is

$$\frac{d\sigma_{el}}{dt} \leq \left[\frac{\ln(s/s_o)\sigma_{el}}{4\pi\mu(-t)^{1/2}}\right]$$

We again use $\left.\frac{d\sigma_{el}}{dt}\right|_{t=0} \simeq \frac{\sigma_T^2}{16\pi}$ and the exponential behavior of

$$\frac{d\sigma}{dt} \simeq \frac{\sigma_T^2}{16\pi} e^{bt} \leq \frac{\ln(s/s_o)\sigma_{el}}{4\pi\mu(-t)^{1/2}} \quad \text{then}$$

$$e^{bt}(-t/\mu^2)^{1/2} \leq \frac{4\ln s/s_o}{\sigma_T \mu^2}\left(\frac{\sigma_{el}}{\sigma_T}\right) \cong \frac{11\ln(s/s_o)}{\sigma_T}$$

The maximum on the left side occurs at about $t = 1/2b$, or $.05\ (\text{GeV}/c)^{-2}$ and in that case the left side becomes roughly 1. Certainly the bound is very close and if σ_T

rises as $\ln^2 s$ the right hand side can only decrease.

d) Lower Bound Theorems

There are some lower bound theorems which, according to the data available, are trivially satisfied, because of the weakness of the bounds. One bound is

$$|F(s,o)| \geq c/s^2.$$

This bound, in conjunction with the optical theorem and a rising or even flat cross section, is doubtless satisfied.

The bound on the total cross section $\sigma_T(s)$ is even better satisfied because the lower limit on σ_T is

$$C'/(s^6 \ln^2(s/s_o))$$

The exercise of going through these bounds is satisfactory at this point and at least for the pp collision, there seems to be not even a close miss for any bound. On the other hand, these bounds are supposed to give us confidence that the axioms of QFT are justified, but we cannot say anything critical about these axioms, except that they are eminently satisfactory at the present time.

5.8 Asymptotic Behavior in Some Models

Here we list some of the expected asymptotic behavior[22] of the quantities: the total cross section, the real to imaginary parts, the diffraction slope b (1/b is the slope width), the optical point $\left.\frac{d\sigma}{dt}\right|_{t=0}$ and the opacity σ_{el}/σ_T as $s \to \infty$.

What seems to be happening at the moment in terms of elastic scattering data is:

σ_T rises as $\ln s$ or $\ln^2 s$,

b rises at most as $\ln s$ or may approach a constant,

ρ crosses zero at about 300 GeV, but asymptotic behavior is not yet known.

The ratio σ_e/σ_T seems stable at the van Hove limit of .18. Among the asymptotic behaviors listed in the table the most likely in terms of current data are the dipole Regge model and the complex Regge model. If actual oscillations do occur, as in the complex pole model, then these should likely be determined even with present machines (NAL and ISR), however there is the problem of the extremely stable opacity σ_e/σ_T which contradicts these models.

Table 5.1
Asymptotic Behavior

	Simple Regge Model	Pomeron violating model	Regge dipole model	Even signature Regge cut	Odd signature Regge cut	Poles + Complex Regge Poles
$\sigma_T(s)$	C	C_1, C_2	$c\ln s+c'$	$c-c'/\ln s$	$c\pm c'/\ln s$	c+ damped oscillations
$\rho(s)$	$\ln^{-1}s$	$c'\ \ln s$	c''	$c''\ln^{-2}s$	$c''\ln^{-1}s$	$s^{-1/2}$
$b(s)\equiv 1/\Delta(s)$	$\ln s$	$\ln^2 s$	$\ln s$	$\ln s$	$\ln s$	$\ln s$
$\left.\frac{d\sigma}{dt}\right\|_{t=0}=\frac{\sigma_T^2(1+\rho^2)}{16\pi}$	c	$\ln^2 s$	$\ln^2 s$	c	c	c
σ_{el}/σ_T	$\ln^{-1}s$	$\ln^{-2}s$	c'''	$\ln^{-1}s$	$\ln^{-1}s$	$\ln^{-1}s$

5.9 Summary

We have measured the quantities b, ρ and σ_T, and have presented here the results on b and ρ for proton-proton scattering.

The slope parameter, b, has been found to increase approximately as $\ln s$, with a slight curvature down. This may be due to saturation, oscillations, or merely a local effect. Saturation can be explained in a purely geometric model or through group-theoretical calculations[2,4] (although allowance for an increase has been built into the geometrical model based on the rise of the total cross section[2]). Oscillations may be produced in a complex Regge pole model; the overall behavior of the slope parameter is still an increase as $\ln s$ asymptotically. At present, it seems therefore that the inability to distinguish between the various possibilities is due to the order of accuracy of present experiments. Therefore, the variation of the slope parameter is not a very sensitive test for models; this may, in part, be a reflection of: the goodness of the forward diffraction slope parametrization as a pure exponential, and the location of the region of momentum transfer used in such parametrizations.

Based on more accurate data, it is conceivable that an investigation of the region of the "break" in the

differential cross section could be related, through impact parameter calculations, to the opacity of the proton, in order to obtain a clearer picture of the hadronic structure of the proton. The distinguishing of core and fringe regions as derived in some models[11,13,14], and the energy dependence of their dimensions can be very helpful insofar as optical diffraction models are applicable, while we lack knowledge of the dynamics of strong interactions.

The real-to-imaginary ratio, ρ, has been found to become positive at about 300 GeV. This is a sensitive test as to the rise of the total cross section because ρ and σ_T are related through dispersion relations. Based on our calculation it is possible to predict a rising cross section, up to a few thousand GeV, and indications are that causality is justified down to distances of the order of $5 \cdot 10^{-17}$ cm. Further accurate data on the real-to-imaginary ratio (see Fig. 5.9a) and the total cross section of antiproton-proton scattering will be valuable in distinguishing different energy variations for both the proton-proton and antiproton-proton cross sections at very high energies. Justification of the Pomeranchuk theorem will also be contained in such data.

References for Chapter V

1. C. Bourrely, J. Soffer, and D. Wray, Centre de Physique Theorique - C. M. R. S., 74/P.597; J. Soffer and D. Wray, Phys. Lett. 43B, (1973) 514.
2. A. D. Krisch, Phys. Rev. Lett. 19, (1967) 1149; A. D. Krisch, University of Michigan Report No. HE 72-24; a newer version of the Krisch model predicts $b \sim A^2\beta^2\sigma_T/\sigma_T(\infty)$ - A. D. Krisch, Phys. Lett. 44, (1973) 71.
3. R. A. Carrigan, Jr., Phys. Rev. Lett. 24, (1970) 168; this article points out the increase in the slope parameter at small $|t|$.
4. E. Leader and M. R. Pennington, Phys. Rev. Lett. 27, (1971) 1325.
5. S. Barshay and Y.-A. Chao, Phys. Lett. 38B, (1972) 225.
6. T. T. Wu and C. N. Yang, Phys. Rev. 137, (1965) 709.
7. T. T. Chou and C. N. Yang, Phys. Rev. 170 (1968) 1591.
8. L. Durand, III, and R. Lipes, Phys. Rev. Lett. 20 (1968) 637; the figures in Fig. 5.3 are taken from, a and b: J. V. Allaby et al., Nucl. Phys. B52 (1973) 316; and c from; The Aachen-CERN-Geneva-Harvard-Turin collaboration (data presented at the XVI Intern. Conf. on High-Energy Physics, Chicago, 1972).
9. J. Tran Thanh Van, Laboratoire de Physique Theoretique et des Particules Elementaries, Orsay, France, LPTHE-73/8 (1973).
10. E. Leader and U. Maor, Westfield College preprint, London (1973).
11. S. Barshay and V. Rostokin, University of Copenhagen Report (1973).

12. L. Van Hove, Rev. Mod. Phys. 36, (1964) 655; L. Van Hove, Theoretical Problems in Strong Interactions at High Energies, CERN, TH 65-22 (1965).

13. P. Heckman and R. Henzi, Phys. Lett. 41B, (1972) 189; R. Henzi and P. Valin, McGill University Report, (1973), (to be published); E. H. de Groot and N. I. Miettinen, Rutherford High Energy Laboratory Report No. RL-73-003 (1973); F. S. Henyey, R. Hong Tuan and G. L. Kane, University of Michigan Preprint - UM HE-73-18 (1973).

14. H. Cheng, J. K. Walker and T. T. Wu, preprint submitted to the XVI Intern. Conf. on High-Energy Physics, Chicago, 1972; H. Cheng, J. K. Walker and T. T. Wu, Phys. Lett. 44B, (1973) 97; Phys. Lett. 44B, (1973) 283; J. K. Walker, N.A.L. preprint NAL-Conf-73/28 (1973); H. Cheng and T. T. Wu, Phys. Lett. 45B, (1973) 367.

15. Some comprehensive reviews on the subject of Regge Poles can be found in: V. Barger, Rev. Mod. Phys. 40, (1968) 129; C. B. Chiu, Rev. Mod. Phys. 41 (1969) 640; G. E. Hite, Rev. Mod. Phys. 41 (1969) 669; J. D. Jackson, Rev. Mod. Phys. 42, (1970) 12; V. Barger and R. J. N. Phillips, Nucl. Phys. B32, (1971) 93; C. B. Chiu, Rev. Nucl. Phys. 22, (1972) 255.

16. D. M. Austin and W. Rarita, Phys. Rev. D4, (1971) 3507; V. Barger, R. J. N. Phillips and K. Geer, Nucl. Phys. B47, (1972) 29.

17. V. Barger and R. J. N. Phillips, Phys. Rev. Lett. 24, (1970) 291.

18. V. Barger, K. Geer and R. J. N. Phillips, Phys. Lett. 36B, (1971) 350; Phys. Lett. 36B, (1971) 343.

19. G. F. Chew and D. R. Snider, Phys. Lett. 31B (1970) 75.

20. C. F. Chan, C. K. Chen and W. Rarita, Phys. Lett. 47B, (1973) 512.

21. R. J. Eden, Phys. Rev. Lett. 16, (1966) 39; R. J. Eden, Rev. Mod. Phys. 43, (1971) 15; S. M. Roy, Physics Reports C5, No.3 (1972) 125; F. J. Yndurain, Rev. Mod. Phys. 44 (1972) 645.

22. R. J. Eden and G. D. Kaiser, Nucl. Phys. B28, (1971) 253.

23.a. References for σ_T:

Bartenev, PRL 29, 1755-72;

Chapman, PRL 29, 1686-72;

Charlton, PRL 29, 515-72;

Dao, PRL 29, 1627-72;

Amaldi, PL 44B, 112-73;

Amendolia, PL 44B, 119-73;

Denisov, PL 36B, 415-71;

I-H. Chiang - private communication;

Longo, PRL 32, 441-74;

Bellettini, PL 19, 705-66;

Foley, PRL 19, 857-67;

Galbraith, PR 138B, 913-65;

Ginestet, NPB 13, 283-69;

Taylor, PL 14, 54-65;

Bugg, PR 146, 980-66;

Holder - ACGHT, Batavia-72.

23.b. References for $\bar{\sigma}_T$:

Allaby, PL 30B, 500-69;

Denisov, PL 36B, 528-71;

Galbraith, PR 138B, 913-65;

I-H. Chiang - private communication;

24.a. References for b^{pp}; ($t \leq .1$):

Bartenev, PRL 29, 1755-72;

Bartenev, PRL 31, 1088-73;

Barbiellini, PL 39B, 663-72;

Amaldi, PL 36B, 504-71;

Beznogikh, PL 30B, 274-69;

Chernev, PL 36B, 266-71;

Bellettini, PL 14, 164-65;

Dalkhazhav, Sov. JNP 8, 196-69;

Ambats, PR 9D, 9-74;

Holder, PL 36B, 400-71;

Lasinski, PR 179, 1426-69.

b. References for b^{pp}; ($t \geq .1$);

Fujii, PR 128, 1836-62;

Clyde, UCRL rep. 16275;

Cork, PR 107, 859-57;

Harting, NC 38, 60-65;

Allaby, PL 28B, 67-68;

Foley, PRL 11, 425-63;

Holder, PL 36B, 400-71;

Barbiellini, PL 39B, 663-72.

c. References for $b^{\bar{p}p}$;

Foley, PRL 11, 503-63;

Birnbaum, PRL 23, 663-69;

Ambats - private communication;

Ambats, PR 9D, 9-74.

25. References for ρ^{pp};

Bartenev, PRL 31, 1367-73;

Foley, PRL 14, 74-65; PRL 19, 857-67;

Amaldi, CERN report Dec. 73;

Dowell, PL 12, 252-64;

Dutton, PL 26B, 679-68; PL 25B, 245-67;

Kirillova, JETP 23, 52-66;

Grossmann, Czech JP B17, 830-67;

Taylor, PL 14, 54-65;

Bellettini, PL 14, 164-65; PL 19, 705-66;

Lohrmann, PL 13, 78-64;

Beznogikh, PL 39B, 411-72;

Vorobyov, PL 41B, 639-72;

Chernev, PL 36B, 266-71.

APPENDIX A

In this appendix we refer to a phenomenological method of obtaining estimates of the inelastic contribution for different masses and various t values, $d^2\sigma/dtdM^2$.

The "empty target" subtraction presumably produces distributions without much background. One can obtain the central channel for histograms of both low and high energy jets. A rough estimate of elastic events can be achieved within (1-2)% accuracy. The low energy histogram is shifted (actually stretched) channel-wise until its elastic peak centers on the one from the high energy. Generally, 50 or 100 GeV data have extremely little inelastic contributions, at the t values we are working with. Therefore a direct subtraction, according to ratios of elastic events, of low from high energy histograms yields an inelastic distribution. Various manipulations can improve the accuracy of the simple process explained above. We did not attempt this procedure in our data analysis to any large extent. However, other members of our group undertook a complete analysis of inelastics data up to .1 $(GeV/c)^2$, obtained for diffraction peak analysis. Thesedata were presented at the Aix-en-Provence Conference (1973).